Contributions en simulation, expérimentation et modélisation destinées à l'analyse des instabilités de combustion hautes fréquences des moteurs fusées à ergols liquides

Manuel Gonzalez Flesca

NNT : 2016SACLC088

THÈSE DE DOCTORAT DE L'UNIVERSITÉ PARIS-SACLAY,

préparée à CentraleSupélec.

ÉCOLE DOCTORALE N°579

Sciences mécaniques et énergétiques, matériaux et géosciences.

Spécialité Combustion.

Présentée par

Manuel Sébastien GONZALEZ-FLESCA

Simulation, experimentation and modeling contributions to the analysis of high frequency combustion instabilities in liquid propellant rocket-engines

Thèse soutenue à Châtenay-Malabry, le 28/11/2016.

Composition du jury :

Mme. BAILLOT, Françoise, Professeur des Universités, Université de Rouen, Rapporteur
Mme. CUENOT, Bénédicte, Chercheur senior, HDR, CERFACS, Rapporteur
M. BAILLY, Christophe, Professeur des Universités, Ecole Centrale de Lyon, Président du jury
M. ROCCHI, Jean-Philippe, Ingenieur PhD, Airbus Safran Launchers, Examinateur
Mme. THERON, Marie, Ingenieur PhD, CNES - Direction des Lanceurs, Examinateur
M. CANDEL, Sébastien, Professeur des Universités, U. Paris-Saclay CentraleSupélec, Directeur de Thèse
M. DUCRUIX, Sébastien, Directeur de recherche, CNRS, U. Paris-Saclay CentraleSupélec, Co-Directeur de Thèse
M. SCHMITT, Thomas, Chargé de recherche, CNRS, U. Paris-Saclay CentraleSupélec, Co-encadrant de thèse

To my parents

Remerciements

Le travail présenté dans ce mémoire a été réalisé au laboratoire EM2C de l'école CentraleSupélec sous la direction de Monsieur le professeur Sébastien Candel. Je le remercie vivement d'avoir su m'orienter vers un domaine de recherche pour lequel je ressens un vif intérêt et de m'avoir apporté de précieux conseils pour la réalisation de ce travail.
Je tiens à remercier très sincèrement monsieur Sébastien Ducruix, Directeur du laboratoire EM2C, pour son encadrement et sa volonté d'améliorer la qualité de mon travail.
En cette occasion je tiens à témoigner toute ma reconnaissance à Thomas Schmitt, chargé de recherche au CNRS, pour l'aide prodiguée lors de la réalisation des nombreux calculs hautes performances.
Je tiens à remercier tout particulièrement Monsieur le professeur Christophe Bailly d'avoir accepté de faire partie du jury de cette thèse ainsi que Madame le professeur Françoise Baillot et Madame Bénédicte Cuenot, chercheur au CERFACS, d'avoir accepté de juger cette thèse et de tous les conseils donnés pour améliorer le manuscrit.
Je remercie aussi les partenaires industriels : le Centre National d'Etudes Spatiales et Airbus Safran Launchers en les personnes de Marie Théron et Jean-Philippe Rocchi pour leur participation au financement de ce travail et pour avoir apporté un point de vue industriel à ces recherches.
Que Monsieur Philippe Scouflaire, ingénieur de recherche au CNRS, trouve en cette occasion l'expression de toute ma reconnaissance pour l'aide plus que précieuse apportée pour la réalisation des dispositifs expérimentaux.
Je souhaite aussi remercier l'ensemble du personnel ITA pour leur participation à nos projets. En effet, bien que rarement au devant de la scène, leur apport fait que notre action est plus sûre et plus complète.
Tout mon entourage au laboratoire EM2C m'a toujours manifesté sympathie et amitié et a été pour moi un soutient précieux. J'en remercie tous les membres très sincèrement.
J'ai une pensée particulière pour Macole Sabat, Maxime Philip et Thomas Epalle dont la chaleur de leur amitié a été pour moi une source d'encouragement permanent.
Mes remerciements vont aussi à ma famille qui a toujours été à mes côtés dans les moments de peine ou de joie.

Abstract

This research concerns some of the issues raised by high frequency combustion instabilities in rocket engines. These instabilities are known to have detrimental effects leading, in some cases, to the destruction of the propulsion system. To avoid the appearance of such instabilities it is important to gain an understanding of the processes driving such dynamical phenomena. One has to consider the complex coupling between injection, combustion and the acoustic resonances of the system. The present work contributes to this objective by developing three items.

The first deals with numerical simulations of non-reactive and reactive jets submitted to different modulation conditions to understand the interaction between jets, flames and their environment. Numerical simulations of non-reactive round jets as well as more complex flames formed by coaxial injectors operating under transcritical conditions were carried out using large eddy simulation (LES) adapted to real gas situations by making use of the AVBP-RG flow solver. Round jets were submitted to transverse velocity fluctuations. It has been found that for all amplitudes and frequencies of modulation, the modulated jet is deformed and oscillates. This behavior can be represented by a model. The coaxial flames were submitted to mass flow rate and pressure modulation. For these cases it has been found that the modulation induces variations of the global heat release rate. A mathematical relationship between the modulated parameters and the heat release rate has been proposed.

The second item includes experimental investigations. For this purpose a New Pressurized Coupled Cavities (NPCC) laboratory test rig has been developed. The possible coupling between the plenum and the thrust chamber was studied. A model, linking pressure and velocity fluctuations between the plenum and the thrust chamber, has been developed. The laboratory test rig was also used to gather some knowledge on the levels of damping and the damping coefficients could be determined.

The last item of this document deals with the development of a reduced order dynamical model which includes some of the driving and damping mechanisms of high frequency combustion instabilities. This dynamical description was implemented in a high frequency stability code (STAHF). This code was used to examine a 87 MW liquid rocket engine (BKD operated at DLR, Germany) exhibiting high frequency oscillations. After the adjustment of some control

parameters, STAHF was able to retrieve some the features observed in experiments carried out at DLR.

Résumé

Cette recherche se focalise sur les problèmes d'instabilités de combustion hautes fréquences dans les moteurs fusées. Ces instabilités sont connues pour avoir des effets néfastes et peuvent, dans certains cas, causer la destruction du système propulsif. Pour éviter l'apparition de ces instabilités, il est important de connaître les mécanismes qui entretiennent ces phénomènes dynamiques et de comprendre le couplage complexe entre l'injection, la combustion et la résonnance acoustique du système. Ce travail comprend trois parties.
La première partie traite de la simulation numérique de jets non-réactifs et réactifs soumis à différentes conditions de modulation afin de comprendre les interactions entre les jets, les flammes et leur environnement. Les calculs numériques de jets ronds non-réactifs ainsi que des flammes plus complexes formées par des injecteurs coaxiaux dans des conditions transcritiques ont été effectuées avec des simulations aux grandes échelles (SGE), adaptées aux conditions gaz réels à l'aide du solveur AVBP-RG. Les jets ronds ont été soumis à des fluctuations de vitesse transverse. Il a été trouvé que pour toutes les amplitudes et fréquences de modulation, le jet est déformé et oscille dans la direction transverse. Ce comportement peut être représenté par un modèle. Les flammes coaxiales ont été soumises à une modulation de débit et de pression. La modulation induit des variations du dégagement de chaleur global. Un modèle mathématique reliant les paramètres modulés au dégagement de chaleur est proposé.
La seconde partie contient les travaux expérimentaux. Dans ce cadre, un nouveau banc expérimental a été développé pour l'étude de cavités couplées pressurisées (NPCC). Le couplage entre le plénum (ou dôme) et la chambre a été étudié. Un modèle reliant les fluctuations de pression et de vitesse en sortie des injecteurs a été développé et comparés aux données d'essais. Le banc NPCC a aussi été utilisé pour acquérir plus de connaissances sur le niveau d'amortissement. Les coefficients d'amortissement ont été déterminés.
La dernière partie de ce document traite du développement d'un modèle ordre réduit qui représente des mécanismes qui entretiennent et amortissent les instabilités de combustion hautes fréquences. Cette description dynamique a été incorporée dans un code de stabilité haute fréquence (STAHF). Ce code a été utilisé pour étudier un moteur à ergols liquides d'une puissance de 87 MW (le banc BKD du DLR en Allemagne) qui présente des instabilités hautes fréquences. Après le recalage de certains paramètres de contrôle, STAHF a

été capable de retrouver des résultats obtenus d'essais au DLR.

Publication and communications of the author during the PhD research

Publication

M. Gonzalez-Flesca, T. Schmitt, S. Ducruix and S. Candel. *Simulation of round transcritical jet dynamics under transverse acoustic modulation.* Phys. Fluids 28, 055106 (2016).

Communications

M. Gonzalez-Flesca, T. Schmitt, S. Ducruix and S. Candel. *Simulation of round transcritical jet dynamics under transverse acoustic modulation*, 6^{th} European Conference for Aeronautics and Space Sciences (Kraków POLAND, 2015).

M. Gonzalez-Flesca, T. Schmitt, P. Scouflaire, S. Ducruix and S. Candel. *Experimental study of injection dynamics and damping rates in rocket engines*, 13^{th} Rocket Engine Stability Workshop (Garching GERMANY, 2015).

M. Gonzalez-Flesca, T. Schmitt, P. Scouflaire, S. Ducruix and S. Candel. *Low order stability modeling of liquid rocket engines with the STAHF-tool* , 15^{th} International Conference on Numerical Combustion (Avignon FRANCE, 2015).

M. Gonzalez-Flesca, T. Schmitt, S. Ducruix and S. Candel. *Low order modeling of the HF-7 test case with the STAHF-tool*, 3^{rd} Rocket Engine Stability Research Initiative Workshop (Vernon FRANCE, 2014).

Contents

List of Tables

List of Figures

Introduction

Background and objective

Problems of combustion instability arise in many practical situations and motivate the large scale research effort in combustion dynamics. In addition to the many scientific challenges these problems also have important technical implications. High frequency combustion instability is a dynamical phenomenon induced by a resonant coupling between flow dynamics, combustion and acoustic modes of the chamber. This coupling can be represented by a feedback interaction as shown in figure 1. Combustion instabilities can lead to high

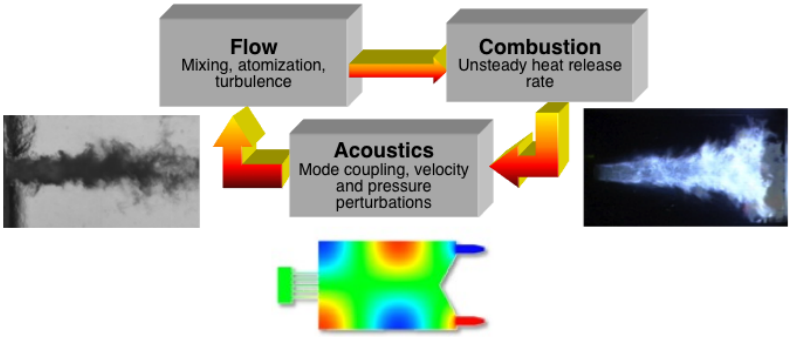

Figure 1: *Schematic representation of the feedback mechanism governing the coupling combustion, acoustics and flow dynamics.*

amplitude pressure oscillations and a quick increase of the heat fluxes and mechanical stress to walls and injection head that may end, in some cases, in the complete destruction of the whole propulsive system (figure 2). While instabilities are observed in a wide range of systems they constitute an important problem in gas turbines in which premixed combustion is employed to reduce NO_x emissions. The corresponding advanced combustor architectures are less well damped, feature larger energy densities and are more sensitive to resonant acoustic coupling leading to oscillations. A considerable amount of work has been devoted to these problems to mitigate dynamical phenomena and their consequences on mechanical integrity and life duration of the combustor. Instability may cause important damages in systems where the energy density takes

(a) 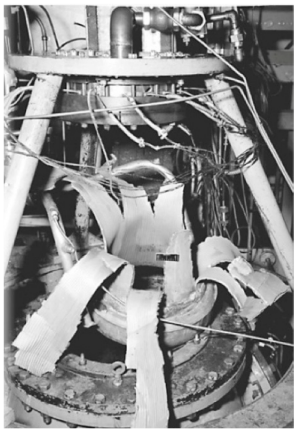 (b) 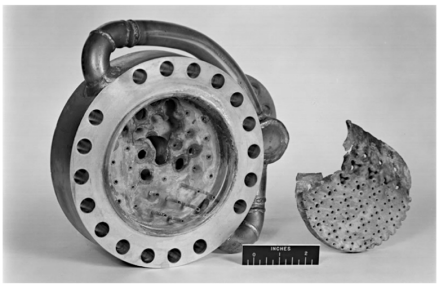

Figure 2: *(a) Result of a high frequency instability on a NASA rocket engine test rig. (b) Injection head damaged by high frequency combustion instabilities.*

large values as is the case in aeroengine combustors. In terms of energy density rocket engine thrust chambers feature extreme values with levels in excess of 50 GW.m^{-3} and these systems have also had the most destructive type of instabilities. Many of the early rocket developments faced instability problems and required time consuming efforts for their mitigation. The instability crisis encountered during the development of the F1 engine of the Saturn 5 rocket described by Oefelein and Yang (1993) contains a detailed account of the actions taken and full scale testing that were required to fix the problem and finalize the thrust chamber design. Because the problem can always arise it has been the subject of continuous attention giving rise to many fundamental or more technical investigations. The effort has mainly concerned high frequency instabilities coupled by transverse modes of the thrust chamber because these modes are less well damped than longitudinal oscillations and as a consequence give rise to the highest levels of perturbation.

In this context, the present thesis proposes contributions on a few facets of high frequency combustion instabilities in liquid rocket engines. The case of cryogenic engines which are the workhorse of the European launcher adventure is specifically considered. The thesis is number five in a series prepared at EM2C laboratory, CNRS in the framework of the Rocket Stability (REST) program launched in the year 2000 by CNES, DLR, Airbus Defense and Space and Snecma. Previous investigations carried out at EM2C are those of Cédric Rey (Rey (2004)), Franck Richecoeur (Richecoeur (2006)), Yoaan Méry (Méry (2010)) and Layal Hakim (Hakim (2013)). The main results of these previous investigations are summarized in Figure 3. The general ideas of the previous studies have been to combine experiments on model scale hot fire configurations, numerical simulations in the LES framework and dynamical modeling.

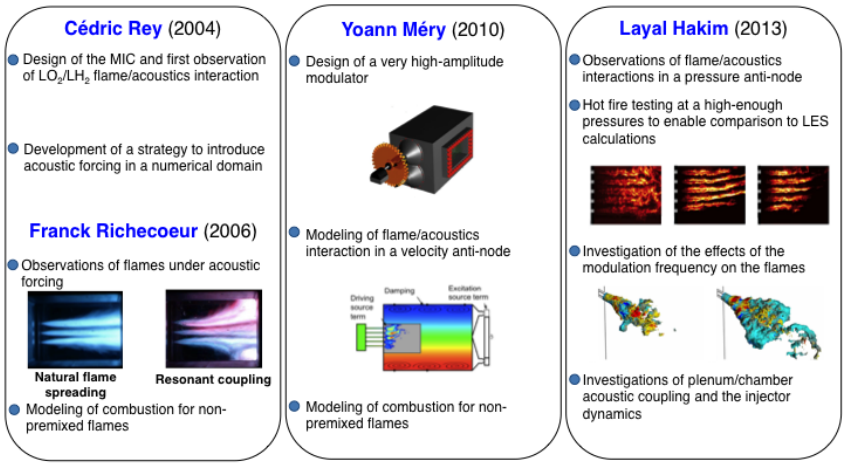

Figure 3: *Overview of the previous studies on the subject of high frequency combustion instabilities in rocket engines.*

In addition to these three subjects it was found useful to examine specific issues in cold flow configurations reproducing some of the processes existing in rocket thrust chambers. The present investigation is carried out at three of the levels described previously. Large eddy simulations are used to investigates two important aspects of the interaction between transverse acoustic modes and transcritical jets or jet flames. Model scale experiments are carried out under cold flow conditions to examine problems of coupling between the chamber and the dome and to study the injector response and the effect of head losses on the damping in the system. Low order modeling is advanced and applied to the analysis of an experimental rocket engine (the BKD test rig DLR (2013)) and see if the modal expansion state space approach can be used to predict the instabilities observed in this system.

State of the art

At this point it is worth briefly reviewing the state of the art to provide the proper perspective to the present research. We will successively examine the literature on cryogenic combustion, transcritical injection conditions (combustion implying propellants which are in a transcritical state characterized by a high pressure in excess of the critical pressure and a low injection temperature below the critical value). We then examine the literature dealing with instabilities in liquid rocket engines.

Cryogenic combustion investigations

It is logical to first review studies dealing with combustion of cryogenic propellants. This type of combustion characterizes engines used in the Ariane family

launchers. It is known that many of the early developments of these engines and in fact of most of such devices have relied on testing. A number of issues encountered in this process were solved by full scale experimentation. Lessons were learnt from failures and successes. This has advanced the technological maturity of propulsion systems and helped design generations of space launchers from Ariane 1 to Ariane 5. After some failures during the 1980s it was felt that design and reliability could be improved by developing a fundamental understanding of the combustion processes under the extreme conditions existing in liquid rocket thrust chambers. This was needed to sort out the main control parameters, guide analysis, derive design methodologies and reduce cost. Fundamental investigations were developed in the framework of a GDR (Groupement de Recherche) focused on combustion in rocket engines and more specifically on issues of cryogenic propellant combustion which provides the highest specific impulse and is exploited in the third stage engine (HM7) of the Ariane 4 launcher and in the Ariane 5 main stage (Vulcain family) and ECA upper stage (Herding et al. (1996); Herding (1997); Snyder et al. (1997); Herding et al. (1998); Candel et al. (1998); Kendrick et al. (1999); Juniper et al. (2000); Tripathi (2001); Juniper (2001); Juniper and Candel (2003a); Juniper and Candel (2003c); Juniper et al. (2003); Juniper and Candel (2003b)).

Results of this research effort have provided basic information on flame structures, effects of geometrical and operational parameters, combustion processes at elevated pressure (pressure values exceeding the critical value). The liquid oxygen and gaseous hydrogen couple was investigated first (LO_x/GH_2) while LO_x/GCH_4 and LO_x/LCH_4 (Singla (2005); Singla et al. (2005); Singla et al. (2006); Singla et al. (2007); Singla et al. (2007)) were considered at a later stage. Interest in this alternative couple is related to the fact that methane stored in liquid form is much denser than hydrogen so that the oxygen/methane combination leads to systems which are more compact with an improved structural efficiency. Liquid methane is also easier to handle and store than hydrogen but it gives rise to issues of combustion efficiency. In general, engines fed by cryogenic propellants operate at high pressure above the critical value. This unusual situation was examined experimentally providing data needed for the development and validation of computational tools.

One important issue in the field of cryogenic combustion is that of transcritical injection conditions. This designates a situation where the chamber pressure exceeds the critical pressure while the injection temperature is below the critical value. This situation is typically found in rocket engines used in the Ariane program. Under nominal operation, the reduced pressure for oxygen $p_R = p/p_c(O2)$ (where $p_c(O2)$ is the critical pressure of oxygen and p the pressure) in the Vulcain thrust chamber is 2.18 and about 1.19 in the Vinci engine. In both cases $T_R = T/T_c < 1$ at injection.

It is known that at a supercritical pressure the surface tension and latent heat of vaporization vanish and the fluid behavior differs markedly from that of a perfect gas. The flow structure established by coaxial injectors is also quite distinct from that found under subcritical-pressure conditions were two phases are present Chehroudi et al. (2002); Oschwald and Schik (1999); Mayer et al. (2003); Segal and Polikhov (2008). One also expects that the flame dynamics will notably differ from that corresponding to the subcritical case.

The unusual situation corresponding to high pressure and low injection temperature has many scientific implications. Under transcritical conditions the working fluid behaves like a liquid but as the temperature increases the fluid is very much like a gas. There are important changes in density and rapid changes of the fluid thermodynamic and transport properties. To reflect these complexities in simulations requires descriptions of real gas thermodynamics and transport properties Poling et al. (2001).
On the experimental side, there was a need for detailed investigations. These were carried out in new model scale cryogenic combustion facilities allowing optical access (in particular at Mascotte operated by Onera or at the P8 testbed at DLR Lampoldshausen). These facilities reproduced conditions prevailing in liquid rocket engines but in an idealized single injector configuration. Studies of liquid oxygen and gaseous hydrogen combustion have provided fundamental information on flame structures, influence of geometrical parameters and operating conditions and combustion processes at elevated pressure. Observations indicated that the atomization and spray formation processes prevailing at subcritical pressure are no longer present Habiballah et al. (2006); Mayer et al. (1998). Instead, the dense jet breaks down into high density pockets and dissolves in the surrounding stream Candel et al. (2006). Under hot fire conditions it is found that combustion is fast, when compared with mixing in cryogenic propellant flames as indicated by Candel et al. (2006). This is also confirmed by numerical simulations of strained flames Pons et al. (2008); Ribert et al. (2008). The flame structure in the injector near field revealed by combining emission imaging of OH* radicals and backlighting indicates that the flame is close to the dense oxygen stream and that the flame edge is very close to the injector lip. This is exemplified in Figure 4 where an Abel transform of the mean OH* emission is superimposed on a backlighting image of the dense oxygen jet. The flame is anchored near the oxygen channel lip (the distance is less than the lip thickness) Juniper et al. (2000); Singla et al. (2007); Juniper and Candel (2003a). Flame stabilization issues were also considered with theoretical and numerical modeling tools leading to flame holding criteria discussed in Juniper and Candel (2003a); Singla et al. (2007).
Further clues deduced from liquid oxygen/methane combustion studies indicated that LO_x/GCH_4 flames were similar to those formed by LO_x/GH_2. It was noted however that a distinct flame structure was formed in the case of doubly transcritical injection LO_x/LCH_4 with two reaction concentric layers

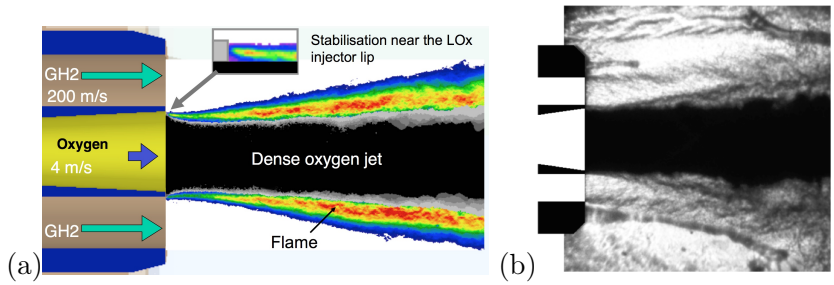

Figure 4: *(a)OH^* radical emission and (b) backlight visualization of reacting shear flows of LO_x/H_2 at 7 MPa.*

spreading outwards Singla et al. (2005); Candel et al. (2006).

Transcritical flame simulations

The previous data have served to guide computational methodologies for transcritical injection and combustion. Flow solvers have been equipped with real gas thermodynamics and transport models and a suitable treatment of boundary conditions. Geometrically simple problems have been simulated including combustion of spherical pockets Yang (2000) or of strained flames formed by the counterflow of transcritical and supercritical streams Ribert et al. (2008); Pons, Darabiha, Candel, Ribert, and Yang (2009); Pons, Darabiha, Candel, Schmitt, and Cuenot (2009). Calculations of complex flames formed by transcritical injection of reactants have been carried out using RANS models but much of the recent effort has been focused on the adaptation of computational tools to the large-eddy simulation of transcritical combustion.

Oefelein and Yang Oefelein and Yang (1998) present one of the first calculation of this type but with a computational domain limited to the vicinity of the injector outlet. Further simulations are due to Zong and Yang (2007). Full scale jet flame configurations have been calculated more recently Schmitt et al. (2011) using a novel combustion model. Simulations were able to retrieve most of the features found experimentally. Similarly, calculations of LO_x/GH_2 flames reported in Schmitt et al. (2009) were also shown to closely follow experimental data. The previous results and many others show that it is possible to obtain reasonable predictions of transcritical flames and that such simulations can be used to explore engineering issues in propulsion technology.

Liquid rocket engines high-frequency instabilities

Combustion dynamics received considerable attention during the early period of rocket propulsion development. The development of these high performance combustion systems was hindered by instability problems with dramatic consequences (Culick (2006); Oefelein and Yang (1993)). Pioneering research carried

out by Tsien Tsien (1952a), Crocco Crocco (1951); Crocco and Cheng (1956) and Marble Marble (1953), underlined the importance of delays in the combustion process noting that delays generally destabilize dynamical systems and could be viewed as a fundamental cause of instability. This gave rise to the Sensitive Time Lag model (STL) concept developed during the 1950s and used in many studies covering the second half of the 20^{th} century. The central idea was that the delay was a function of conditions prevailing in the system like pressure, temperature and so on, and that this sensitivity to state parameters was causing burnt gas mass flow rate perturbations and correspondingly heat release rate fluctuations. After about twenty years of investigations, research in liquid rocket instability was synthesized in a well known and widely distributed NASA report (SP172) Harrje and Reardon (1972). About twenty more years later a book edited by Yang and Anderson Yang and Anderson (1995) collected further contributions to the liquid rocket engine instability analysis. There are also some general reviews discussing combustion dynamics issues with a lesser focus on the specific application to liquid rocket engines (see for example McManus et al. (1993); Candel (2002); Culick (2006)). One finds that much of the recent effort has been focused on well controlled experiments intended to sort out the driving and coupling mechanisms. These studies were carried out in combination with developments of reduced order models relying on detailed descriptions of the acoustics of the systems. With progress in computational resources and computational fluid dynamics, much of the effort has also been targeted at combustion dynamics issues. Advances in this area have been made mainly in the large eddy simulation framework. This was initially derived to solve non reactive flow problems which was extended more recently to deal with reactive flow problems of the type encountered in combustion.

While sensitive time lag models have been around for a long time, it is well known that they do not account in a detailed manner for the processes which give rise to driving mechanisms of combustion instabilities. It was known for some time that progress in combustion instability analysis required detailed experimental data but it was also clear that conditions prevailing in real engines could bot be easily reproduced in model scale experiments. Modeling has generally relied on full scale test data, in the form of pressure signals detected at the chamber walls during unstable oscillation. These tests indicated that high frequency oscillations coupled by azimuthal modes were the most dangerous. In some model scale experiments streak visualizations obtained by viewing the combustion region through a thin slit and recording the motion with a high speed film demonstrated that combustion was modulated in a "zig zag" fashion at a frequency corresponding to the resonant acoustic mode involved in the pressure oscillation. Evolution in recent years has been driven by (1) Experiments with cryogenic propellant combustion Candel et al. (2006), (2) Optical diagnostics allowing high speed visualizations in combination with computer data processing, (3) Simulation methods for unsteady transcritical combustion Oefelein and Yang (1998); Schmitt et al. (2010); Schmitt et al. (2011); Schmitt

et al. (2012); Schmitt et al. (2014); Hakim et al. (2015).
Much work has been carried out in the framework of the REST program including model scale experiments designed to take advantage of the existence of the Mascotte and P8 test facilities Richecoeur et al. (2006); Méry et al. (2009); Hardi et al. (2011). These investigations were designed to reproduce some of the features observed in full scale engines like the very high levels of oscillation observed in unstable rocket engines. In Richecoeur et al. (2006); Méry et al. (2009), a multiple injector combustor (MIC) is fed with cryogenic propellants (liquid oxygen and gaseous methane) and operates at elevated subcritical or supercritical pressures. This combustor is representative of rocket engines and allows for collective interactions between adjacent jet flames. Initial experiments were carried out by modulating the system with a lateral actuator using a rotating toothed wheel periodically blocking a side nozzle. A novel modulator was then designed in a second step (Very high amplitude modulator, VHAM) to reach higher levels of modulations of up to 20% of the chamber pressure (Richecoeur et al. (2006); Méry et al. (2009)). The principle of the VHAM was to alternatively block two exhaust nozzles. This was used to observe strong coupling between transverse disturbances and combustion. Under acoustic modulation the flame structure was notably modified with an augmented expansion angle and more compact combustion. In some cases the flow becomes strongly asymmetric when the level of modulation becomes high Méry (2010).
Computational methods have also allowed important progress in the analysis of the response of cryogenic flames to transverse modulations. Most of the work has concerned configurations where the flame was at a velocity antinode Hakim et al. (2015). This article examines interactions by making use of large eddy simulations. In the case of an azimuthal instability, the flame can be placed in a velocity antinode, a pressure antinode or an intermediate situation. In accordance with experimental observations reported by Méry (2010), the flame features a transverse oscillation which follows the external modulation. Calculations indicate the flame expands in the spanwise direction and that its length is substantially reduced. Flame dynamics is, to a certain extent, reminiscent of a jet in a cross flow when the external flow oscillates and produces kidney-shaped counter rotating vortices. The flame dynamics is influenced by a strong transverse acoustic modulation with an amplitude representative of those found in rocket engine instabilities. Some of the most recent calculations reported in Hakim (2013) and Hakim et al. (2015) nicely reproduce the dynamics of the MIC under external modulation with the VHAM.

Objectives of the present investigation and thesis organization

The present work pursues research described in the previous sections. It is specifically focused on the development and validation of low order modeling for high frequency combustion instability analysis. The objective is to develop a predictive tool based on recent advances in experimentation and simulation. The thesis comprises three parts. Each part of this work deals with a specific aspect of the study of combustion instabilities in rocket engines; Simulation, experimentation and modeling. As illustrated in figure 5, those three aspects operate together to better understand combustion instabilities.

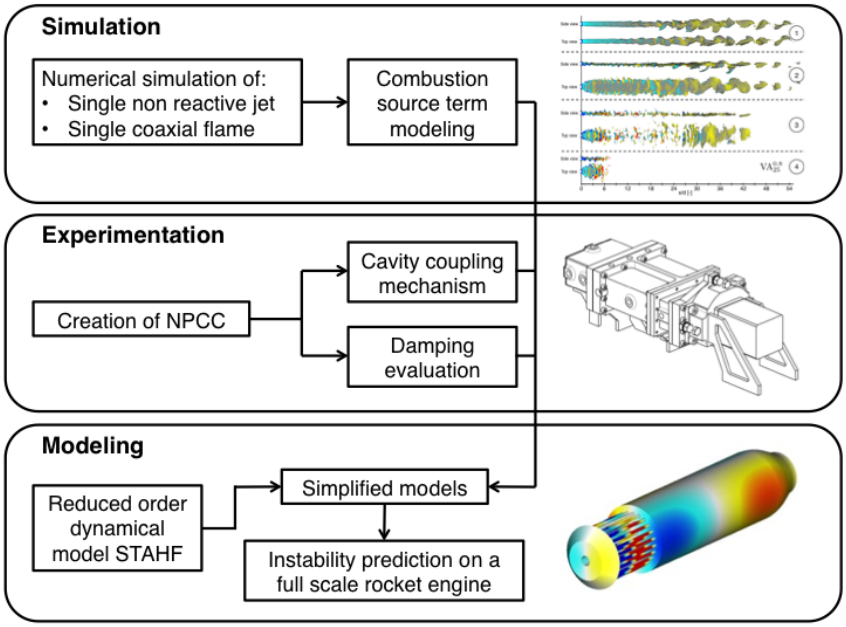

Figure 5: *Illustration of the research logic followed in the present work.*

In part I, large eddy simulations of single jets or single jet flames are carried out. These studies are intended to provide information on important processes in cryogenic injection and combustion dynamics. Chapter 1 focuses on a single non reactive jet in a transverse velocity anti-node. The objective is to derive a simple model for the jet motion that could be used in dynamical low order simulations. Chapter 2 investigates the interaction between mass flow rate modulations and pressure modulations with the flame. These two types of perturbations may have a notable effect on the combustion response. The first corresponds to the injector response to changes in the chamber. One generally considers that the injector offers a certain impedance and this is reflected in the mass flow rate oscillations that are induced in these devices by oscillations

in the thrust chamber. It is also known that combustion is sensitive to pressure perturbations and this needs to be quantified. In turn the information gathered with these simulations will serve to identify driving mechanisms of combustion instabilities.

Part II of this thesis deals with injection problems, coupling between dome and chamber and damping levels. The study is carried out with a model scale cold flow experimental simulator designated as NPCC (New Pressurized Coupled Cavities) that uses the VHAM concept to modulate the flow in the system in a configuration presented in chapter 3. This facility is used to examine injector impedance and validate dynamical injector models in chapter 4. Chapter 5 explores an experimental method of damping determination using the VHAM equipped with a specially designed perforated wheel.

Part III contains a synthesis of the principles of dynamical modeling in chapter 6 and then describes, in chapter 7 a dynamical low order model designed to integrate all submodels devised in this thesis using large eddy simulations, experimental results and modeling ideas. The corresponding code, STAHF, is first validated by making use of the NPCC test rig and it is then used to examine instabilities in an experiment developed at DLR and designated as the BKD (chapter 8). The BKD exhibits stable and unstable regimes of operation which are examined with the STAHF code. It is shown that the behavior observed experimentally can be retrieved but that this requires suitable estimates of the damping rate in the system.

Part I

Numerical determination of the unsteady combustion source term

The key parameter in the study of combustion instabilities is the unsteady heat release rate. This quantity coupled with the unsteady pressure fluctuations drives unstable oscillations. To predict the occurrence of combustion instabilities one has to understand how the unsteady heat release rate acts as a source of acoustic energy. There is a wide variety of processes that can induce unsteady heat release rates. It is considered that one effective mechanism is linked to the displacement of the reactive layers by the acoustic field. Another possible mechanism is associated with the response of injectors to pressure modulations in the thrust chamber. In turn, the velocity modulations generated in this process generate mass flow rate fluctuations and the burning of the injected propellants after a certain delay gives rise to an unsteady heat release. Since the conversion process is influenced by the pressure in the chamber, an oscillation of this parameter produces unsteady heat release fluctuations. These three driving mechanisms are considered in the first part of this document. The first investigation is concerned with the dynamics of a round jet subjected to a transverse acoustic excitation. Previous numerical results as well as experimental data, suggest that under transcritical conditions and for flames established by a coaxial injector, the dense central core of the jet drives the whole flame. Rather than studying an entire transcritical flame, one can reduce the study to a single round jet in order to get a better understanding of the interaction of a transcritical jet and a transverse acoustic field. The second topic covered in this part concerns the response of an injector to ambient pressure perturbations. The goal of this study is to investigate the response in terms of heat release fluctuations. The next problem is that of the flame response to pressure perturbations. These three problems are investigated using large eddy simulations.

Chapter 1

Simulation of a round transcritical jet under transverse acoustic modulation

This chapter reports numerical computations of a turbulent round jet of transcritical fluid (low temperature nitrogen injected under high pressure conditions) surrounded by the same fluid at rest under supercritical conditions (high temperature and high pressure) and submitted to transverse acoustic modulations. The numerical framework relies on large eddy simulation in combination with a real-gas description of thermodynamics and transport properties. A stationary acoustic field is obtained by modulating the normal acoustic velocity at the lateral boundaries of the computational domain. This study specifically focuses on the interaction of the jet with the acoustic field to investigate how the round transcritical jet changes its shape and mixes with the surrounding fluid. Different modulation amplitudes and frequencies are used to sweep a range of conditions. When the acoustic field is established in the domain, the jet length is notably reduced and the jet is flattened in the spanwise direction. Two regimes of oscillation are identified: for low Strouhal numbers a large amplitude motion is observed, while for higher Strouhal numbers the jet oscillates with a small amplitude around the injector axis. The minimum length is obtained for a Strouhal number of 0.3 and the jet length increases with increasing Strouhal numbers after reaching this minimum value. The mechanism of spanwise deformation is shown to be linked with dynamical effects resulting from reduction of the pressure in the transverse direction in relation with increased velocities on the two sides of the jet. A propagative wave is then introduced in the domain leading to similar effects on the jet, except that a bending is also observed in the acoustic propagation direction. A kinematic model, combining hydrodynamic and acoustic contributions, is derived in a second stage to represent the motion of the jet centerline.This

model captures details of the numerical simulations quite well. These various results can serve to interpret observations made on more complex flow configurations such as coaxial jets or jet flames formed by coaxial injectors.

1.1 Introduction

The use of cryogenic propellants in liquid rocket engines (LRE) under pressures exceeding the critical value gives access to high efficiency propulsion systems for launch vehicles. The pressure in the thrust chamber of these devices is higher than the critical pressure of both liquid oxygen (LO_x) and liquid hydrogen (LH_2), which are used as propellants but the injection temperature of LO_x is below the critical value and this reactant is injected in a dense state under conditions designated as "transcritical". Such injection conditions give rise to many questions regarding the evolution of the propellants inside the combustion chamber. High frequency combustion instabilities in rocket engines constitute a difficult issue because the coupling between transcritical coaxial jet dynamics, combustion processes and resonant acoustic modes of the chamber is not well understood. Throughout this paper the term "acoustic" refers to the sound waves and their interactions with the physical environment. It is however worth noting that the amplitude of oscillation may be quite large but the corresponding perturbations are only a fraction of the mean values in the system. Experience gained during the initial years of LRE development (see for example Crocco (1951)) indicated that transverse and spinning modes were the most destructive. Much of the early work in this field relied on full scale testing. Knowledge was gained through successes and failures which is exemplified by the extensive program undertaken during the development of the F-1 engines, to solve the problems linked with combustion instabilities Oefelein and Yang (1993). While a considerable amount of knowledge has been accumulated, it is important at this point in time to take a new look at the fundamental mechanisms controlling combustion instabilities in LREs and in this way help improve space propulsion technology. This can be done by exploiting novel simulation methods and high performance computing.
Many studies have already been carried out on transcritical combustion simulations Oefelein (2005); Hakim et al. (2015); Hakim et al. (2015); Schmitt et al. (2011); Masquelet et al. (2009); Candel et al. (2013). Direct Numerical Simulation (DNS) can be used to solve the Navier-Stokes equations Oefelein (2005) providing precise information regarding the flow and the reacting process. While DNS provides results which can be used to interpret the anchoring mechanism Juniper (2001) or details of the flow and flame dynamics, it cannot be used to calculate high Reynolds number reactive flows. One must then turn to Large Eddy Simulation (LES), which is less demanding in terms of resources than DNS, and has been developed extensively in the last period. Progress made in reactive LES has been quite substantial. LES methods for transcriti-

cal flames have been derived more recently and this has allowed some successful calculations of various laboratory scale cryogenic combustion configurations operating under realistic flow conditions Candel et al. (2013). It has been possible to retrieve quite nicely the structure and features of LO_x/GH_2 and LO_x/GCH_4 flames, thus validating the computational methodology Schmitt et al. (2011). The new LES tools, which includes real gas effects, have also been used to examine combustion instability issues as exemplified in Hakim et al. (2015); Hakim et al. (2015); Wawrzak et al. (2015) and give access to the unsteady rate of heat release induced by the transverse acoustic velocity modulations. It is indicated in these studies that the flames are periodically displaced by the velocity perturbations. In configurations of one Hakim et al. (2015) and five Hakim et al. (2015) injectors it has been shown that the dense core of LO_x is flattened in the spanwise direction and that its axial length is notably diminished when the modulation amplitude is sufficient. It is also found that the flame is essentially driven by the dense inner jet dynamics and its response to the acoustic modulation. Predicting the complex interaction between the dense core and a given acoustic field is essential to the global understanding of combustion instabilities in rocket engines. It is then logical to consider interactions of non-reacting single species jets injected under transcritical conditions. This is already explored in Schmitt et al. (2012); Zong and V.Yang (2006) to identify the evolution of characteristic parameters such as density, as a function of longitudinal distance. Acoustic modulation of non-reacting flows have also been carried out in Schmitt et al. (2012) in a coaxial flow configuration. The interaction of transverse acoustic waves with transcritical flows and its influence on mixing efficiency has been studied on experimental rigs as well. The impact of acoustics on a non-reacting shear coaxial jet was investigated in Schmitt et al. (2012); Leyva et al. (2008); Rodriguez et al. (2008). The objective of the present study is to pursue this analysis of a non-reacting transcritical jet submitted to transverse modulations. This is done in a systematic fashion where both the frequency and amplitude of oscillation are varied. In addition we consider the case where the mode is standing and the jet is located at a velocity antinode and the case of a jet submitted to a propagating wave as a way to mimic the effects of a spinning mode. The jet response is characterized in detail, the transient phase is examined showing how the jet is broken into pockets with a notable reduction of its length and a model is proposed to represent the jet centerline kinematics when a steady state is reached.

This chapter is organized as follows. The governing equations, modeling assumptions and numerical approach are described in Section 1.2. The jet established in the absence of modulation is examined in Section 1.3 and this serves as a baseline flow. Section 1.4 is devoted to an examination of the transient evolution of the jet when the acoustic field is switched on. The jet behavior under steady modulation is analyzed in Section 1.5. Calculations are carried out in a situation where the jet is placed at a velocity antinode in a standing mode. It is also interesting to examine situations where the jet is submitted

to a spinning mode. This is accomplished in Section 1.6, where the jet is submitted in this model configuration to a traveling wave in order to represent the spinning mode. The modeling of the jet dynamics is then considered in Section 1.7, where a kinematic model is derived to represent the motion of the jet centerline. Unfortunately there are no experimental data to which the calculated test cases could be compared for validation. However, experiments under high pressure conditions, document the dynamical behavior of coaxial transcritical jets in transverse acoustic fields Méry et al. (2013); Hardi et al. (2014). On a phenomenological level the present results are in line with these studies.

1.2 Governing Equations, models and numerical approach

The simulation strategy described in Schmitt et al. (2010) for the simulation of a single species transcritical jet is retained in the present analysis. Calculations are carried out with an extension of the AVBP solver developed by CERFACS and IFPEN Schönfeld and Rudgyard (1999); Moureau et al. (2004). More details on the program can be found in appendix B. This extension designated as AVBP-RG, jointly developed by CERFACS and EM2C is used to simulate transcritical flows using the Peng-Robinson equation of state (EOS) Peng and Robinson (1976) and adapted transport models proposed by Chung et al. Chung et al. (1988). The filtered Navier-Stokes equations are integrated in this framework:

$$\frac{\partial \overline{\rho}}{\partial t} + \frac{\partial \overline{\rho}\widetilde{u}_j}{\partial x_j} = 0 \tag{1.1}$$

$$\frac{\partial \overline{\rho}\widetilde{u}_i}{\partial t} + \frac{\partial \overline{\rho}\widetilde{u}_j\widetilde{u}_i}{\partial x_j} = -\frac{\partial \overline{p}}{\partial x_i} + \frac{\partial \overline{\tau_{ij}}}{\partial x_j} - \frac{\partial \overline{\tau_{ij}}^t}{\partial x_j} \tag{1.2}$$

$$\frac{\partial \overline{\rho}\widetilde{E}}{\partial t} + \frac{\partial \overline{\rho}\widetilde{u}_j\widetilde{E}}{\partial x_j} + \frac{\partial \overline{p}\widetilde{u}_j}{\partial x_j} = -\frac{\partial \overline{q_j}}{\partial x_j} + \frac{\partial \widetilde{u}_i\overline{\tau_{ij}}}{\partial x_j} - \frac{\partial q_j^t}{\partial x_j} \tag{1.3}$$

Where ρ is the density, $\boldsymbol{u} = (u, v, w)$ the velocity vector, E the total energy (*i.e.* the sum of internal and kinetic energies), p the pressure, $\boldsymbol{x}$ the spatial coordinate vector, t the time. $\boldsymbol{\tau}$ is the viscous stress tensor and $\boldsymbol{q}$ the heat flux vector. The turbulent stresses
$overline\tau_{ij}{}^t$ is computed using the WALE model Ducros et al. (1998), well-suited for the treatment of shear flows of the type considered in this chapter. The sub-grid scale energy flux is solved using a gradient transport assumption, with a turbulent Prandtl number set equal to 0.7. The TTGC scheme Colin and Rudgyard (2000) is chosen to solve the conservation equations. This centered numerical scheme, third order in space and time, is essentially non-dissipative and thus well adapted for LES of turbulent flows. Cryogenic flows are characterized by large density gradients in the mixing layer and localized artificial

viscosity is used to avoid spurious oscillations (see Schmitt et al. (2010) for details).

1.2.1 Computational domain, mesh and boundary conditions

The computational domain consists in a large rectangular box of dimension 1 m × 0.5 m × 0.5 m (figure 1.1). The jet is established by a round injector with a 5 mm diameter. The injector diameter serves as a reference length d. The mesh shown in figure 1.1 comprises 2 100 000 nodes corresponding to 12 300 000 tetrahedra. It is highly refined in the vicinity of the injector, with a characteristic size $\Delta = 0.125$ mm, and is progressively coarsened towards the domain outlet. Nitrogen is injected at a temperature $T_{inj} = 100$ K in a chamber at

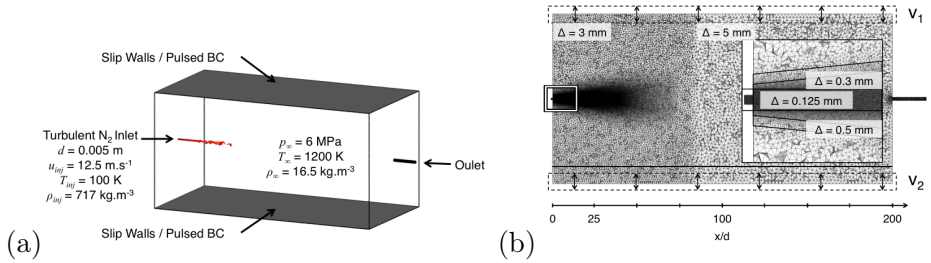

Figure 1.1: *(a) Three-dimensional visualization of the computational domain including a round jet illustration at scale as well as the boundary conditions. All boundaries are slip walls for the unmodulated case while the top and bottom boundaries become pulsed walls for the modulated cases. (b) Longitudinal cut of the mesh and characteristic cell sizes for the different refined areas.*

$T_\infty = 1200$ K and $p_\infty = 6.0$ MPa. This pressure is chosen so that, even with a 20% pressure modulation one can expect that the pressure in the domain will remain above the critical value for N_2 (the critical temperature and pressure for nitrogen are T_c=126.2 K and p_c=3.396 MPa, respectively) To characterize real gas effects it is also possible to check the thermodynamic state with respect to the Widom-line Simeoni et al. (2010); Banuti (2015). The initial temperature in the computational domain is set to mimic a hot gas environment such as the one corresponding to the hot burnt gases in a LO_x/GCH_4 combustion under rich methane injection conditions Singla et al. (2007). In this configuration, the fluid undergoes a transcritical injection. Nitrogen injection density is $\rho_{inj} = 717$ kg.m^{-3} and the reservoir density is $\rho_\infty = 16.5$ kg.m^{-3}, leading to a density ratio S_ρ=43.4. The inlet bulk velocity is set to $u_{inj} = 12.5$ m.s^{-1} and a turbulent profile is assumed (figure 1.2). Turbulent fluctuations are added at the inlet, following the profile prescribed in figure 1.2 obtained from prior channel calculations with the same grid resolution, using the methodology adopted by Smirnov et al. Smirnov et al. (2001). Injection conditions are summarized in table 1.1. Inlet and outlet are represented using non-reflecting Navier-Stokes Characteristics Boundary Conditions (NSCBC) Poinsot et al. (1994); Bellan

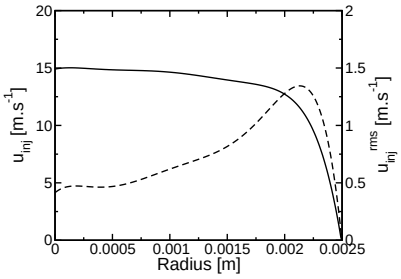

Figure 1.2: *Radial profiles of mean and rms velocities at the inlet.– Mean velocity, –– rms velocity.*

$p_{R,\infty}$ [-]	$T_{R,inj}$ [-]	$T_{R,\infty}$ [-]	S_ρ[-]	Re [-]
1.77	0.79	9.51	43.4	5.2 10^5

Table 1.1: *Injection characteristics of the simulated cases. The reduced pressure is $p_{R,\infty} = p_\infty/p_c$, $T_{R,inj} = T_{inj}/T_c$ and $T_{R,\infty} = T_\infty/T_c$ are the reduced temperature at injection and in the ambience, respectively, $S_\rho = \rho_{inj}/\rho_\infty$ is the density ratio and Re is the Reynolds number at the inlet.*

(2000). No slip adiabatic conditions are used at the injector walls, while all chamber boundaries are treated as adiabatic slip walls. This last choice is made to allow a suitable injection of acoustic modulations through these boundaries. This is achieved by modulating the normal velocity at the upper and lower boundaries (figure 1.1), according to the method proposed by Rey et al. Rey et al. (2005):

$$v_1(t) = A_1 \sin(2\pi f^{ac} t) \tag{1.4}$$
$$v_2(t) = A_2 \sin(2\pi f^{ac} t + \phi^{ac}) \tag{1.5}$$

Where A_1 and A_2 are the modulation amplitudes at the upper and lower boundaries, f^{ac} the modulation frequency and ϕ^{ac} the phase between the two velocity modulations. Two types of transverse modulations are considered:

- A standing wave forming a velocity anti-node at the injector exit, generated by setting $A_1 = A_2$ and $\phi^{ac} = \pi$. Acoustic pressure and transverse velocity during one period of modulation at the injector exit are shown in figure 1.3(a). It is worth noting that the resulting acoustic velocity amplitude at the injector exit is $v_0'^{ac} = A_1 + A_2 = 2A_1$, while $p_0'^{ac}/p_\infty \approx 0$.
- A propagating wave that can be used to model a purely spinning mode, obtained by setting $A_2 = 0$, so that acoustic modulation is only injected at the upper boundary. The acoustic field generated at the injector exit is shown in figure 1.3(b). Contrary to the previous case, the acoustic velocity amplitude at the injector exit is here directly given by $v_0'^{ac} = A_1$ and $p_0'^{ac}/p_\infty = (\rho c v_0'^{ac})/p_\infty = 0.07$, where c is the local speed of sound.

In all cases, lateral boundaries are non-reflecting at the frequencies of interest so that acoustic waves can properly leave the domain as they reach the opposite boundary without any spurious reflections.

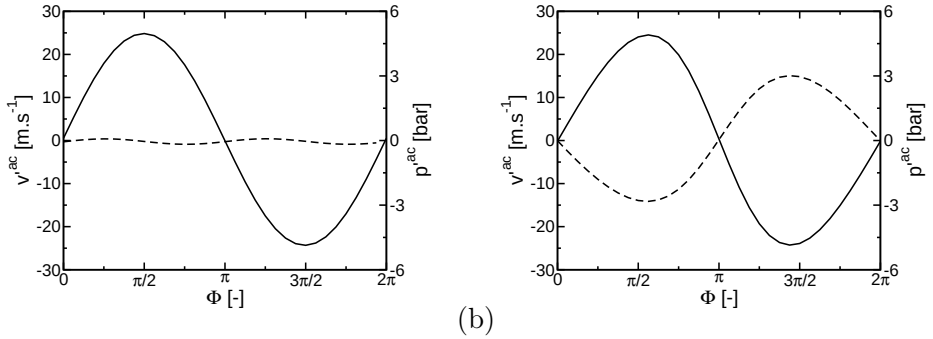

Figure 1.3: *Acoustic pressure p'^{ac} and transverse velocity fluctuations v'^{ac} over one period of excitation (flow is initially at rest, without jet). (a) Case with $A_1 = A_2$ and $\phi^{ac} = \pi$ (Standing wave, velocity anti-node). (b) Case with $A_2 = 0$ (Propagating wave). This case is affected by non-linear effects that makes the modulation non purely sinusoidal. − Transverse velocity, −− pressure.*

1.2.2 Simulated cases and simulation procedure

Three types of modulation are considered in this study:

- "NM" corresponding to a natural jet developing in the absence of modulation
- "VA" pertaining to a situation where the jet is in a velocity anti-node formed by a standing mode
- "TR" where the jet is modulated by a travelling wave.

All the modulated cases are referred to as $\mathrm{X}^{\mathrm{St}}_{v_0'^{ac}}$, where X is the case (i.e. VA or TR), $\mathrm{St} = f^{ac}d/u_{inj}$ is the Strouhal number and $v_0'^{ac}$ defines the amplitude of velocity fluctuation on the jet axis. Case NM serves as a base line solution and the corresponding flow is used to initiate the modulated cases (table 1.2). The cases VA, gathered in table 1.3, serve to explore the effects of modulation

Case	Mesh	Cells [-]	$\Delta_{x,min}$ [mm]	N_τ [-]
NM^{fine}	Fine	28 millions	0.0625	150
NM	Intermediate	12 millions	0.125	750
NM^{coarse}	Coarse	3.8 millions	0.25	450

Table 1.2: *Cases without acoustic modulation (NM). Main characteristics of the simulations. τ_{conv} corresponds to one convective time defined as $\tau_{conv} = d/u_{inj}$. N_τ is the number of convective times used in the simulations. $\Delta_{x,min}$ is the minimum cell characteristic length.*

frequency and amplitude on the jet response.

Case	f^{ac} [Hz]	St [-]	$v_0'^{ac}$ [m.s^{-1}]
$VA_{25}^{0.1}$	**250**	0.1	25
$VA_{25}^{0.3}$	**750**	0.3	25
$VA_{25}^{0.8,fine}$	**2000**	0.8	25
$VA_{25}^{0.8}$	**2000**	0.8	25
$VA_{25}^{0.8,coarse}$	**2000**	0.8	25
$VA_{25}^{1.6}$	**4000**	1.6	25
$VA_{25}^{3.2}$	**8000**	3.2	25
$VA_{12.5}^{0.8}$	2000	0.8	**12.5**
$VA_{6.25}^{0.8}$	2000	0.8	**6.25**
$VA_{12.5}^{1.6}$	4000	1.6	**12.5**
$VA_{6.25}^{1.6}$	4000	1.6	**6.25**

Table 1.3: *Operating conditions in the velocity anti-node cases (VA). The bold font represents the simulation parameters that change from one simulation case to the next.*

Similar calculations are also carried out in the TR case and the main characteristics of these cases are shown in table 1.4.

Case	f^{ac} [Hz]	St [-]	$v_0'^{ac}$ [m.s^{-1}]
$TR_{25}^{0.3}$	**750**	0.3	25
$TR_{25}^{0.8}$	**2000**	0.8	25
$TR_{25}^{1.6}$	**4000**	1.6	25
$TR_{25}^{3.2}$	**8000**	3.2	25
$TR_{12.5}^{0.8}$	2000	0.8	**12.5**
$TR_{6.25}^{0.8}$	2000	0.8	**6.25**
$TR_{12.5}^{1.6}$	**4000**	1.6	12.5
$TR_{12.5}^{3.2}$	**8000**	3.2	12.5

Table 1.4: *Operating conditions corresponding to the traveling wave modulation cases (TR). The bold font represents the simulation parameters that change from one simulation case to the next.*

Calculations are initiated by starting from a modulation free solution NM. The NM solution is established over a minimum period of 150 convective times for the finer mesh where $\tau_{conv} = d/u_{inj}$. After a transient phase, the flow features a steady oscillatory motion. This permanent phase is examined through phase-averaged solutions calculated by averaging instantaneous snapshots over 30 cycles. The study has been carried out by calculating all cases shown in tables 1.3 and 1.4.

1.2.3 Grid convergence

It is important to make sure that grid convergence is achieved before performing any systematic numerical investigation. This is accomplished by performing simulations on three different meshes, with and without modulation. The fine, intermediate and coarse grids respectively comprise 28 million, 12 million and 3.8 millions cells. The extreme cases are referred to as X^{coarse} and X^{fine} in tables 1.2 and 1.3. Centerline profiles of mean and rms densities are plotted in figure 1.4 for cases NM^{fine}, NM and NM^{coarse}. Results for cases NM^{fine} and NM are quite similar, both in terms of mean and rms values, while departures are visible with the coarser grid. Similar conclusions hold in the modulated cases (figure 1.5). The intermediate mesh is then appropriate for the current study, and is used for all the simulations. The occurrence of peaks in the axial density evolution, at various distances from the injection plane (figure 1.5), can be explained by the presence of nodes in the jet motion where the maximum density is constant. Between the nodes, density fluctuates as a result of the jet motion. This has been observed in all our simulated cases. In figure 1.4, it can be seen that the first part of the curve shows a strong density gradient in the longitudinal direction. This is typical of a transcritical jet. The second part of the curve shows only a small gradient of density in the longitudinal direction. This one represents a gaseous-like behavior. The point of transition between these two states has been taken at a density 100 $kg.m^{-3}$ (which corresponds approximately to the crossing point of the linear extrapolation of these two parts). In the rest of the document, this value has been taken as the reference (ρ_{ref}(marking the limit between atmosphere ($\rho < \rho_{ref}$) and dense jet ($\rho > \rho_{ref}$).

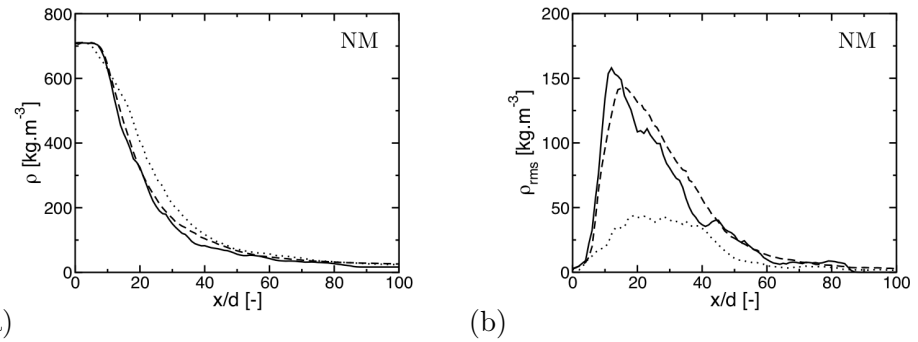

(a) (b)

Figure 1.4: *Evolution of density along the central axis for the fine, intermediate and coarse meshes in NM case, (a) mean density (b) rms density. − fine, −− intermediate, ··· coarse.*

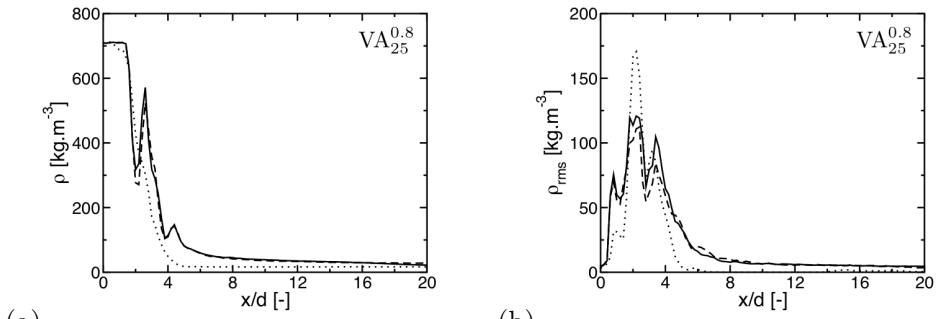

(a) (b)

Figure 1.5: *Evolution of density along the central axis for the fine, intermediate and coarse meshes in VA$_{25}^{0.8}$. (a) Mean density (b) rms density. – Fine, –– intermediate,··· coarse.*

1.3 Jet characteristics in the absence of modulation, NM case

Transcritical round jets have already been thoroughly studied in the past Zong and V.Yang (2006); Schmitt et al. (2011); Schmitt et al. (2009); Schmitt et al. (2010); Petit et al. (2013); Terashima and Koshi (2013); Petit et al. (2015); Müller et al. (2016). They are here used as a baseline solution and will serve as a reference in comparisons with the modulated cases.

1.3.1 Jet structure

An instantaneous snapshot of the jet without modulation is displayed in figure 1.6, which shows a side view of the jet colored by axial velocity as well as an axial cut of density. The interface plotted in this figure corresponds to a density of 100 kg.m^{-3} which suitably reflects the jet dynamics. The iso-density surface features ripples due to the high shear rate between the dense transcritical stream and the lighter environment. Near the injection plane, the transcritical jet maintains its round shape for a few injection diameters. Further downstream, the jet loses its round section because of mixing with the surrounding fluid. The shear interactions with the hot environment, as well as the mixing mechanisms, break the jet into pockets. In the axial cut it is visible that the jet keeps its round section as long as the density remains high. As soon as the density decreases the jet breaks down. As explained in Zong and V.Yang (2006) a transcritical jet can be decomposed into three zones: (1) The potential core corresponding to a region extending over a few injection diameters where the jet maintains a round shape and features a nearly constant density. (2) A transition region where the jet starts to break down. (3) A developed region where the transverse jet profiles become self-similar. In this region the flow has lost the memory of its injection conditions and parameters such as normalized

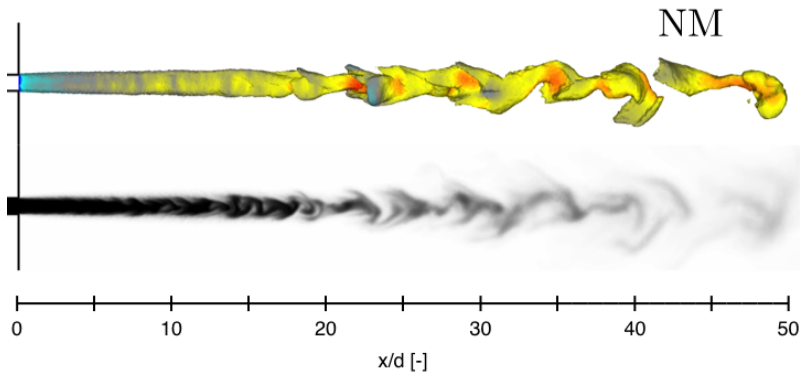

Figure 1.6: *Iso-density surface of 100 kg.m^{-3} colored by axial velocity (red: 15 m.s^{-1}; blue: 0 m.s^{-1}) and axial cut of the domain colored by density (black: 700 kg.m^{-3}; white: 0 kg.m^{-3}).*

density (as defined below) become nearly self similar in the transverse direction. The normalized density is defined as:

$$\rho^* = \frac{\overline{\rho} - \overline{\rho}_\infty}{\overline{\rho}_c - \overline{\rho}_\infty} \tag{1.6}$$

Where $\overline{\rho}$ is the mean density on a slice at a given distance of the injection plane, $\overline{\rho}_\infty$ is the mean density at a distance far away from the injection and $\overline{\rho}_c$ is the mean density on the axis. It is also useful to define the half radius $r_{1/2}$ (full-width-half-maximum) where a given quantity like the reduced density reaches half its value on the axis. Previous studies Zong and V.Yang (2006); Schmitt et al. (2010) indicate that $r_{1/2}$ is nearly constant near the injector and then increases linearly along the central axis.
The constant part of the curve characterizes the potential core of the jet. It is known from studies carried out at relatively low density ratio values ($S_\rho = \rho_{inj}/\rho_\infty$ less than 10) that the jet spreading rate (which is defined as the opening of the jet in the self-similar region) is typically close to 0.1 (see for example Chen and Rodi (1980)). Here S_ρ is around 44 (close to the density ratio observed in rocket engines) and one expects that the jet will spread at a much lower rate. This is indeed the case with a spreading rate that is of the order of 0.02.
The dense core region of the jet is easily identified in the longitudinal profiles of mean and rms density (figure 1.7(a)) and mean and rms axial velocity (figure 1.7(b)) The density remains at its injection value, in figure 1.7(a) up to about $7.6d$ approximately, characterizing the dense core region of the jet. Then the density rapidly decreases to the surrounding value, reached at about $75d$. In the longitudinal profile of axial velocity displayed in figure 1.7(b), one observes that the velocity remains nearly constant in the dense core region of the jet and then slowly decreases in a nearly linear fashion. This distinguishes such

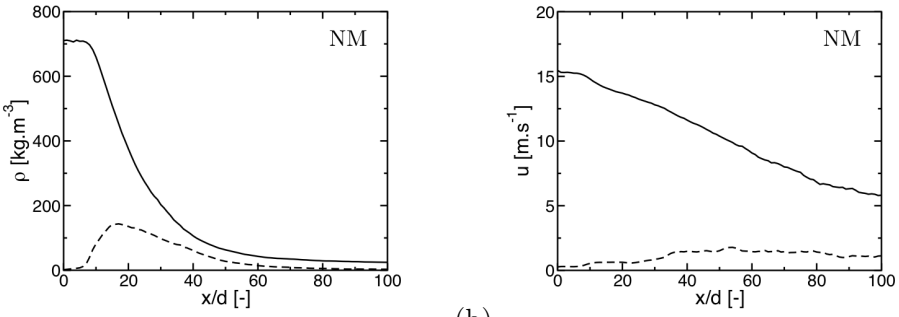

(a) (b)

Figure 1.7: *Evolution of (a) density and (b) axial velocity along the central axis for NM. − Mean value, −− rms value.*

jets from the more standard decay found in constant density flows, where the velocity decreases as a hyperbolic function of the axial coordinate.
Two length scales are defined, the first characterizes the length of the dense core while the second defines the entire jet. The dense core length $l_{99\%}$ corresponds to the length at which the reduced density (defined in equation 1.6) is equals to 0.99. The entire jet length $l_{10\%}$ corresponds to the length at which the reduced density equals 0.1. Table 1.5 gathers the characteristic lengths for case NM.

Case	$l_{99\%}^{NM}/d$ [-]	$l_{10\%}^{NM}/d$ [-]
NM	7.6	47

Table 1.5: *Characteristic length scales of the jet for case NM.*

1.3.2 Flow dynamics

It is interesting at this stage to characterize the natural frequencies of the jet. This is done by placing a sensor at the estimated end of the dense core region. The sensor records the three velocity components giving access to the corresponding power spectral densities (PSD). The maximum power density is found around f_d= 900 Hz. This frequency corresponds to a Strouhal number S_d= 0.36 usually associated with the preferred frequency of the jet Crow and Champagne (1971).
In the absence of modulation, the jet only features eddies with a typical size of the order of the jet diameter. These structures are convected at the injection velocity. It is convenient to define the jet centerline as the locus of transverse positions weighted by density (equation 1.7).

$$y_d(x_0) = \frac{\int_S \rho(x_0, y, z) y dS}{\int_S \rho(x_0, y, z) dS} \tag{1.7}$$

Where y is the transverse coordinate associated with the acoustic propagation direction ($y = 0$ in the center of the injector). This will be used in what follows

to characterize the jet motion. In the naturally developing jet, the jet centerline coincides with the injector axis.

1.4 Analysis of the transient phase

The initial jet (figure 1.6) is a long cylindrical stream with a round cross section. Under acoustic modulation the shape and length of the jet are changed. It is first interesting to examine the transient phase. This is done by considering $VA^{0.8}_{6.25}$ and $VA^{1.6}_{6.25}$ corresponding to Strouhal numbers 0.8 and 1.6 at a low amplitude of modulation. In a second step, the amplitude of oscillation is increased to 25 m.s^{-1}. This is representative of amplitudes encountered in practical systems undergoing instabilities and has also been considered in the reactive flow configurations Hakim et al. (2015) and Hakim et al. (2015). It is found that in this second situation the jet response is slightly more sensitive to the Strouhal number value.

1.4.1 Low amplitude modulation

In this first set of calculations the modulation level of oscillation is low (6.25 m.s^{-1}). As the acoustic field corresponding to this low amplitude modulation is established in the domain, the jet evolves and after a transient phase takes a new shape. Figure 1.8 shows the evolution of an iso-density surface (set to 100 kg.m^{-3}) at different times for a modulation frequency of 2000 Hz (St=0.8). The jet evolution observed in figure 1.8 can be divided into four phases numbered from 1 to 4. In figure 1.8 (1) there is no modulation the jet is in its initial state with a jet length of $47d$, (2) When the acoustic field reaches the axis the jet responds and its round cross section is flattened but the stream retains its original length, (3) The acoustic mode induces an intense mixing leading to a break down of the stream into pieces, it is dramatically shortened from $47d$ to $23d$, (4) In the final stage, the jet oscillates transversally around the injector axis. A similar evolution can be observed for the case $VA^{1.6}_{6.25}$, which corresponds to a higher Strouhal number but to the same low modulation amplitude. It is interesting to examine the evolution of the surface area A of an iso-density surface at the reference density ($\rho = 100$ kg.m^{-3}). This is plotted as a function of time in figure 1.9 for the two cases ($VA^{0.8}_{6.25}$ and $VA^{1.6}_{6.25}$). One finds that for both the modulation frequencies, the jet responds in a similar manner. As in figure 1.8, one can identify the same four phases in figure 1.9. In the first period, the surface area does not change, because it takes some time before the modulation reaches the round jet. During the second period the jet responds to the presence of acoustic modulation and flattens, a process leading to an increase of the surface area of the density surface. During the third period acoustically induced mixing breaks the jet in the downstream region and the surface area rapidly decreases. In the fourth period the jet is shortened and oscillates with a quasi-constant surface of exchange. For both modulated cases

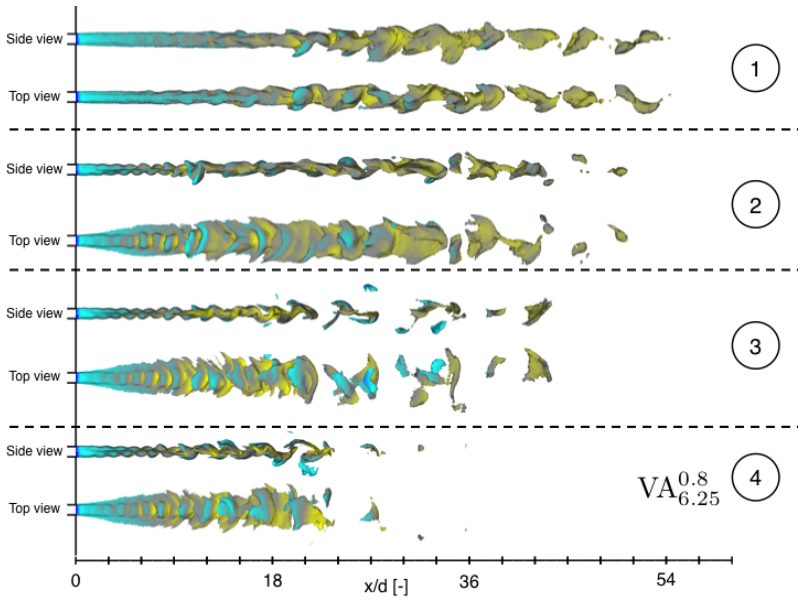

Figure 1.8: *Evolution of density iso-surface during the transient phase (ρ=100 kg.m^{-3}) colored by axial velocity (red: 20 m.s^{-1}; blue: 0 m.s^{-1}) for $VA^{0.8}_{6.25}$. Four instants are represented, corresponding to four characteristic stages in the transient phase.*

it can be seen that the increase and decrease of the jet length are approximately the same, which is also true for the duration of the transient phase. This indicates that the modulation frequency has little impact on the evolution of the exchange surface area for both modulated cases. When the transient phase is terminated, the jet appears significantly shorter and oscillates around the injector axis. A steady state of motion is reached, that second phase will be analyzed in section 1.5.

1.4.2 High amplitude modulation

In this second step a large amplitude oscillation (25 m.s^{-1}) is imposed. Calculations are carried out for Strouhal numbers ranging from 0.1 to 3.2. As in the low amplitude modulation cases, the jet is flattened and shortened in the presence of the acoustic modulation. The evolution of an iso-density surface is plotted in Figure 1.10 as a function of time for a modulation frequency of 2000 Hz (St=0.8) and a modulation amplitude of 25 m.s^{-1}. Figures 1.10 and 1.11 show similar phases, leading to jet break down. During stage 1, there is no modulation; the jet appears in its initial state with a jet length of approximately 47d. In stage 2, when the acoustic field has reached the jet, the stream is flattened but the length remains constant. In stage 3, the well established acoustic field induces mixing and breaks the jet down, shortening it dramatically from 47d to 6d in length. Stage 4 then corresponds to the regime of stable

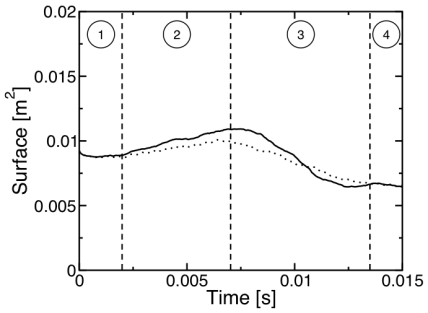

Figure 1.9: *Evolution of the integral of the iso-density surface equal to 100 kg.m^{-3} with time during the transient phase. — $VA^{0.8}_{12.5}$, ··· $VA^{1.6}_{12.5}$. Four instants are presented corresponding to four characteristic stages in the transient phase.*

jet oscillations. The surface area of the iso-density surface plotted versus time for the different modulation frequencies appears in figure 1.11.

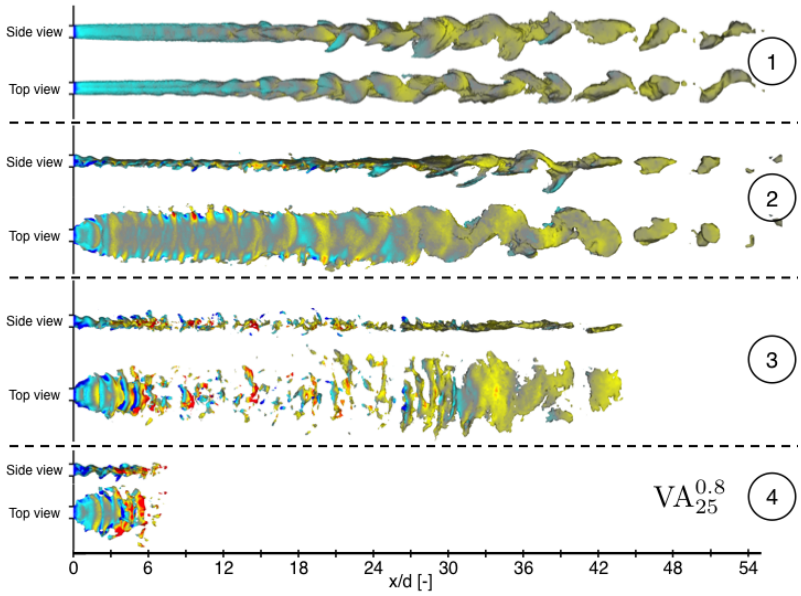

Figure 1.10: *Iso-density surface (ρ=100 kg.m^{-3}) colored by axial velocity (red: 20 m.s^{-1}; blue: 0 m.s^{-1}) for $VA^{0.8}_{25}$. Four instants are represented, corresponding to four characteristic stages in the transient phase.*

The evolution in surface area displayed in figure 1.11 is quite similar in all cases indicating a weak dependence on the Strouhal number. The final level reached after the transient period is in this case much lower than that corresponding to the natural jet. One identifies in figure 1.11 the same four stages described previously. The total duration of the transient phase is 4.5 ms. The higher the modulation amplitude, the shorter the jet.

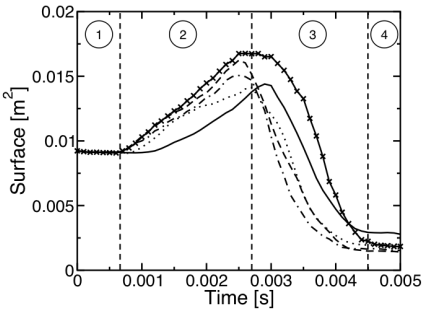

Figure 1.11: *Evolution of the iso-density surface equal to 100 kg.m^{-3} with time during the transient period for a constant modulation amplitude of 25 m.s^{-1} (a) – $VA_{25}^{0.1}$, $\cdots$ $VA_{25}^{0.3}$, $\cdot - \cdot$ $VA_{25}^{0.8}$, $--$ $VA_{25}^{1.6}$, $\times - \times$ $VA_{25}^{3.2}$.*

1.4.3 Duration of the transient phase

It is visible from figures 1.9 and 1.11 that the modulation frequency little impacts the duration of the transient phase contrary to the modulation amplitude. The duration of the transient phase is defined by the duration of stages 2 and 3 of figures 1.9 and 1.11. Figure 1.12 presents the impact of the modulation amplitude on the transient phase.

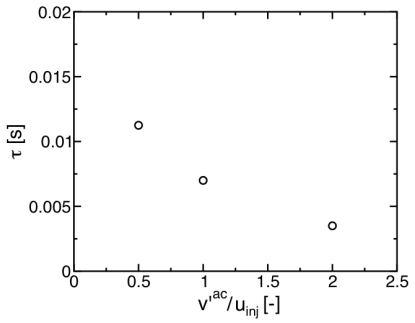

Figure 1.12: *Evolution of the duration of the transient phase with modulation amplitude for the three situations envisaged in the present paper: 6.25 m.s^{-1}, 12.5 m.s^{-1} and 25 m.s^{-1}, u_{inj}=12.5 m.s^{-1}.*

As expected, it shows that the duration of the transient phase is inversely evolving with the modulation amplitude.

1.5 Jet characteristics for standing modes, VA cases

We now consider the oscillatory regime obtained when the jet is submitted to a standing mode. The steady state reached after the transient period is examined by considering the jet geometry, mean flow statistics and flow dynamics.

1.5.1 Jet geometry

The jet dynamics is investigated by making use of phase averaging techniques. The jet geometry is observed by plotting a phase averaged iso-density surface. Phase averaging is used to eliminate the natural fluctuations and focus on the periodic component. Figure 1.13 shows results obtained for the different modulation amplitudes at a single modulation frequency of 2000 Hz (St=0.8) and three amplitudes of modulation.

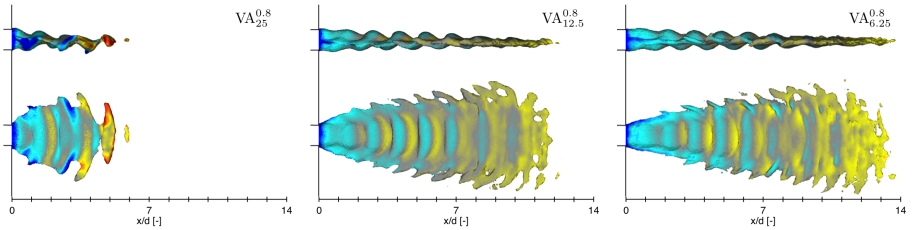

Figure 1.13: *Phase averaged iso-density surface (100 kg.m^{-3}) colored by axial velocity (red: 20 m.s^{-1}; blue: 0 m.s^{-1}) for decreasing amplitudes: $VA^{0.8}_{25}$, $VA^{0.8}_{12.5}$ and $VA^{0.8}_{6.25}$.*

The modulation amplitude does not change the behavior of the jet centerline, except that for higher modulation amplitudes, the oscillation level of the jet is larger. The modulation amplitude influences the jet length, a point that will be analyzed later on.
Figure 1.14 displays side and top views of phase averaged jets corresponding to a range of Strouhal numbers simulated for a single modulation amplitude of 25 m.s^{-1}. For low values of the Strouhal numbers the jet is highly deformed; it exhibits a highly curved centerline and the oscillation amplitude is large. This flag-like motion is found for Strouhal numbers 0.1 and 0.3. The term "flag-like" is used in the present context to describe the jet motion in an intuitive way with no connection with the real fluid dynamics of a flag in the wind. For higher Strouhal numbers of 1.6 and 3.2, the jet centerline deformation becomes less important and as the frequency increases it becomes less visible. The amplitude of oscillation of the jet is quite small and its centerline vibrates around its central position. For intermediate Strouhal numbers (0.8) the jet centerline displays a sinusoidal shape around the central axis.
The ripple wavelengths measured in figures 1.13 and 1.14 are well represented by $\lambda = u_{inj}/f^{ac}$. These ripples are visible in a Strouhal number range from 0.3 to 1.6. At higher Strouhal numbers however, the jet executes a limited sinusoidal motion, which cannot be extracted because it is too small. For lower Strouhal numbers the wavelength is so large that the jet is dissipated in the surrounding atmosphere before one entire wavelength can be seen. The power spectral density analysis of the jet, at the end of the dense core region, reveals that as expected the transverse and axial velocity components of the jet feature a dominant contribution at the modulation frequency.

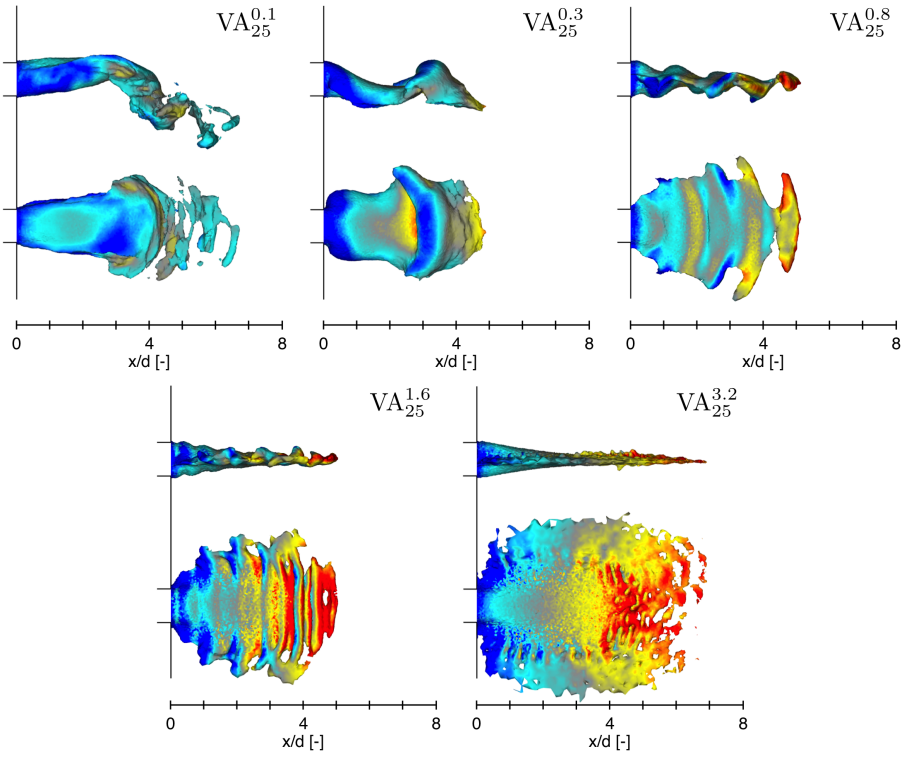

Figure 1.14: *Phase averaged iso-density surface (100 kg.m^{-3}) colored by axial velocity (red: 20 m.s^{-1}; blue: 0 m.s^{-1}) for a fixed modulation amplitude and a variable frequency: $VA_{25}^{0.1}$, $VA_{25}^{0.3}$, $VA_{25}^{0.8}$, $VA_{25}^{1.6}$ and $VA_{25}^{3.2}$.*

1.5.2 Mean flow statistics

1.5.2.1 Jet lengths

Figure 1.15 displays the influence of modulation amplitude and frequency on the parameters $l_{99\%}$ and $l_{10\%}$ defined in section 1.3.

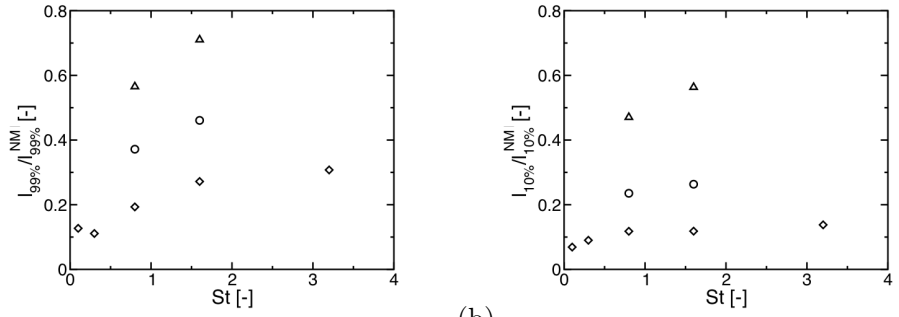

(a) (b)

Figure 1.15: *Influence of the modulation frequency and the modulation amplitude on (a) $l_{99\%}$ and (b) $l_{10\%}$. △ Modulation amplitude of 6.25 $m.s^{-1}$,○ modulation amplitude of 12.5 $m.s^{-1}$, ◇ modulation amplitude of 25 $m.s^{-1}$.*

The jet length scales $l_{99\%}$ and $l_{10\%}$ in figure 1.15 are affected by both the modulation frequency and amplitude. The shortest jets are obtained with a Strouhal number close to 0.5 and seem to reach a limit value for high Strouhal. The characteristic jet lengths decrease with the modulation amplitude at a nearly constant rate. This can be explained by the fact that higher transverse velocities allow better mixing of the jet with the environment. It is interesting to evaluate the influence of the modulation parameters on the jet length scales $l_{99\%}$ and $l_{10\%}$. Figure 1.16 represents the normalized jet length scales against the modulation amplitude.

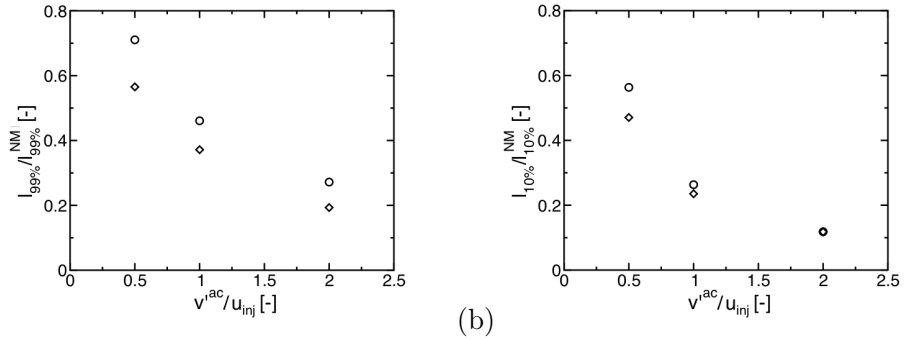

(a) (b)

Figure 1.16: *Influence of the modulation amplitude on (a) $l_{99\%}$ and (b) $l_{10\%}$. ○ Strouhal number of 1.6, ◇ Strouhal number of 0.8.*

The modulation amplitude shows a strong influence on the jet length. The re-

duction is inversely evolving with the modulation amplitude. While $l_{99\%}$'s evolution seems inversely proportional to the modulation amplitude figure 1.16(a), $l_{10\%}$ shows a saturation effect for large amplitudes.

1.5.2.2 Jet spreading

Figures 1.13 and 1.14 also clearly show that the jet is flattened. The acoustic field inside the domain crushes the jet in the vertical direction allowing it to spread in the spanwise direction. This phenomenon is especially visible in the top views in figures 1.13 and 1.14. When the Strouhal number is increased the spreading in the spanwise direction is enhanced. The modulation amplitude does not appear to affect this dilation, but only influences the jet length. In figure 1.13 the width of the jet is equivalent for the three modulation amplitudes. The smaller amplitudes of modulation allows the jet to move more freely inside the domain, however the modulation seems still strong enough to crush the jet at its tip, inducing a dilation in the spanwise direction.

1.5.3 Flow dynamics

It is now interesting to examine the jet centerline motion to describe the dynamics of the flow. Figure 1.17 illustrates the evolution of the jet centerline for $\mathrm{VA}^{0.8}_{12.5}$ and $\mathrm{VA}^{0.8}_{6.25}$.

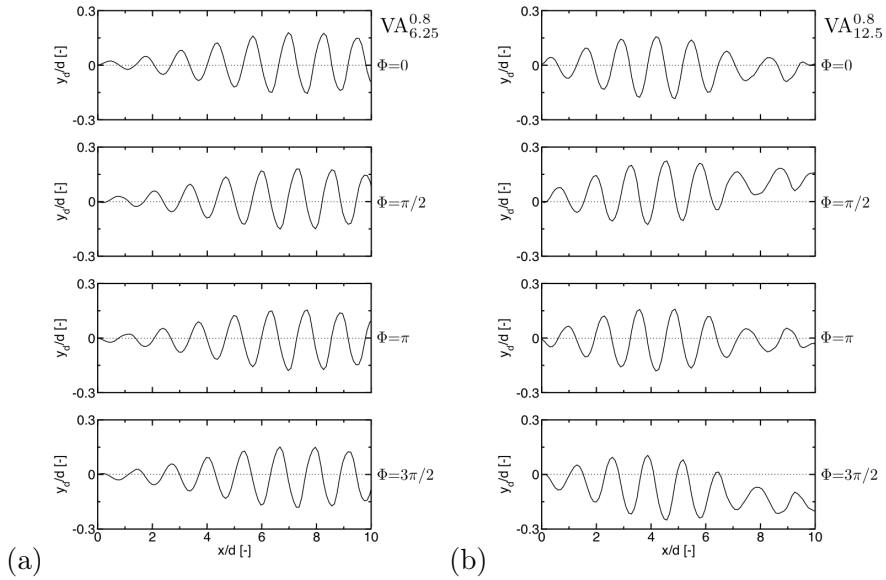

Figure 1.17: *Evolution of the jet centerline for (a) $VA^{0.8}_{6.25}$ and (b) $VA^{0.8}_{12.5}$. – Phase averaged centerline position, ··· average centerline position.*

The same behavior can be observed for both modulation amplitudes. In the dense core region, the jet exhibits a sinusoidal shape while the centerline oscil-

lates vertically around its mean position. Figure 1.18 displays the jet centerlines for $VA_{25}^{0.8}$ and $VA_{25}^{1.6}$ at four different phases of the modulation. The vertical jet displacement is noted y_d. Strouhal numbers of 0.8 and 1.6 have been selected because at those values, the jet motion is the most visible. For higher Strouhal numbers the jet motion is too limited to be resolved on the selected mesh. At Strouhal numbers lower than 0.8 the dense core region is shorter than a jet wavelength, and one cannot distinguish the wavelike behavior exemplified previously.

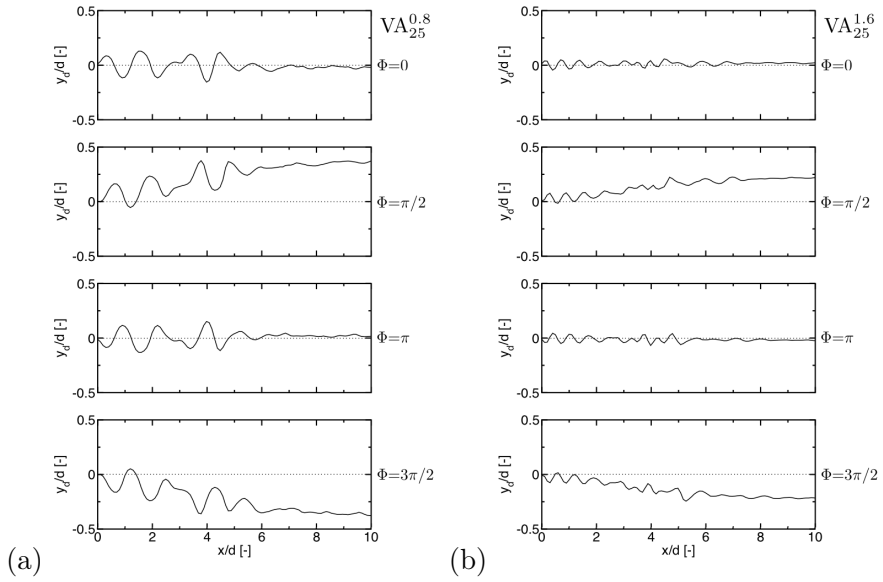

Figure 1.18: *Evolution of the jet centerline for (a) $VA_{25}^{0.8}$ and (b) $VA_{25}^{1.6}$. – Phase averaged centerline position, ··· average centerline position.*

Analysing figure 1.18 for both Strouhal numbers, a common behaviour is visible. In the first part of the jet, near the injection plane, the jet exhibits a sinusoidal wavelike motion. This reflects the flag-like motion described previously. At a distance of approximately $6d$ for the Strouhal numbers considered here, the sinusoidal wave shape slowly turns into a bulk motion of the jet centerline that reflects the jet vibration uncovered previously.

1.6 Jet dynamics under a traveling wave modulation, TR cases

In a full size LRE some of the most destructive instabilities are transverse spinning instabilities Oefelein and Yang (1993). It is not easy to reproduce spinning modes experimentally, however using the boundary conditions defined in figure 1.1, the equivalent of a spinning mode for Cartesian geometries is relatively simple to setup. By modulating one boundary condition only, one

generates a propagating wave featuring pressure nodes and antinodes traveling in the domain from top to bottom. The transverse velocity in the domain also has nodes and antinodes that move from top to bottom at the speed of sound (figure 1.3(b)).

1.6.1 Jet geometry

Results of the interaction between the acoustic field and the round transcritical jet are similar to those found in the standing mode case, the jet is shortened, flattened and is made to oscillate around a mean position. The only difference with a standing mode modulation is that the time averaged position of the jet does not coincide with the central injection axis but instead, the mean jet centerline is bent in the direction of propagation as illustrated in figures 1.19 and 1.20.

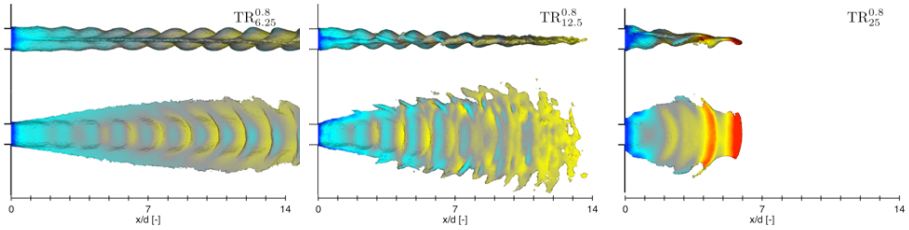

Figure 1.19: *Phase averaged iso-density surface (100 kg.m^{-3}) colored by axial velocity (red: 20 m.s^{-1}; blue: 0 m.s^{-1}) at a given phase for $TR^{0.8}_{6.25}$, $TR^{0.8}_{12.5}$ and $TR^{0.8}_{25}$. Top: side view, bottom: top view.*

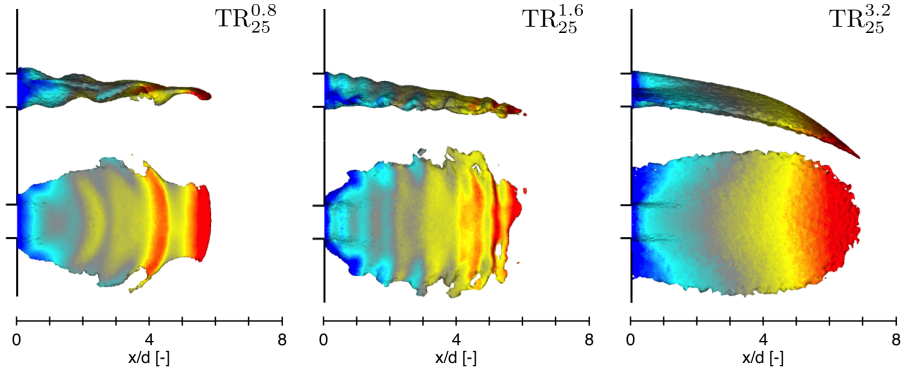

Figure 1.20: *Phase averaged iso-density surface (100 kg.m^{-3}) colored by axial velocity (red: 20 m.s^{-1}; blue: 0 m.s^{-1}) at a given phase for $TR^{0.8}_{25}$, $TR^{1.6}_{25}$ and $TR^{3.2}_{25}$. Top: side view, bottom: top view.*

During the transient phase, the dense core of the jet maintains a straight mean jet centerline at first and then bends in the direction of the acoustic flux. Such a bending has already been observed for jets in stationary acoustic field in

numerical and experimental studies (Baillot et al. (2009); Carpentier et al. (2009); Hakim et al. (2015)). Current studies suggest that non-linear acoustic effects such as acoustic radiation pressure cause the bending of the jet center line (Borgnis (1953); Lee and Wang (1993)), which would then behave like a cylindrical but deformable obstacle Wu et al. (1990); Hasegawa et al. (1993); Wei et al. (2004); Baillot et al. (2009).

1.6.2 Flow dynamics

To get a better view of the jet bending induced by the traveling mode, it is useful to plot the average jet position, as well as the jet centerlines at different instants during the modulation cycle (figures 1.21 and 1.22). These plots show that bending takes place in the direction of the acoustic flux and becomes more pronounced as the amplitude and frequency are augmented. The jet is also seen to oscillate around its average centerline position, just as in the VA cases.

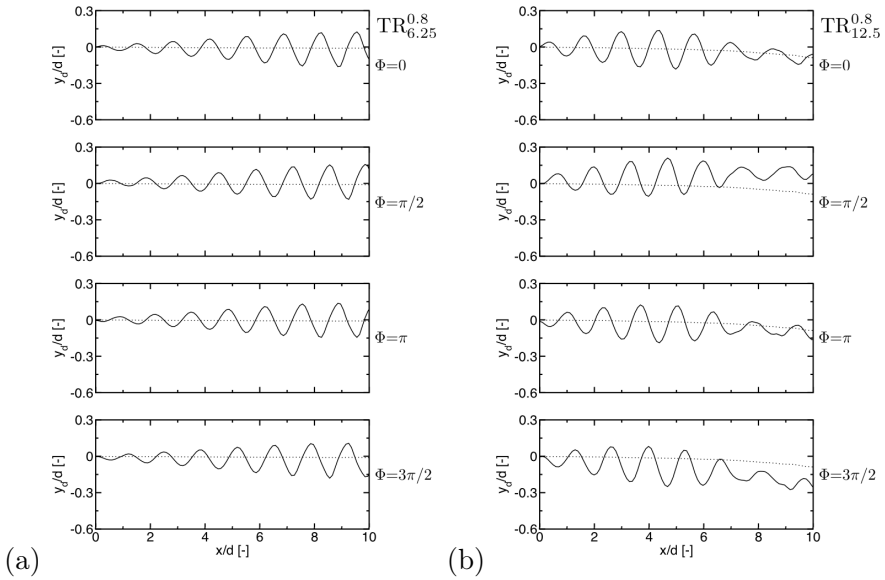

Figure 1.21: *Evolution of the jet centerline for (a) $TR^{0.8}_{6.25}$ and (b) $TR^{0.8}_{12.5}$.– Phase averaged centerline position, $\cdots$ average centerline position.*

To facilitate the comparison between traveling and standing mode cases TR and VA, it is convenient to remove the average jet position $< y_d >$ (where $<>$ denotes a temporal averaging) from the phase averaged jet position and superimposed $y_d - < y_d >$ for both cases. Results are plotted in figures 1.23 and 1.24. For each moment in the cycle the centerlines corresponding to TR and VA cases nearly coincide, indicating that their dynamics around their average position is nearly identical. Similar results are obtained for all the simulated cases except for very large amplitudes and high Strouhal numbers where a small phase shift is observed. In terms of flow dynamics, imposing a transverse

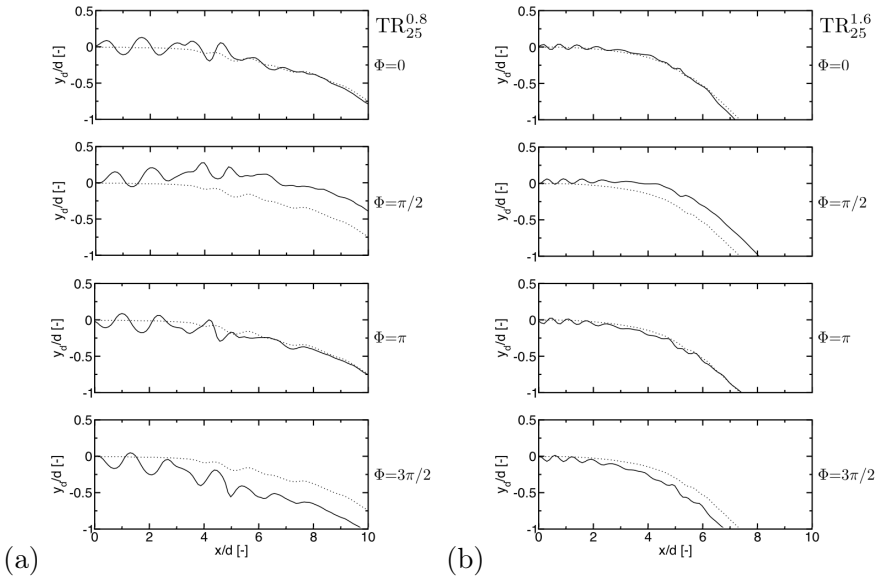

Figure 1.22: *Evolution of the jet centerline for (a) $TR_{25}^{0.8}$ and (b) $TR_{25}^{1.6}$. – Phase averaged centerline position, ⋯ average centerline position.*

acoustic traveling wave has the same effects as a transverse acoustic velocity modulation, if one accounts for a bending of the jet centerline in the direction of the acoustic flux.

1.7 Jet dynamic modeling

At this stage it is useful to analyze two of the features uncovered by the previous simulations. The jet deformation and flattening is considered first. The motion of the jet centerline is examined in a second step.

1.7.1 Jet flattening

It has already been indicated that the spreading of the flow in the spanwise direction is linked to the presence of low pressure regions on both sides of the dense fluid stream (figure 1.25). It is however important to see if the order of magnitude of the corresponding pressure drop can be obtained from first principles.
This can be done by estimating the pressure drop on both sides of the jet by applying the unsteady Bernoulli theorem:

$$\frac{\partial \phi}{\partial t} + \frac{p}{\rho} + \frac{v^2}{2} = 0 \tag{1.8}$$

Where ϕ is the velocity potential. This equation is written for the fluid flow induced by the acoustic modulation around the dense jet. The jet core can be

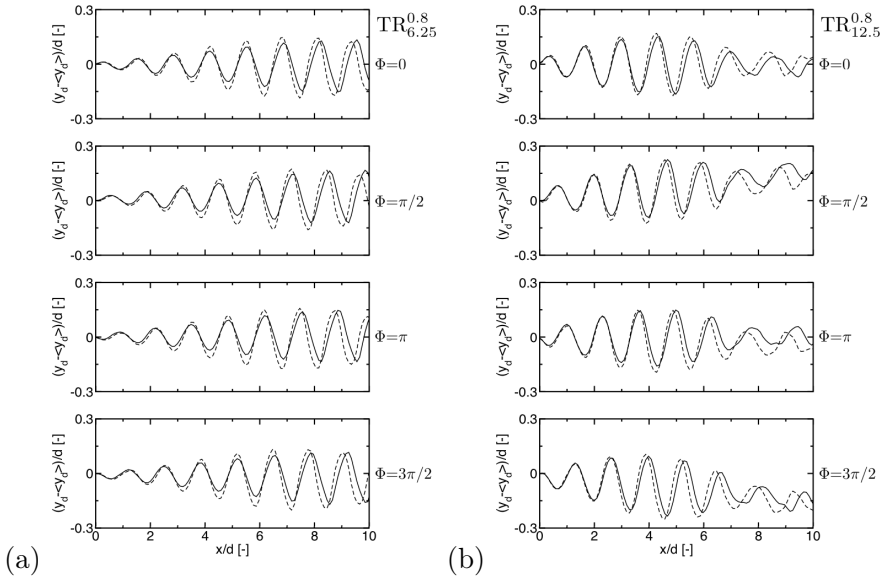

Figure 1.23: *Jet centerline dynamics ($y_d - < y_d >$). (a) – $TR^{0.8}_{6.25}$ and –– $VA^{0.8}_{6.25}$ and (b) – $TR^{0.8}_{12.5}$ and –– $VA^{0.8}_{12.5}$.*

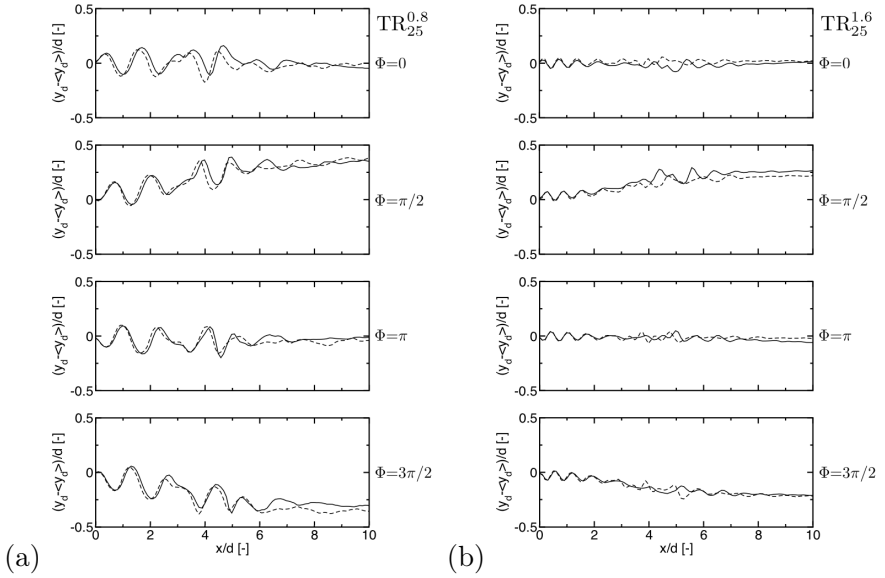

Figure 1.24: *Jet centerline dynamics ($y_d - < y_d >$). (a) – $TR^{0.8}_{25}$ and –– $VA^{0.8}_{25}$ and (b) – $TR^{1.6}_{25}$ and –– $VA^{1.6}_{25}$.*

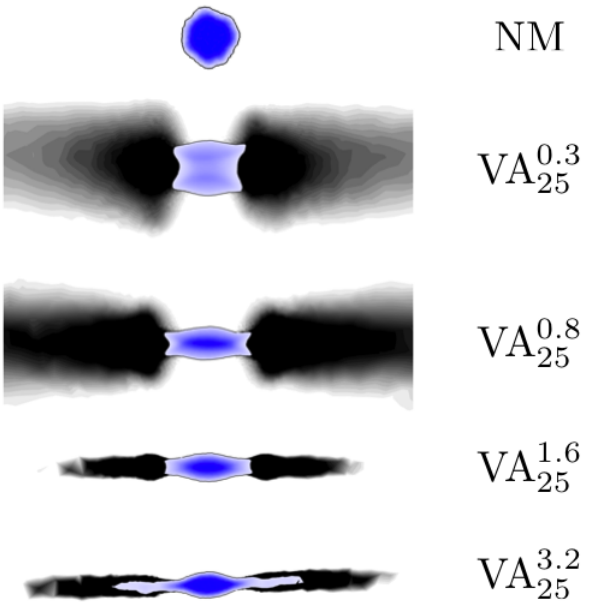

Figure 1.25: *Transverse cut across the averaged jet at a distance of 3d from the injector exit plane. Pressure plotted on a grey level scale (white: 6 MPa; black: 5.998 MPa). The jet is colored by density (white: 100 kg.m^{-3}; blue: 700 kg.m^{-3}). .*

roughly modeled as a cylindrical obstacle. The light ambient fluid is locally accelerated around the jet and this generates a low pressure region on its side. The following development is based on the work proposed in Hakim (2013). In cylindrical cordinates (r, θ) one may express the velocity potential in the form:

$$\phi(r, \theta, t) = v(t) \left(r + \frac{R^2}{r} \right) \cos\theta \tag{1.9}$$

Where R is the initial jet radius. On the cylinder surface ($r = R$) the radial velocity is equal to zero but the tangential velocity is given by:

$$v_\theta(t) = \frac{1}{r} \frac{\partial \phi}{\partial \theta} = -2v(t) \sin\theta \tag{1.10}$$

Note that outside the jet ($r \geq R$) the amplitude of the transverse velocity is v_0, the amplitude of the acoustic modulation. The pressure is then given by:

$$p(\theta, t) = 2\rho R v_0 \omega^{ac} \sin(\omega^{ac} t) \cos\theta - 2\rho v_0^2 \cos^2(\omega^{ac} t) \sin^2\theta \tag{1.11}$$

The mean pressure drop at an angle of $\theta = \pi/2$ is $-\rho v_0^2$ and this drop in pressure does not depend on the acoustic frequency f_{ac}. The case of a modulation frequency of $VA_{25}^{0.8}$ has been investigated. This gives a pressure drop of 62,500 Pa on the side of the jet on a iso-density surface where ρ=100 kg.m^{-3}.

1.7.2 Flow dynamics

The objective is to model the jet centerline dynamics illustrated previously, in particular in figures 1.17 and 1.18. The central idea is to decompose the jet motion as a sum of acoustic and hydrodynamic components. The first is responsible for the bulk motion of the jet centerline in the externally imposed acoustic field, the latter is induced by the acoustic disturbance and takes the form of a convective wave traveling along the jet. These two components are estimated in what follows.

1.7.2.1 Acoustic motion

The bulk oscillation of the jet centerline follows the acoustic motion up to a distance from the injection plane where the jet does not exist anymore and the transverse motion of the medium is defined by the acoustic modulation. To estimate the velocity induced by the acoustic field, it is important to account for the changes in impedance from the outer region to the jet centerline. This may be modeled by assuming that an interface separates the ambient region from the inner core. The transverse velocity v_{jet} inside the jet is given by:

$$v_{jet} \simeq v'^{ac} t_{12} \tag{1.12}$$

Where t_{12} represents the transmission coefficient from the outer medium (region 1) to the inner jet (region 2) : $t_{12} = 2\rho_1 c_1/(\rho_1 c_1 + \rho_2 c_2)$.

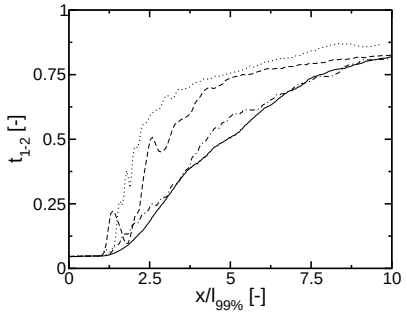

Figure 1.26: *Evolution of the transmission coefficient* t_{12} *for* $-$ *NM,* $\cdot - \cdot$ $VA^{0.8}_{12.5}$, $--$ $VA^{0.8}_{25}$, $\cdots$ $VA^{1.6}_{25}$.

The evolution of the transmission coefficient plotted in figure 1.26 indicates that in the very dense core region there is little penetration of the acoustic field inside the jet. As the density decreases, the transverse acoustic motion reaches the jet center. In all simulations, the transmission coefficient evolves in a similar way. In the rest of this work the transmission coefficient t_{12} will be that of case NM.
The jet displacement due to acoustic field y_d^{ac} is obtained by integrating the acoustic velocity in the jet over time. The acoustic velocity is given by $v_{jet}^{ac} =$

$v_{jet}\cos(2\pi f^{ac}t)$. The acoustic jet displacement is then given by:

$$y_d^{ac}(t) = \frac{v_0'^{ac}}{2\pi f^{ac}} \frac{2\rho_1 c_1}{\rho_1 c_1 + \rho_2 c_2} \sin(\omega^{ac} t) \tag{1.13}$$

The integration of the acoustic velocity in the jet gives rise to an integration constant, which in this case represents the initial position of the jet a $t = 0$. Four different phases of the jet displacement induced by acoustics are displayed in figure 1.27.

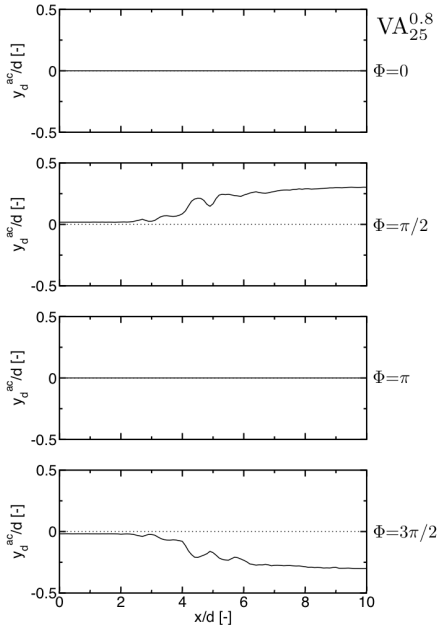

Figure 1.27: *Evolution of the jet centerline as described by the acoustic model of equation 1.13 for* $VA_{12.5}^{0.8}$. $-$ y_d^{ac}, $\cdots$ *average jet position.*

The acoustic motion corresponds to the jet behavior in the downstream region but this model does not account for the jet kinematics in the injector nearfield. To better quantify the transverse displacement of the jet, a spatially averaged jet position is computed. This average position $\overline{y_0}$ is defined by equation 1.14.

$$\overline{y_0} = \frac{1}{x_2 - x_1} \int_{x_1}^{x_2} (y_d - \langle y_d \rangle)\, dx \tag{1.14}$$

Where $[x_1, x_2]$ is the averaging interval and $\langle y_d \rangle$ is the time average of y_d. Figure 1.28 represents the average position of the jet during a period.
In figure 1.28 a sine function, representative of a pure acoustic displacement, was added to be compared to the average position of the jet. It can be seen that the averaging from $50d$ to $100d$ matches the sine function well, which means that for densities lower than the injection density, the jet is only affected by the

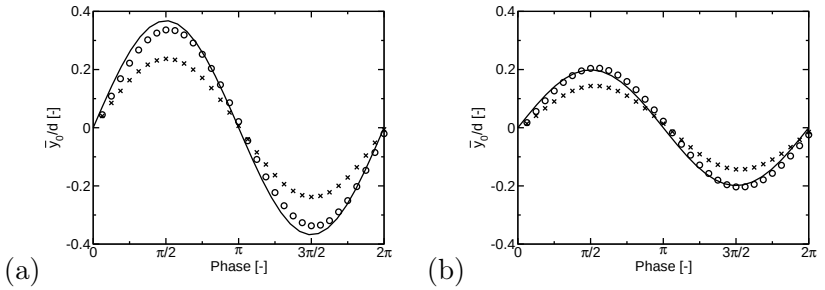

Figure 1.28: *Theoretical and numerical jet displacement for (a) $VA^{0.8}_{12.5}$ and (b) $VA^{0.8}_{25}$.– Pure sine wave using $v_0'^{ac}/\omega^{ac}\sin(\omega^{ac}t)$, ∘ average jet position for 50d ≤ x ≤ 100d, × average jet position for x ≤ 100d.*

acoustic field. For the averaging between $0d$ and $100d$, close to the injection plane, the amplitude behaves differently, which suggests that there is another phenomenon that takes place in the interaction between the jet and the acoustic modulation.

1.7.2.2 Hydrodynamic response

There are many circumstances where a jet submitted to an acoustic modulation features a hydrodynamic response. This is the case for example when an acoustic wave is introduced on the upstream side of a jet formed by an injector or a nozzle. The response of a jet to waves impinging from the side is less well documented. The purely hydrodynamic response of the jet can be estimated using a propagating wave motion (equation 1.15).

$$y_d^h(x,t) = \frac{A_h(x)}{\omega^{ac}}\sin(\kappa^h x - \omega^{ac}t) \tag{1.15}$$

Where A_h is a function that gives the spatial distribution of the hydrodynamic amplitude and κ^h is the hydrodynamic wave-number $\kappa^h = \omega^{ac}/u_{inj}$. The shape and amplitude of the function A_h (equation 1.16) has been chosen assuming an exponential growth rate of the fluctuation along the jet.

$$A_h(x) = \alpha\exp\left[-\left(\frac{x-l_A}{\sigma_A}\right)^2\right] \tag{1.16}$$

Where l_A is the axial position at which the hydrodynamic fluctuation is maximum, σ_A is a constant used to set $A_h(0) \sim 0$ and α is an adjustment parameter used to set the model for one case and is kept constant in all other cases. In order to be in good agreement with LES data the following values have been chosen for the A_h function parameters: $l_A = 1.7\,l_{99\%}$, $\sigma_A = l_{99\%}$ and $\alpha = u_{inj}$. This hydrodynamic displacement has a wavelike behavior which represents the flapping motion observed in low Strouhal number cases. This hydrodynamic

component can now be added to the acoustic displacement given by equation 1.13. Equation 1.17 gives the general form of the jet motion.

$$y_d^m(x,t) = y_d^{ac}(t) + A_h(x) y_d^h(x,t) \tag{1.17}$$

Where y_d^m is the sum of two contributions the acoustic response and the hydrodynamic response. The complete model of the jet centerline behavior is then given by equation 1.18.

$$y_d^m(x,t) = \frac{v_0'^{ac}}{\omega^{ac}} t_{12}(x) \sin(\omega^{ac} t) + \frac{A_h(x)}{\omega^{ac}} \sin(\kappa^h x - \omega^{ac} t) \tag{1.18}$$

This expression is examined for different modulation frequencies and different modulation amplitudes. Figure 1.29 displays results obtained for modulation amplitudes of 6.25 m.s^{-1} and 12.5 m.s^{-1}.

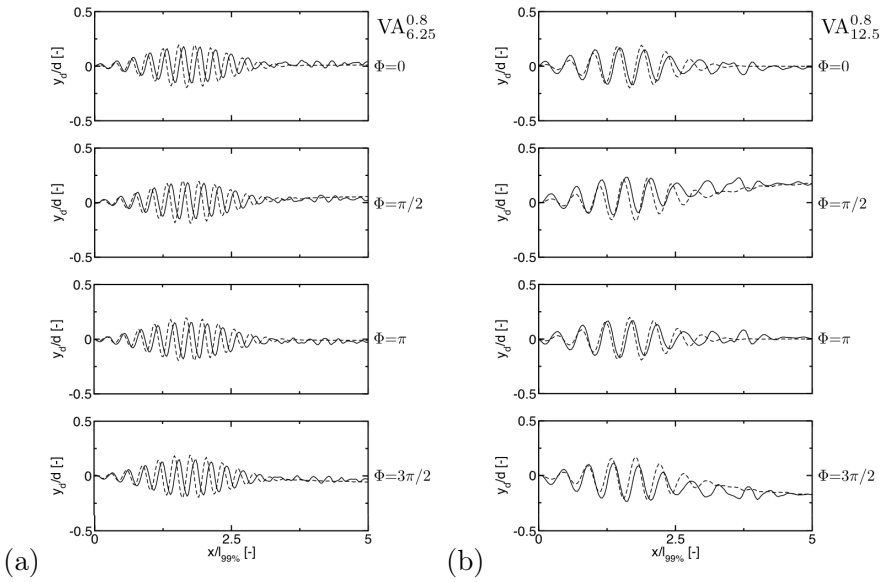

Figure 1.29: *−− Modeled jet centerline displacement and − simulated jet displacement for (a) $VA^{0.8}_{6.25}$ and (b) $VA^{0.8}_{12.5}$.*

It can be seen that the model suitably retrieves the jet behavior displayed in figure 1.17. The wavelengths and maximum amplitudes are well represented. The model does not recreate point for point the jet centerline dynamics as extracted from the simulation, however the jet response to the acoustic forcing is well obtained. The length of the jet displayed in figure 1.29 stops at 5 $l_{99\%}$ because the characteristic length of VA$^{0.8}_{6.25}$ and VA$^{0.8}_{12.5}$ are so long that it is hard to distinguish jet from atmosphere beyond this point. Figure 1.30 displays the jet centerline model for Strouhal numbers of 0.8 and 1.6.
Again the jet behaviour displayed in figure 1.18 is well retrieved especially in the transition region. The model is relatively simple and can easily be

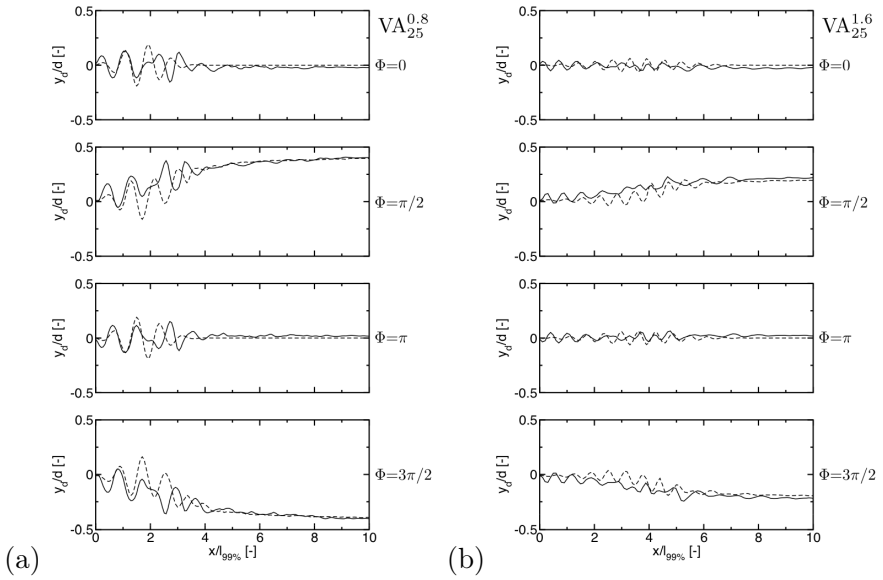

Figure 1.30: *−− Modeled jet centerline displacement and − simulated jet displacement for for (a) $VA_{25}^{0.8}$ and (b) $VA_{25}^{1.6}$.*

implemented in a low order dynamical description dedicated to combustion instability analysis.
For TR cases, all conclusions from the VA cases are still valid provided that the bending is accounted for by adding a mean centerline displacement. In the case of a traveling mode, the displacement of the jet centreline y_d^s is then given by:

$$y_d^s(x,t) = y_d^m(x,t) + y_d^b(x) \tag{1.19}$$

Where $y_d^b(x)$ is the function defining the mean jet bending.

1.8 Conclusions

This chapter describes the dynamics of a round transcritical jet interacting with a transverse acoustic modulation. The jet is injected under transcritical conditions into a hot environment. The influence of the modulation frequency is investigated by considering Strouhal numbers ranging from 0.1 to 3.2. Effects of modulation amplitude are also investigated by imposing weak and strong levels from 6.25 m.s^{-1} to 25 m.s^{-1}. Simulations were carried out in two steps. The first step was dedicated to the study of the transient phase (when the jet breaks down) and the second step during the stationary phase when the jet oscillates periodically. The solutions recorded during the second step were also used to generate phase averaged solutions. Different characteristics of the modulated jets were analyzed. The study of five different modulation frequencies reveals

that in the presence of acoustic modulation the jet shrinks in the axial direction and stretches in the spanwise direction giving rise to a flat stream. After a finite time, iso-density surfaces flap around the central position. It is also found that the mean jet length is nearly constant for high modulation frequencies and that the smallest mean jet length corresponds to a Strouhal number of 0.3, close to the preferred jet Strouhal number. There are two regimes of oscillation: within the low frequency range a flag like motion where the jet flaps and is notably deformed and within the high frequency range a bulk oscillation, where the jet exhibits smaller oscillation amplitudes and such that the centerline remains essentially straight. The oscillation amplitudes follows a $1/f$ law indicating that for very high modulation frequencies there is little oscillation of the jet. The simulations indicate that low pressure regions are formed on both sides of the jet and this may explain the observed spanwise stretching. This is supported by an order of magnitude estimation of the pressure drop induced when the lighter fluid, driven by the transverse acoustic velocity, meets the dense core of the jet and is accelerated to bypass the dense jet region. Calculations carried out by placing the jet in a traveling acoustic wave field uncover an interesting effect whereby the jet is bent in the direction of propagation of the acoustic field. It is shown that the jet response is otherwise quite similar to that observed in the standing mode case. A model is finally proposed to describe the jet centerline kinematics. It is shown that the motion can be decomposed in acoustic and hydrodynamic components, which when suitably combined, retrieve the motion observed in the simulations. This study gives a detailed view of an interaction, which may be of fundamental importance in combustion instabilities in rocket engines and results obtained here may be used in the design of low order modeling tools.

Chapter 2

Simulation of a coaxial jet under mass flow rate and pressure modulations

This chapter explores possible driving mechanisms of combustion instabilities in liquid rocket engines. Large eddy simulations are carried out in a single coaxial injector situation. The jet flame is first characterized in the absence of modulation. The length, heat release rate and general appearance of the flame is observed in order to determine the impact of mass flow rate modulation as well as pressure modulation on the flame. The mass flow rate modulation introduces convective structures inside the domain. These structures locally generate an increase of the heat release rate. In order to evaluate this increase, the heat release rate is compared to the velocity of the annular jet. A transfer function is established between the heat release rate and the velocity of the annular flow to predict how the mass flow rate modulation impacts the heat release rate. It is found that the flame acts as a low pass filter, with strong heat release fluctuations for frequencies under 5 kHz. A similar analysis is done on the influence of pressure modulations. The flame shows a larger response for cases with pressure modulation than for cases with only mass flow rate modulation, for all studied frequencies. Analytical transfer functions are derived, with a reasonable agreement with LES results, both in terms of gain and phase. These transfer functions are of importance for reduced order modeling.

2.1 Introduction

Large eddy simulations allows considerable progress in the analysis of combustion instabilities (Duchamp de Lageneste and Pitsch (2001); Mahesh et al. (2002); Pierce and Moin (2004); Candel et al. (2011)). This is supported by several examples of applications (Schönfeld and Poinsot (1999); Angelberger

et al. (2000); Selle et al. (2004); Martin et al. (2006); Roux et al. (2007); Wolf et al. (2009); Wolf et al. (2012); Hakim et al. (2015); Urbano et al. (2016)). In the liquid rocket engine field, LES applications are more recent because of the many complexities arising from the extreme operating conditions prevailing in those engines. LES could not be carried out without taking into account real gas thermodynamics and transport phenomena (Schmitt (2009)). It was also necessary to derive a combustion model providing a suitable description of the heat release rate. These specific aspects have to be considered before carrying out any simulations for the analysis of combustion instabilities. Studies carried out during a period of about ten years have led to the development of a LES software relying on the AVBP flow solver (Moureau et al. (2005); Gourdain et al. (2009); Gourdain et al. (2009)) and designated as AVBP-RG (Pons (2009); Schmitt (2009)). More details on this software can be found in appendix B. This code combines the AVBP flow solver with real gas thermodynamics, transport phenomena and real gas characteristic boundary conditions. Most of the combustion dynamic simulations reported in the literature have been carried out with this software. Simulations of flame/acoustic interactions have been studied previously in situations where the flames were established near a velocity anti-node. These studies have been performed on the Multiple Injector Combustor (MIC) (Méry et al. (2009); Méry et al. (2013)), on the Common Research Chamber in Marseille (Cheuret and Searby (2003); Cheuret and Searby (2004)) and at DLR Lampoldshausen (Hardi et al. (2011); Hardi et al. (2014)). It was thought that the velocity induced motion could be an important source of heat release fluctuation which in turn could bring energy to the acoustic transverse mode. Interactions between a dense transcritical jet, a coaxial jet or a cryogenic flame with a transverse acoustic perturbation are now well documented (Richecoeur et al. (2006); Davis and Chehroudi (2006); Leyva et al. (2008); Carpentier et al. (2009); Baillot et al. (2009); Lespinasse et al. (2013); Méry et al. (2013); Hakim et al. (2015); Hakim et al. (2015)). Calculations have also been carried out in multiple jet flame configurations operating in the transcritical range. In the full simulation of the Multiple Injector Combustor reported by Hakim et al. (2015), it is shown that the simulated jet dynamics is in good agreement with experimental results. Under acoustic modulations the flames are shortened and flattened in the spanwise direction (perpendicular to the plane containing the flames and transverse velocity perturbations). At this stage it is also important to examine other possible interactions and specifically those which were initially considered to drive instabilities in liquid rocket engines. Recent simulations indicate that they may play a crucial role for the prediction of combustion instabilities (Urbano et al. (2016); Urbano et al. (2016)). In the early models, effects of mass flow and pressure were emphasized. In the classical sensitive time lag model, the analysis indicates that the relative heat release rate fluctuations can be written as a function of the

pressure or mass flow at time t and a delayed pressure at time $t - \tau$:

$$\frac{\dot{Q}'}{\overline{\dot{Q}}} = n\frac{\phi(t) - \phi(t-\tau)}{\overline{\phi}} \tag{2.1}$$

Where ϕ is a fluctuating parameter (here either the pressure or the mass flow rate), n is the interaction index and τ is the time lag. This sort of relationship has been used in early studies on combustion instabilities such as (Tsien (1952a); Marble (1953); Crocco and Cheng (1956)). The objective of this chapter is to understand how combustion processes are affected by modulated injection conditions and ambient pressure fluctuations. This chapter is organized as follows: The governing equations are presented in section 2.2. Calculations of the flame structure in the absence of modulations are discussed in section 2.3. In section 2.4 the flame is submitted to mass flow rate modulations and the heat release rate is analyzed in order to characterize the influence of the modulation on it. A model is then developed to predict the response of the heat release rate to mass flow rate modulations. The flame is then submitted to pressure modulations in section 2.5. After a detailed analysis of the flame response, a model that gives the heat release rate fluctuations in terms of pressure fluctuations is derived. The developed models will then serve as additional instability driving mechanisms in a reduced order code derived in the third part of this document.

2.2 Governing equations, models and numerical approach

The global approach for this simulation follows the stategy described in Schmitt et al. (2010); Hakim (2013); Hakim et al. (2015). Calculations are carried out with the AVBP flow solver developed by CERFACS and IFPEN (Moureau et al. (2004); Schönfeld and Rudgyard (1999)) and extended to supercritical pressure flows by Schmitt et al. (2010) and Schmitt et al. (2011). This software designated as AVBP-RG includes a real gas thermodynamics description based on the Peng-Robinson equation of state (EOS) (Peng and Robinson (1976)) and adapted transport models of the type proposed by Chung et al. (1988). The filtered Navier-Stokes equations solved in this study are given by equations

(2.2) to (2.5):

$$\frac{\partial \overline{\rho}}{\partial t} + \frac{\partial \overline{\rho}\widetilde{u}_j}{\partial x_j} = 0 \tag{2.2}$$

$$\frac{\partial \overline{\rho}\widetilde{Y}_k}{\partial t} + \frac{\partial \overline{\rho}\widetilde{u}_j\widetilde{Y}_k}{\partial x_j} = -\frac{\partial \overline{J_{k,j}}}{\partial x_j} - \frac{\partial \overline{J_{k,j}}^t}{\partial x_j} + \overline{\dot{\omega}}_k \tag{2.3}$$

$$\frac{\partial \overline{\rho}\widetilde{u}_i}{\partial t} + \frac{\partial \overline{\rho}\widetilde{u}_j\widetilde{u}_i}{\partial x_j} = -\frac{\partial \overline{p}}{\partial x_i} + \frac{\partial \overline{\tau_{ij}}}{\partial x_j} - \frac{\partial \overline{\tau_{ij}}^t}{\partial x_j} \tag{2.4}$$

$$\frac{\partial \overline{\rho}\widetilde{E}}{\partial t} + \frac{\partial \overline{\rho}\widetilde{u}_j\widetilde{E}}{\partial x_j} + \frac{\partial \overline{p}\widetilde{u}_j}{\partial x_j} = -\frac{\partial \overline{q_j}}{\partial x_j} + \frac{\partial \widetilde{u}_i\overline{\tau_{ij}}}{\partial x_j} - \frac{\partial q_j^t}{\partial x_j} + \overline{\dot{\omega}}_T \tag{2.5}$$

Where ρ is the density, $\boldsymbol{u} = (u_1, u_2, u_3)$ the velocity vector, E the total energy (*i.e.* the sum of internal and the kinetic energy), p the pressure, $\boldsymbol{x}$ the spatial coordinate vector, t the time and Y_k is the mass fraction of the species k. $\boldsymbol{\tau}$ is the viscous stress tensor, $\boldsymbol{q}$ the heat flux vector and $\boldsymbol{J}_k$ is the species diffusive flux. The turbulent stresses $\overline{\tau_{ij}}^t$ and turbulent species fluxes $\overline{J_{j,k}}^t$ are computed using the WALE model (Ducros et al. (1998)), well suited for the treatment of shear flows of the type considered in this chapter. The sub-grid scale energy flux is solved using a gradient transport assumption, with a turbulent Prandtl number set equal to 0.7. $\overline{\dot{\omega}}_T$ and $\overline{\dot{\omega}}_k$ are the heat and species source term respectively. The TTGC scheme (Colin and Rudgyard (2000)) is chosen to solve the conservation equations. This centered numerical scheme, third order in space and time, is essentially non dissipative and thus well adapted for LES of turbulent flows. Cryogenic flows are characterized by large density gradients in the mixing layer, localized artificial viscosity is then used to avoid spurious oscillations (Schmitt et al. (2010)). The combustion model is based on a fast chemistry assumption hypothesis well adapted to the representation of high pressure non premixed flames formed by pure CH_4 and O_2 propellants. The model relies on an Infinitely Fast Chemistry Model (IFCM2) (Schmitt et al. (2011); Hakim (2013)) in combination with a chemical equilibrium assumption to describe the state of burnt gases formed by the flame together with, a β-probability density function (PDF) depending both on the mixture fraction $\widetilde{Z}$ and its variance $\widetilde{Z}"^2$. The mixture fraction $\widetilde{Z}$ and its variance Z''^2 are transported quantities and the equilibrium mass fractions $\widetilde{Y}_k^+$ are tabulated with respect to $\widetilde{Z}$ and Z''^2. This allows the estimation, at each time step, of the source terms for the species (equation 2.6).

$$\widetilde{\dot{\omega}}_k = \frac{\widetilde{Y}_k - \widetilde{Y}_k^+}{C_r \Delta t} \tag{2.6}$$

Where $\widetilde{Y}_k$ are the species mass fractions and C_r is a relaxation constant. This constant is typically set to a value of the order of 100 after the initial solution has been convected out of the region of interest of the computational domain. Six species are considered in the present calculations including the fuel, oxidizer,

carbon dioxide, vapor water, carbon monoxide and hydrogen: CH_4, O_2, CO_2, H_2O, CO and H_2.

2.2.1 Computational domain, mesh and boundary conditions

2.2.1.1 Computational domain and mesh

The geometry is the same as the one used in the work of Hakim (2013); Hakim et al. (2015). The coaxial injector, that operates with oxygen and methane, is placed inside a large domain (figure 2.1) to avoid interactions between the walls and the jet. The numerical setup is the same as the one adopted for the round jet study reported in chapter 1. The characteristic dimensions of

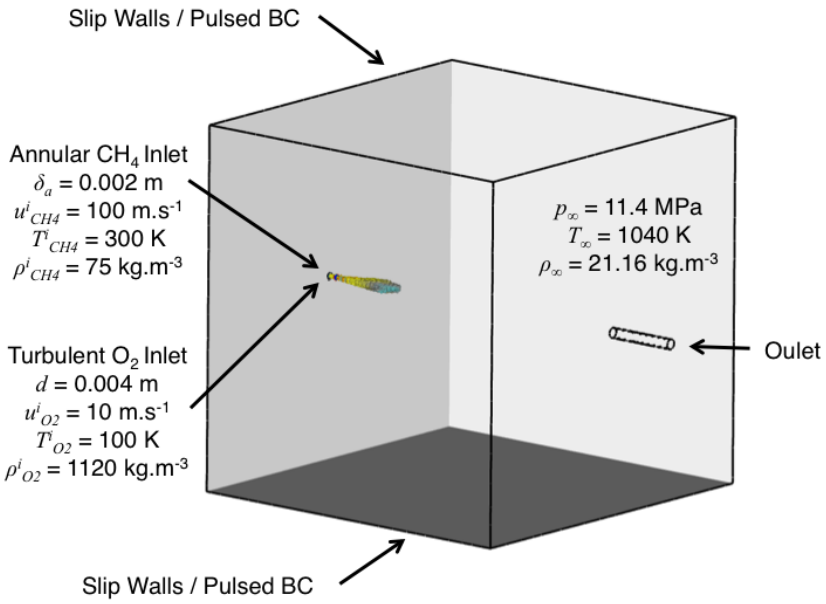

Figure 2.1: *Three-dimensional visualization of the computational domain showing the jet flame established by the coaxial injector. The flame is here represented by a temperature iso-surface and colored by axial velocity (blue: 0 $m.s^{-1}$; red: 100 $m.s^{-1}$).*

the injector can be seen in figure 2.2. The oxidizer (O_2) is injected at low temperature (100 K) through the central injector which has a diameter $d = 4$ mm. The fuel (CH_4) is injected at room temperature through the annular ring which has a $\delta_a = 2$ mm thickness. The coaxial injector has a 1 mm thick lip δ_{lip}. The mesh contains 2 516 000 nodes and 14 583 000 tetrahedral elements. It is highly refined near the injector plane in order to properly capture density, temperature and velocity profiles. The mesh is progressively coarsened from the injector plane to the outlet.

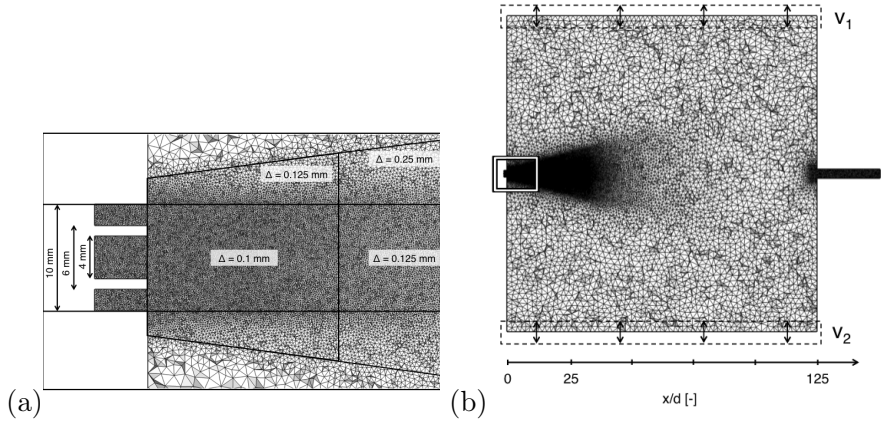

Figure 2.2: *(a) Close up view of the injector mesh, (b) Global view of the mesh adopted for the computational domain.*

2.2.1.2 Injection conditions and boundary conditions

Liquid oxygen is injected in the central post of the injector at a temperature $T^i_{O_2}$=100 K with a bulk injection velocity $\overline{u}^i_{O_2}$=10 m.s^{-1}. Gaseous methane is injected in the annular post at a temperature $T^i_{CH_4}$=300 K with a bulk injection velocity $\overline{u}^i_{CH_4}$=100 m.s^{-1}. The domain is initially filled with hot gases at equilibrium at a pressure p_∞=11.4 MPa and temperature T_∞=1040 K. The burnt gas composition is listed in table 2.1. Under such conditions the injection densities are $\rho^i_{O_2}$=1120 kg.m^{-3} and $\rho^i_{CH_4}$=75 kg.m^{-3} for the oxygen and methane respectively. All the injection properties are summarized in table 2.2. The boundaries of the injection channels are wall law boundaries. A

T_∞ [K]	$Y^{eq}_{CH_4}$ [-]	$Y^{eq}_{O_2}$ [-]	$Y^{eq}_{CO_2}$ [-]	$Y^{eq}_{H_2O}$ [-]	Y^{eq}_{CO} [-]	$Y^{eq}_{H_2}$ [-]
1040	0.655	0	0.1253	0.0854	0.116	0.0183

Table 2.1: *Initial temperature and mass fractions in the burnt gases of the chamber.*

p_∞ [MPa]	$T^i_{O_2}$ [K]	$T^i_{CH_4}$ [K]	Re_c [-]	Re_a [-]	J [-]
11.4	100	300	2.6 10^5	2.4 10^6	7.7

Table 2.2: *Injection characteristics of the simulated cases. Re_c and Re_a are the Reynolds numbers associated with the central and annular jet respectively. J is the momentum flux ratio defined by: $J = \rho^i_{CH_4}(\overline{u}^i_{CH_4})^2/\rho^i_{O_2}(\overline{u}^i_{O_2})^2$.*

turbulent injection profile is defined at the channel inlet with the same shape as that used in figure 1.2 of chapter 1. Slip boundary conditions are used for all chamber walls.

2.2.2 Simulated cases and simulation procedure

Three types of modulations are considered in this study:

- "NM" corresponding to a natural jet in the absence of modulation
- "MF" pertaining to a situation where the annular injection velocity is modulated
- "PA" where the jet is in a pressure anti-node formed by a standing wave.

All the modulated cases are referred to as $X_A^{St_c}$, where X is the simulation case (either MF or PA) and $St_c = f^{ac} d/\overline{u}^i_{O_2}$ is the Strouhal numbers for central jet. For MF, $A = A_{MF}$ is the amplitude of injection velocity whereas for PA, $A = A_{PA}$ is the amplitude of the pressure fluctuation at the injector exit. The cases MF, shown in table 2.3, are used to explore the effects of annular mass flow rate modulations on heat release rate. The values of the velocity fluctuations u'_e measured at the injector exit are displayed in table 2.3. They

Case	f^{ac} [Hz]	St_c [-]	St_a [-]	A_{MF} [m.s^{-1}]	u'_e [m.s^{-1}]
$\mathrm{MF}_{10}^{0.8}$	2000	0.8	0.08	10	9.5
$\mathrm{MF}_{10}^{1.4}$	3500	1.4	0.14	10	7.75
$\mathrm{MF}_{10}^{2.0}$	5000	2.0	0.2	10	6.5
$\mathrm{MF}_{10}^{2.6}$	6500	2.6	0.26	10	5
$\mathrm{MF}_{10}^{3.2}$	8000	3.2	0.32	10	4

Table 2.3: *Operating conditions in the modulated mass flow rate cases (MF). $St_a = f^{ac} 2\delta_a/\overline{u}^i_{CH_4}$ is the Strouhal number for the annular jet, $2\delta_a$ is chosen as the characteristic length of the annular flow. u'_e is the effective velocity fluctuation measured at the injector exit.*

slightly differ from the imposed velocity fluctuations because of the relaxed, and essentially non reflecting, boundary condition used at the inlet. In this study, only the annular velocity is modulated as preliminary calculations indicate that the modulation of the velocity of the central injector has little to no effect on the flame. Similar simulation conditions are also carried out in the PA cases as shown in table 2.4. The unmodulated case NM was simulated for 60 convective

Case	f^{ac} [Hz]	St_c [-]	St_a [-]	A_{PA} [bar]
$\mathrm{PA}_2^{0.8}$	2000	0.8	0.08	2
$\mathrm{PA}_2^{1.4}$	3500	1.4	0.14	2
$\mathrm{PA}_2^{2.0}$	5000	2.0	0.2	2
$\mathrm{PA}_2^{2.6}$	6500	2.6	0.26	2
$\mathrm{PA}_2^{3.2}$	8000	3.2	0.32	2

Table 2.4: *Operating conditions in the pressure anti-node cases (PA). $St_a = f^{ac} 2\delta_a/\overline{u}^i_{CH_4}$ is the Strouhal number for the annular jet, $2\delta_a$ is chosen as the characteristic length of the annular flow.*

times in regard to the central injection post ($\tau_{conv}(O_2) = d/\overline{u}^i_{O_2}$). The well

established flame of the NM case is then used as an initial solution for MF and PA cases.
Mass flow rate fluctuations or acoustic pressure oscillations are generated by respectively modulating the injection velocity or normal velocity of the lateral boundaries (figure 2.2).

- The modulated velocity u_{mod} is defined by equation 2.7 and shown in figure 2.3(a).

$$u_{mod}(t) = \overline{u}^i_{CH_4}\left(1 + A_{MF}\sin(2\pi f_{mod}t)\right) \tag{2.7}$$

  Where f_{mod} is the modulation frequency.
- Pure pressure modulations is achieved by modulating in phase the normal velocity of the top and bottom boundary conditions of the domain as explained in Rey et al. (2005).

$$v_1(t) = v_2(t) = \frac{A_{PA}}{\rho c}\sin(2\pi f^{ac}t) \tag{2.8}$$

  Where f^{ac} is the modulation frequency. This modulation procedure generates a standing wave in the domain with a pressure anti-node at the injector exit. The pressure at the center of the domain during one period of modulation is shown in figure 2.3(b).

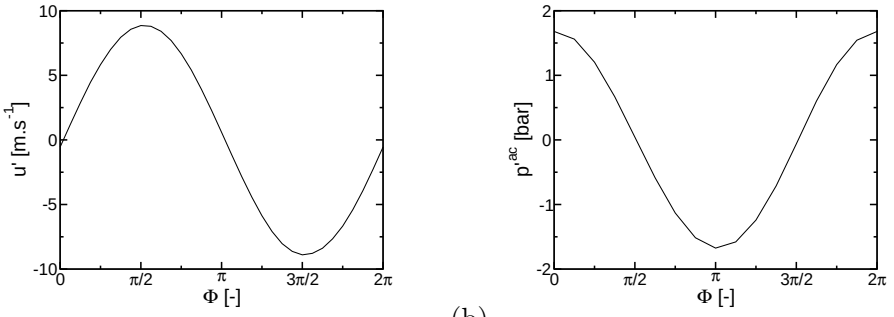

(a) (b)

Figure 2.3: *(a) Annular velocity fluctuation* $u' = u_{mod} - \overline{u}^i_{CH_4}$ *over one period of excitation. Case where* $a = 0.1$ *and* $f_{mod} = 2000Hz$*. (b) Acoustic pressure* p'^{ac} *over one period of excitation (flow is initially at rest without jet). Case with* $A_0 = 10m.s^{-1}$ *and* $f^{ac} = 2000Hz$*.*

2.3 Flame structure in the absence of modulation

Before going into further details on modulated cases, it is useful to look at the general structure of the unmodulated flame NM. The statistics shown in this section were carried out by averaging 1000 solutions over 15 convective times in regard to the central injection post. The following section provides information on the structure of the unmodulated flame and characterizes the general structure of the flame.

2.3.1 Instantaneous solution

An instantaneous solution is displayed in figure 2.4. This figure represents the flame with a surface of iso-temperature colored by axial velocity, a longitudinal cut colored by axial velocity and a longitudinal cut of density. The overall aspect of the flame has already been well documented in previous studies (Hakim et al. (2015)). Large structures appear on the surface of the flame at about $5d$. The dense core does not feature large structures like the annular jet and remains nearly straight before disappearing through turbulent mass transfer.

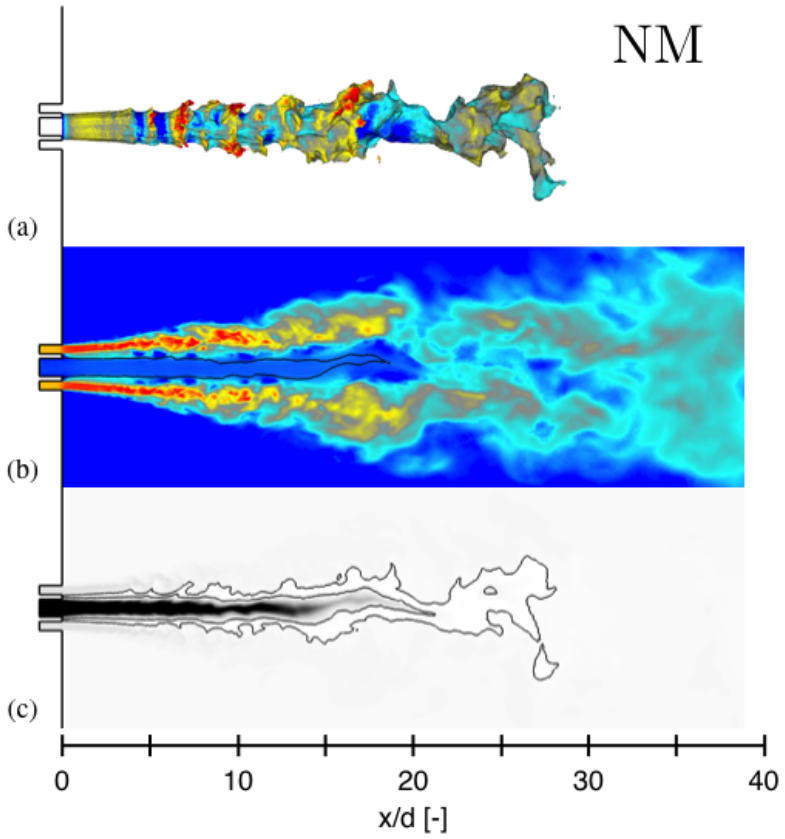

Figure 2.4: *Transcritical CH_4/O_2 flame without modulation. (a) Surface of iso-temperature (1500 K) colored by axial velocity (blue: 0 $m.s^{-1}$; red: 100 $m.s^{-1}$). (b) Longitudinal cut of axial velocity (blue: 0 $m.s^{-1}$; red: 125 $m.s^{-1}$) with a super-imposed contour of iso-oxygen mass fraction (black: 0.5). (c) Longitudinal cut of density (white: 0 $kg.m^{-3}$; black: 800 $kg.m^{-3}$) with a super-imposed contour of iso-temperature (black: 1500 K).*

2.3.2 Averaged solution

A longitudinal slice of the average oxygen mass fraction in the domain is represented in figure 2.5. It can be seen that the flame (represented by the contour

of iso-temperature) wraps around the dense oxygen jet. In this work the characteristic jets lengths are characterized with the longitudinal average profile of oxygen mass fraction. The oxygen core length $l_{99\%}^{NM}$ corresponds to the length at which the longitudinal average profile of oxygen mass fraction is equal to 0.99. The flame length $l_{10\%}^{NM}$ is defined as the length at which the longitudinal average profile of oxygen mass fraction is equal to 0.1. Figure 2.6 shows the evolution of oxygen mass fraction along the central axis. The corresponding

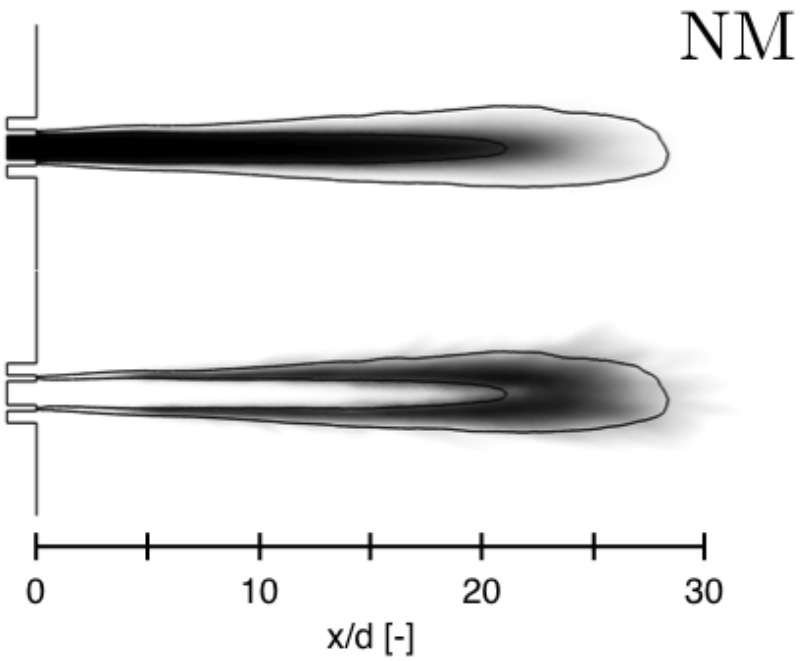

Figure 2.5: *Averaged transcritical CH_4/O_2 flame without modulation. Longitudinal cut of oxygen mass fraction (white: 0; black: 1) with a super-imposed contour of iso-temperature (black: 1500 K). Longitudinal cut of rms oxygen mass fraction (white: 0; black: 0.4) with a super-imposed contour of iso-temperature (black: 1500 K).*

lengths are displayed in table 2.5.

Case	$l_{99\%}/d$ [-]	$l_{10\%}/d$ [-]
NM	12.6	24.7

Table 2.5: *Characteristic length scales of the jet for case NM.*

The computed average total heat release rate is $\overline{\dot{Q}}$ =1.234 MW. Using Hess's law between the injection conditions and the equilibrium state (equation 2.9),

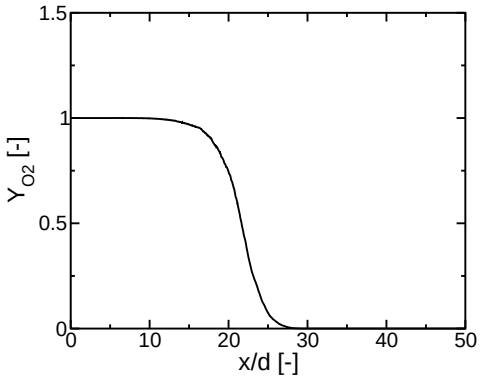

Figure 2.6: *Evolution of oxygen mass fraction in the domain.*

the theoretical value of the average heat release rate is given by:

$$\begin{aligned}\overline{\dot{Q}} = (\dot{m}_{O_2} + \dot{m}_{CH_4})(\Delta h_f^{CH_4}(Y_{CH_4}^{eq} - Y_{CH_4}^{i}) + \Delta h_f^{O_2}(Y_{O_2}^{eq} - Y_{O_2}^{i}) \\ +\Delta h_f^{CO_2}(Y_{CO_2}^{eq} - Y_{CO_2}^{i}) + \Delta h_f^{H_2O}(Y_{H_2O}^{eq} - Y_{H_2O}^{i}) + \Delta h_f^{CO}(Y_{CO}^{eq} - Y_{CO}^{i}) \\ +\Delta h_f^{H_2}(Y_{H_2}^{eq} - Y_{H_2}^{i})) = 1.228\text{MW}\end{aligned} \tag{2.9}$$

where $(\dot{m}_{O_2} + \dot{m}_{CH_4})$ is the total injected mass flow rate, Δh_f^X is the formation enthalpy for species X at 300 K, all values of formation enthalpy used are shown in table 2.6. The heat release rate predicted by equation 2.9 is close to the simulation value. The axial distribution of heat release rate, is computed

Species	CH_4	O_2	CO_2	$H_2O_{(gas)}$	CO	H_2
Δh_f [kJ.mol^{-1}]	-74.8	0	-393.5	-242	-111	0

Table 2.6: *Formation enthalpy of the species of the burnt gases.*

by integrating the volumetric heat release rate over slices of thickness equal to 0.5 mm (figure 2.7). The heat release rate is maximum around $7d$ which corresponds to the axial position where the inner jet starts to destabilize.

2.3.3 Flame dynamics

The flame dynamics can be observed by examining the Power Spectral Density (PSD) of axial velocity and heat release rate. In order to capture the velocity fluctuations of the central jet, a probe is set at the end of the oxygen core, which corresponds to a distance of $l_{99\%}$ from the injection plane. The probe records the axial velocity over 15 $\tau_{conv}(O_2)$. Another probe is set at a distance of $4\delta_a$ from the injection plane in the middle of the annular injector to capture

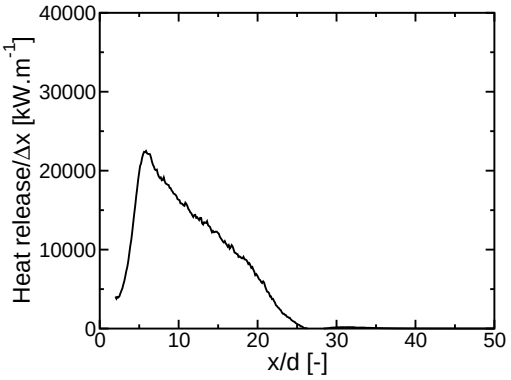

Figure 2.7: *Evolution of the heat release rate along the central axis. The length of the integration slices is Δx=0.5 mm. The graph does not start at 0 to avoid accounting dissipation errors caused by the mesh quality.*

the annular velocity fluctuations. Figure 2.8 displays the PSD of central and annular flow. The central velocity PSD features a response at a frequency of

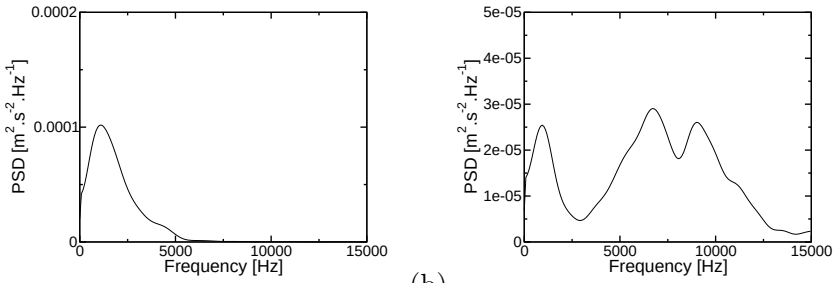

Figure 2.8: *Power spectral density of the axial velocity using Welch's method, with 5 blocks, 50 % overlapping, zero-padding and a frequency resolution of Δf = 170 Hz. (a) In the inner jet at $l_{99\%}$ from the injection plane, (b) in the middle outer jet at $4\delta_a$ from the injection plane.*

1100 Hz, corresponding to $St_c = 0.44$. The peak of the central flow at 1100 Hz can also be found in the PSD of the annular flow. For the velocity of the annular flow, the response frequencies are 6700 Hz and 9000 Hz, which correspond to St_a=0.268 and St_a=0.36 respectively. As expected the response Strouhal of the velocities is around 0.3 (Crow and Champagne (1971)). The PSD of heat release rate is displayed in figure 2.9. The response frequency in the PSD of heat release rate is 680 Hz, which corresponds to $St_c = 0.272$. Figure 2.9 shows that the heat release rate has a strong low frequency content close to the natural frequency of the central jet.

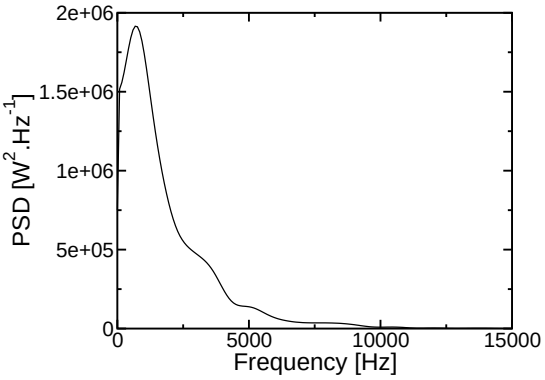

Figure 2.9: *Power spectral density of the heat release rate using Welch's method, with 5 blocks, 50 % overlapping, zero-padding and a frequency resolution of Δf = 170 Hz.*

2.4 Influence of injection mass flow rate modulation

The last NM solution is used as the initial solution of all MF cases. The modulation is applied during 30 $\tau_{conv}(O_2)$ for every MF case in order to have a well established modulated flow. In this section the effects of the velocity modulation on heat release rate are investigated.

2.4.1 Jet geometry and flow dynamics

In order to remove turbulent fluctuations from the the fluctuations induced by the harmonic modulation, phase averaged solutions are used. The averaging is carried out over 30 cycles of the modulation for each simulation case. The corresponding phases of the MF cases are plotted in figure 2.3.
Figure 2.10 represents a longitudinal cut of phase averaged axial velocity fluctuation for $MF_{10}^{0.8}$. It can be seen that the mass flow rate modulation induces structures of high and low axial velocity, which are convected downstream. These structures are clearly visible until $15d$. Because of turbulent diffusion and the limited number of solutions available, the structures are no longer visible further downstream. The axial velocity fluctuations do not effectively penetrate the high density inner jet, therefor the inner jet is only weakly affected by the annular modulation.
The field of the phase averaged unsteady heat release rate is displayed in figure 2.11. Between the annular flow and the dense core region structures of heat release rate fluctuation can be found. These structures are elongated and begin at the inner dense jet. Near the injection plane, between $0d$ and $2.5d$, the heat release rate structures move alternatively towards and away from the inner jet. These structures are especially visible between $5d$ and $15d$. They still exist beyond $15d$ but their intensity decreases due to turbulent diffusion.

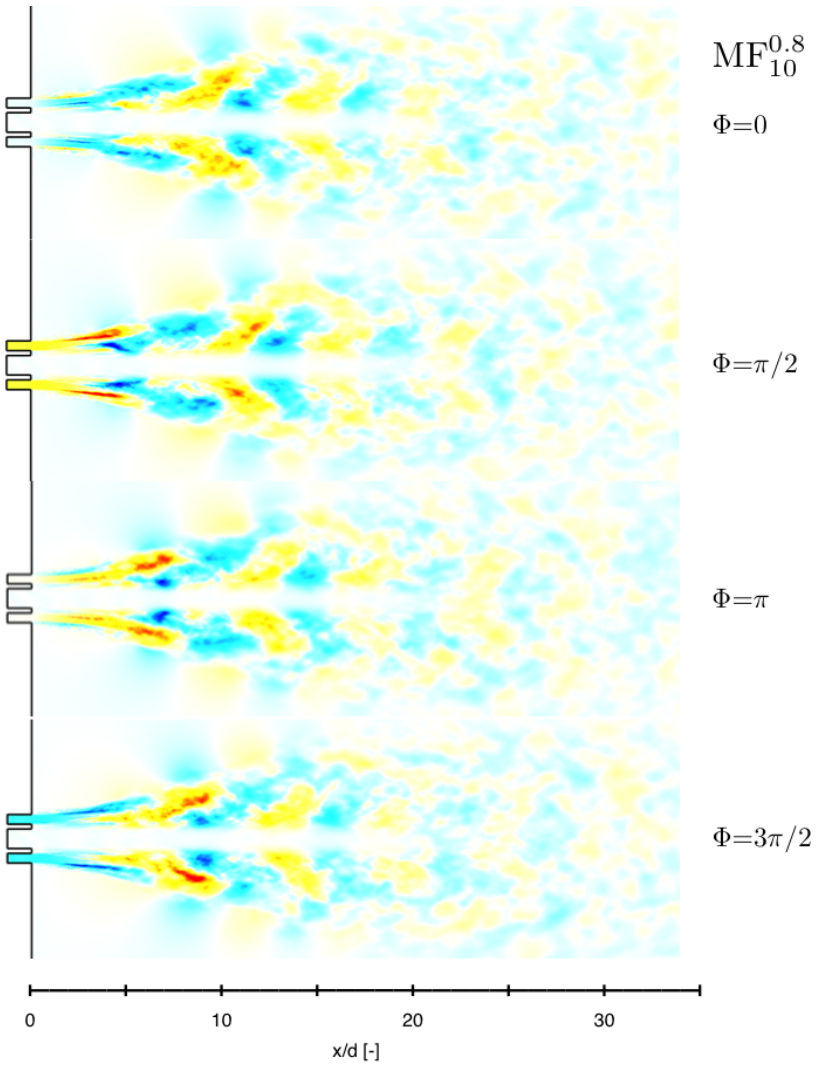

Figure 2.10: *Cut of the domain colored by the phase averaged velocity fluctuation (blue: -25 m.s^{-1}; red: 25 m.s^{-1}) at four different phases of the modulation for $MF_{10}^{0.8}$.*

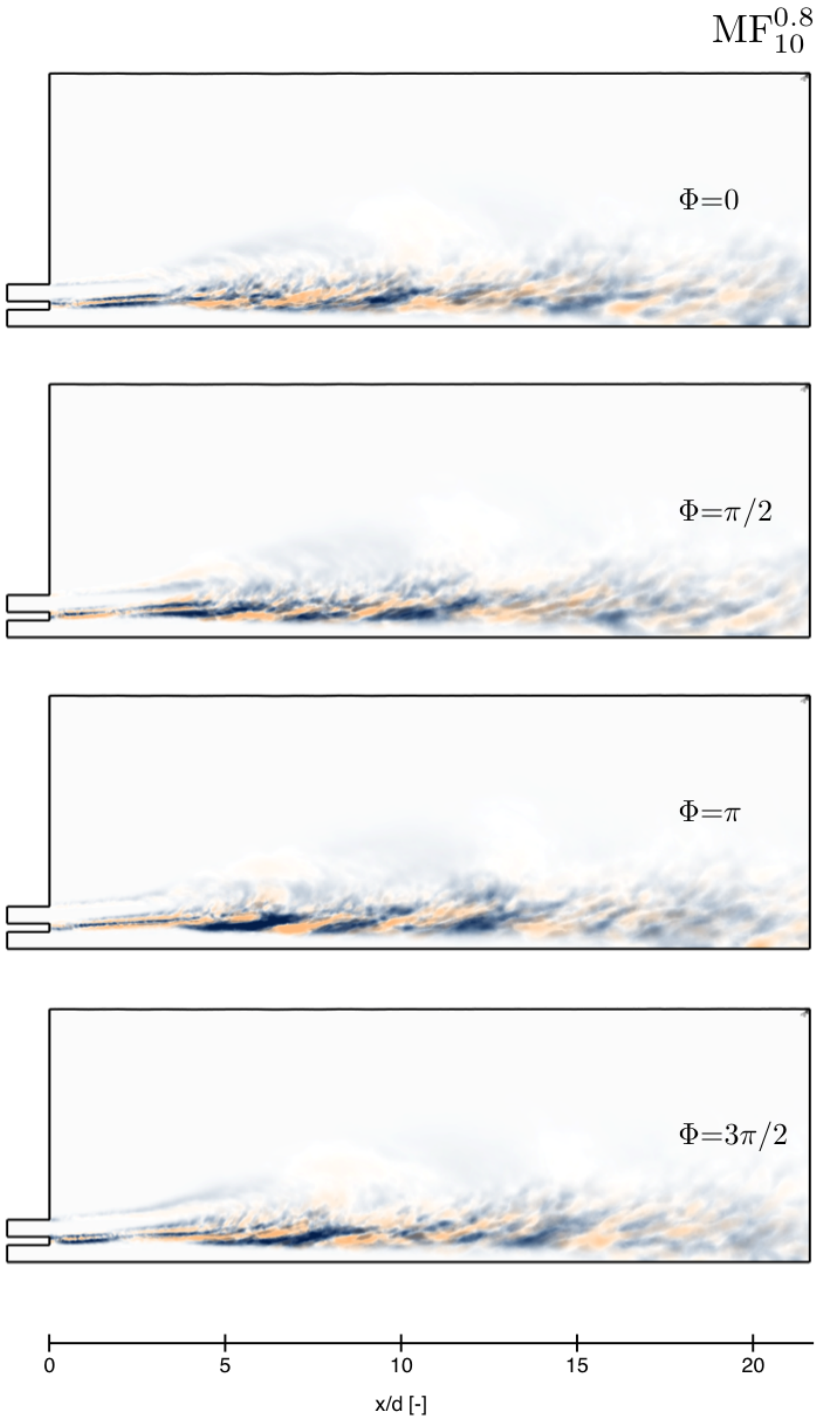

Figure 2.11: *Azimuthal cuts of the domain colored by the phase averaged unsteady volumetric heat release rate (blue: -1.10^{11} W.m^{-3}; beige: 1.10^{11} W.m^{-3}) at four different phases of the modulation for $MF_{10}^{0.8}$.*

The axial velocity fluctuations and heat release rate fluctuations of $MF_{10}^{2.0}$ and $MF_{10}^{3.2}$ are similar to the velocity fluctuations and heat release rate fluctuations of $MF_{10}^{0.8}$. The axial velocity fluctuation fields of $MF_{10}^{2.0}$ and $MF_{10}^{3.2}$ are presented in figures 2.12 and 2.13 respectively. The axial velocity structures are visible

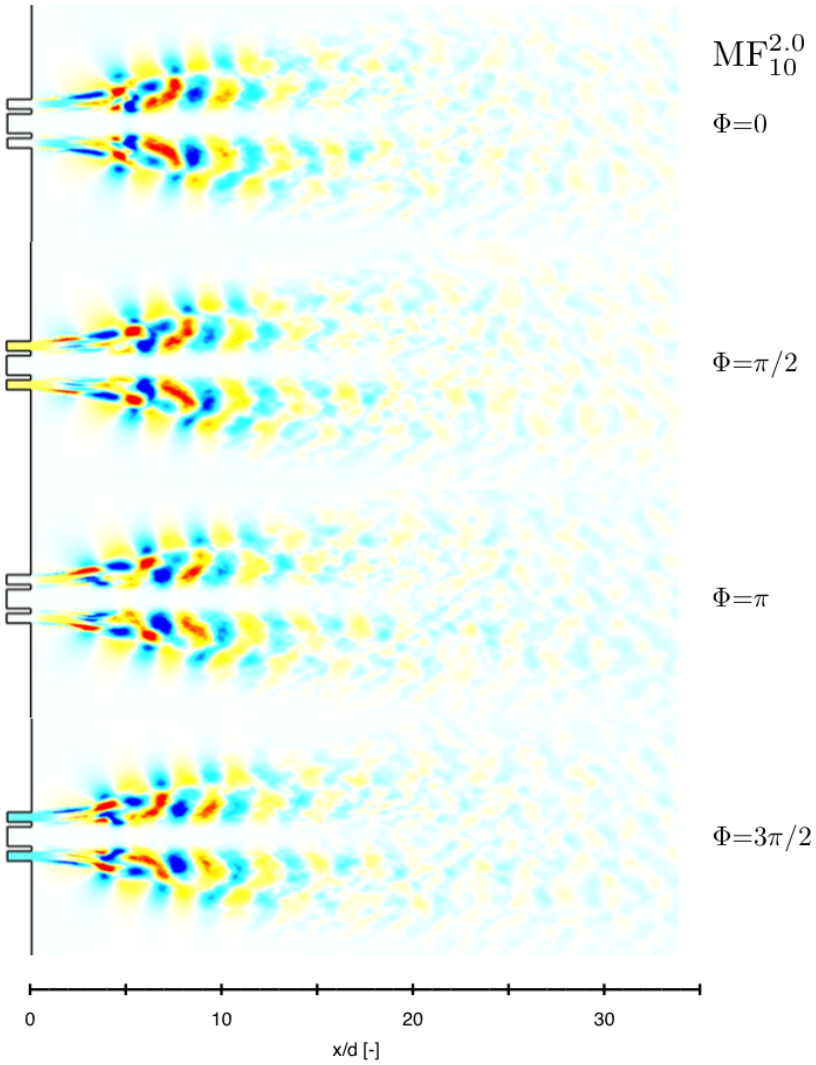

Figure 2.12: *Cut of the domain colored by the phase averaged velocity fluctuation (blue: -25 $m.s^{-1}$; red: 25 $m.s^{-1}$) at four different phases of the modulation for $MF_{10}^{2.0}$.*

in figures 2.12 and 2.13. Again, these structures appear clearly until $15d$ but are less visible beyond that distance. The length of the periodic structures are measured using figures 2.10, 2.12 and 2.13. Table 2.7 displays the the wavelength λ of these structures as well as the theoretical value of the wavelength. It can be seen from table 2.7 that $\lambda = v/f_{mod}$ where v is the average axial velocity between $5d$ and $15d$.

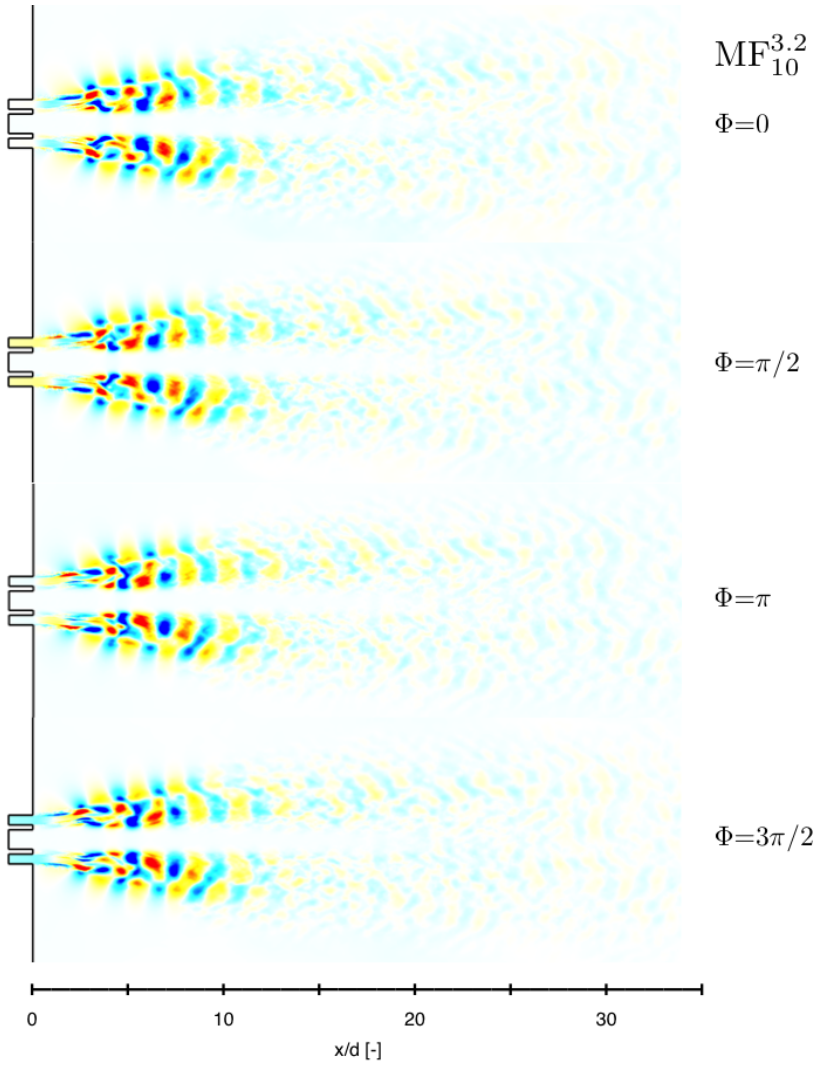

Figure 2.13: *Cut of the domain colored by the phase averaged velocity fluctuation (blue: -25 $m.s^{-1}$; red: 25 $m.s^{-1}$) at four different phases of the modulation for $MF_{10}^{3.2}$.*

Case	$MF_{10}^{0.8}$	$MF_{10}^{2.0}$	$MF_{10}^{3.2}$
λ [m]	0.029	0.012	0.008
Theoretical λ [m]	0.03	0.012	0.0075

Table 2.7: *Wavelengths of the periodic axial velocity structures.*

Figures 2.14 and 2.15 show the heat release rate fluctuations for $MF_{10}^{2.0}$ and $MF_{10}^{3.2}$ respectively. The heat release rate structures appear to be shorter and more important in number for higher modulation frequencies.
Figure 2.16 displays the evolution of oxygen mass fraction in the domain for cases NM, $MF_{10}^{0.8}$, $MF_{10}^{2.0}$ and $MF_{10}^{3.2}$. It can be seen in figure 2.16 that the longitudinal profiles of oxygen mass fraction for NM, $MF_{10}^{0.8}$, MF_{10}^{2} and $MF_{10}^{3.2}$ are very similar. The characteristic jet lengths, $l_{99\%}$ and $l_{10\%}$, do not vary by much for all mass flow rate modulation Strouhal numbers.

2.4.2 Flow statistics

The total heat release rate is obtained by integrating the volumetric heat release rate over the whole flame. The integration excludes the region of the jet near injector because of mesh limitations leading to excessive numerical dissipation. The injection velocity is measured at the injection plane in the middle of the annular injector. The power spectral density of annular velocity and heat release rate are plotted in figures 2.17 to 2.21. The low frequency content of the PSD of the annular velocity and the PSD of heat release rate of NM (figures 2.8(b) and 2.9) can be found in figures 2.17 to 2.21 with a super imposed frequency located at the value of the modulation frequency. The PSD of NM defines the signature of the jet which is also found in all PSDs of the modulated cases. Slight differences between the PSD of NM and the low frequency content of the PSD of the modulated cases in figures 2.17 to 2.21 can attributed to the limited number of solutions obtained by the solver. In the PSD of annular velocity, the peak of the modulation frequency is retrieved.
The PSDs of heat release rate feature an important low frequency content. Figure 2.22 displays the temporal unsteady heat release rate signals for $MF_{10}^{0.8}$, $MF_{10}^{2.0}$ and $MF_{10}^{3.2}$. No clear periodic signal appears in figure 2.22 that is dominated by a low frequency content. The heat release rate has been filtered with a Butterworth pass band filter. The width of the filter is equal to 400 Hz around the modulation frequency (200 Hz prior and past the modulation frequency). Figures 2.23 to 2.27 display the temporal signal of the normalized filtered annular velocity and the normalized filtered heat release rate. It can be seen, in the temporal signals in figures 2.23 to 2.27, that there is a difference in phase and amplitude between the filtered velocity and the filtered heat release rate.

2.4.3 Flame transfer function of the heat release rate fluctuations induced by inlet velocity fluctuations

The Flame Transfer Function (FTF), which defines the flame response to any incoming perturbation (Candel (2002)) can be deduced from the annular velocity and heat release rate signals (equation 2.10).

$$FTF_U(f_{mod}) = S_{hr-u}(f_{mod})/S_{u-u}(f_{mod}) \tag{2.10}$$

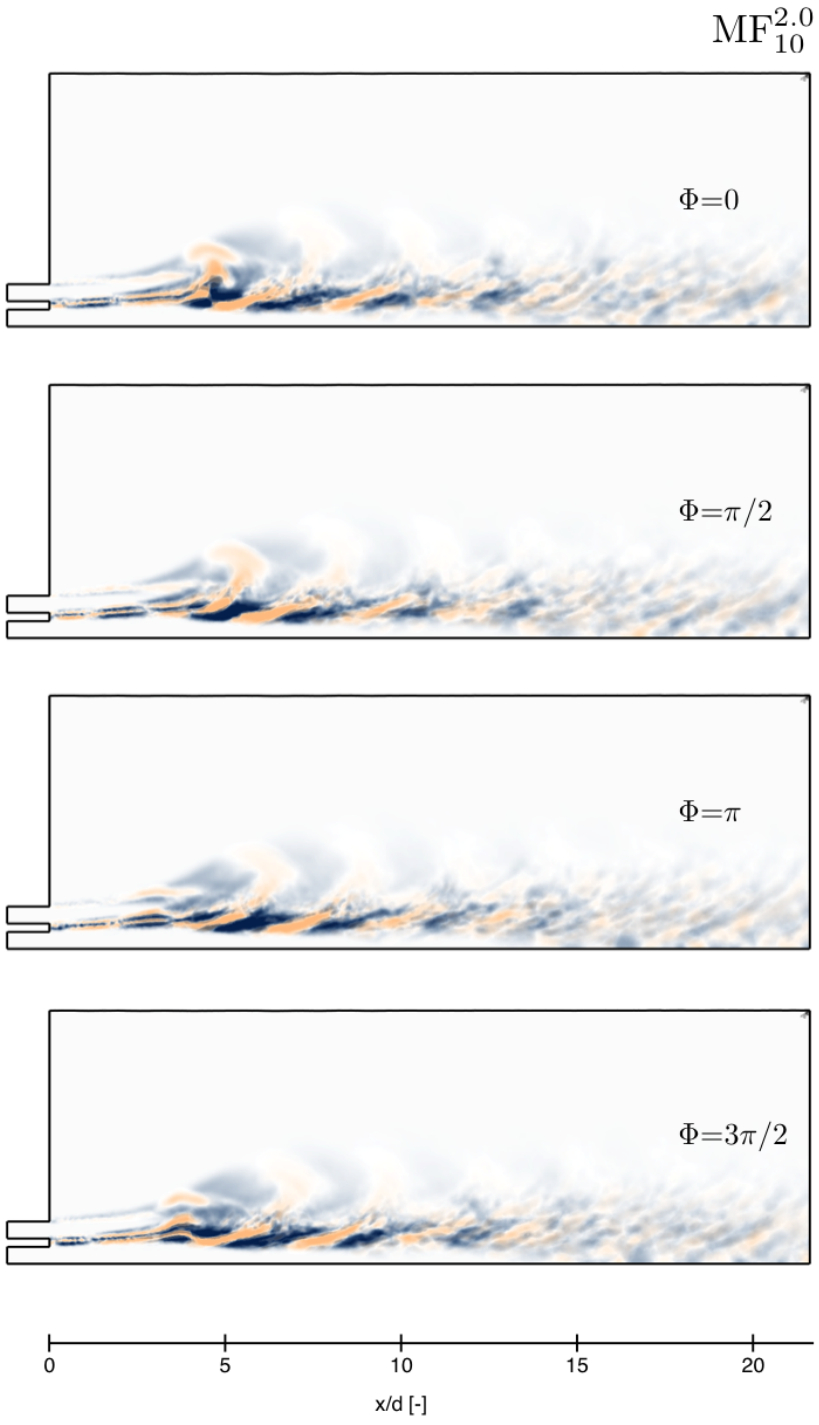

Figure 2.14: *Azimuthal cuts of the domain colored by the phase averaged unsteady volumetric heat release rate (blue: -1.10^{11} W.m^{-3}; beige: 1.10^{11} W.m^{-3}) at four different phases of the modulation for $MF_{10}^{2.0}$.*

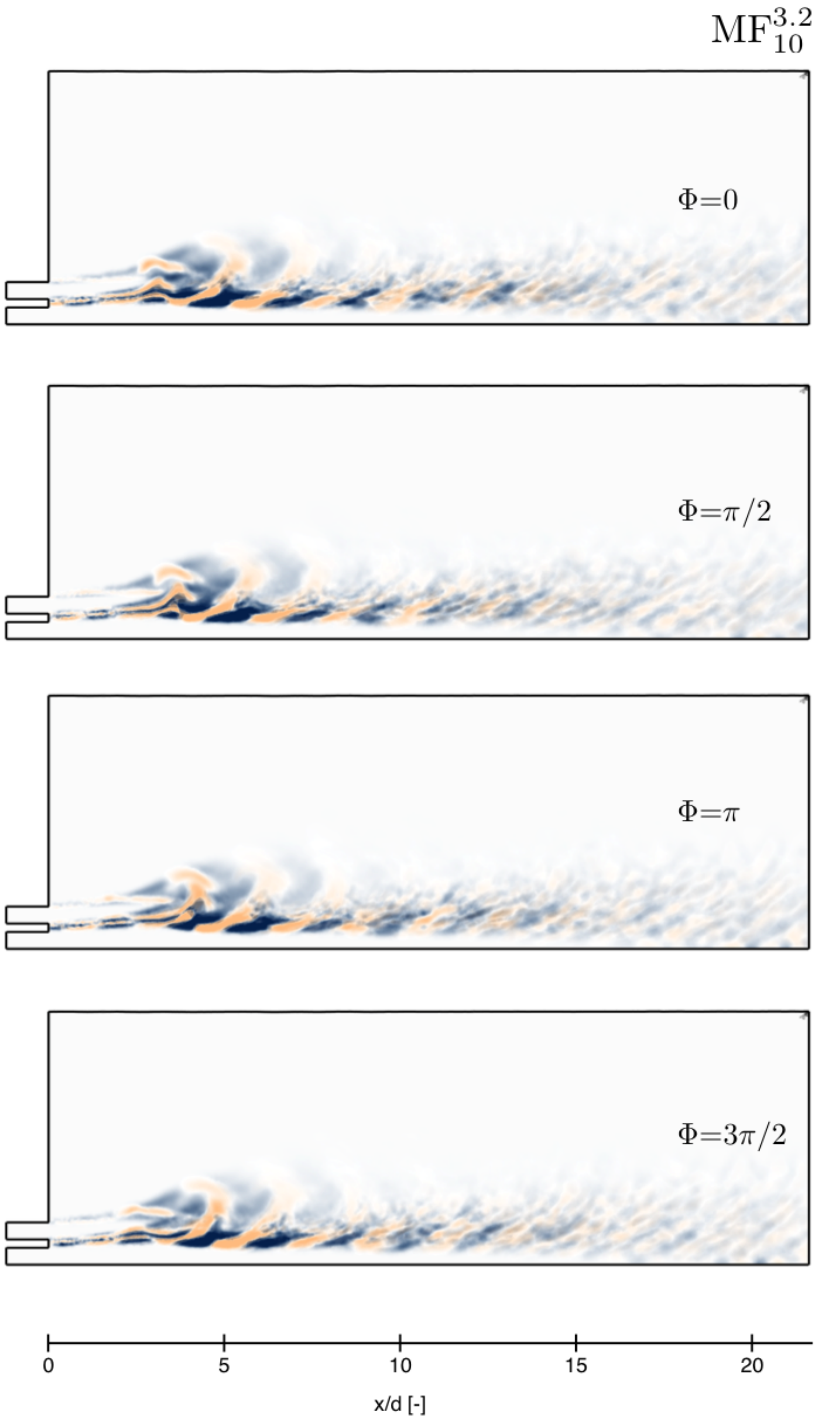

Figure 2.15: *Azimuthal cuts of the domain colored by the phase averaged unsteady volumetric heat release rate (blue: -1.10^{11} W.m^{-3}; beige: 1.10^{11} W.m^{-3}) at four different phases of the modulation for $MF_{10}^{3.2}$.*

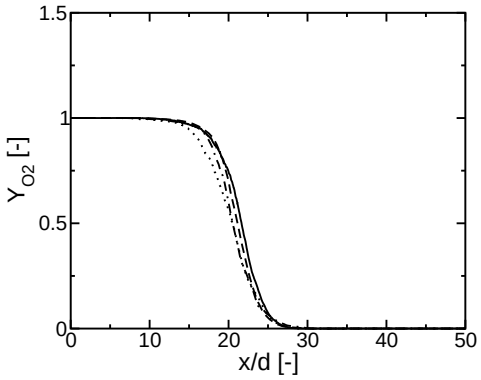

Figure 2.16: *Evolution of oxygen mass fraction in the domain.* $-$ *NM,* $--$ $MF_{10}^{0.8}$, $\cdots$ $MF_{10}^{2.0}$ *and* $\cdot - \cdot$ $MF_{10}^{3.2}$.

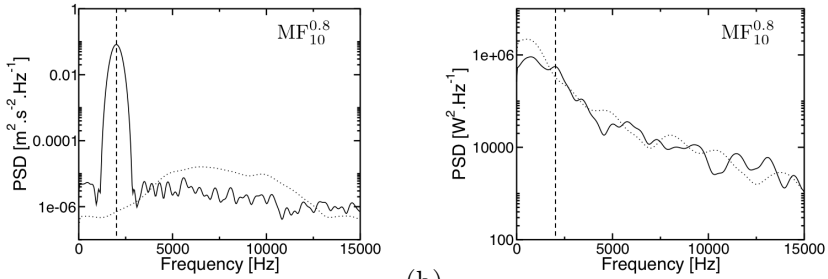

(a) (b)

Figure 2.17: *Power spectral density of (a) the annular velocity and (b) the heat release rate using Welch's method, with 5 blocks, 50 % overlapping, zero-padding and a frequency resolution of* $\Delta f = 170$ *Hz.* $\cdots$ *NM,* $-$ $MF_{10}^{0.8}$.

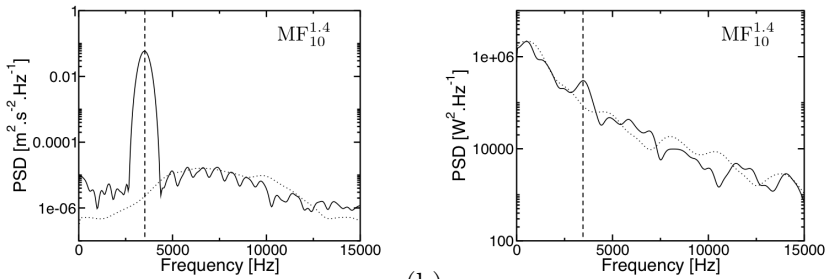

(a) (b)

Figure 2.18: *Power spectral density of (a) the annular velocity and (b) the heat release rate using Welch's method, with 5 blocks, 50 % overlapping, zero-padding and a frequency resolution of* $\Delta f = 170$ *Hz.* $\cdots$ *NM,* $-$ $MF_{10}^{1.4}$.

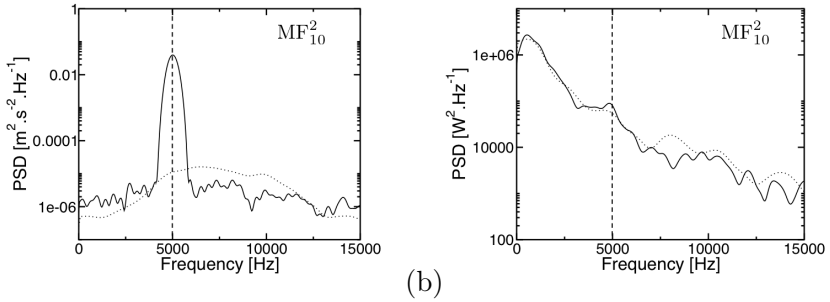

(a) (b)

Figure 2.19: *Power spectral density of (a) the annular velocity and (b) the heat release rate using Welch's method, with 5 blocks, 50 % overlapping, zero-padding and a frequency resolution of Δf = 170 Hz. $\cdots$ NM, $-$ MF^2_{10}.*

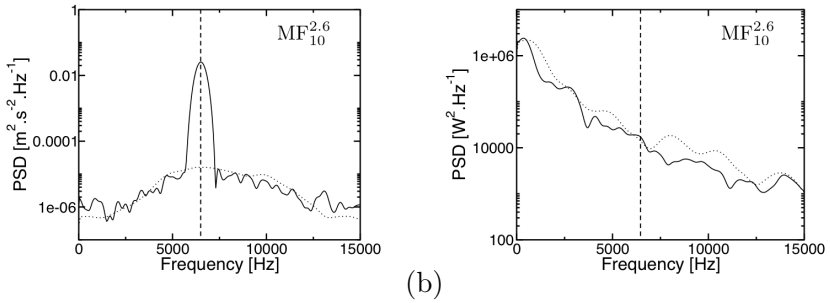

(a) (b)

Figure 2.20: *Power spectral density of (a) the annular velocity and (b) the heat release rate using Welch's method, with 5 blocks, 50 % overlapping, zero-padding and a frequency resolution of Δf = 170 Hz. $\cdots$ NM, $-$ $MF^{2.6}_{10}$.*

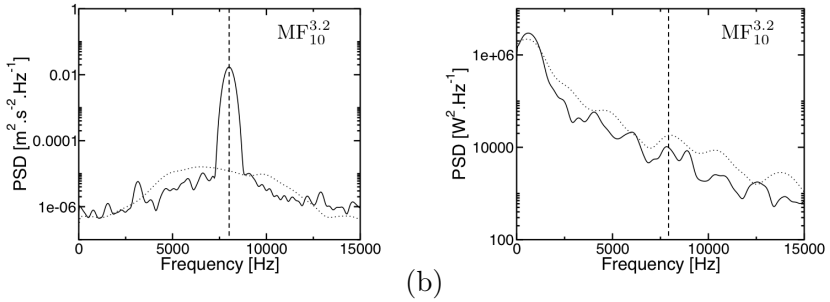

(a) (b)

Figure 2.21: *Power spectral density of (a) the annular velocity and (b) the heat release rate using Welch's method, with 5 blocks, 50 % overlapping, zero-padding and a frequency resolution of Δf = 170 Hz. $\cdots$ NM, $-$ $MF^{3.2}_{10}$.*

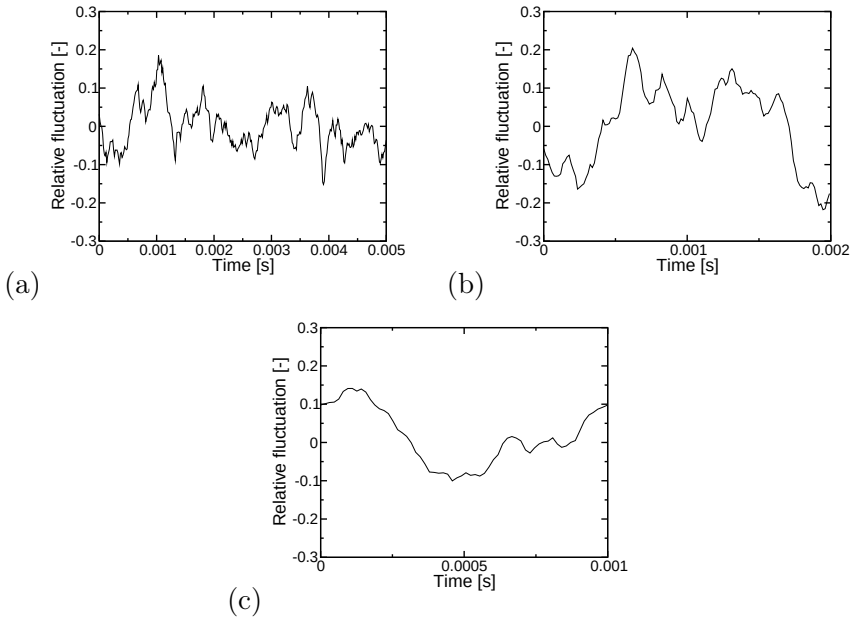

Figure 2.22: *Temporal signal of unsteady heat release rate for (a) $MF_{10}^{0.8}$, (b) $MF_{10}^{2.0}$ and (c) $MF_{10}^{3.2}$.*

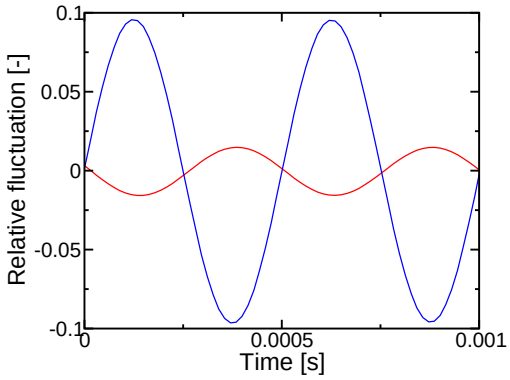

Figure 2.23: *Temporal evolution of the filtered relative fluctuation of annular velocity at the injection plane and the heat release rate for $MF_{10}^{0.8}$. — Annular velocity, — heat release rate. The width of the pass band filter is 400 Hz around the modulation frequency.*

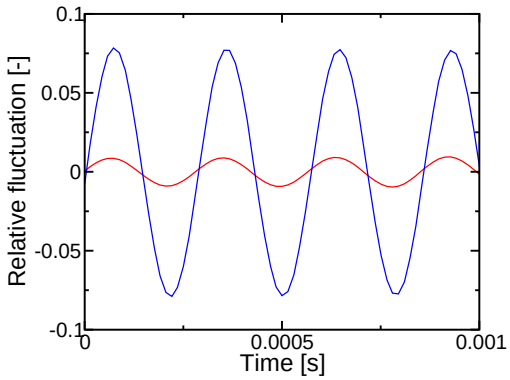

Figure 2.24: *Temporal evolution of the filtered relative fluctuation of annular velocity at the injection plane and the heat release rate for* $MF_{10}^{1.4}$. *– Annular velocity, – heat release rate. The width of the pass band filter is 400 Hz around the modulation frequency.*

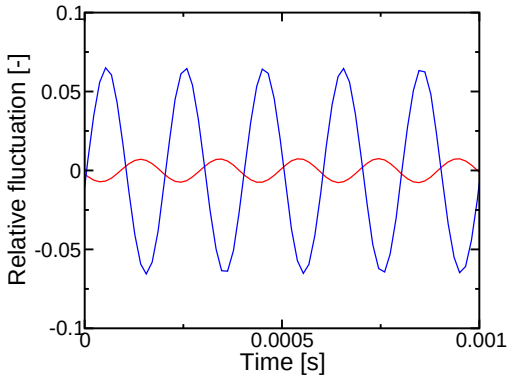

Figure 2.25: *Temporal evolution of the filtered relative fluctuation of annular velocity at the injection plane and the heat release rate for* MF_{10}^{2}. *– Annular velocity, – heat release rate. The width of the pass band filter is 400 Hz around the modulation frequency.*

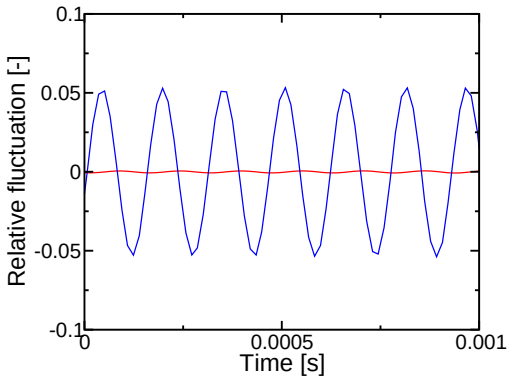

Figure 2.26: *Temporal evolution of the filtered relative fluctuation of annular velocity at the injection plane and the heat release rate for* $MF_{10}^{2.6}$. *– Annular velocity, – heat release rate. The width of the pass band filter is 400 Hz around the modulation frequency.*

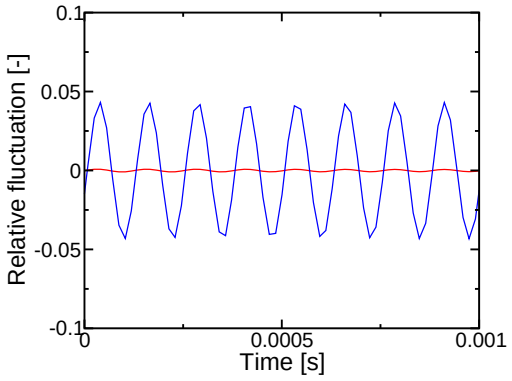

Figure 2.27: *Temporal evolution of the filtered relative fluctuation of annular velocity at the injection plane and the heat release rate for* $MF_{10}^{3.2}$. *– Annular velocity, – heat release rate. The width of the pass band filter is 400 Hz around the modulation frequency.*

Where S_{hr-u} is the cross power spectrum of heat release rate and annular velocity, and S_{u-u} is the power spectrum of the annular velocity. The FTF is only valid at the modulation frequency f_{mod}. The gain and the phase of the FTF are the modulus and the argument of the complex number $FTF_U(f_{mod})$. Gain and phase are plotted in terms of modulation frequency for the MF cases in figure 2.28. The gain of the FTF decreases with the modulation frequency while the phase linearly increases with the modulation frequency. This type of behavior is reminiscent of a low pass filter, often found for flame responses (Poinsot and Veynante (2001); Noiray et al. (2008)).

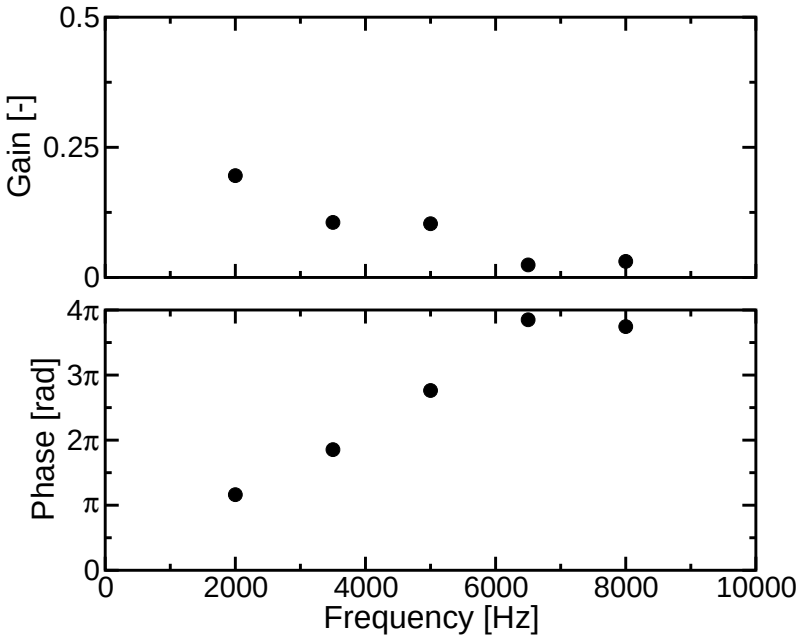

Figure 2.28: *Flame transfer function of the mass flow rate modulation cases.*

2.4.4 Flame Transert Function modeling

A simplified model explaining the link between mass flow rate fluctuations and unsteady heat release rate can be written. This model is based on the concept that strain rate variations cause heat release rate variations (Poinsot and Veynante (2001); Durox et al. (2009); Birbaud et al. (2007)).

2.4.4.1 The one-constant model

In this model, the flame is represented as a truncated cylinder attached to the lip of the injector. The cross section of the flame is S, its length is L and the thickness of the flame front is δ_x (figure 2.29). The length of the flame can be assumed to be the distance from the injector to a point where the mean heat

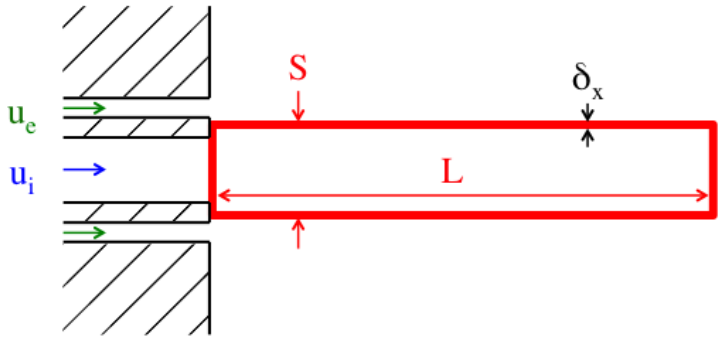

Figure 2.29: *Schematic view of the injector for the flame model.*

release on a cross section is equal to 5% of the theoretical mean heat release rate of the combustion process under consideration. In the present simulations, the annular stream is submitted to mass flow rate modulation which means that the axial velocity of the annular jet (index e and i for annular and central jet respectively) can be written as:

$$u_e = \overline{u}_e + u'_e = \overline{u}_e \left[1 + a \sin\left(\omega t\right)\right] \tag{2.11}$$

A sinusoidal modulation is added to the mean injection velocity in equation 2.11, where a and ω are the amplitude and the angular frequency respectively. The different injection velocities as well as the presence of modulation, induces oscillating strain rates, which may be assumed to follow the modulations. If ϵ designates a characteristic strain rate applied to the flame, it is here assumed to be of the form:

$$\epsilon(x,t) \propto \frac{u_e(x,t) - u_i(x,t)}{\delta} \tag{2.12}$$

where δ is a typical scale of the shear flow in the flame region. The annular injection velocity is much greater than the central injection velocity then u_i can be neglected with respect to u_e. Equation 2.12 becomes:

$$\epsilon(x,t) \propto u_e(x,t)/\delta \tag{2.13}$$

The modulation at the outlet produces a wavelike disturbance on the axial velocity with a wavenumber $\kappa = \omega/\overline{u}_e$. Assuming that the modulation remains approximately constant in the region of interest one obtains the following estimate for the characteristic strain rate

$$\epsilon(x,t) \propto \frac{\overline{u}_e}{\delta} \left[1 + a \sin\left(\omega t - \kappa x\right)\right] \tag{2.14}$$

Equation 2.14 defines the strain rate imposed to the flame along the central axis at any given time. It is known that in strained diffusion flames under

fast chemistry assumption, the heat release rate per unit of flame surface is proportional to the square root of the strain rate (Ribert et al. (2008)), which leads to equation 2.15.

$$\dot{q}_s(x,t) \propto \sqrt{\epsilon(x,t)} \tag{2.15}$$

Where $\dot{q}_s$ is the heat release rate per unit surface. The total rate of heat release is then obtained by integrating this quantity over the flame surface (equation 2.16).

$$\dot{Q} = \int_S \dot{q}_s dS \propto \int_S \sqrt{\epsilon} dS \tag{2.16}$$

By injecting equation 2.14 into equation 2.16 and assuming that a is small compared to 1, it can be written:

$$\dot{Q} \propto S\sqrt{\frac{\overline{u}_e}{\delta}} + \frac{aS\sqrt{\overline{u}_e}}{2\kappa L\delta}\left[\cos\left(\omega t - \kappa L\right) - \cos\left(\omega t\right)\right] \tag{2.17}$$

The global heat release rate can be written as a sum of a mean term and a fluctuation, as described by equation 2.18.

$$\dot{Q} = \overline{\dot{Q}} + \dot{Q}' \tag{2.18}$$

By combining equations 2.17 and 2.18, the unsteady integrated heat release rate becomes:

$$\dot{Q}' = \frac{a\overline{\dot{Q}}}{2\kappa L}\left[\cos\left(\omega t - \kappa L\right) - \cos\left(\omega t\right)\right] \tag{2.19}$$

This expression indicates that the relative heat release rate fluctuation is proportional to the relative velocity modulation and that it is inversely proportional to the product of the wave-number by the characteristic length scale of the flame in the axial direction κL. The previous expression may be cast in a form which is easier to interpret by making use of a standard trigonometric expression $\cos a - \cos b = 2\sin(a+b)/2\sin(b-a)/2$. One finds:

$$\frac{\dot{Q}'}{\overline{\dot{Q}}} = \frac{a}{2}\left[\frac{\sin(\kappa L/2)}{(\kappa L/2)}\sin\left(\omega t - \frac{\kappa L}{2}\right)\right] \tag{2.20}$$

In equation the flame length L becomes an adjustment parameter. The flame length L is somewhat arbitrary but it is natural to use the characteristic length of the unmodulated heat release rate profile of figure 2.7 (approximately $25d$).

2.4.4.2 The two-constant model

In this two-constant model, the flame is represented as a truncated cylinder detached from the injectors' lips. The cross section of the flame is S, δ_x is the

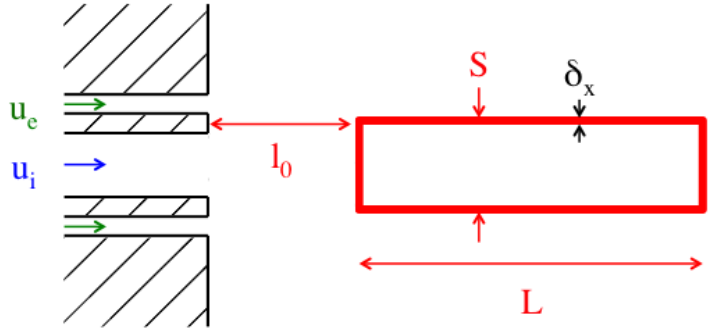

Figure 2.30: *Schematic view of the injector for the 2-constant flame model.*

thickness of the flame, the overall length of the flame is L and the distance of the flame to the injector is l_0 (figure 2.30). l_0 is designed to act as an adjustable delay of the modulation on the flame. Following the same strategy as in previous section, one obtains:

$$\frac{\dot{Q}'}{\overline{\dot{Q}}} = \frac{a}{2}\left[\frac{\sin(\kappa L/2)}{(\kappa L/2)}\sin\left(\omega t - \frac{\kappa L}{2} + \frac{\omega l_0}{\overline{u}_e}\right)\right] \tag{2.21}$$

In equation 2.21 there are two adjustable parameters, L and l_0. The flame length L is taken equal to the characteristic length of the unmodulated heat release rate profile of figure 2.7 (approximately $25d$). The length l_0 can be taken arbitrarily to fit the available data. The best agreement between the simulation and the model for the phase shift between heat release rate and annular velocity is found for $l_0 = 6d$. This two-constant model has the same gain as the one-constant model, the L parameter influences the gain and l_0 the phase shift.

2.4.4.3 Using average heat release rate from LES

The previous models relied on the assumption that the heat release rate profile is constant when in fact simulations prove that this is not the case. Figure 2.31 shows some of the heat release rate profiles for different modulation frequencies. It can be seen that there are some differences between all the heat release rate profiles and that the heat release rate is not constant. The NM heat release rate profile is now used to model the heat release rate response. Assuming a linear response of the heat release rate per unit of surface $\dot{q}_s(x,t)$ and the strain rate $\epsilon(x,t)$ to the velocity fluctuations, one can write:

$$\dot{q}_s(x,t) = \overline{\dot{q}_s}(x) + \dot{q}'_s(x,t) \tag{2.22}$$

$$\epsilon(x,t) = \bar{\epsilon}(x) + \epsilon'(x,t) \tag{2.23}$$

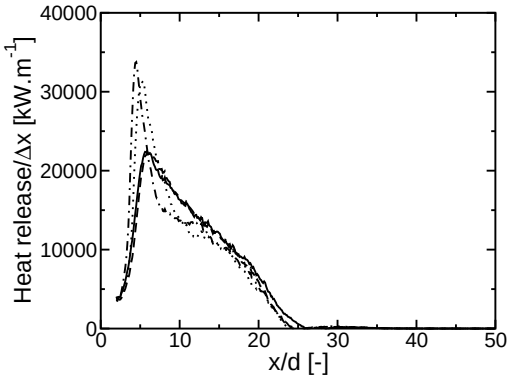

Figure 2.31: *Evolution of the heat release rate along the central axis.* $-$ *NM,* $--$ $MF_{10}^{0.8}$, $\cdots$ MF_{10}^{2} *and* $\cdot - \cdot$ $MF_{10}^{3.2}$.

here $\overline{\dot{q}_s}(x)$ and $\overline{\epsilon}(x)$ are the time averaged heat release rate per unit if surface and strain rate respectively. $\dot{q}'_s(x,t)$ is the heat release rate fluctuation per unit of surface and $\epsilon'(x,t)$ is the strain rate fluctuation due to the velocity modulation. Under a fast chemistry assumption and for a steady flame, the heat release rate per unit of surface is proportional to the square root of the strain rate Ribert et al. (2008). Assuming small fluctuations of $\epsilon'(x,t)$ around $\overline{\epsilon}(x)$, one obtains:

$$\frac{\dot{q}'_s(x,t)}{\overline{\dot{q}_s}(x)} = \frac{\epsilon'(x,t)}{2\overline{\epsilon}(x)} \tag{2.24}$$

Using equation 2.12, one obtains:

$$\frac{\dot{q}'_s(x,t)}{\overline{\dot{q}_s}(x)} = \frac{u'_e(x,t)}{2\overline{u_e}} \tag{2.25}$$

$$= \frac{a\sin(\omega t - \kappa x)}{2} \tag{2.26}$$

The total heat release rate fluctuation is then obtained by integrating over the flame region:

$$\dot{Q}'(t) = \int_S \overline{\dot{q}_s}(x)\frac{a\sin(\omega t - \kappa x)}{2} dS \tag{2.27}$$

Equation 2.27 is integrated numerically. This model does not require arbitrary constants. It does, however, require a distribution of mean heat release rate in the flame, which is deduced from large eddy simulation.
All three models are plotted alongside the simulation results in figure 2.32. The models qualitatively reproduce the trends of the heat release rate for the gain as well as the phase. The one-constant reproduces the behavior of the gain of

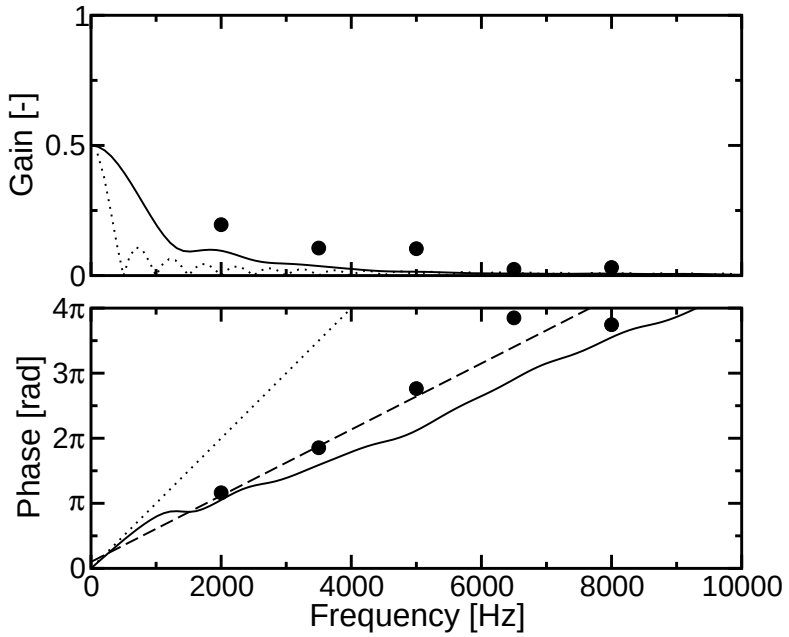

Figure 2.32: *Flame transfer function of the mass flow rate modulation cases.* • *FTF results from the large eddy simulations of mass flow rate modulation,* − *model based on a realistic heat release rate profile,* ··· *1-constant model based on a simplified heat release rate profile* ($L = 25d$) *and* −− *2-constant model based on a simplified heat release rate profile* ($L = 25d$ *and* $l_0 = 6d$).

the simulation results. The length L can be adjusted to better fit the gain of the simulation data. The phase, however is not well described, which means that an additional parameter is needed. The two-constant model has the same gain as the one-constant model. The phase is adjusted with l_0 and it can be seen that the simulation data is well described in this way. The realistic model is the closest to the simulation in terms of gain and phase, a strong gain for low frequencies and a weak one for high frequencies. As already indicated, this type of behavior is characteristic of flame responses (Poinsot and Veynante (2001); Noiray et al. (2008)). The phase between the annular velocity and the heat release rate is linear in figure 2.32, which means that there is a constant delay between the two phenomena. Equation 2.28 shows the link between the phase and the delay.

$$\phi = 2\pi f_{mod}\tau \tag{2.28}$$

Where ϕ is the phase shift between annular velocity and heat release rate and τ is the delay. One finds in this case that the delay is equal to 0.27 ms and that this value is approximately equal to the distance L divided by a mean velocity in the annular stream.

2.5 Influence of pressure modulation

In this section the influence of the pressure fluctuation on heat release rate will be analyzed in order to determine the behavior of a flame in a pressure anti-node. The last NM solution is used as the initial solution of all PA cases. The pressure modulation was simulated for 30 $\tau_{conv}(O_2)$ in order to achieve a well established standing mode in the domain with a pressure anti-node in front of the injector.

2.5.1 Influence of the pressure modulation on the injector dynamics

The dynamical response of an actual injector submitted to pressure oscillations at its exit depends on several parameters such as the geometry or the thermodynamic conditions. In this numerical study, the injector is truncated. Only a few diameters of the feeding lines are computed. The choice of the inlet numerical boundaries is important, because the dynamical response of the injector may vary. Injection may be modified by the pressure modulation and produce an additional perturbation of the flame. In this section, the dynamics of the numerical injector is studied for two limiting cases: a fully reflective and a non-reflective boundary condition.
Figure 2.33 shows a simplified view of the injector and the acoustic wave present in the simulation. The general solution of the one dimensional wave equation inside the injector results from a combination of two traveling waves propagating in opposite directions (Poinsot and Veynante (2001)) as displayed in

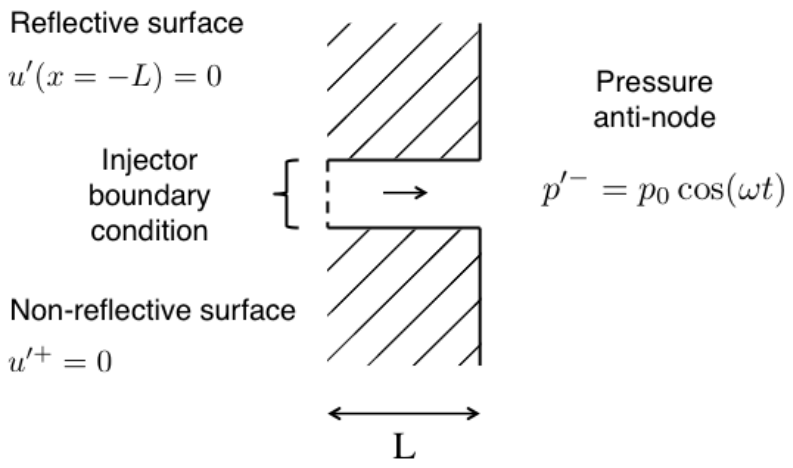

Figure 2.33: *Schematic view of an injector with a pressure anti-node in front of it. Two possible boundary conditions are considered; completely reflective or non-reflective.*

equations 2.29 and 2.30.

$$p'(x,t) = A^+ \exp(i(\kappa x - \omega t)) + A^- \exp(-i(\kappa x + \omega t)) \tag{2.29}$$

$$u'(x,t) = \frac{1}{\rho_0 c_0}\left[A^+ \exp(i(\kappa x - \omega t)) - A^- \exp(-i(\kappa x + \omega t))\right] \tag{2.30}$$

Where A^+ and A^- are the amplitudes of the traveling wave going outside (to the right) the injector and inside (to the left) of the injector respectively, ω is the angular frequency, κ is the wave number, c_0 is the sound velocity and ρ_0 is the density. The injector is submitted to a pressure modulation at its exit of the form $p'_{mod} = p_0 \cos(\omega t)$ (p_0 is the amplitude of the modulation), which generates a wave $p'^{-} = p_0 \cos(\omega t + \kappa x)$ travelling inside the injector.
For a completely reflective inlet boundary condition with velocity imposed, $u'(x = -L) = 0$. This limit conditions turn equations 2.29 and 2.30 into equation 2.31 and 2.32.

$$p'(x,t) = p_0 \exp(i(\kappa(x+2L) - \omega t)) + p_0 \exp(-i(\kappa x + \omega t)) \tag{2.31}$$

$$u'(x,t) = \frac{p_0}{\rho_0 c_0}\left[\exp(i(\kappa(x+2L) - \omega t)) - \exp(-i(\kappa x + \omega t))\right] \tag{2.32}$$

In the case of a completely reflective boundary, the pressure wave travels through the injector and reflects on the boundary generating a pressure wave propagating in the opposite direction which may perturb the injection velocity. A non reflective boundary is then chosen for the central and annular injectors.

These limit conditions turn equations 2.29 and 2.30 into equation 2.33 and 2.34.

$$p'(x,t) = p_0 \exp(-i(\kappa x + \omega t)) \tag{2.33}$$

$$u'(x,t) = -\frac{p_0}{\rho_0 c_0} \exp(-i(\kappa x + \omega t)) \tag{2.34}$$

In the case of a non reflecting inlet boundary, like an infinite injector pipe for example, only the wave generated at the injector exit by the acoustic modulation travels inside the injector. This acoustic wave leads to an acoustic velocity fluctuation, that can not be avoided, inside the injector ($u' = -p'/(\rho_0 c_0)$). It is observed in the simulations that these acoustic fluctuations are converted into convective velocity fluctuations at the injector exit (see Noiray et al. (2009) and Urbano et al. (2016)). This finally leads to a modulation of the injection velocity, similar to the ones imposed in the previous case MF. All simulations presented in this section were carried out using non-reflective boundary conditions for the annular injection post and the central injection post.

2.5.2 Jet geometry and flow dynamics

It is convenient to use phase averaged solutions for the analysis. The phases of the PA cases are defined in figure 2.3. Fluctuations are obtained by subtracting the time-average field from the phase averaged solution. Figure 2.34 represents a transverse cut of the domain colored by the fluctuation of pressure induced by the transverse modulation for $PA_2^{0.8}$. The pressure modulation introduces a

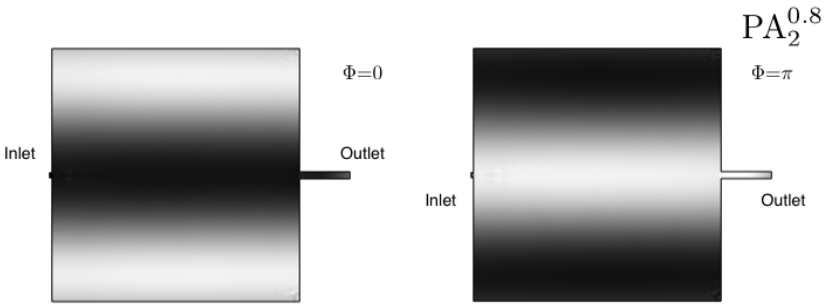

Figure 2.34: *Cut of the domain colored by the phase averaged pressure fluctuation (white: -2.10^5 Pa; black: 2.10^5 Pa) at two different phases of the modulation for $PA_2^{0.8}$.*

stationary mode inside the domain with a pressure anti-node located in front of the injector. The wavelength of the modulated pressure field is large enough compared to the size of the injector to consider that pressure variations at the injector exit are essentially uniform.
The resulting heat release rate fluctuations induced by the modulation for $PA_2^{0.8}$ are displayed in figure 2.35. The field of volumetric heat release rate fluctuations

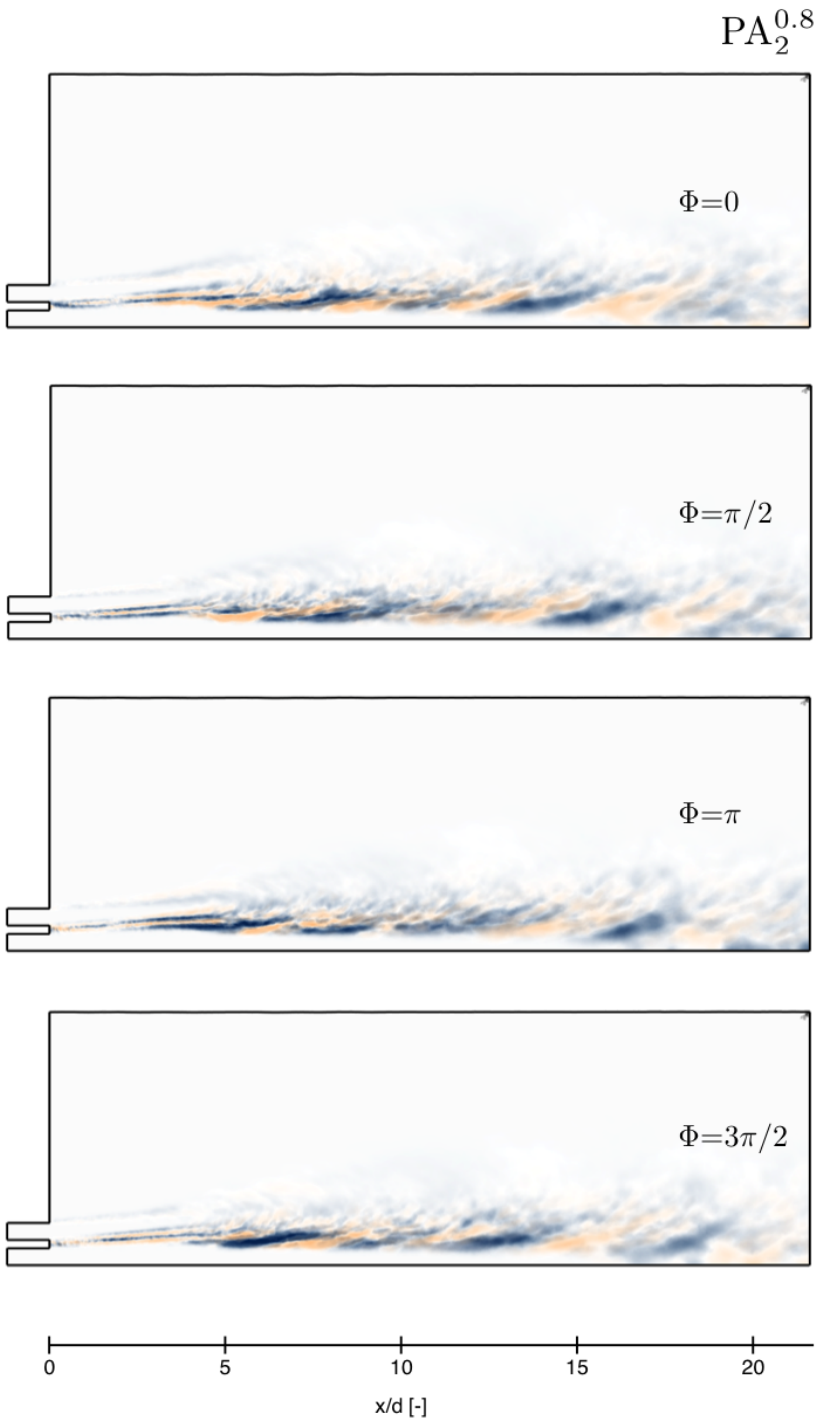

Figure 2.35: *Azimuthal cuts of the domain colored by the phase averaged unsteady volumetric heat release rate (blue: -1.10^{11} W.m^{-3}; beige: 1.10^{11} W.m^{-3}) at four different phases of the modulation for $PA_2^{0.8}$.*

features elongated structures of positive and negative values. These structures are similar to those found for $MF_{10}^{0.8}$.
The other simulated cases behave very similarly to $PA_2^{0.8}$. The pressure fields of $PA_2^{2.0}$ and $PA_2^{3.2}$ are displayed in figures 2.36 and 2.37. When the modulation

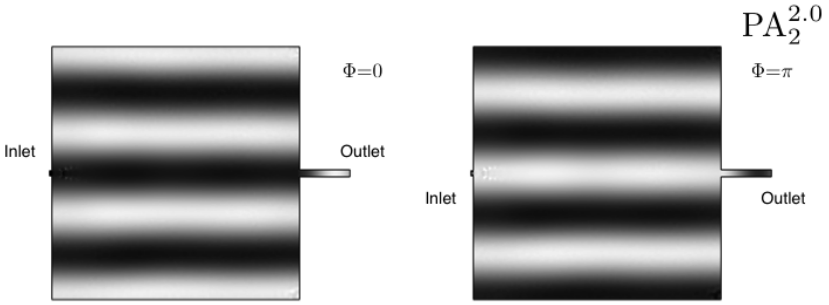

Figure 2.36: *Cut of the domain colored by the phase averaged pressure fluctuation (white: -2.10^5 Pa; black: 2.10^5 Pa) at two different phases of the modulation for $PA_2^{2.0}$.*

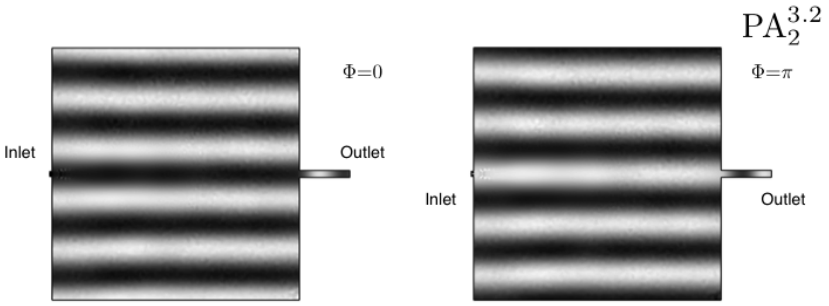

Figure 2.37: *Cut of the domain colored by the phase averaged pressure fluctuation (white: -2.10^5 Pa; black: 2.10^5 Pa) at two different phases of the modulation for $PA_2^{3.2}$.*

frequency f^{ac} increases, the wavelength of the pressure field, λ_{ac}, decreases. These wavelengths are displayed in table 2.8. It is verified that all cases feature

Case	$PA_2^{0.8}$	$PA_2^{2.0}$	$PA_2^{3.2}$
λ_{ac}/d [-]	100	40	25

Table 2.8: *Wavelengths of the pressure field for the PA cases.*

wavelengths much larger than the injector inner diameter d. It ensures that the modulation remains purely transverse and does not generate longitudinal acoustic waves.
The elongated structures of heat release rate seen in figure 2.35 ($PA_2^{0.8}$) are also

seen in figures 2.38 and 2.39 ($PA_2^{2.0}$ and $PA_2^{3.2}$ respectively). Just like the MF cases, the apparent wavelength of the heat release rate structures is smaller for larger modulation frequencies. They also appear to be more compact for higher modulation frequencies, whereas for smaller modulation frequencies they are stretched to a greater extent in the axial direction. It seems that MF and PA show a similar disturbance of the heat release field.
The fields of axial velocity fluctuations of $PA_2^{0.8}$, $PA_2^{2.0}$ and $PA_2^{3.2}$ are displayed in figures 2.40 to 2.42. The length of the periodic structures are measured from figures 2.40, 2.41 and 2.42. Table 2.9 displays the the wavelength λ of these structures as well as the theoretical value of the wavelength. It can be

Case	$PA_2^{0.8}$	$PA_2^{2.0}$	$PA_2^{3.2}$
λ [m]	0.03	0.011	0.008
Theoretical λ [m]	0.03	0.012	0.0075

Table 2.9: *Wavelengths of the periodic axial velocity structures.*

seen from table 2.9 that $\lambda = v/f^{ac}$ where v is the average axial velocity between $5d$ and $15d$.
Harmonic velocity fluctuations are created in the annular stream. They are the consequence of the pressure modulation that produces a convective modulation at the injector exit. This is the result of an acoustic to convective mode conversion of the acoustic wave created in the injector by the pressure modulation (Noiray et al. (2009)). The unsteady heat release rate displayed in figure 2.35, 2.38 and 2.39 is actually caused by the dual action of the pressure fluctuation and the induced axial velocity fluctuation. It is possible to devise a method that can disconnect the effects of pressure and velocity fluctuations on heat release rate fluctuations. This will be described later on in this chapter.

2.5.3 Flow statistics

For all PA cases, the pressure fluctuations are measured in the middle of the domain, far away from the flame to avoid measurement perturbations by small vortices generated near the jet. As for MF cases, the total heat release rate is obtained by integrating the volumetric heat release rate over a volume containing the flame omitting a small portion near the injection plane. The Power Spectral Density (PSD) of pressure as well as the PSD of heat release rate for all the PA cases are displayed in figures 2.43 to 2.47. The PSD of the pressure signals exhibits a distinct peak at the modulation frequency for all cases. There is a secondary peak located at twice the modulation frequency corresponding to the first harmonic of the fundamental frequency. These frequencies are no longer dominant in the PSDs of heat release rate. The spectral contents of the modulated cases are indeed close to the one corresponding to the unmodulated case, where low frequencies (close to the preferred frequency of the flame) dominate the signal. A response of the flame is nevertheless noticed at the

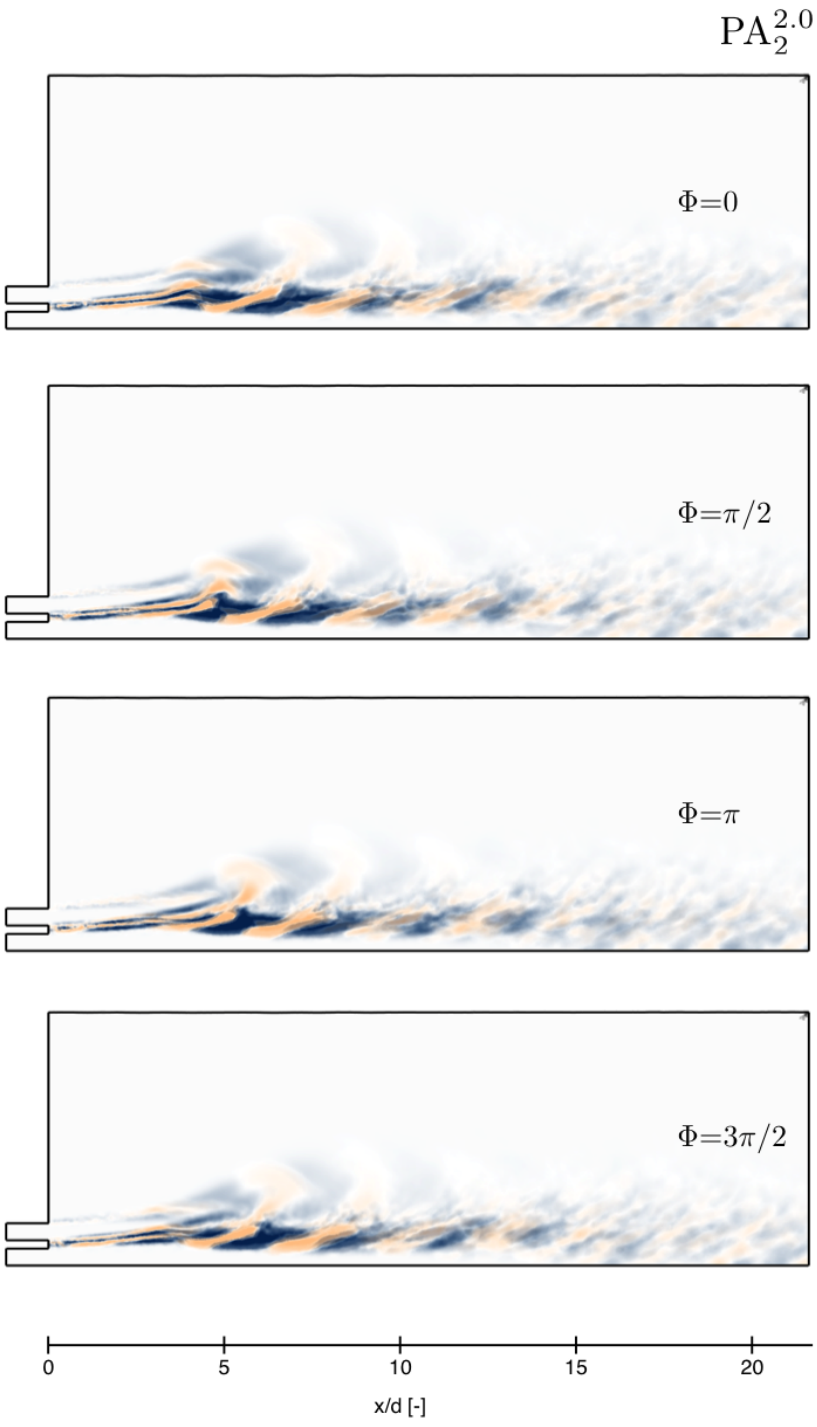

Figure 2.38: *Azimuthal cuts of the domain colored by the phase averaged unsteady volumetric heat release rate (blue: -1.10^{11} W.m^{-3}; beige: 1.10^{11} W.m^{-3}) at four different phases of the modulation for $PA_2^{2.0}$.*

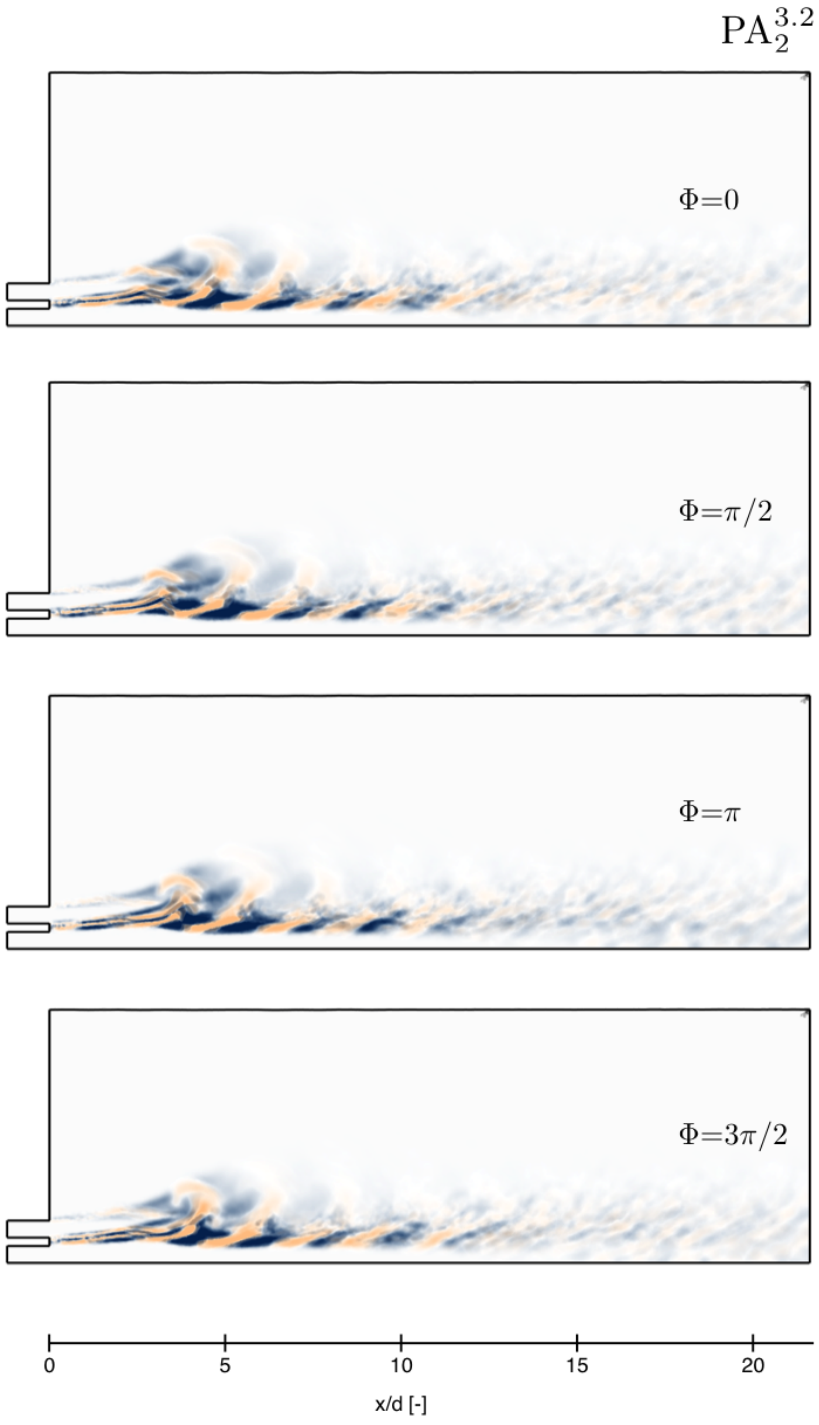

Figure 2.39: *Azimuthal cuts of the domain colored by the phase averaged unsteady volumetric heat release rate (blue: -1.10^{11} W.m^{-3}; beige: 1.10^{11} W.m^{-3}) at four different phases of the modulation for $PA_2^{3.2}$.*

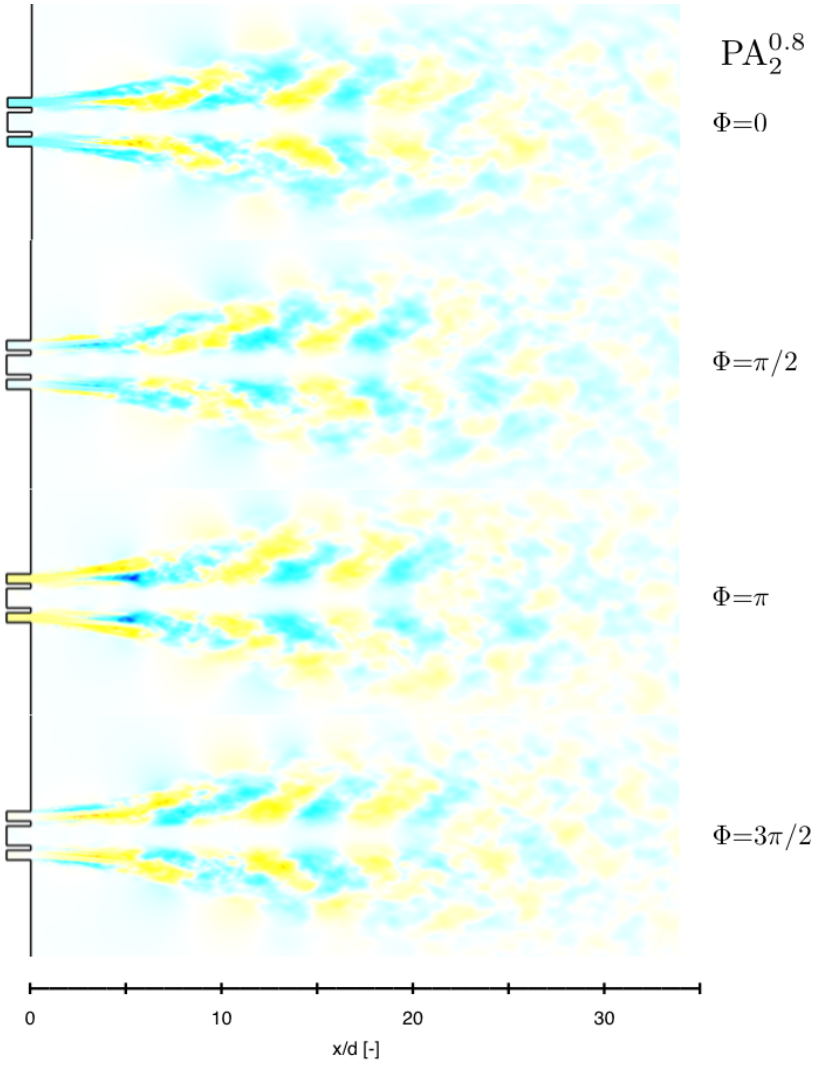

Figure 2.40: *Cut of the domain colored by the phase averaged velocity fluctuation (blue: -25 $m.s^{-1}$; red: 25 $m.s^{-1}$) at four different phases of the modulation for $PA_2^{0.8}$.*

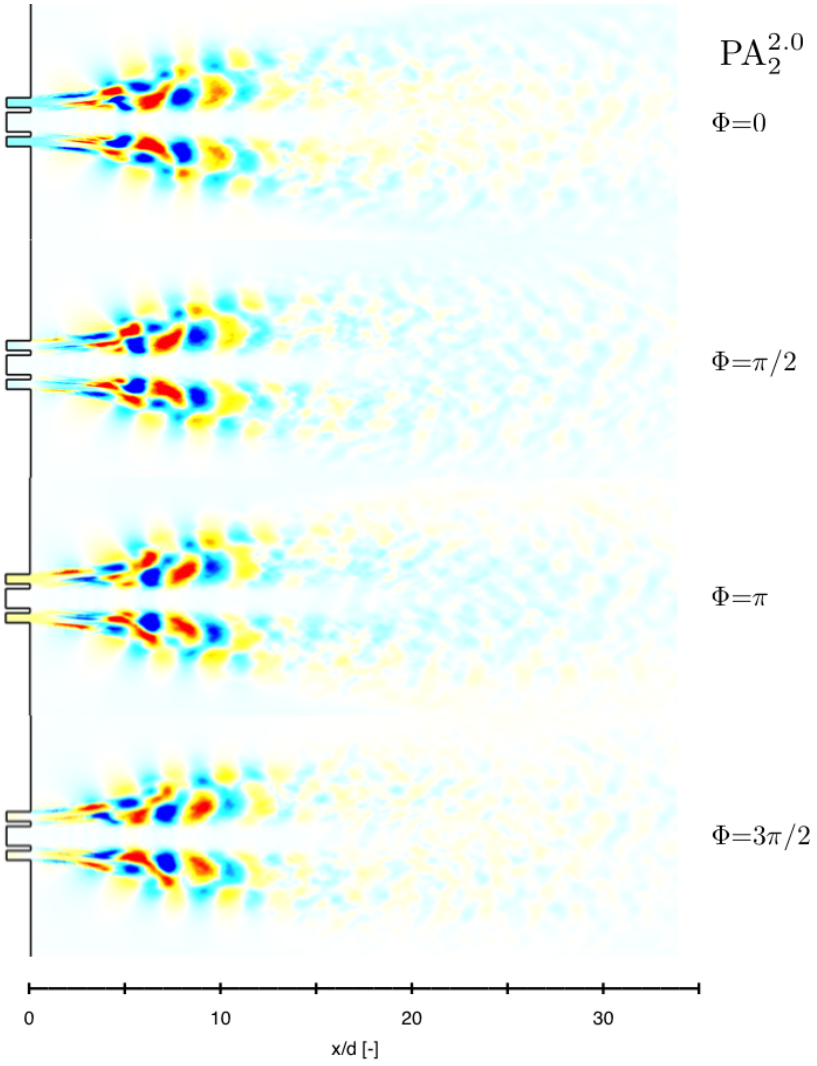

Figure 2.41: *Cut of the domain colored by the phase averaged velocity fluctuation (blue: -25 $m.s^{-1}$; red: 25 $m.s^{-1}$) at four different phases of the modulation for $PA_2^{2.0}$.*

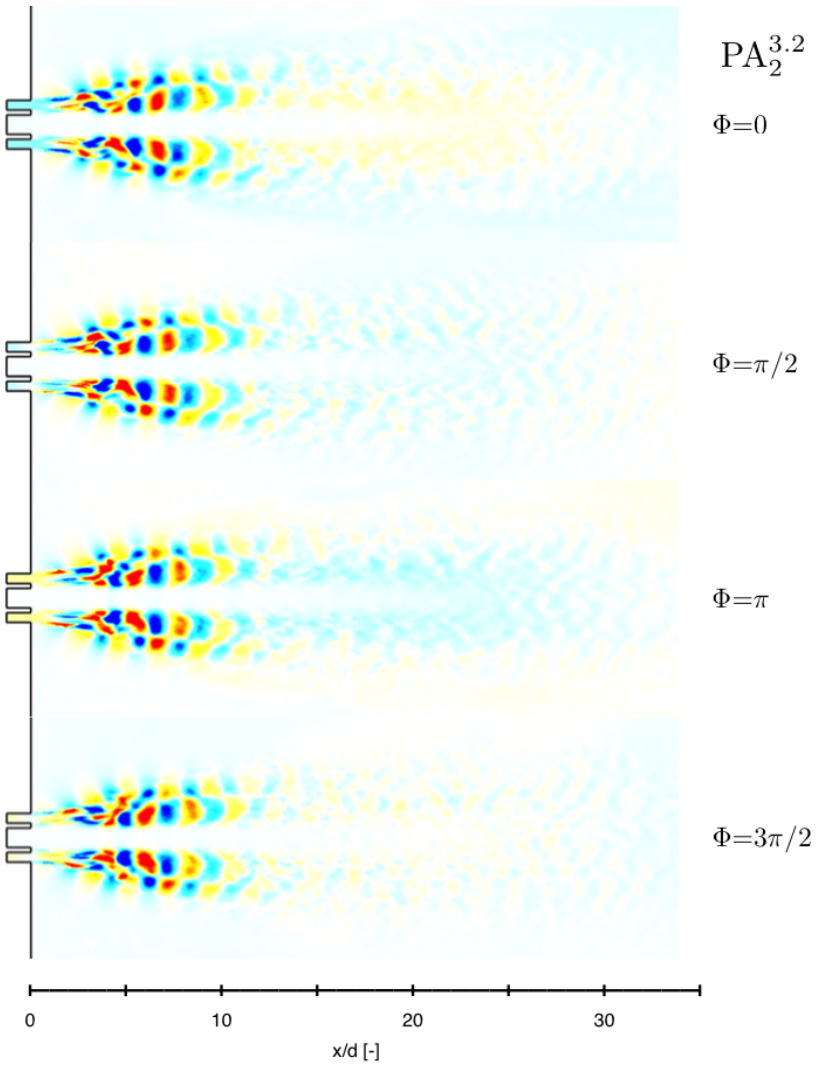

Figure 2.42: *Cut of the domain colored by the phase averaged velocity fluctuation (blue: -25 $m.s^{-1}$; red: 25 $m.s^{-1}$) at four different phases of the modulation for $PA_2^{3.2}$.*

modulation frequency for all cases. It is more clearly visible in the PSDs of modulation frequencies above 3500 Hz.

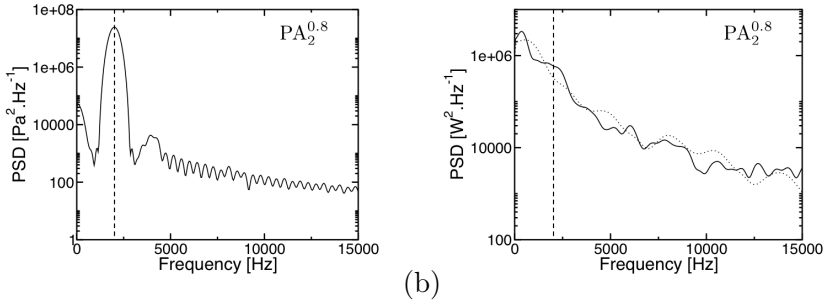

Figure 2.43: *Power spectral density of (a) pressure and (b) the heat release rate using Welch's method, with 5 blocks, 50 % overlapping, zero-padding and a frequency resolution of* $\Delta f = 170$ *Hz.* $\cdots$ *NM,* $-$ $PA_2^{0.8}$.

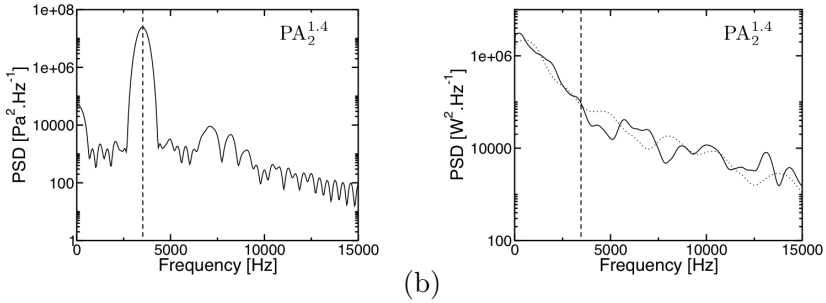

Figure 2.44: *Power spectral density of (a) pressure and (b) the heat release rate using Welch's method, with 5 blocks, 50 % overlapping, zero-padding and a frequency resolution of* $\Delta f = 170$ *Hz.* $\cdots$ *NM,* $-$ $PA_2^{1.4}$.

In order to extract the temporal evolution of heat release rate at the modulation frequency, the heat release rate is filtered with a Butterworth band pass filter. The width of the filter is equal to 400 Hz around the modulation frequency. Figures 2.49 to 2.53 display the temporal signal of the normalized pressure fluctuation and the normalized filtered heat release rate. All the modulated cases show a clear response of the heat release rate to the pressure modulation. The amplitude and phase shift between the pressure and heat release rate signals do not follow a monotone trend.

It is difficult to deduce a general behavior from figures 2.49 to 2.53 because of the simultaneous action of the pressure fluctuations and the induced velocity fluctuations. In order to evaluate the impact of pressure and induced axial velocity, it is necessary to find a relationship between them. Figures 2.54 to 2.58 display the temporal evolution of normalized pressure fluctuation in a pressure anti-node and the normalized induced velocity fluctuation at the injection plane.

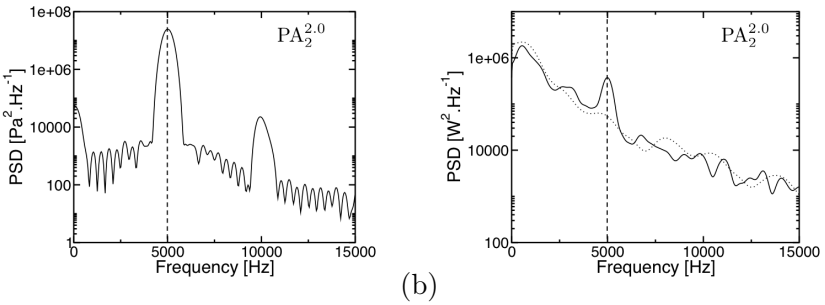

Figure 2.45: *Power spectral density of (a) pressure and (b) the heat release rate using Welch's method, with 5 blocks, 50 % overlapping, zero-padding and a frequency resolution of* Δf *= 170 Hz.* $\cdots$ *NM,* $-$ $PA_2^{2.0}$.

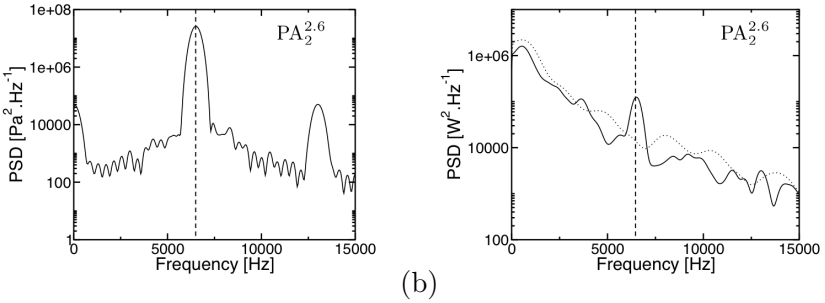

Figure 2.46: *Power spectral density of (a) pressure and (b) the heat release rate using Welch's method, with 5 blocks, 50 % overlapping, zero-padding and a frequency resolution of* Δf *= 170 Hz.* $\cdots$ *NM,* $-$ $PA_2^{2.6}$.

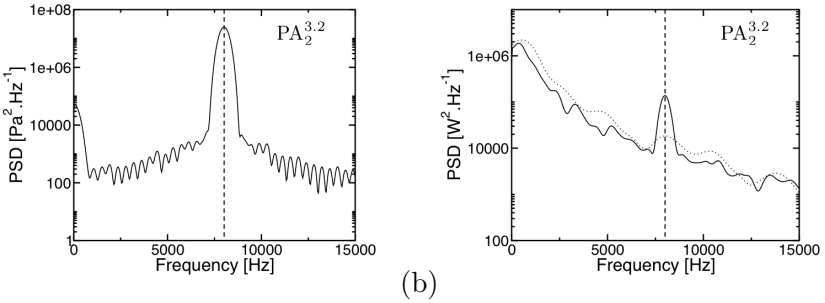

Figure 2.47: *Power spectral density of (a) pressure and (b) the heat release rate using Welch's method, with 5 blocks, 50 % overlapping, zero-padding and a frequency resolution of* Δf *= 170 Hz.* $\cdots$ *NM,* $-$ $PA_2^{3.2}$.

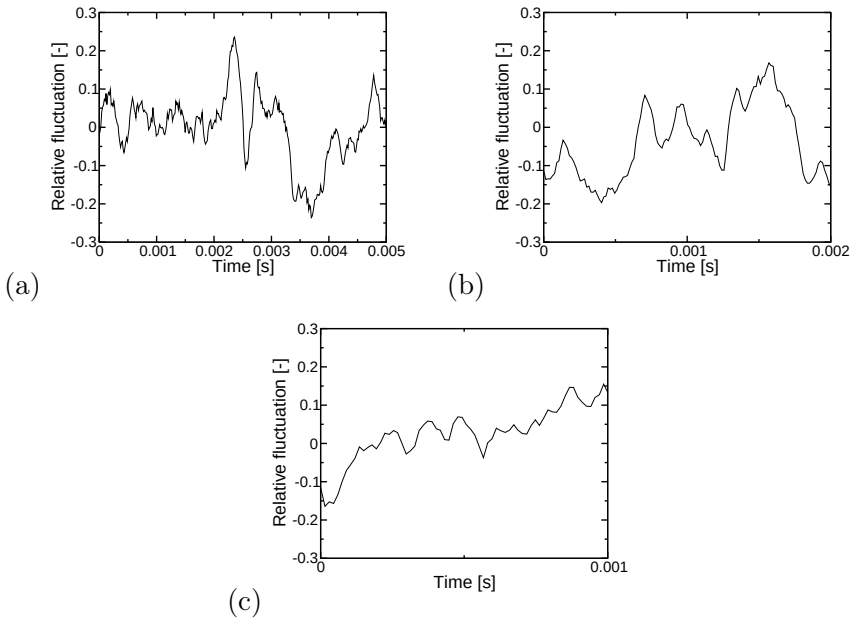

Figure 2.48: *Temporal signal of unsteady heat release rate for (a) $PA_2^{0.8}$, (b) $PA_2^{2.0}$ and (c) $PA_2^{3.2}$.*

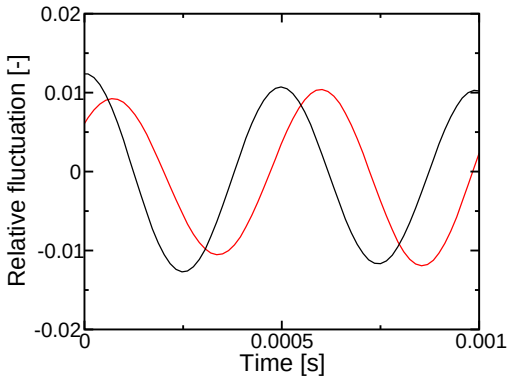

Figure 2.49: *Temporal evolution of the filtered relative fluctuation of pressure in the domain and the heat release rate for $PA_2^{0.8}$. — Pressure, – heat release rate. The width of the pass band filter is 400 Hz around the modulation frequency.*

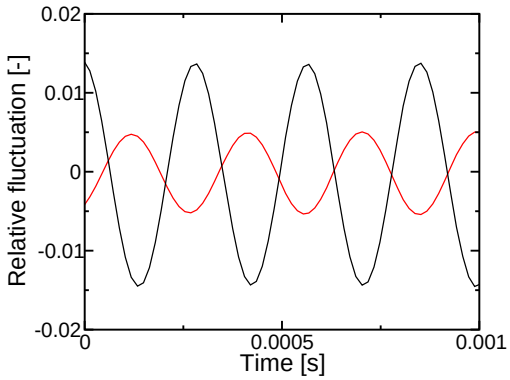

Figure 2.50: *Temporal evolution of the filtered relative fluctuation of pressure in the domain and the heat release rate for $PA_2^{1.4}$. — Pressure, – heat release rate. The width of the pass band filter is 400 Hz around the modulation frequency.*

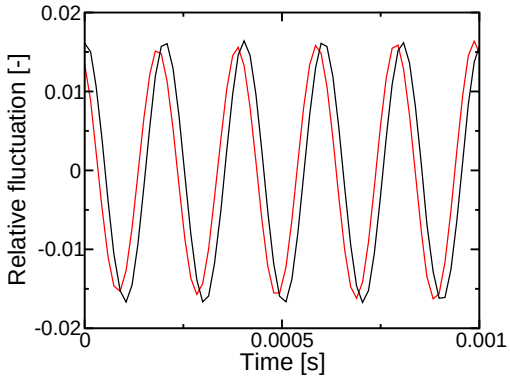

Figure 2.51: *Temporal evolution of the filtered relative fluctuation of pressure in the domain and the heat release rate for $PA_2^{2.0}$. — Pressure, – heat release rate. The width of the pass band filter is 400 Hz around the modulation frequency.*

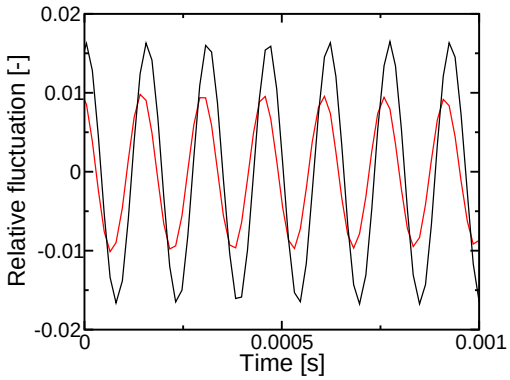

Figure 2.52: *Temporal evolution of the filtered relative fluctuation of pressure in the domain and the heat release rate for* $PA_2^{2.6}$. *— Pressure, – heat release rate. The width of the pass band filter is 400 Hz around the modulation frequency.*

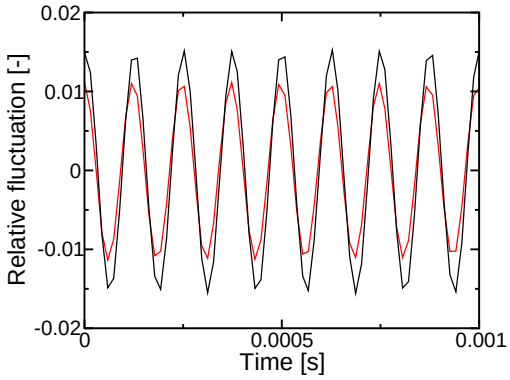

Figure 2.53: *Temporal evolution of the filtered relative fluctuation of pressure in the domain and the heat release rate for* $PA_2^{3.2}$. *— Pressure, – heat release rate. The width of the pass band filter is 400 Hz around the modulation frequency.*

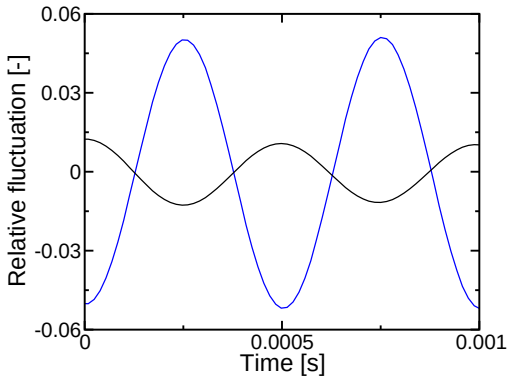

Figure 2.54: *Temporal evolution of the filtered relative fluctuation of pressure in the domain and annular velocity for $PA_2^{0.8}$. — Pressure, – annular velocity. The width of the pass band filter is 400 Hz around the modulation frequency.*

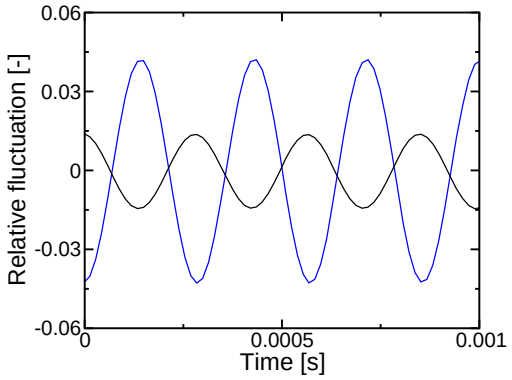

Figure 2.55: *Temporal evolution of the filtered relative fluctuation of pressure in the domain and annular velocity for $PA_2^{1.4}$. — Pressure, – annular velocity. The width of the pass band filter is 400 Hz around the modulation frequency.*

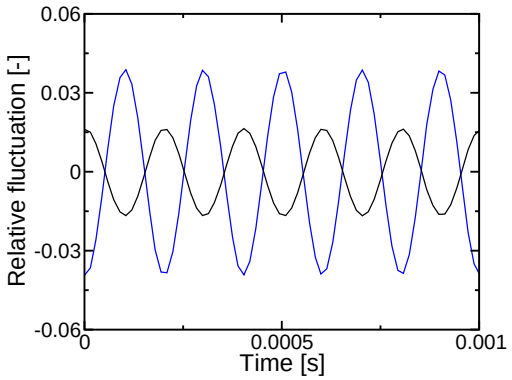

Figure 2.56: *Temporal evolution of the filtered relative fluctuation of pressure in the domain and annular velocity for $PA_2^{2.0}$. — Pressure, – annular velocity. The width of the pass band filter is 400 Hz around the modulation frequency.*

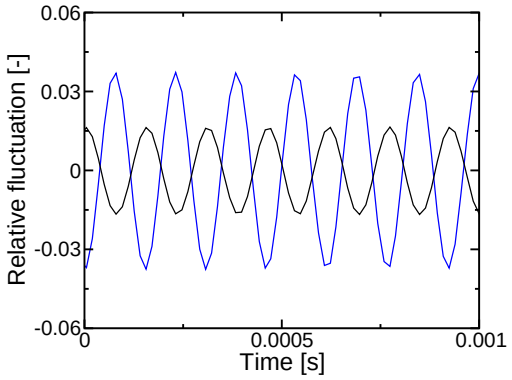

Figure 2.57: *Temporal evolution of the filtered relative fluctuation of pressure in the domain and the annular velocity for $PA_2^{2.6}$. — Pressure, – annular velocity. The width of the pass band filter is 400 Hz around the modulation frequency.*

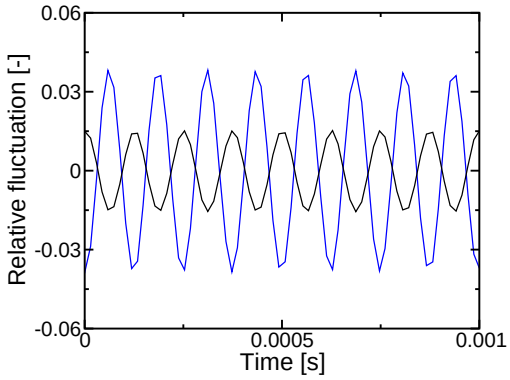

Figure 2.58: *Temporal evolution of the filtered relative fluctuation of pressure in the domain and annular velocity for* $PA_2^{3.2}$. *– Pressure, – annular velocity. The width of the pass band filter is 400 Hz around the modulation frequency.*

It can be seen that for every modulation frequency, that there is a constant relationship between the pressure and the induced velocity in the annular stream. This relationship is presented in equation 2.35.

$$p'(x=0,t) = -u'(x=0,t)\rho^i_{CH_4}c_0 \tag{2.35}$$

Where c_0 is the sound velocity in the annular flow. Now that the relationship between the pressure fluctuation and the induced annular velocity is established, it is possible to subtract the heat release rate resulting from the induced velocity from the global heat release rate. This is done using a flame transfer function description.

2.5.4 Flame transfer function of the heat release rate fluctuations induced by transverse pressure modulations

2.5.4.1 Global description

The FTF between the pressure signal and the heat release rate signal is determined by the equation 2.36.

$$FTF_G(f^{ac}) = S_{hr-p}(f^{ac})/S_{p-p}(f^{ac}) \tag{2.36}$$

Where S_{hr-p} is the cross power spectrum of heat release rate and pressure and S_{p-p} is the power spectrum of the pressure. The FTF is only valid at the modulation frequency f^{ac}. In order to determine the global FTF of the heat release rate response, the FTF is evaluated at every modulation frequency. The gain and the phase of the FTF are the modulus and the argument of the complex number $FTF_G(f_{mod})$ respectively. Gain and phase are plotted for all PA cases in figure 2.59. The flame weakly responds to a modulation frequency

of 3500 Hz but responds more effectively at 5000 Hz. In figure 2.59 both effects of pressure and induced velocity are visible, this shows again that it is necessary to separate the effects in order to obtain a model for the influence of pressure modulation. The relationship between pressure and velocity, given in equation

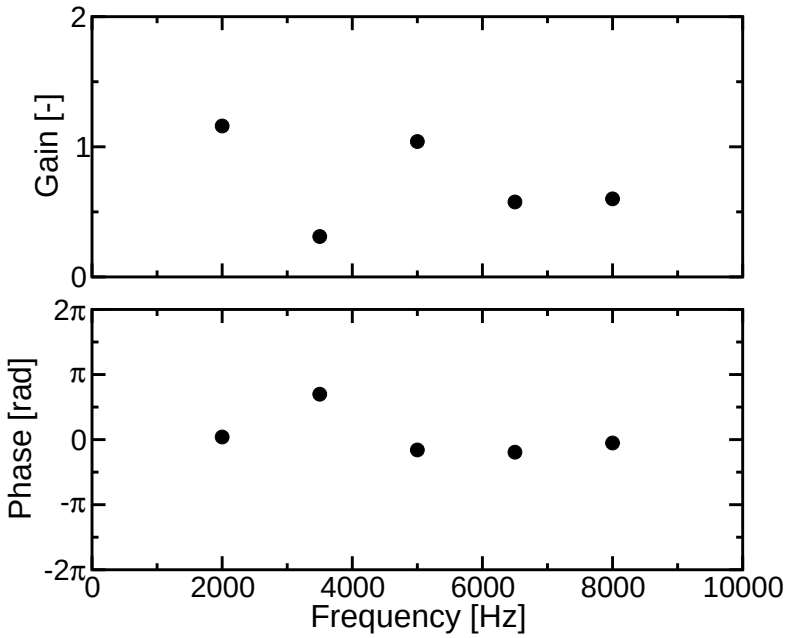

Figure 2.59: *Flame transfer function of the pressure modulation cases.*

2.35, is particularly useful when included in the complex function FTF_G.

2.5.4.2 Description without velocity fluctuations

Under the assumption of a linear response of the flame, the FTF can be rewritten as equation 2.37.

$$\frac{\dot{Q}'}{\overline{\dot{Q}}} = FTF_G \frac{p'}{\overline{p}} \tag{2.37}$$

Where FTF_G is the global FTF between pressure and heat release rate. FTF_P is the FTF between pressure and heat release rate and FTF_U is the FTF between annular velocity and the heat release rate described in section 2.4. By reworking equation 2.37, the equation for FTF_P yields:

$$FTF_P = FTF_G + FTF_U \frac{\overline{p}}{\overline{u}\rho^i_{CH_4} c_0} \tag{2.38}$$

Using the equation 2.38 it is possible to plot the FTF of the influence of pressure (figure 2.60). Gain and phase of FTF_P are plotted in figure 2.60. In the range

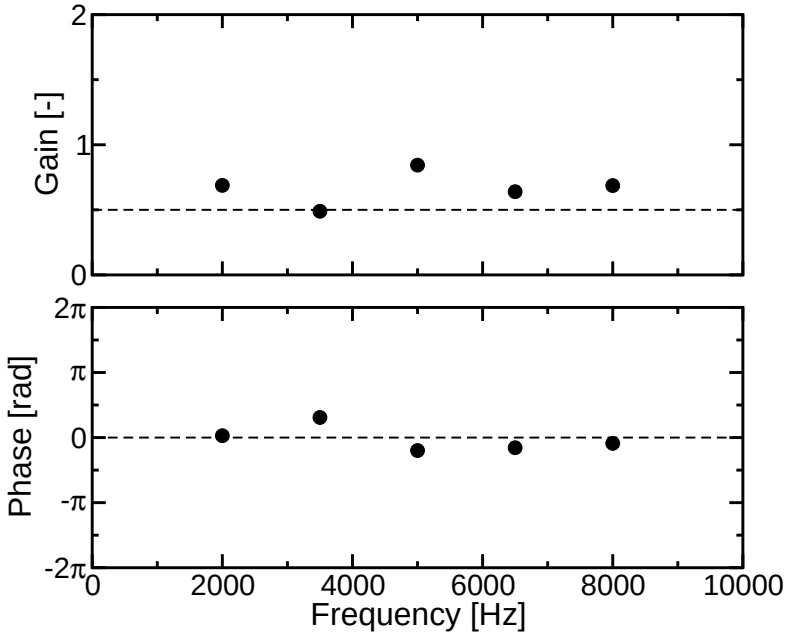

Figure 2.60: *Flame transfer function of the pressure modulation cases. • FTF results from the large eddy simulations of pressure modulation without the influence of the induced velocity, –– modeled flame transfer function.*

of frequencies studied here, the gain and phase of the FTF are now quasi constant, around 0.5 and 0, respectively. This indicates that heat release rate fluctuations are induced by pressure modulations in an essentially quasi-steady fashion, at least in the range of frequencies considered in the present study (Poinsot and Veynante (2001); Pons et al. (2008); Pons et al. (2009)). In the present situation combustion of cryogenic propellants can be considered to be infinitely fast and the conversion rate in the local flame elements follows a square root law as a function of pressure. This is exploited further in the model derived in the next subsection.

2.5.4.3 Pressure fluctuation model

The heat release per unit of surface is now considered to be proportional to the square root of the pressure (Pons et al. (2008)), equation 2.39.

$$\dot{q}_s(\mathbf{i_{inj}}, t) \propto \sqrt{p}(\mathbf{i_{inj}}, t) \tag{2.39}$$

Where $\mathbf{i_{inj}}$ is the index of an injector. The derivation follows the same lines of reasoning used in the case of mass flow rate modulations (section 2.4). The unsteady heat release rate can be linked to the pressure fluctuations by equation

2.40.

$$\dot{Q}'(\mathbf{x_{inj}}, t) = \frac{\overline{\dot{Q}}}{2\overline{p}} p'(\mathbf{x_{inj}}, t) \tag{2.40}$$

There is no delay between the pressure fluctuations and the heat release rate fluctuations. Furthermore the gain of the model is constant and equal to 0.5. The trend displayed in figure 2.60 is in good agreement with the model however the gain is greater in the simulation results than in the model. This might be caused by an insufficient level of statistical averaging in the determination of the various transfer functions.

2.6 Conclusion

The objective of this chapter has been to examine two possible driving mechanisms of combustion instabilities in liquid rocket engines. Modulation of the injected mass flow rate and modulation of the average chamber pressure were specifically considered. The analysis relies on large eddy simulation of a single coaxial injector.

The simulations of mass flow rate modulation showed that, near the injector lip, the mass flow rate fluctuation generates concentrated regions of heat release rate fluctuations. The heat release rate perturbations are located in the injector vicinity and in the entire region where reactants are converted into products. The global effects of the mass flow rate modulation heavily depend on the number of wavelengths that can fit in the flame since the positive and negative structures of heat release rate tend to compensate each other. To explain these findings an analytical model was formulated, which relies on a description of the effect of a variable strain rate on the flame elements formed by the coaxial injector. It is concluded from this model that velocity modulations, corresponding to mass flow rate perturbations, may not be an important source of heat release rate fluctuations. The main driving processes include a time lag defined by the flame length and the outer stream velocity while the amplitude depends on the mean heat release rate profile along the central axis.

The simulations of pressure modulation revealed the presence of an induced velocity fluctuation. The separation of these two effects was difficult. This is because velocity fluctuations appear in the presence of pressure modulation even with a non-reflective injector boundary condition. It is however possible to extract the influence of the pressure alone from the heat release rate. The analysis shows that the heat release rate of the flame responds in the same way regardless of the modulation frequency (at least in the range of frequencies considered in this study). The flame responds with no delay to the pressure modulation. This was explained by the fact that the chemistry can be considered to be infinitely fast. It was also shown that the heat release rate depends on the square root of the pressure fluctuations.

Both models developed from these simulations describes well the general behavior of the flame when submitted to mass flow rate and pressure modulations. These models will be used later on in this work as part of instability driving mechanisms in a reduced order dynamic model designed to predict combustion instabilities.

Part II

Experimental investigation of acoustic damping rate and injector dynamics

As indicated in the previous section and demonstrated through a set of calculations, the unsteady heat release rate is the main driving mechanism of combustion instabilities. This driving term is balanced by damping mechanisms and the level of damping defines to a great extent conditions that lead to instability. If the system is highly damped and growth rates are lower than the damping rates the system will be linearly stable. Damping is generally produced by boundary mechanisms like friction in acoustic boundary layers but the levels of damping associated with these processes are generally too low to explain the levels observed in practice. Damping may also arise from the nozzle impedance. A certain amount of acoustic energy is radiated away from the thrust chamber and this corresponds to damping. In general, it is not easy to evaluate the damping rate in a particular geometry from theoretical analysis. It is then natural to examine this problem experimentally. This is done in this part by considering a configuration including many of the relevant physical phenomena but for a simpler geometry than that prevailing in practical situations. A dedicated test rig (designated as NPCC) has been designed for that purpose. This comprises two cavities representing the dome and chamber of an engine. These two cavities are connected by injection channels. The objective is to obtain estimates of the damping rates, examine the injector dynamics and the coupling between the two cavities. These experiments are also used to verify the low order modeling code STAHF in a well controlled configuration.

Chapter 3

The NPCC test rig experimental setup

Some important issues in rocket engine combustion instability are associated with injector dynamics and the coupling between the thrust chamber and the dome feeding the chamber. Another important aspect is the estimation of the damping rate. This chapter describes how these various questions may be addressed by making use of a cold flow experiment representing, in a simplified way, the geometry of typical engines. The system designated as New Pressurized Coupled Cavities (NPCC) comprises two rectangular cavities linked by injection channels. Air injected in the dome is exhausted by a set of two nozzles which are alternatively aked by a rotating perforated wheel. This arrangement is used to modulate the flow and to excite the transverse modes of the system making possible the study of the injector dynamics by simultaneously recording pressure and velocity signals. The system also gives access to the coupling mechanism between the two cavities and allows measurements of the global damping rate. Finally, effects of head losses in the injection system may also be quantified. The objective is here to see whether these losses can contribute to uncouple the dome and chamber.

3.1 Introduction

One important issue in combustion instability is that of the possible coupling between the injection system and the combustion chamber. In liquid rocket engines this essentially involves the propellant manifold and injectors. In a typical engine like Vulcain shown in figure 3.1 propellants are conveyed to the injectors through domes. The liquid oxygen dome directly feeds the central channels of the coaxial injectors while the annular channels are fed by the hydrogen dome. These domes are linked to the chamber through an injection plate often comprising several hundreds injectors forming a system which looks

somewhat like a shower head (figure 3.1). The large number of injectors allows, from an acoustic point of view, good communication between the domes and the thrust chamber.

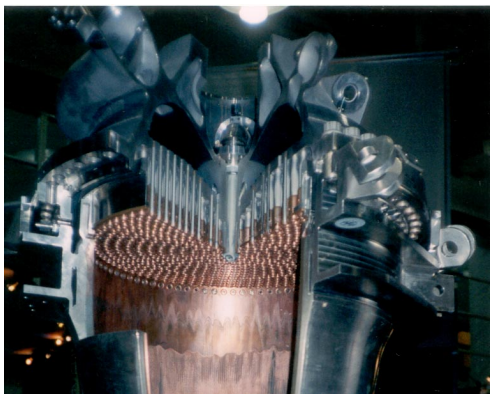

Figure 3.1: *Injector head of the Vulcain 2 engine. It comprises 566 injectors fed with liquid oxygen and gaseous hydrogen.*

It is then quite possible that this may lead to a coupling, or interaction, between injection and combustion. It is known from experiments that this interaction may be reduced by making sure that the head loss induced by the injection system is sufficient. The standard rule is to design a system which will introduce a head loss of about 15%, a value which is relatively high but is usually adopted to avoid potential coupling mechanisms. Unfortunately, it is not easy to investigate this kind of phenomena on real engines and it is also quite difficult to design model scale hot fire experiments to examine this aspect in detail. There are some indications from previous experiments carried out on the Mascotte facility but the data do not give sufficient clues on the coupling processes and on their consequences. It is then reasonable to try to study these mechanisms in a separate facility which retains the essential features but is simpler to operate and allows systematic investigations. The central idea is then to examine the coupling mechanisms between dome and chamber in a non reacting situation. One is then led to design a model scale configuration featuring a geometry having similarities with that used in the MIC experiments on the Mascotte rig and using the same Very High Amplitude Modulator (VHAM) scheme. This cold flow system allows a number of investigations including studies of the modulation actuator, studies of the interaction between a simplified dome and chamber, analysis of the injector dynamics, characterization of damping rates and effects of head losses on damping by the injection system. Some of these aspects have already been considered in the recent past. For example, Richecoeur (2006) used a pressurized steel box comprised of to cavities and a single lateral nozzle to examine the modulation by a lateral toothed wheel periodically blocking the side nozzle. Méry (2010) reports experiments on the Transparent Pressurized Cavity (TPC), a single cavity test rig with two nozzles, where the flow field

induced by the VHAM was investigated by high frequency Particle Image Velocimetry (PIV) (Méry et al. (2009)). This configuration was then improved to include a dome and investigate injector dynamics in a coupled cavity configuration designated as Transparent Pressurized Coupled Cavities (TPCC) (Hakim (2013)). These studies are here pursued by making use of a new configuration (NPCC) which is used to examine injector dynamics and damping. This new facility is also used to partially validate the low order modeling exploited in STAHF.
This chapter begins with a brief summary of the main conclusions of the previous cold flow experiments (3.2). The features of the new test facility NPCC are then described in section 3.3. A set of results obtained with this experimental facility are then reported in section 3.4.

3.2 A review of previous experiments on coupling and injector dynamics

It is here interesting to review previous studies to explain how the current NPCC rig was designed. The general objective is to examine injector dynamics in configurations comprising multiple cavities acting as dome and chamber and to examine such systems under an external modulation. It would be possible to reproduce a cylindrical geometry of the type existing in real engines but it has been found more practical and less demanding in terms of design to use a rectangular geometry somewhat similar to the Multiple Injector Combustor developed for the Mascotte facility. This choice was made for the various test rigs used previously at EM2C.
A first investigation of a cold flow configuration is reported by Richecoeur (2006). A rectangular steel box comprising a perforated plate (with three or sixty holes) was used to understand the coupling between cavities through the perforated plate (which served as an injector plate). Acoustic modulation was generated by a toothed wheel blocking a lateral nozzle (figure 3.2).
This configuration was used to optimize the acoustic modulation in the Multiple Injector Combustor (MIC) (Richecoeur et al. (2006); Richecoeur et al. (2009)). This system was to be fitted on the Mascotte test facility operated by ONERA (Vingert et al. (1997); L. Vingert and Traineau (1999); Vingert et al. (2000); Habiballah et al. (2006)) to study the response of cryogenic combustion submitted to externally imposed transverse modulations. The initial MIC also comprised a lateral nozzle which was periodically blocked by a toothed wheel. Cold flow experiments were carried out to define conditions which led to the highest levels of modulation.
The cold flow pressurized cavity was used in a second stage to investigate the possibility of generating a transverse modulation by making use of a new concept designated as VHAM. In essence the combustion chamber is fitted with two identical nozzles and a rotating toothed wheel now blocks these nozzles

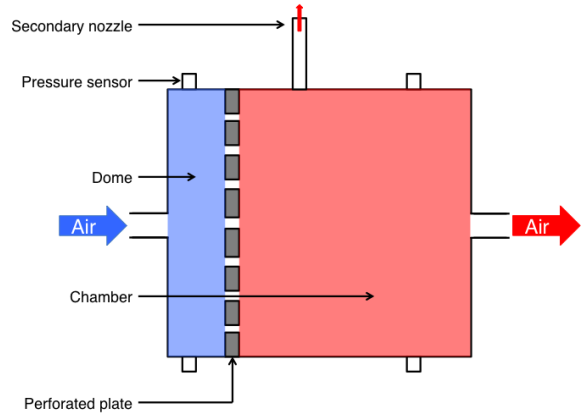

Figure 3.2: *Schematic view of the cross section of the first cold flow experiment used at EM2C to improve the coupling between the chamber and the lateral nozzle and actuator from Richecoeur (2006).*

in an alternate fashion. This induces a transverse modulation in the cavity. Further studies of the acoustic field induced by the VHAM were carried out in another configuration designated as the TPC (figures 3.3 3.4) (Méry (2010)).

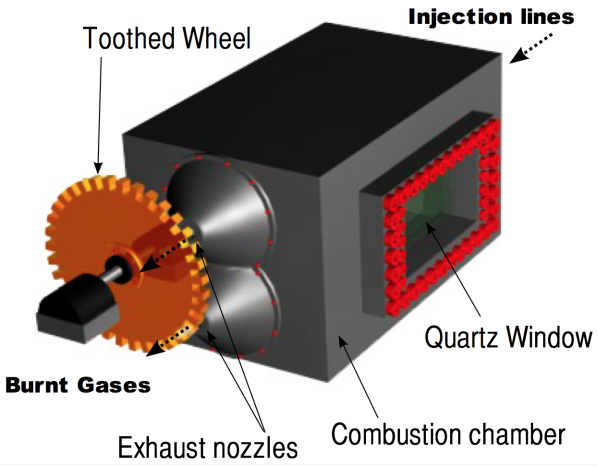

Figure 3.3: *The Multiple Injector Combustor (MIC) equipped with the VHAM from Méry (2010).*

This system was designed to operate under cold flow conditions with the objective of studying the acoustic field induced in the cavity by the VHAM. The chamber is transparent with Plexiglas lateral walls to allow optical measurements inside the cavity. The acoustic velocities induced by the VHAM were sufficient to allow direct Particle Image Velocimetry measurements Méry (2010). It was found that the flow induced by the VHAM under resonant conditions (i.e. at one of the transverse eigenfrequencies) agreed well with the acoustic

velocities of the corresponding acoustic mode (Méry et al. (2009)).

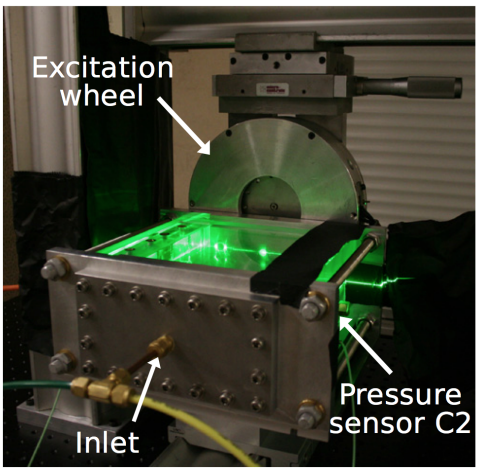

Figure 3.4: *General view of the Transparent Pressurized Cavity (TPC) test rig equipped with the VHAM from Méry (2010).*

The TPC test rig was modified by Hakim (2013) to allow studies of injector dynamics and dome-chamber coupling using a new configuration designated as TPCC test rig (figure 3.5). Just like its predecessor the TPCC test rig had transparent plexiglas lateral walls to perform optical diagnostics. A dome was added on the upstream side of the chamber. The dome fed with air was connected to the chamber by three cylindrical injectors. The chamber had the same dual nozzle arrangement allowing modulation by a toothed rotating wheel using the VHAM principle employed on the TPC. This facility allowed detailed studies of modal coupling and injector impedance.

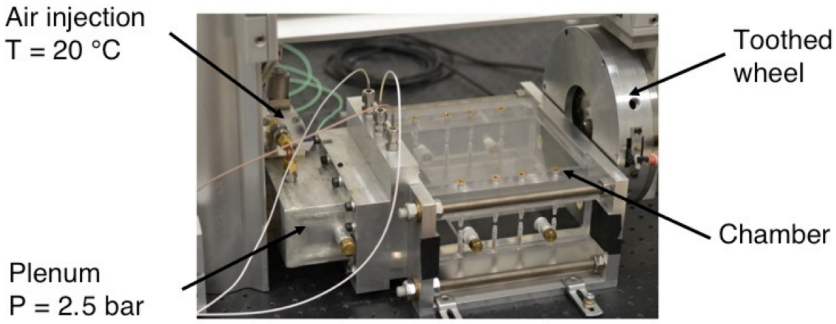

Figure 3.5: *The Transparent Pressurized Coupled Cavities (TPCC) test rig featuring a plenum (dome), a transparant chamber and the VHAM.*

It was clear that more work could be done in this direction but that this required some improvements of the experimental configuration.

3.3 Presentation of the NPCC test configuration

The New Pressurized Coupled Cavities test rig has been designed in view of previous work to deal with a set of interrogations that emerged from that work.

3.3.1 Requirements

One aspect that needs more consideration is that of the injector impedance and its influence on the stability of the thrust chamber. In practice, the rocket engines are designed to obtain a sufficient level of head loss in each injector to minimize the coupling between the combustion chamber and the feeding manifold and modify the injector impedance. It is then worth examining this dependence and quantifying the effects associated with the injection head loss. It is also important to examine acoustic damping and determine the damping rate in a simple configuration to obtain estimates of this rate in practical systems. The coupling between cavities also needs further analysis and for that it is convenient to be able to change the geometry of the system to scan situations where the size of the dome and that of the chamber allow a perfect match between eigenmodes of these two cavities. These three issues motivate the development of a new configuration allowing an easier matching between the nozzles and rotating actuator wheel and facilitating changes in the injector head loss and in the geometry. These various aspects are covered in what follows.

3.3.2 Overall description

The New Pressurized Coupled Cavities (NPCC) configuration is similar to the TPCC (figures 3.6 and 3.7). Injectors can accommodate different diaphragms allowing changes in head losses. The structure is optimized to allow identification of the modal structure and a determination of damping rates using two methods. NPCC comprises rectangular dome and chamber. These cavities are connected by three 6 mm in diameter cylindrical injectors. The air, regulated by a flow meter, is injected in the dome and it is exhausted through two nozzles. The Very High Amplitude Modulator (VHAM) is flush mounted against the nozzle exhaust planes. The inner dimensions of the dome and chamber were chosen so that the first transverse eigenmode of the dome ($1T^d$) corresponds to the first transverse first longitudinal eigenmode of the chamber ($1T1L^c$).
Assuming a uniform flow at rest, the acoustic eigenmodes and eigenfrequencies can be calculated by the Helmholtz equation together with boundary conditions. A simple cavity with rigid walls has the following eigenfrequencies:

$$f_{m,n,p} = \frac{c}{2}\sqrt{\left(\frac{m}{l_x}\right)^2 + \left(\frac{n}{l_y}\right)^2 + \left(\frac{p}{l_z}\right)^2} \tag{3.1}$$

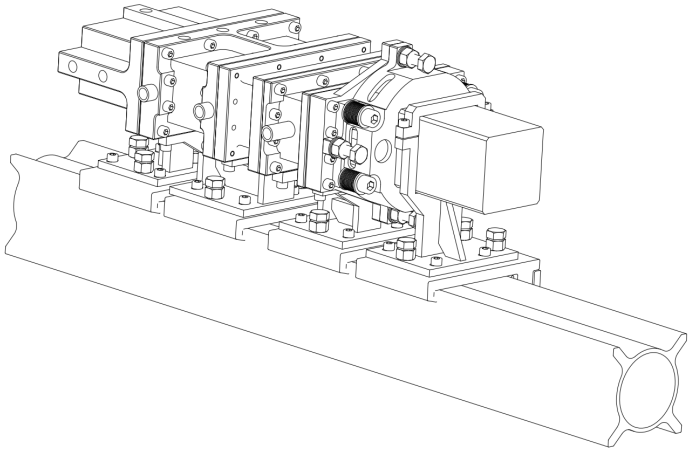

(a)

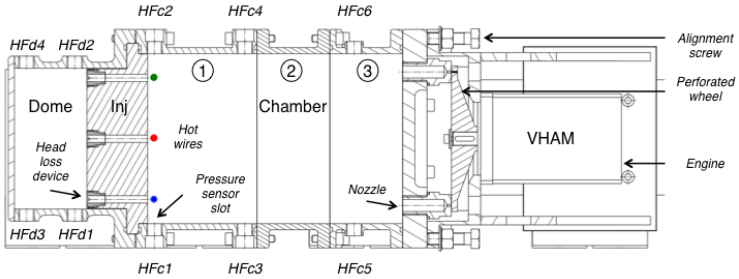

(b)

Figure 3.6: *(a) Overall view of the entire NPCC test rig. (b) Transverse cut of the NPCC test rig featuring dome, injectors chamber and VHAM. The chamber is divided into three sectors: (1) Fixed upstream chamber block with pressure taps, (2) Interchangeable chamber block, (3) Fixed downstream chamber block with two pressure taps. Hot wires HW1, HW2 and HW3 are located in the near vicinity of the injector exhaust sections.*

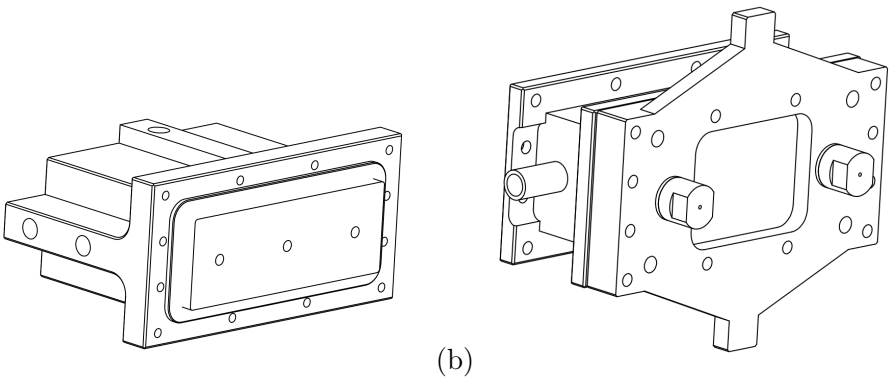

(a) (b)

Figure 3.7: *Close up view of the NPCC (a) Dome and injectors and (b) Chamber end section with nozzles.*

Where c is the speed of sound which is in air at room temperature $c = 343\,\mathrm{m.s}^{-1}$, $m\,n\,p$ are integers identifying the different eigenmodal frequencies and l_x, l_y, l_z are the dimensions in the x, y, z directions. Here x is the axial coordinate, y is the transverse coordinate in the plane containing the two nozzle axis while z is perpendicular to the previous two directions and corresponds to the smallest dimension of the two cavities. In what follows, we only consider modes which have no transverse component in the z direction. These modes correspond to $p = 0$. The internal dimensions of the test rig were chosen to optimize the coupling between the dome and the chamber. Previous studies (Richecoeur (2006)) indicate that a suitable coupling can be achieved between the $1\mathrm{T}^d$ mode of the dome and the $1\mathrm{T1L}^c$ mode of the chamber. The length of the chamber is $l_x^c = 210\mathrm{mm}$ and the transverse dimension is $l_y^c = 140\mathrm{mm}$. For the dome the transverse length is $l_y^d = 116\mathrm{mm}$. Using these dimensions in equation 3.1, the 1T mode in the dome (corresponding to $m = 0, n = 1, p = 0$) is at $f^d_{0,1,0} = 1478$ Hz and the 1T1L mode in the chamber (corresponding to $m = 1, n = 1, p = 0$) is at $f^d_{1,1,0} = 1472$ Hz. These frequencies are quite close and by suitably changing the axial size of the chamber one may obtain a perfect match.
These eigenmodes can be exited by the VHAM. This device comprises a perforated wheel set in rotation by an variable speed motor. The perforated wheel, when in rotation, alternatively blocks and opens the nozzles a mechanism which locally generates nearly null velocities, inducing out of phase perturbations at the two nozzle inlets. Figure 3.8 shows the VHAM and its influence on the nozzles.

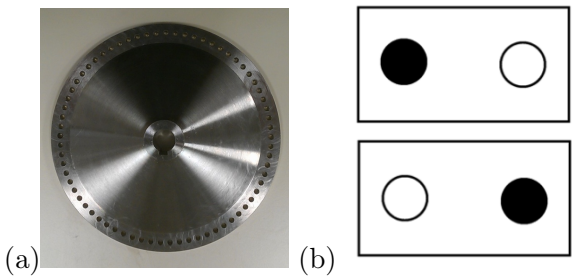

Figure 3.8: *(a) Photograph of the fully perforated wheel of the VHAM. (b) Schematic view of the nozzles, dark means a closed nozzle, white corresponds to open nozzles.*

The alignment of the perforations of the wheel with the nozzles is a critical operation. The wheel needs to be as close and perpendicular to the nozzles as possible. Three screws on the protective shell of the wheel allow a fine adjustment of the clearance between the nozzle front end and the perforated wheel. The objective of this is to minimize the lateral gas leak between the nozzle and the wheel (figure 3.9).
The first area, S_1, is the exit area when the wheel does not block the nozzle: $S_1 = \pi d^2/4$. The second area, S_2, is the area available when the wheel is

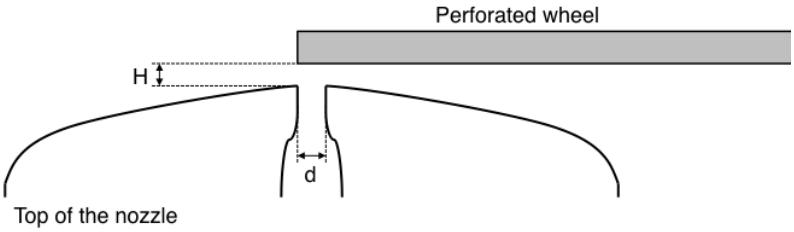

Figure 3.9: *Schematic view of the position of the wheel with regard to the nozzle.*

supposed to block the nozzle: $S_2 = \pi dH$. Hence, the ratio of these two areas is $\Sigma = S_2/S_1 = 4H/d$.
The electric motor (Kollmorgen DBL3H00065-0R2-00K-S40), has a maximum rotation speed of 6000 rpm. The engine is controlled with a dedicated program, which defines a slow increase in rotation speed associated with a linear frequency ramp or it can run at a constant frequency in a continuous wave mode of operation. With the N =69 perforations of the standard wheel the maximum modulation frequency of the VHAM is 6900 Hz.
In order to identify the acoustic field generated by the VHAM, the test rig is implemented with a set of pressure sensor taps. In these pressure sensor taps, pressure sensors are placed to measure pressure fluctuations (firue 3.6).
Three hot wire sensors are placed in the immediate vicinity of the injector exhaust sections on the chamber side. The hot wire sensors measure the axial velocity fluctuations at the injector outlets (figure 3.6).

3.3.3 Instrumentation

As indicated previously the NPCC test rig comprises a number of pressure sensors. Four are located in the dome with two on each lateral wall and six others in the chamber, three on each lateral wall (figure 3.6(b)). The positions of the pressure sensors in the domain were chosen in order to clearly identify the modes generated by the VHAM (the pressure sensors are located near the pressure anti-nodes of the first few modes that can be generated by the VHAM). The chamber, as well as the dome, are equipped with 701A Kistler high frequency pressure sensors. The entire chain of pressure measurement actually comprises the piezoelectric sensor (figure 3.10(a) and an amplifier (figure 3.10(b). The amplifier is a 5018 Kistler charge amplifier. The role of the amplifier is to convert the electric charge induced on the sensor into an electric voltage which can be acquired by a computer or visualized on an oscilloscope. This amplifier has multiple settings; a short setting giving the instantaneous value of the relative pressure; a long setting providing the average pressure in the cavity. Both of these settings are useful in the present study.
Hot wire sensors are used to measure the instantaneous injection velocity fluc-

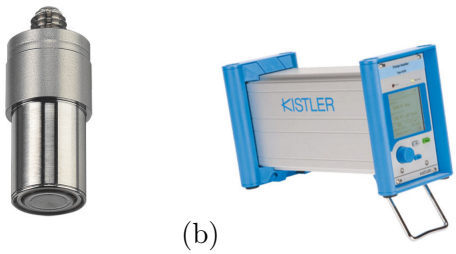

(a) (b)

Figure 3.10: *Photograph of (a) The Kistler 701A pression sensor and (b) The Kistler 5018 amplifier. Kistler Group, Eulachstrasse 22, CH-8408 Winterthur, Switzerland.*

tuation. They are positioned (figure 3.11) at the injector outlets. The hot wire sensors, before use, are calibrated at the operating pressure. The operating pressure is 2.5 bar above the atmospheric pressure. This is achieved by blocking a nozzle and, with the help of a tap, slowly opening the other nozzle in order to keep the pressure at a constant value. The air stream is controlled by a flow meter. Knowing the injector dimension and the thermodynamic conditions of the flow, the flow velocity is determined. The hot wire may be described by King's law which establishes a direct relation between the flow velocity and the voltage delivered by the hot wire conditioning system. King's law is given by:

Figure 3.11: *Photograph of the three hot wires mounted in the near vicinity of the injection plate.*

$$V^2 = A + Bu^{1/2} \tag{3.2}$$

where V is the voltage, u is the velocity, A and B are the calibration constants, which need to be determined. The calibration is made for several axial injection velocities. The results of calibration are displayed in figure 3.12 which shows V^2 as a function of $u^{1/2}$. The relation appears as an affine function from which the coefficients A and B can be directly read.

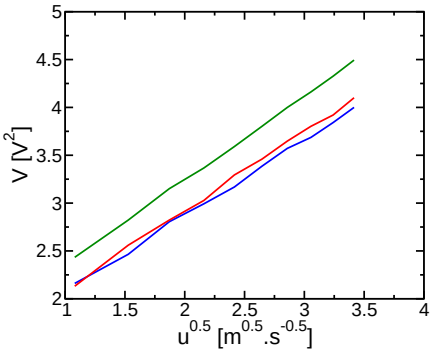

Figure 3.12: *Calibration curves of the hot wires. The square of the voltage is plotted as a function of the square root of the flow velocity HW1, HW2 and HW3.*

3.3.4 New features of the NPCC configuration

One of the new features of the NPCC is its modular design. The chamber cavity comprises three separate blocks. The upstream block, which holds the hot wires, four pressure slots, maintains the injector plate in place. This block is fixed to the dome. The downstream block, which holds the nozzles and two pressure slots, is fixed to the wheel protective casing. The middle block was designed to be interchangeable. The inner dimensions of the cavities were chosen to match particular eigenmodes and the middle block may be used to change the chamber length to allow a fine tuning in the matching of modes between the dome and the chamber. The entire NPCC test rig is mounted on a rail. This solution was chosen to improve the alignment of the nozzles with the perforated wheel. Once alignment is achieved every element is bolted in. In case of a change in the geometry, for instance swapping a middle chamber block, the rail allows easy access the different components of the rig and also reassembling the whole system.
In order to study the acoustic damping, it was necessary find a method of excitation allowing a sudden interruption of the modulation. The half-perforated wheel (figure 3.13) can generate an acoustic mode in the domain when the perforates pass in front of the nozzles and the modulation ceases when the smooth part of the wheel passes in front of the nozzles. The smooth part half opens the nozzles to evacuate the flow at constant rate by providing a constant exhaust surface area. This design prevents any mean pressure varition during the test. Another important feature of this test facility is the possibility to change the value of the singular head loss in each injector. A close up view of the system displayed in figure 3.14 shows that a diaphragm may be placed in the injector. The size of the central perforation defines the level of the head loss. Three different diaphragms with perforation diameters lower or equal to the injection channel diameter are available. The ξ coefficient defines the head loss:

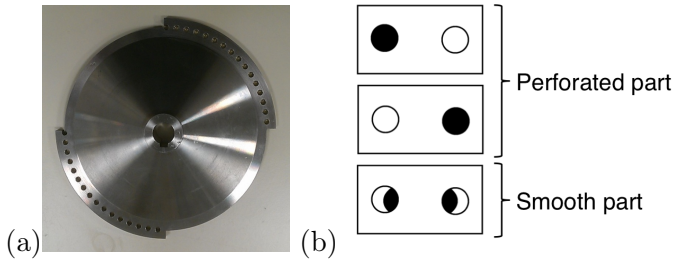

Figure 3.13: *(a) Photograph of the half perforated wheel used to study damping in the system. (b) Schematic view of the nozzles, dark means a closed nozzle, white corresponds to an open nozzle, half black means half open.*

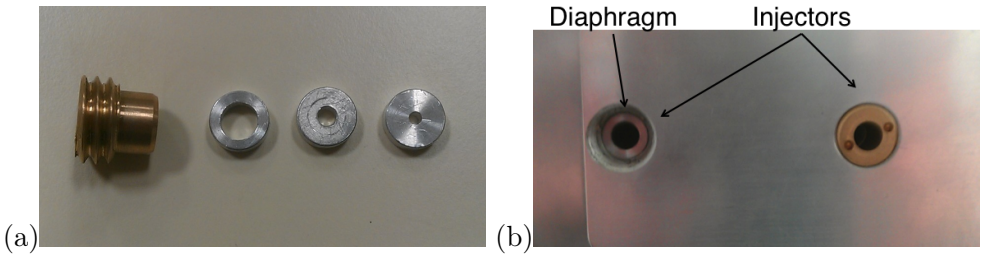

Figure 3.14: *(a) From left to right, photograph of the hollow screw and pressure loss diaphragm of 6 mm, 3 mm and 2 mm. (b) Photograph of the pressure loss device mounted in the injectors.*

$$\xi = \frac{\Delta P}{\frac{1}{2}\rho u^2} \tag{3.3}$$

Where ΔP is the pressure difference between the dome and the chamber, ρ is the density of the fluid flowing in the channel and $\bar{u}$ is the bulk inlet velocity. The head losses obtained experimentally with the different diaphragms are listed in table 3.1. Different pressure loss diaphragms can easily be manufactured for other studies.

Diameter of the diaphragm [mm]	$\Delta P/\overline{p}$ [%]	Head loss coefficient ξ [-]
6	0.04	4
3	0.3	30
2	4.8	400

Table 3.1: *Head loss coefficients corresponding to the different diaphragm diameters.*

3.4 Eigenmodes and eigenfrequencies

The eigenmodes of the system are important because they define the resonant frequencies at which the system responds with the greatest intensity. For a single box-like cavity with rigid walls equation 3.1 is sufficient to determine the eigenmodes. However, for coupled cavities the situation is much more complicated. The ramp mode of operation of the motor is well suited for the determination of the eigenmodes of the domain. The frequency of modulation is slowly increased from 0 Hz to 3000 Hz during a ramp of 99 s. As an illustration, pressure oscillations are observed at HFc1 and HFd1 (figure 3.15(a)). The recordings show a strong pressure response at few intervals during the experiment. It is then possible to determine the times of maximum response and obtain the corresponding frequencies, which characterize the different eigenmodes. The time frequency analysis shown in figure 3.15(b) also provides the eigenfrequencies of the system.
Figure 3.16 shows the temporal response of pressure sensor HFc1 during a ramp test for all head loss diaphragms. One finds that the intensity of the pressure response is diminished when the head loss is increased, especially for eigenmodes having a strong longitudinal component (1T3L$_c$ mode for example as seen in figure 3.17). The recordings in figure 3.16 indicate that the injector head loss has a notable impact on the pressure response of the system and that the effect is most perceptible when the mode has a longitudinal component. An extended analysis of these results will be presented in chapter 5.
To identify each eigenmode one can visualize the phase shift between key pressure sensors for instance HFc1, HFc2 and HFc5. Here the results of the ramp test will be compared with results provided by a numerical Helmholtz solver.

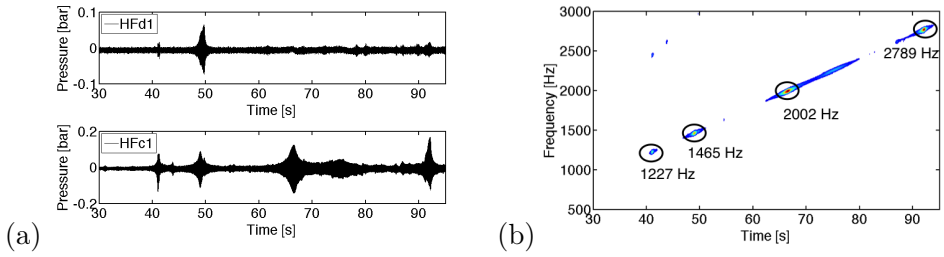

Figure 3.15: *(a) Pressure signal recorded at HFd1 and HFc1 as a function of time during a ramp test, each peak corresponds to an eigenmode in the cavity. (b) Short time Fourier transform analysis of the signal detected by HFc1.*

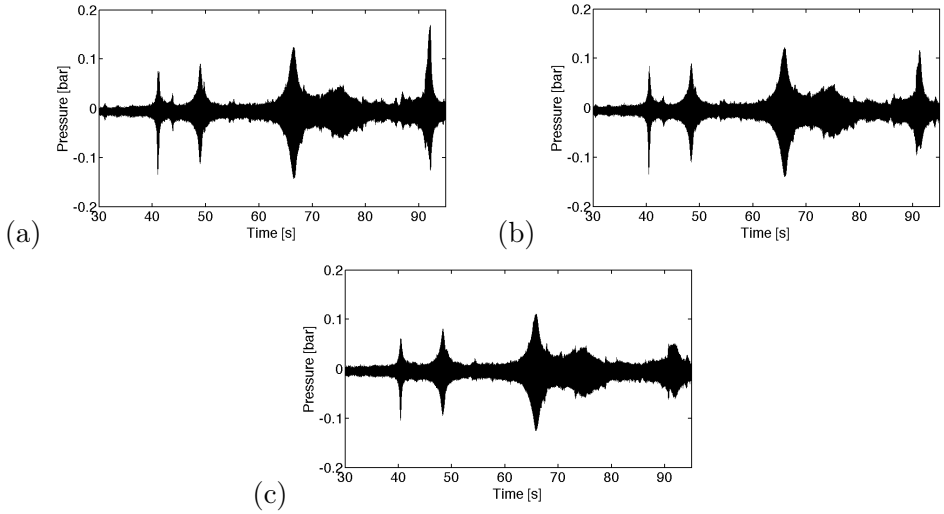

Figure 3.16: *Pressure response to a ramp recorded at HFc1 (a) for the nominal configuration ($\xi = 4$), (b) with a 3 mm diaphragm ($\xi = 30$) and (c) 2 mm diaphragm ($\xi = 400$).*

The results of the AVSP (Nicoud et al. (2007)) simulation are displayed in figure 3.17. The AVSP code is cover in section 6.4 of chapter 6. It is clear that transverse and longitudinal eigenmodes can be found for this range of frequencies. In particular the 1T1L mode of the chamber does correspond to a 1T mode in the dome. A summary of all the eigenmodes found in this experiment is displayed in table 3.2. The values deduced with the Helmholtz solver are quite close to those obtained with the ramp mode of operation.

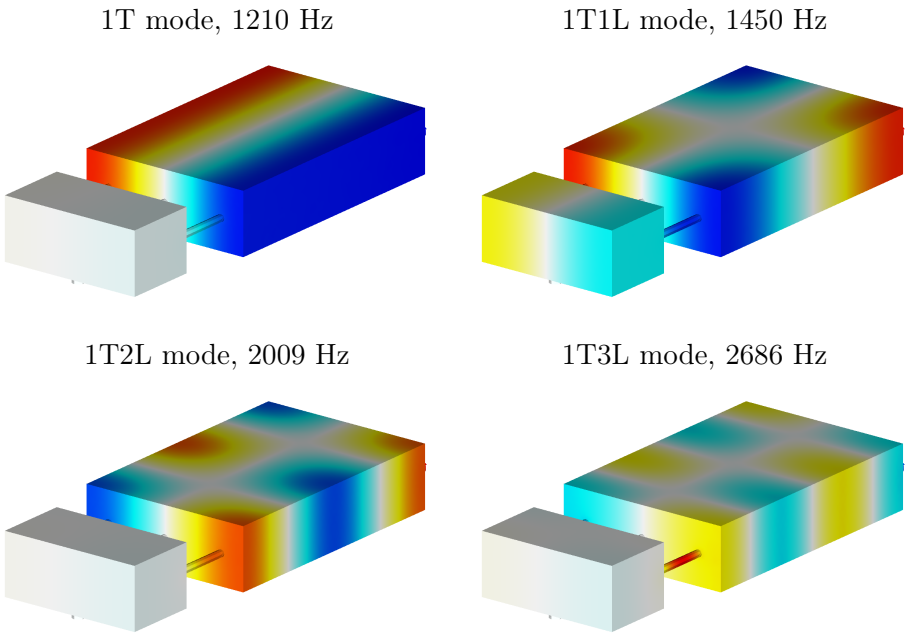

Figure 3.17: *A selected set of eigenmodes of the NPCC configuration, as found by the AVSP solver.*

Eigenmode	1T	1T1L	1T2L	1T3L
Calculated frequency [Hz]	1210	1450	2009	2686
NPCC frequency [Hz]	1227	1465	2002	2789

Table 3.2: *Eigenfrequencies obtained from AVSP and deduced from experiments on the NPCC configuration.*

The values obtained experimentally are important because they are used in subsequent studies carried out at a constant rotation rate of the VHAM in single frequency modulation experiments.

3.5 Conclusion

Issues associated with injector dynamics, coupling between dome and chamber and damping rate estimation are considered in this chapter. It is first indicated that these various aspects are not easily examined on full scale engines and that they are also difficult to extract from hot fire model scale experiments. It is then argued that these problems may be analyzed by making use of cold flow experiments. While such experiments have already been carried out at EM2C on various rigs, there was room for a new facility allowing systematic investigations. The chapter describes the new test rig designated as NPCC. This test configuration features various improvements with respect to its predecessors and in particular a modular design, a better interface between the exhaust nozzles and the rotating wheel of the VHAM modulator an easier access to the injector plate and the possibility to change the injector head losses. The addition of pressure sensors in the two cavities allows the proper determination of the acoustic mode generated by the VHAM. The mounting on a common rail adds robustness and permits a fine alignment of the VHAM wheel with the nozzles of the system. This configuration can be used to determine the global damping rate associated with each eigenmode, examine the system response, identify eigenmodes and eigenfrequencies and analyze effects induced by changes in injector head losses. These various aspects are illustrated in the next chapter.

Chapter 4

Injector impedance in the NPCC test rig

This chapter deals with the coupling between the dome and the chamber in rocket engines and also with the response of injectors to acoustic modulations. This problem is investigated experimentally by making use of the NPCC test rig. This configuration is a simplified geometry which contains several features found in rocket engines. Two cavities representing the dome and chamber are linked by three injectors. The system is modulated externally using the VHAM to excite the various resonant modes. A linear frequency sweep first unravels the modal eigenfrequencies and provides a first indication of the damping rate. The system is then modulated at the frequencies of the various eigenmodes. Pressure signals in the chamber and the dome are recorded as well as velocity fluctuations at the injector outlets. Data collected can be used to determine an injector impedance model. Head losses in the injector channels can be changed. This is accomplished by placing diaphragms of various sizes in the injectors. It is found that the injector impedance model suitably represents responses observed in the system. This model is simple enough to be used in a reduced order dynamical model description of combustion instabilities.

4.1 Introduction

It was indicated in previous chapters that the coupling between dome and thrust chamber may be of importance in the development of combustion instabilities in rocket engines. In engineering practice one tries to reduce the possibility of a coupling by setting a sufficient amount of head loss in the injection channels, typically 10 to 15% of the chamber pressure. It is important to understand the possible coupling between chamber and dome and to experimentally determine injector response to acoustic modulation. It is also important to measure changes in dissipation rate associated with injection head loss and to examine

effects of these losses on modal coupling. This investigation is carried out in the NPCC test rig described in chapter 3. The NPCC test rig comprises a dome and a chamber and it is modulated externally by the Very High Amplitude Modulator (VHAM),as briefly reviewed in section 4.2. The injector response is then analyzed by introducing a simple dynamical model (section 4.3). The validation of this model is discussed in section 4.4.

4.2 Experimental setup

The experimental configuration has been described in the previous chapter. It is here briefly reviewed. The NPCC test rig is fed with air and its internal geometry is fairly simple. It comprises two rectangular cavities coupled by three injectors. The upstream cavity corresponds to the dome or plenum while the downstream cavity represents the thrust chamber. The dome is fed with air and then it passes through the injectors inside the chamber. The air is exhausted through two nozzles. The air flow rate is periodically modulated by the Very High Amplitude Modulator (VHAM), the perforated rotating wheel. The VHAM generates high levels of pressure fluctuations in the chamber and because the nozzles are alternately blocked by the wheel this system favors transverse acoustic modes. Pressure is measured at various locations on the walls of the chamber and dome. Velocity is measured with hot wires mounted in the near vicinity of the injector outlets.
The eigenfrequencies determined for this set up are reported in table 3.2. These values serve in the rest of this study to define the rotation rate of the wheel to excite a particular mode and to perform continuous wave measurements. One fundamental question is that of the possible contribution of the injection system to the instability dynamics and the possible coupling between the chamber and the feeding manifold. It is in particular interesting to examine the injector impedance and see how the pressure loss inside an injector modifies its dynamics, changes its impedance and impacts the damping rate in the system. This investigation is carried out with the different pressure loss diaphragms defined in chapter 3.

4.3 Injector model

At this point, it is worth analyzing the injector response. This can be achieved by making use of a one dimensional representation. The resulting model may be verified using the NPCC test rig. The injector represented schematically in figure 4.1 comprises a cylindrical channel of length l and section A. The index 1 corresponds to the inlet section in the dome while the index 4 corresponds to the exhaust section in the chamber. There is a singular head loss between sections 1 and 2 as well as another singular head loss between sections 3 and 4.

Throughout this document a head loss coefficient ξ is defined by equation 4.1.

$$\xi = \frac{p_1 - p_4}{\frac{1}{2}\rho\overline{v}^2} \tag{4.1}$$

Where p_1 designates the pressure upstream of the injector, p_4 is the pressure downstream of the injector and $\overline{v}$ is the average velocity inside the injector. The system shown in figure 4.1 may be defined by the following:

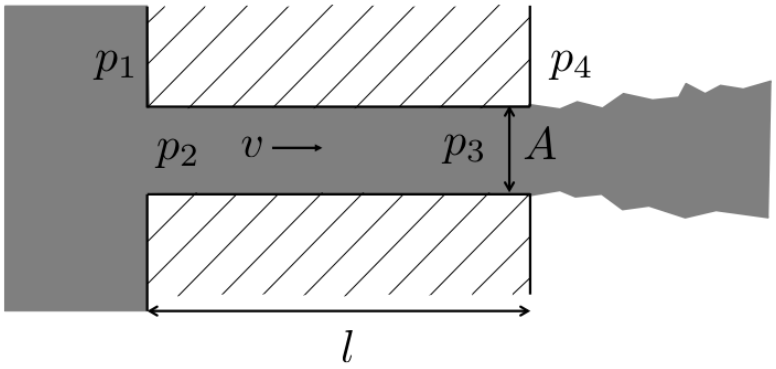

Figure 4.1: *Schematic view of an injector of the NPCC test rig. The injector has a length of l, a cross section A, the pressure in the dome is p_1, p_2 is the pressure upstream of the injector, p_3 is the pressure downstream of the injector, p_4 is the pressure inside of the chamber and v is the velocity inside the injector.*

$$p_1 - p_2 = \sigma_1 \rho \frac{v^2}{2} \tag{4.2}$$

$$p_2 - p_3 = l\rho \frac{dv}{dt} \tag{4.3}$$

$$p_3 - p_4 = \sigma_3 \rho \frac{v^2}{2} \tag{4.4}$$

Equation 4.2 represents the singular head loss between sections 1 and 2, σ_i and p_i are respectively the head loss coefficient and the pressure at section i, v is the axial injection velocity and ρ is the density. Equation 4.3 represents the momentum balance between sections 2 and 3 while equation 4.4 corresponds to the singular head loss between sections 3 and 4. It is assumed that the fluid is incompressible inside the injector, which is a valid hypothesis in rocket engines and is also verified in the present configuration which operates in the low Mach number range. Combining equations 4.2 to 4.4 together yields equation 4.5.

$$p_1 - p_4 = \xi \rho \frac{v^2}{2} + l\rho \frac{dv}{dt} \tag{4.5}$$

where ξ is the global head loss of the injector equal to the sum of the various head loss coefficients ($\xi = \sigma_1 + \sigma_3$). The density is considered to be constant,

while other quantities such as the pressure and the velocity can fluctuate and may be written as a sum of a mean value and a fluctuation:

$$\psi = \bar{\psi} + \psi' \tag{4.6}$$

Inserting this decomposition and only keeping first order terms, equation 4.5 is transformed in the following expression:

$$\frac{dv'}{dt} + \frac{\xi\overline{v}}{l}v' = \frac{p'_1 - p'_4}{l\rho} \tag{4.7}$$

This indicates that the injection velocity fluctuation is driven by the pressure difference fluctuation between the injector inlet and outlet. Equation 4.7 may be written in complex form by assuming that the fluctuating variables oscillate harmonically at an angular frequency ω. Designating the complex amplitudes with a tilde superscript one finds equation 4.8.

$$\frac{\widetilde{v}'}{\widetilde{p_1}' - \widetilde{p_4}'} = \frac{1}{\rho l}\frac{l/(\xi\overline{v})}{1 - i\omega l/(\xi\overline{v})} \tag{4.8}$$

Where $\widetilde{v}'$ is the complex amplitude of the velocity fluctuation, $\widetilde{p_i}'$ is the complex amplitude of the pressure fluctuation in the i^{th} section. One may now consider the asymptotic behavior of this equation 4.8 for low and high frequencies.

In the low frequency range, if $\omega l/(\xi\overline{v}) << 1$, and one may write

$$\frac{\widetilde{v}'}{\widetilde{p_1}' - \widetilde{p_4}'} \simeq \frac{1}{\rho\xi\overline{v}} \tag{4.9}$$

Knowing that the head loss is $\Delta\bar{p} = \bar{p}_1 - \bar{p}_4 = \xi\rho\overline{v}^2/2$, the ratio of the relative longitudinal velocity fluctuation to the relative pressure fluctuation is given by equation 4.10.

$$\frac{\widetilde{v}'/\overline{v}}{(\widetilde{p_1}' - \widetilde{p_4}')/(\overline{p_1} - \overline{p_4})} = \frac{1}{2} \tag{4.10}$$

Equation 4.9 indicates that $\widetilde{v'}$ and $(\widetilde{p'_1} - \widetilde{p'_4})$ are in phase and that the relative fluctuations in velocity and pressure are lined by a proportionality factor of $1/2$.

In the high frequency range, if $\omega l/(\xi\overline{v}) >> 1$,

$$\frac{\widetilde{v}'}{\widetilde{p_1}' - \widetilde{p_4}'} = \frac{i}{\rho l\omega} \tag{4.11}$$

which may also be cast in the form

$$\frac{\widetilde{v}'/\overline{v}}{(\widetilde{p_1}' - \widetilde{p_4}'(/(\overline{p_1} - \overline{p_4})} = i\frac{\Delta p}{\rho l\omega\overline{v}} \tag{4.12}$$

Equation 4.11 indicates that $\widetilde{v'}$ and $(\widetilde{p'_1} - \widetilde{p'_4})$ are in quadrature.
One can notice that for the head losses and the frequencies of the eigenmodes studied here, the high frequency range $(\omega l/(\xi\overline{v}) >> 1)$ is covered. This simple model will be used in what follows to reconstruct the signals recorded on the NPCC test rig. From the measured pressure difference between the dome and the chamber one may deduce a modeled velocity. This velocity is then compared to the signals recorded by the hot wire sensors.

4.4 Model validation

Before attempting to validate the model it is important to note that the complex form given in the previous section corresponds to a purely harmonic oscillation. This means that the pressure gradient inside the injector as well as the modeled velocity must have a narrow frequency spectrum around a single frequency. In order to compare the modeled velocity with the measured hot wire signals, it is necessary to filter the velocity from the hot wire measurements with a pass band filter. The high and low cut-off frequencies are chosen around the value of the modulation frequency of each case. Figure 4.2 shows typical hot wire signals before filtering. The harmonic disturbance is hidden by noise and turbulent fluctuations in the air stream. It is clear that the velocity signals need to be bandpass filtered with a central frequency equal to the modal frequency under consideration.
The high and low cut-off frequencies are chosen to lie at 200 Hz from the modulation frequency. The filtered velocities are displayed in figure 4.3. It is now visible that the velocity signal from HW1 and HW3 are indeed in opposition, which was expected since all the eigenmodes solicited have a 1T transverse component. It was expected, however, that the central hot wire (HW2) would not feature any velocity fluctuation since HW2 is located in the pressure node of the transverse eigenmodes. This was not the case in many experiments for some undetermined cause. This is why the signal from HW2 will not be displayed in most cases. The most intense response of the injection velocity is recorded for the 1T3L mode.
It can be seen in figure 4.3 that the injection velocity features a well defined harmonic oscillation in response to the modulation. This response gradually increases with the eigenmode solicited. The velocity signals from HW1 and HW3 are indeed in opposition of phase. The filtered velocity signal delivered by HW2 is not displayed in the graphs of 1T, 1T1L and 1T2L. The signal recorded by HW2 for 1T3L has a low level of harmonic oscillation. The pressure signals measured in the dome and the chamber are plotted in figure 4.4.
The pressure trace for the 1T mode features an N waveshape indicating that the modulation of this particular mode also gives rise to harmonics of the fundamental frequency. The pressure fluctuation level in the dome is negligeable except for the 1T1L mode. This corresponds to the fact that the inner dimen-

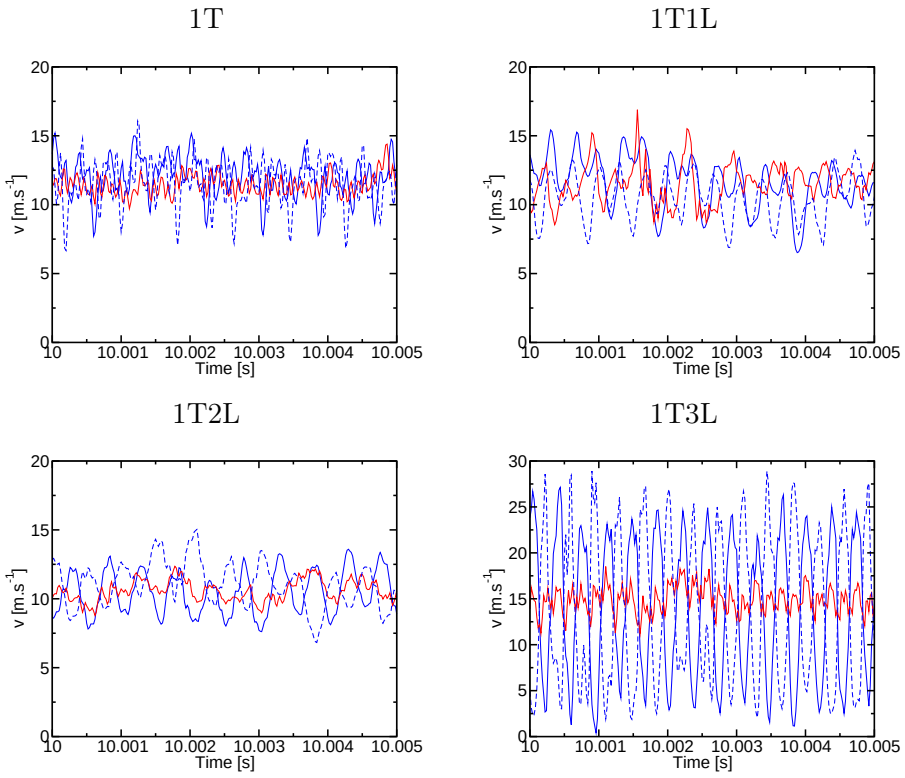

Figure 4.2: *Axial injection velocity at the injector outlets given by the hot wires.* — *Signal for HW1,* — *Signal for HW2 and* — — *Signal for HW3.*

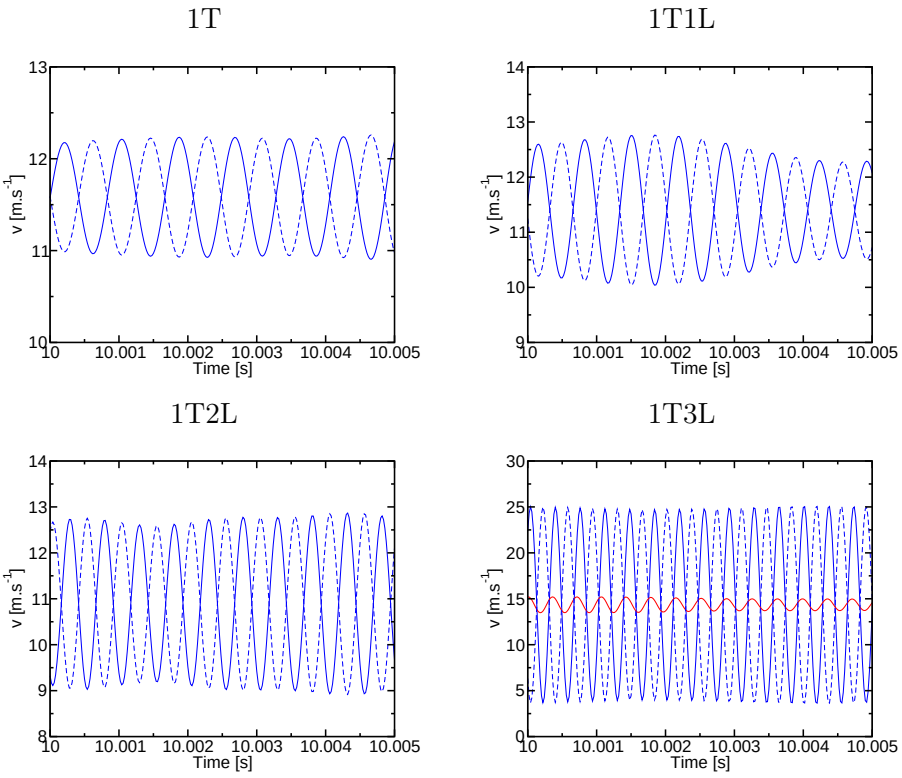

Figure 4.3: *Filtered axial injection velocity at the injecto outlets for the nominal configuration. – Signal for HW1, – Signal for HW2 and –– Signal for HW3.*

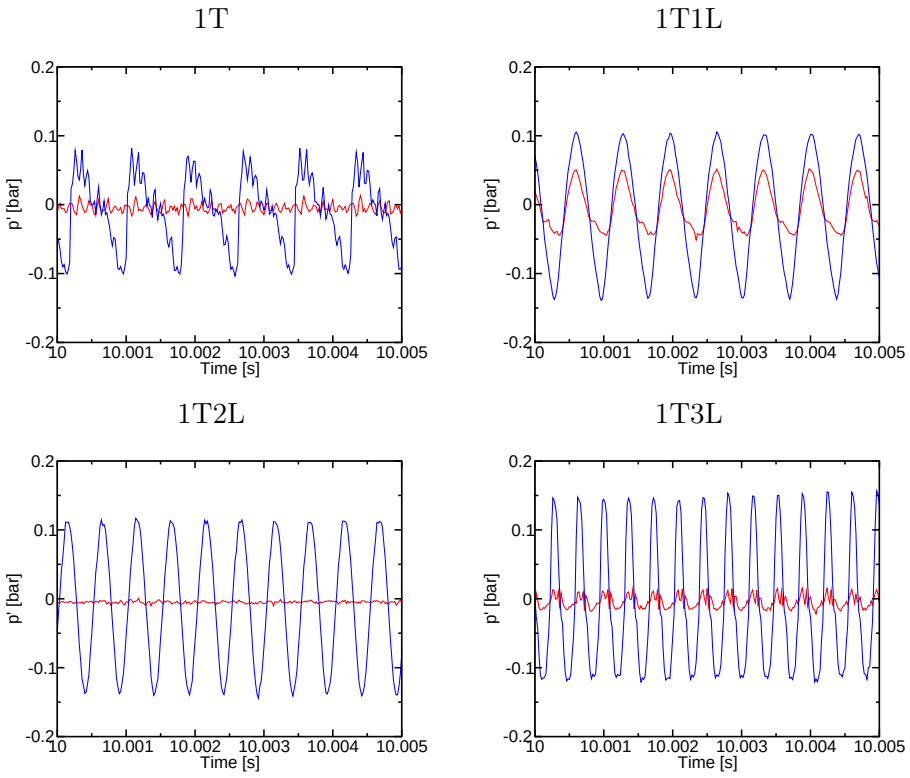

Figure 4.4: *Pressure signal for all modulation frequencies for the nominal configuration. — Signal for HFc1, — Signal for HFd1.*

sions of the NPCC test rig were chosen to ensure that the 1T mode in the dome corresponds to the 1T1L mode of the chamber. The 1T mode in the dome is shown as a red curve together with the 1T1L pressure trace detected in the chamber. One can see that the pressure fluctuations in the dome and chamber are in phase. The pressure upstream and downstream of an injector can be deduced from the signals of HFc1 and HFd1 recorded at the boundary. The amplitude is weighted by a sin function which represents the transverse distribution of pressure. Experimental signals from HFc1 and HFd1 are used in order to determine $\widetilde{p_1}' - \widetilde{p_4}'$ in equation 4.8. The complex number $\frac{1}{\rho l}\frac{l/(\xi\overline{v})}{1-i\omega l/(\xi\overline{v})}$ is then calculated. The real part of the complex velocity fluctuation $\widetilde{v}'$, given by equation 4.8 is compared to the experimental filtered velocity fluctuation measured by the injector outlets by the hot wires. The results of the modeled velocity and the filtered velocity are displayed in figure 4.5 in a case where there are no additional head losses in the injector channel ($\xi = 4$). The model fits the experimental data quite well. Not only is the amplitude well reproduced but the phase is also suitably obtained. These results tend to show that the injector dynamics is controlled by the fluctuation in the pressure difference between the injector inlet and outlet sections.

The simplified model given by equation 4.8 depends on the pressure loss coefficient ξ (table 3.1). It is natural to verify the model for different value of the pressure loss coefficient. Inside the injectors, the nominal pressure loss diaphragm (which defines the nominal configuration) is replaced by a 3 mm in diameter orifice, which corresponds to a pressure loss coefficient ξ of 30. The eigenmodes 1T, 1T1L, 1T2L and 1T3L are generated with the VHAM and pressure and velocity are recorded simultaneously. The filtered velocity signals are displayed in figure 4.6 and the pressure fluctuations in the dome and chamber are displayed in figure 4.7.

By comparing the levels of velocity fluctuation corresponding to a given mode to that obtained in the nominal configuration (figure 4.3), one notices that the oscillation amplitude is reduced when the pressure loss in the injector is increased. For example the peak to peak amplitude of oscillation of the injection velocity for 1T3L decreases from 20 $\mathrm{m.s^{-1}}$ to 15 $\mathrm{m.s^{-1}}$. The pressure fluctuations for a head loss coefficient of $\xi = 30$ are displayed in figure 4.7.

The pressure fluctuations signals are similar to those obtained in the nominal configuration and the amplitude of oscillation for 1T, 1T1L and 1T2L are of the same order of magnitude as those recorded in the nominal configuration. However the amplitude of 1T3L is notably reduced. These results suggest that the pressure loss diaphragms effectively damp modes with a higher order longitudinal modal structure. The comparison between experimental and modeled velocity fluctuation for this configuration is shown in figure 4.8.

The agreement between modeled and experimental velocity is quite good, the amplitude and phase of the velocity is well retrieved. One more head loss diaphragm is available and induces a head loss coefficient of $\xi = 400$ (pressure

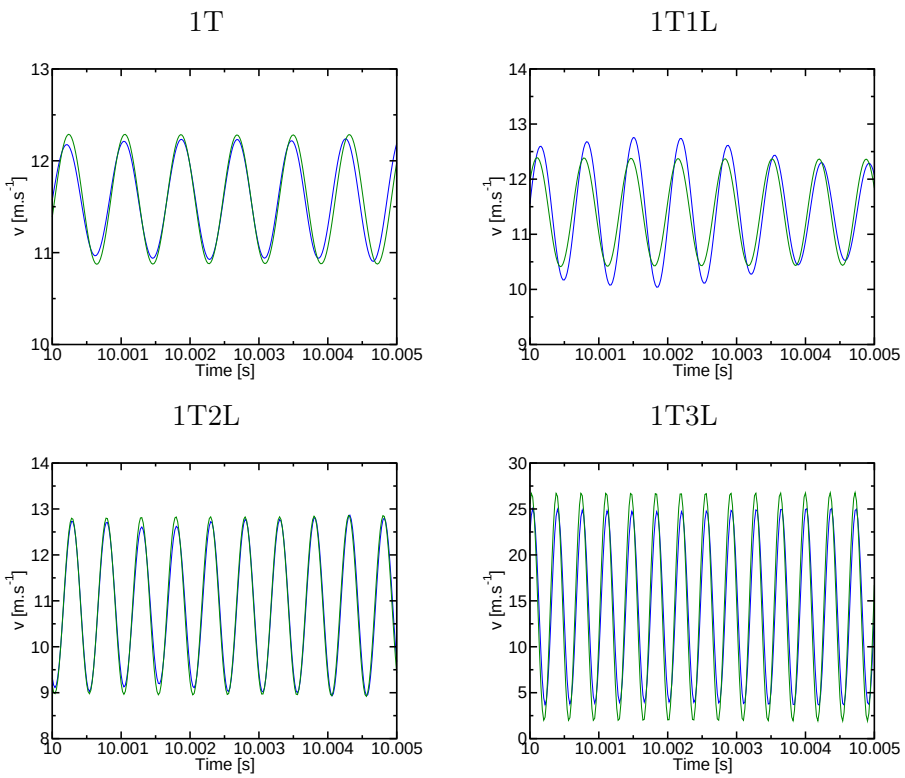

Figure 4.5: *Comparison between the filtered velocity and the modeled velocity for the nominal configuration.* — *Modeled injection velocity,* — *Experimental injection velocity.*

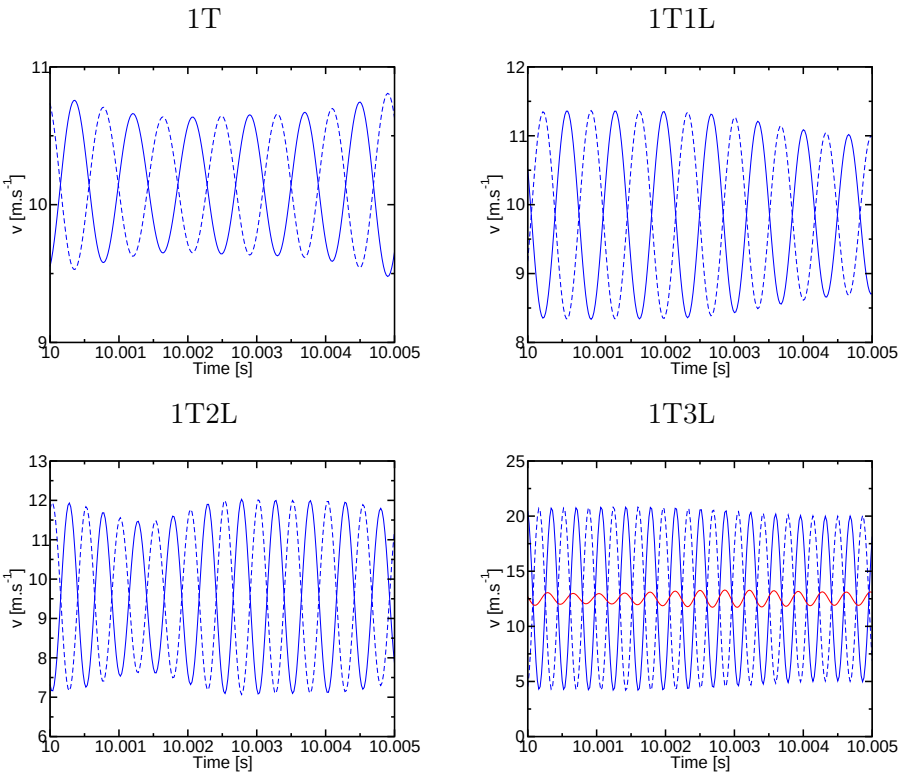

Figure 4.6: *Filtered injection velocity given by the hot wires for a head loss of 30.* — *Signal for HW1,* — *Signal for HW2 and* — — *Signal for HW3.*

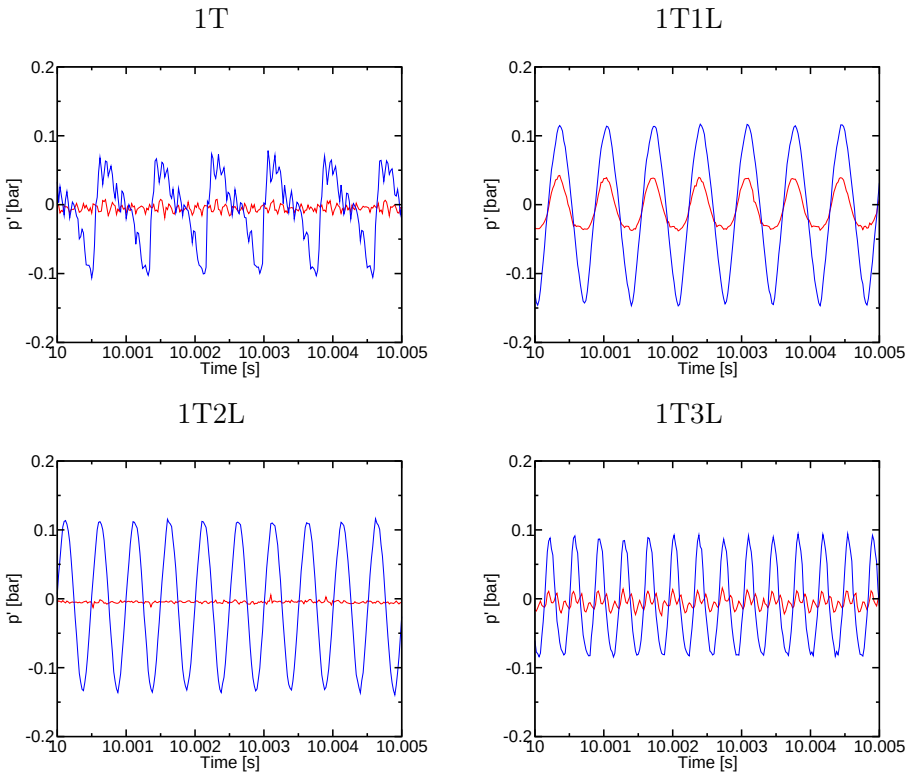

Figure 4.7: *Pressure signal for all modulation frequencies for a head loss of 30. – Signal for HFc1, – Signal for HFd1.*

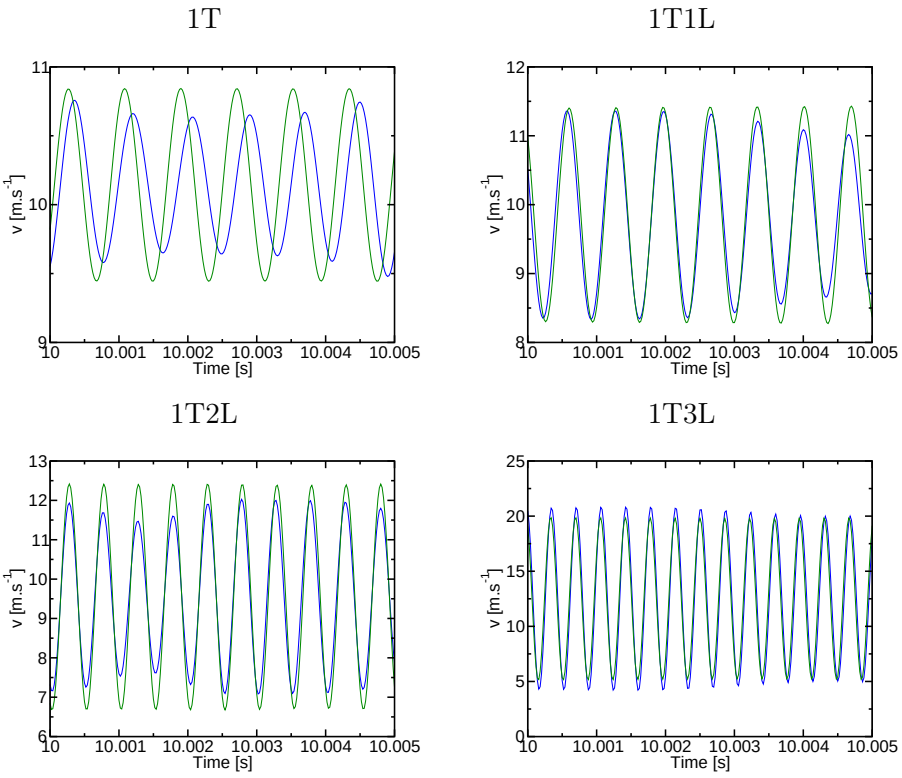

Figure 4.8: *Comparison between the filtered velocity and the modeled velocity for a head loss of 30. — Modeled injection velocity, — Experimental injection velocity.*

loss diaphragms of 2 mm), this last pressure loss diaphragm will serve as a confirmation of the injector response. Figure 4.9 displays the velocity for all four modes for this case.

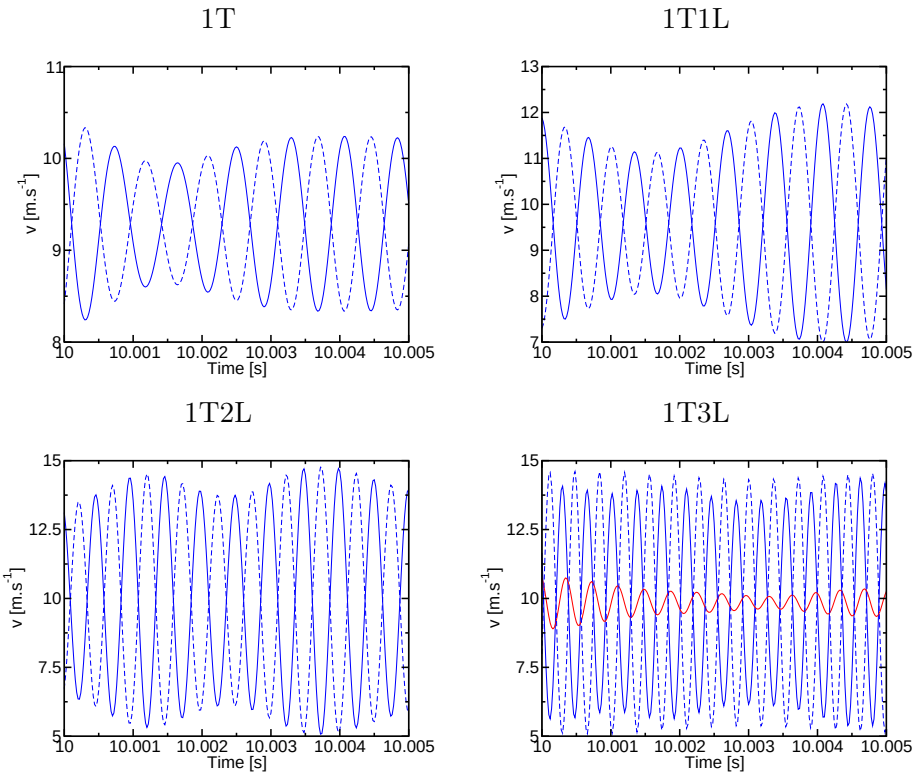

Figure 4.9: *Filtered injection velocity given by the hot wires for a head loss of 400.* – *Signal for HW1,* – *Signal for HW2 and* –– *Signal for HW3.*

By comparing the signals recorded for the various eigenmodes to their counterparts corresponding to lower values of the head loss coefficients it is clear that the amplitude of the velocity fluctuation is diminished. The 1T3L eigenmode has the most visible amplitude decrease in velocity amplitude; from a 20 m.s^{-1} peak to peak amplitude fluctuation in the nominal configuration it drops to a level of 10 m.s^{-1} peak to peak fluctuation. This strong reduction is also visible in the pressure fluctuation (figure 4.10).
The pressure fluctuation for eigenmodes 1T to 1T2L remain at a constant value for all pressure loss coefficients. However the 1T3L responds quite strongly to the head loss in the injector. From an amplitude of 0.25 bar in the nominal configuration it decreases to 0.05 bar with a head loss coefficient of 400. This reduction indicates that the pressure loss diaphragms are particularly effective when the modes have a higher order longitudinal component. This is reminiscent of the fact that nozzles essentially damp longitudinal modes (Marble and Candel (1977)).

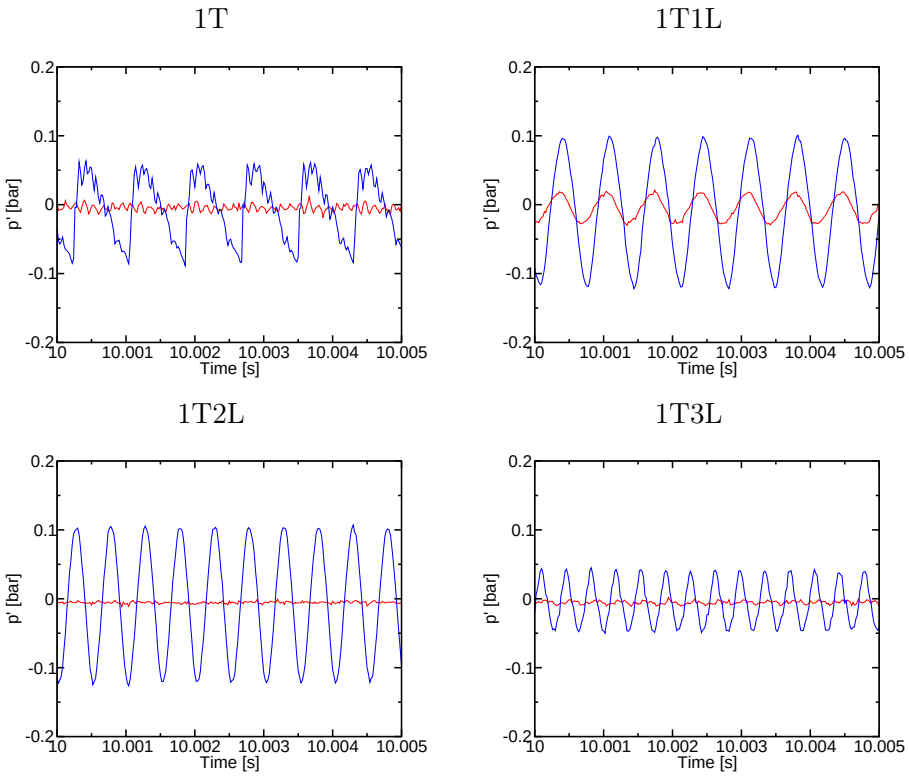

Figure 4.10: *Pressure signal for all modulation frequencies for a head loss of 400.* — *Signal for HFc1,* — *Signal for HFd1.*

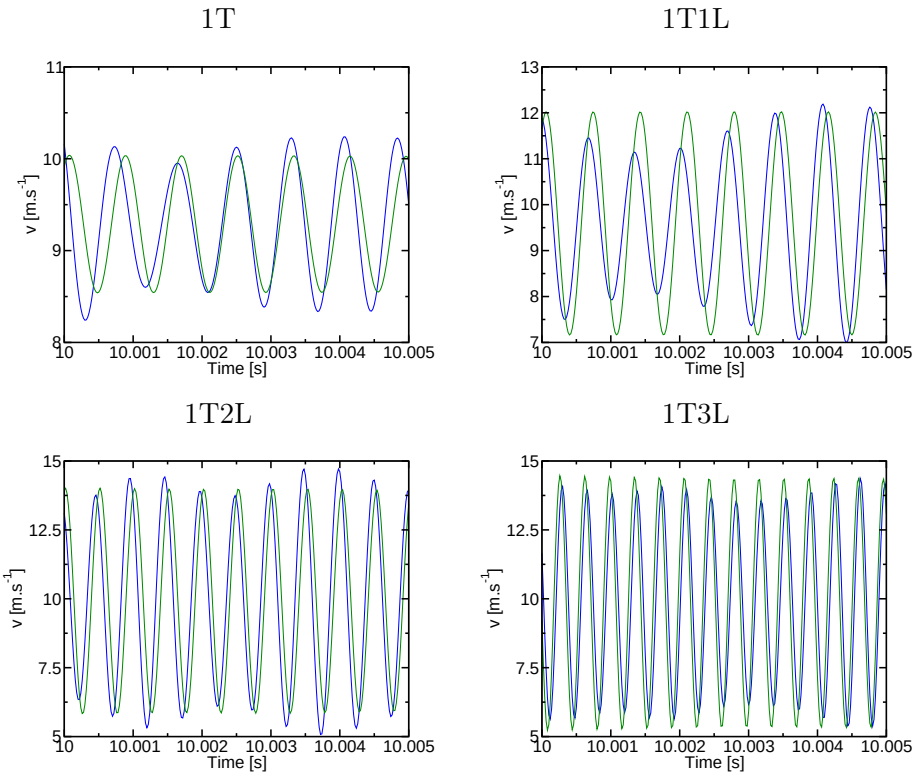

Figure 4.11: *Comparison between the filtered velocity and the modeled velocity for a head loss of 400. — Modeled injection velocity, — Experimental injection velocity.*

Figure 4.11 displays experimental and modeled velocity signals. Even for a high head loss in the injectors, the model suitably retrieves the velocity fluctuations at the exit of the injectors.
The agreement between the values calculated with the model (equation 4.8) and those obtained by the experimental measurements is quite satisfactory (figures 4.5, 4.8 and 4.11) especially taken into account that the two methods are different and totally independent. The small differences observed between the two can be attributed on the one hand, to the model approximations and on the other hand, the variability of the experimental measurements.

4.5 Conclusions

The NPCC test rig is used in this chapter to investigate the injector response acoustic modulation. The injector dynamics is characterized by measuring the velocity fluctuation at the injector outlets and the fluctuation of the pressure differences between the dome and the chamber. The data is then used to validate a simple dynamical model that provides the velocity fluctuation induced by the pressure difference acting on each injector. This model can be integrated in a reduced order dynamical model and then used to represent perturbations induced by pressure oscillations in the mass flow rates of propellants.

Chapter 5

Acoustic damping in coupled cavities

Combustion oscillations are naturally damped by dissipative processes. The damping rate characterizes the strength of this dissipation and its inverse can be defined as the time required to divide the amplitude of oscillation by an amount equal to $e = 2.718$. Damping depends on the geometry of the system, on the operating conditions, on the flow structure inside the domain and on the acoustic mode type. The values of the damping rate and characteristic time are not easily deduced from theory because dissipation arises from a range of processes some of which are not well identified. Under these circumstances it is useful to get some orders of magnitude from well controlled experiments. This is accomplished by making use of the cold flow NPCC experiment. The damping rates are determined for several injector configurations and different modal structures. Results reported in the present chapter indicate that modes featuring a longitudinal structure exhibit greater damping rates than purely transverse modes. Experiments also indicate that the damping rates of such modes are increased when the head loss in the injection channel is augmented. Damping by the nozzle acts mainly when the mode has a longitudinal component and the head losses inside the injection system often correspond to dissipation induced by a diaphragm. This indicates that purely transverse modes are more susceptible to couple acoustics and combustion and to sustain an unstable oscillation.

5.1 Introduction

The wave equation governing pressure fluctuations in a reactive flow features driving and damping terms (see chapter 6). The driving mechanisms tend to increase the pressure oscillation amplitude whereas the damping processes tend to reduce the amplitude of the oscillations. It is difficult to identify all

the mechanisms leading to damping. Damping may be caused by a number of phenomena. In a rocket engine these are thermal, viscous, turbulent dissipation mechanisms and energy transport driven out of the geometric domain across the nozzle, which is commonly referred to as admittance. Admittance has been extensively studied theoretically and experimentally (Tsien (1952b); Crocco (1952); Crocco et al. (1961); Buffum et al. (1966); Culick and Dehority (1969)) and it is still today the subject of ongoing investigations. Thermal dissipation is the process by which a part of acoustic energy is converted into thermal energy, which in turn is transferred to the walls of the chamber. Thermal dissipation has been studied in many fields. One of the first papers dealing with thermal dissipation in acoustic cavities was that of Nielsen (1949). The experimental investigation by Lambert (1953) addressed different aspects of internal dissipation separately including thermal dissipation. More recently, the paper by Searby et al. (2008) provides a comprehensive review of the theory including acoustic absorbers. Viscous dissipation is the component of the damping of acoustic oscillations due to resistance in the flow. Stokes (1868) and Kirchhoff (1868) established the basis for acoustic motions due to the viscosity of the medium. This mode of dissipation has been extensively studied (Tang et al. (1973); Tong and Sirignano (1986); Oschwald et al. (2008)). The work of Searby et al. (2008) provides a good fundamental description of viscous dissipation in the boundary layer and provides the basis of its application to acoustic resonators. Jet and turbulent dissipation is the dissipation of the acoustic energy contributing to the damping by the formation of vortices, which dissipate energy through transport out of the domain or through viscous dissipation. In the work of Searby et al. (2008) resonator theory is used and the jet dissipation is addressed by the application of a resistant boundary layer at the resonator exit. Damping is a complex process, which on a scale of a combustion chamber, is difficult to predict and analyze. It is generally considered that the determination of the damping rate requires experimental testing (Schuller et al. (2003); Oschwald et al. (2008)). This is the approach that has been adopted in this work.
The experimental work has been carried out with the NPCC test rig described in chapter 3. The experimental methodology is briefly described in section 5.2. Damping rates are then obtained for the nominal configuration (section 5.3). Effects of head losses in the injector channels are described in section 5.4 and the data gathered in these experiments are discussed.

5.2 Damping determination methodology

Head loss diaphragms are used in order generate different pressure losses in the three injectors of the test rig (figure 3.14 and table 3.1). The NPCC test rig is modulated by the VHAM with a semi-perforated wheel (figure 3.13). The semi-perforated wheel can generate a pressure modulation inside the domain

and then suddenly stop the modulation so that the pressure fluctuations can be naturally be damped by the test rig. A sensor, located near the chamber backplane at HFc1 (figure 3.6), records the pressure signal induced by the modulation of the VHAM.
The system can be described by a second order oscillator (see chapter 6 for an analysis based on a modal expansion of the pressure field). When the perforations modulate the nozzles, the system is driven and the amplitude increases up to a certain level. This happens during the first half of a wheel rotation. During the second half, the wheel has no perforations and the two nozzles are half open and there is no modulation. During that period, the dynamics is that of a second order system with no forcing. This can be written in the form:

$$\ddot{\eta}(t) + 2\alpha\dot{\eta}(t) + \omega^2\eta(t) = 0 \tag{5.1}$$

where η is the amplitude of the pressure fluctuation based on modal projection (see chapter 6), α is the damping rate and ω is the angular frequency corresponding to one of the eigenmodes of interest.
The analytical solution of the differential equation 5.1 is given in equation 5.2.

$$\eta(t) = e^{-\alpha t}\left(a\exp[it(\omega^2-\alpha^2)^{1/2}] + b\exp[-it(\omega^2-\alpha^2)^{1/2}]\right) \tag{5.2}$$

Where a and b are integration constants. The entire pressure amplitude is multiplied by $e^{-\alpha t}$ indicating that the pressure signal is bounded by an exponential function decreasing at a rate fixed by α that is the damping rate. The approach in this work consists in determining the damping rate α by experimental means as stated previously by using the NPCC test rig.
Records of pressure detected by the acoustic sensor take the form of periodic oscillations containing two main parts: the generation of the acoustic modulation and the subsequent relaxation. The analysis of these recordings allow the determination of the damping rates. During the relaxation of the pressure oscillations the envelope of the signal is $ce^{-\alpha t}$ (figure 5.1(a)). It is possible to evaluate the damping rate by taking the neperien logarithm of the envelope of the damped oscillation, plotting them as a function of time and reading the slope (figure 5.1(b)). This method will be referred to as the relaxation method.
Another method for the determination of the damping rate consists in estimating the size of the eigenmode peaks during a ramp test displayed in figure 3.16. This method, called Full Width at Half Maximum (FWHM), applies to the graphs of energy spectra, which are in the form of P^2. This method, when translated to temporal graphs of pressure, is equivalent to measuring the width at $P_{max}/\sqrt{2}$. The quality factor Q is defined by:

$$Q = \frac{f_0}{\Delta f} \tag{5.3}$$

where f_0 is the resonant frequency and Δf is the FWHM. The quality factor

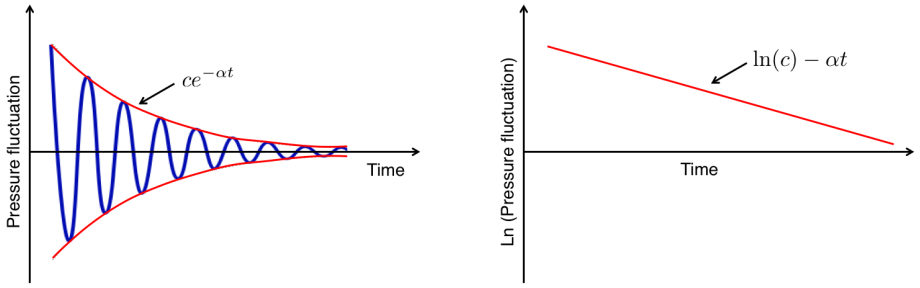

(a) (b)

Figure 5.1: *(a)Schematic view of the damping of pressure oscillations. – Pressure signal at HFc1, – envelope of the pressure signal at HFc1.(b) Schematic view of the logarithm of the envelope of the pressure signal.*

Q is linked to the damping rate α (Siebert (1985)) of equation 5.1 by:

$$2\alpha = \frac{2\pi f_0}{Q} \tag{5.4}$$

Figure 5.2 shows how one can determine the damping rate from the pressure signal from a ramp. During all ramp tests, the frequencies were swept from 0 Hz to 3000 Hz in 99 s. This means that the product of time by 3000/99 gives an estimate of the modulation frequency generated by the VHAM. The damping rate α can then be estimated by equation 5.5 knowing $\Delta t = t_2 - t_1$ from figure 5.2.

$$\alpha = \pi \Delta t \frac{3000}{99} \tag{5.5}$$

5.3 Results and analysis for the nominal configuration

The first case to be studied corresponds to the nominal configuration of the NPCC test rig that is: no head loss diaphragms in the injectors and a head loss coefficient of $\xi = 4$. The semi-perforated wheel is mounted on the VHAM and the modulation is to be set to cover the frequencies of 1T, 1T1L, 1T2L and 1T3L modes of the NPCC test rig. The operating absolute pressure is 3.5 bars and the total mass flow is 3.1 g.s^{-1}. It has to be remembered that in a standing wave field, the pressure sensors have to be positioned in pressure anti-nodes, where the amplitude of oscillation is maximum. The 1T, 1T1L, 1T2L and 1T3L modes that can be generated by the VHAM feature a pressure anti-node at the positions HFc1 and HFc2 (figure 3.17). Therefore, the recording of the pressure signal is done at the position HFc1 for all experimental cases. The recording is carried out during one minute at a sampling frequency of 50 kHz.
Signals recorded at the position HFc1 are displayed in figure 5.3. The roughness in the signal waveform can be attenuated by applying a low pass filter to the

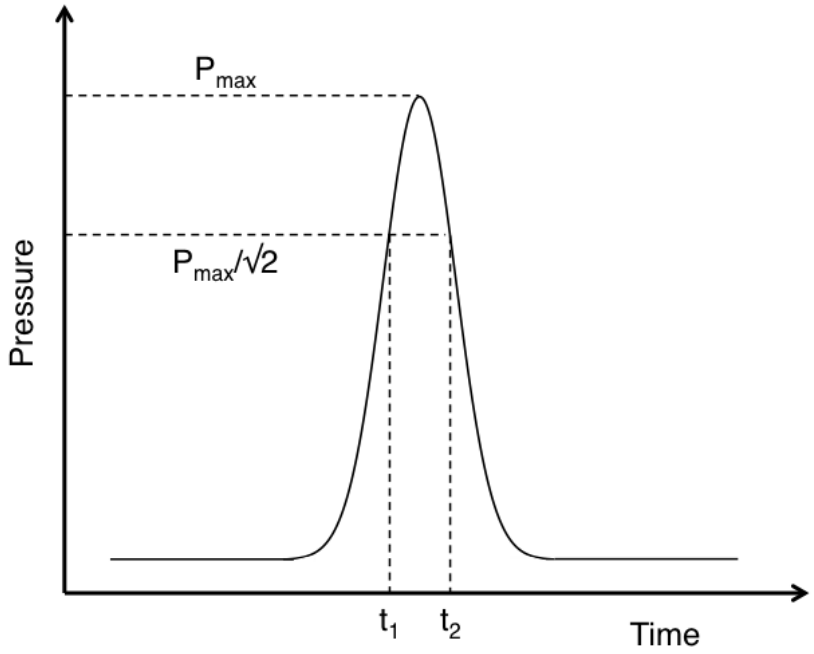

Figure 5.2: *Schematic view of a peak in the temporal pressure signal when the NPCC test rig is submitted to a ramp.*

different waveforms with a cut-off frequency chosen to be above the modulation frequency and below the value of the next eigenfrequency.
The pressure signals at HFc1 are generally similar. They all show periodic wave trains. In each of the pressure bursts, the signal first grows, reaches a maximum and decays to a minimum value. This sequence is repeated and corresponds to the passage of the perforations in front of the nozzles followed by the passage of the smooth part of the wheel. During this second phase, the oscillations induced in the system are naturally damped and the acoustic level drops down. The values of the damping rates are obtained as explained previously by calculating the slope of the envelopes. For each mode, the damping rates are determined for several decreasing slopes. The average values of the damping rates obtained for the nominal configuration as well as the standard deviation of the damping rates are displayed in table 5.1.

Mode	1T	1T1L	1T2L	1T3L
Damping rate [s^{-1}]	36	85	61	101
N - σ [%]	30 - 4	30 - 3	30 - 4	30 - 4

Table 5.1: *Damping rates of four modes with their standard deviation for the NPCC test rig in the nominal configuration ($\xi = 4$). N is the number of slopes used for the determination of the damping rates and σ is the relative standard deviation in percentage.*

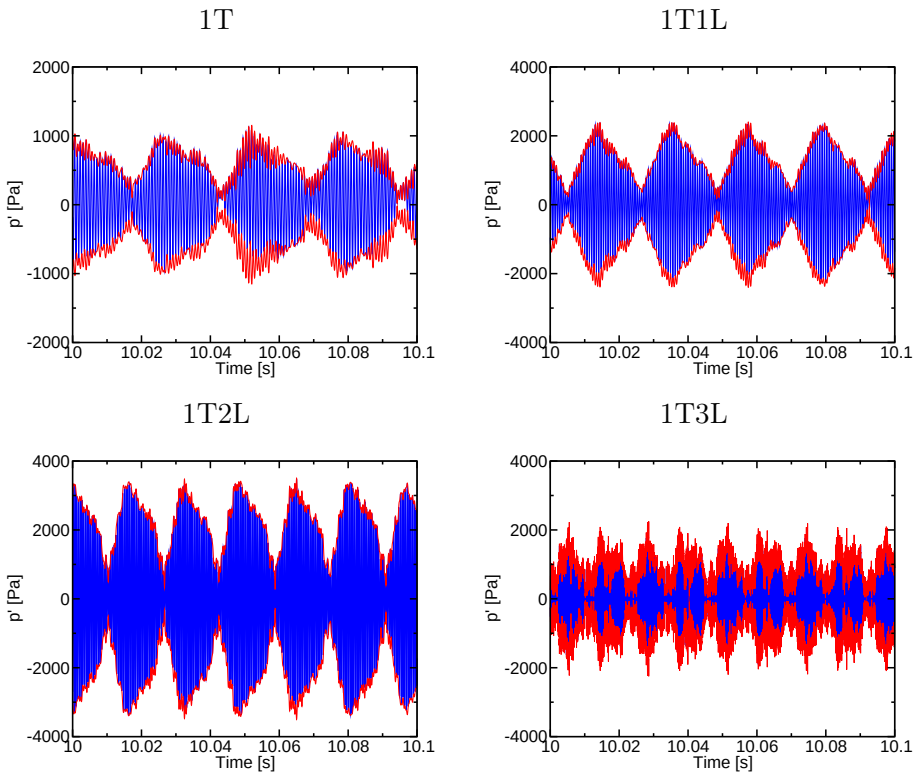

Figure 5.3: *Filtered pressure signal at HFc1 for four different modes without any additional head loss ($\xi = 4$).– Pressure signal at HFc1, – envelope of the pressure signal at HFc1.*

It can be seen that the method exhibits good repeatability since the relative standard deviations are equal to 4% or lower. The damping rate of the 1T mode is the lowest of all the modes investigated. This is not surprising since the only dissipation mechanisms for this mode are thermal and viscous dissipation at the boundary layer. The other three modes have a longitudinal component in the direction of the nozzles that contributes to the dissipation of energy. The stronger the longitudinal component the higher the damping rate. There is an exception, however, with the 1T1L mode which is the only one coupled with an eigenmode of the dome (figures 3.15 and 3.17).
The results of the other method tested, using variable modulation frequencies through a ramp, are displayed in table 5.2. Only a few ramp runs were carried out. The reduced number of runs for this method do not allow to carry a proper statistical analysis. As an indication differences between results has been reported in table 5.2.

Mode	1T	1T1L	1T2L	1T3L
Damping rate [s^{-1}]	34	36	101	54
N - Δ [%]	3 - 28	3 - 50	3 - 11	3 - 9

Table 5.2: *Damping rates of four modes and the maximum difference between calculated damping rates of the NPCC test rig in the nominal configuration ($\xi = 4$) using a ramp. N is the number of runs used for the determination of the damping rates and Δ is the maximum difference between calculated damping rates.*

This method exhibits a certain level of scatter and only the damping rate for the 1T mode is close to the value obtained with the relaxation method.

5.4 Influence of head losses

It is possible to change the head loss in the injector channels by inserting diaphragms of different sizes. The three-millimeter in diameter diaphragm corresponds to a head loss coefficient $\xi = 30$. Figure 5.4 shows the low pass filtered pressure signals detected at HFc1 for 1T, 1T1L, 1T2L and 1T3L.
Table 5.3 shows the values of the damping rates determined in this configuration.

Mode	1T	1T1L	1T2L	1T3L
Damping rate [s^{-1}]	39	77	65	143
N - σ [%]	30 - 6	30 - 4	30 - 5	30 - 4

Table 5.3: *Damping rates of four modes with their standard deviation for the NPCC test rig with 3 mm diaphragms ($\xi = 30$). N is the number of slopes used for the determination of the damping rates and σ is the relative standard deviation in percentage.*

Table 5.4 shows the results obtained with the ramp method for this configura-

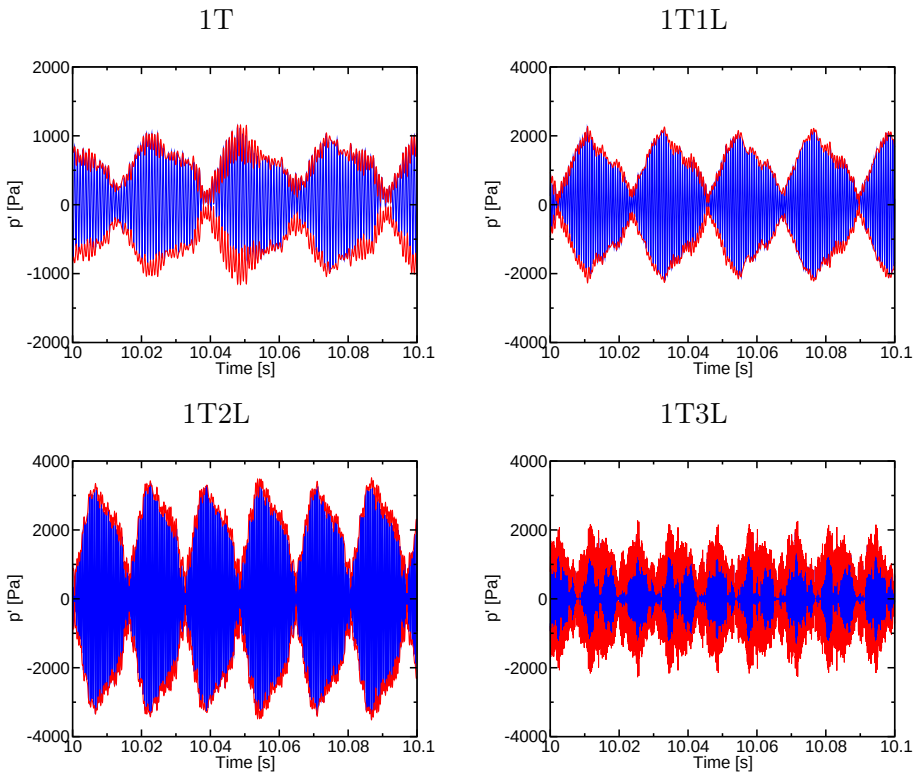

Figure 5.4: *Filtered pressure signal at HFc1 for four different modes with 3 mm diaphragms ($\xi = 30$).– Pressure signal at HFc1, – envelope of the pressure signal at HFc1.*

tion.

Mode	1T	1T1L	1T2L	1T3L
Damping rate [s^{-1}]	32	38	108	80
N - Δ [%]	3 - 32	3 - 44	3 - 5	3 - 36

Table 5.4: *Damping rates of four modes as well as the maximum difference between calculated damping rates of the NPCC test rig with 3 mm diaphragms ($\xi = 30$) using a ramp. N is the number of runs used for the determination of the damping rates and Δ is the maximum difference between calculated damping rates.*

The pressure recordings at HFc1 for the two-millimeter in diameter diaphragms, corresponding to a head loss coefficient of $\xi = 400$, are displayed in figure 5.5. Table 5.5 shows the values of the damping rates determined in this configuration with the relaxation method and table 5.6 the corresponding results using the ramp method.

Mode	1T	1T1L	1T2L	1T3L
Damping rate [s^{-1}]	42	72	83	187
N - σ [%]	30 - 5	30 - 3	30 - 5	30 - 2

Table 5.5: *Damping rates of four modes with their standard deviation for the NPCC test rig with 2 mm diaphragms ($\xi = 400$). N is the number of slopes used for the determination of the damping rates and σ is the relative standard deviation in percentage.*

Table 5.6 shows the results obtained with the ramp method for a head loss of $\xi = 400$.

Mode	1T	1T1L	1T2L	1T3L
Damping rate [s^{-1}]	34	44	107	171
N - Δ [%]	3 - 12	3 - 45	3 - 7	3 - 8

Table 5.6: *Damping rates of four modes as well as the maximum difference between calculated damping rates of the NPCC test rig with 2 mm diaphragms ($\xi = 400$) using a ramp. N is the number of runs used for the determination of the damping rates and Δ is the maximum difference between calculated damping rates.*

In figure 5.6 are plotted the damping rates versus the head loss coefficient for the relaxation method.
From figure 5.6 it can be seen that in general the damping rate increases with the head loss coefficient. In addition it can be seen that the higher the longitudinal component of the mode, the higher the damping rate. This is particularly noticeable for high head losses. For lower head losses the 1T1L mode, coupled with the dome, does not follow the general trend and its damping rate is higher than the damping rate of 1T2L. This could be explained by the fact that the coupling between the cavities offers an extended domain for the dissipation of

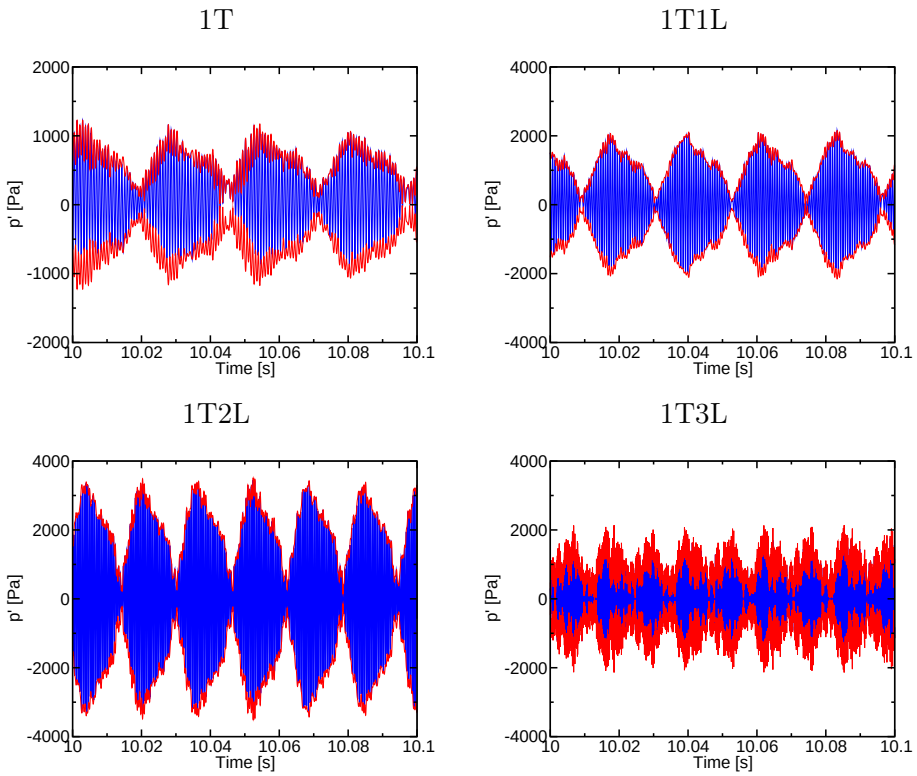

Figure 5.5: *Filtered pressure signal at HFc1 for four different modes with 2 mm diaphragms ($\xi = 400$).– Pressure signal at HFc1, – envelope of the pressure signal at HFc1.*

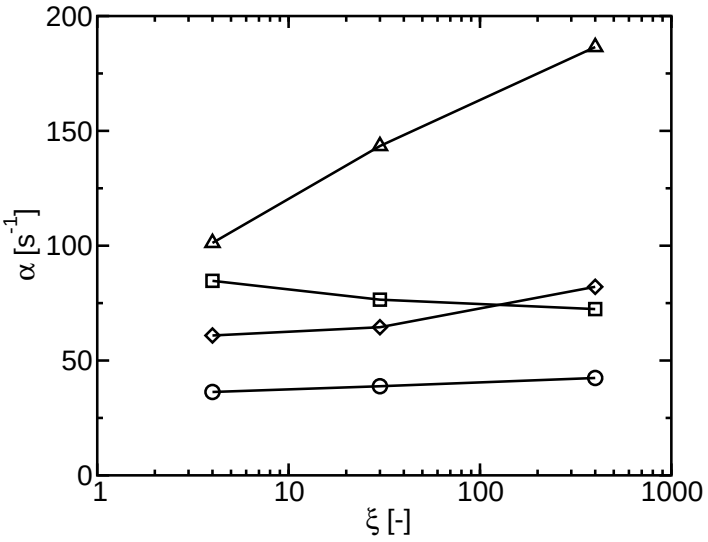

Figure 5.6: *Evolution of the damping rate with the head loss coefficient for ◯ 1T, □ 1T1L, ◊ 1T2L and △ 1T3L obtained with the relaxation method.*

energy. However as head losses increase, the coupling is weakened and at the highest value of the head loss coefficient, the 1T1L mode retrieves the expected general trend.

In figure 5.7 are plotted the damping rates versus the head loss coefficient for the ramp method.

For high values of head losses the expected trend for the different modes is observed, that is the higher the longitudinal component, the greater the damping rate. However for lower head loss coefficients some inconsistencies can be seen. For example the effect of the coupling of the 1T1L mode to the dome does not emerge from the results of this method. Another unexpected result, again for lower head losses, is the poor damping of the 1T3L mode. Though, with the ramp method, the order of magnitude of the damping rates is preserved in comparison to the relaxation method, the inconsistency of some results, particularly at low head losses, remain unexplained. It has to be said that this method, based on the width of the peaks of the pressure response to a ramp, incorporates several frequencies around the frequency of interest (the frequency of the eigenmode) and this may be a source of error. In addition the ramp method exhibits poor repeatability (tables 5.2, 5.4 and 5.6). The ramp method could perhaps be improved by employing a reduced rate of frequency sweep around the mode of interest.

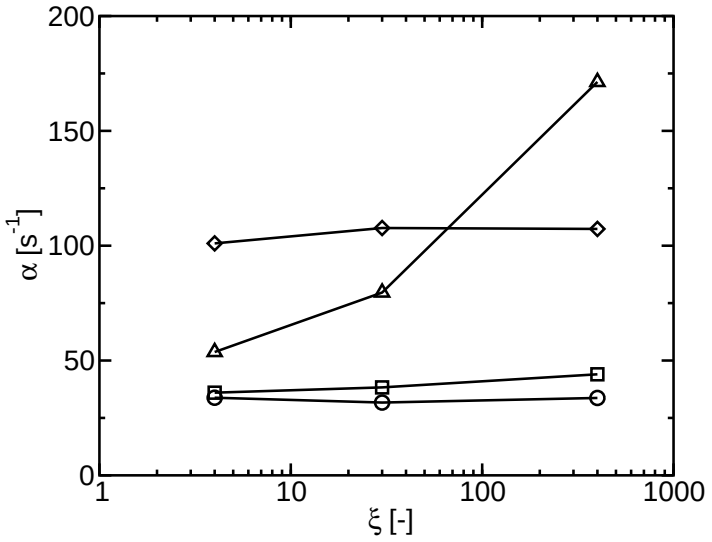

Figure 5.7: *Evolution of the damping rate with the head loss coefficient for ◯ 1T, □ 1T1L, ◇ 1T2L and △ 1T3L obtained with the ramp method.*

5.5 Conclusion

The damping rate plays an important role in the analysis and control of combustion instabilities. Damping of acoustic modes results from dissipation processes and from impedance effects at the boundaries of the system. There are a few processes that allow an analytical estimation of the damping rate but this is not an easy task for all the dissipative mechanisms. The experimental approach adopted here allowed the determination of the damping rates for four eigenmodes of the system. The increase of the damping rate with the head loss coefficient was retrieved as expected. The effect of the coupled 1T1L mode has been revealed showing the behavior of the coupling between cavities for a selected mode. The relaxation method has proved to be robust and exhibits good repeatability. The ramp method, on the other hand, seems less virtuous, failed to predict the evolution of the coupled mode and gave inconsistent results particularly at low head loss levels.

Part III

Reduced order dynamical modeling of combustion instabilities

Large eddy simulations carried out in the first part and experiments reported in the second part of this document are used to provide sub models for the reduced order dynamical description of instability code STAHF. The fundamental principles of this software are first reviewed. The central idea is to use a modal expansion to represent the pressure field. The amplitudes of the various modes are then obtained from a set of second order differential equations. The STAHF code comprises several modules, which represent the different source terms appearing in the right hand side of these differential equations. It is possible to modify these various modules to take into account progress made in the understanding and modeling of the various processes intervening in the problem of combustion instabilities. The code STAHF is partially verified by making use of experiments carried out in the NPCC test rig. It is then used to analyze unstable combustion in a small rocket engine model designated as the BKD and operated by DLR. It is shown that the code retrieves stable and unstable regimes observed experimentally but it is also observed that this requires an adjustment of the damping rates used for the different eigenmodes of the system.

Chapter 6

Principles of reduced order modeling

This chapter deals with the principles of reduced order modeling based on a modal expansion. In this framework, the amplitudes of the different modes are determined by a set of differential equations deduced from the wave equation. The state of the system is then defined by first determining the eigenfrequencies and eigenmodes of the system by making use of a Helmholtz solver. The modal amplitudes are then determined by integrating the differential system. The pressure field is obtained by weighting the normal modes by the modal amplitudes. A central issue in this procedure is to determine the source terms appearing in the amplitude differential equation system. These source terms represent the various processes giving rise to unsteady fluctuations of heat release rate, a topic that is covered in the next chapter.

6.1 Introduction

The objective of low order dynamical modeling of combustion instabilities is to provide a simplified framework for the analysis of combustion dynamics phenomena. This however requires a set of models for the driving and damping mechanisms intervening in this process. Only the most important phenomena are considered according to a selection based on the theory, experiments and simulations. As in any other attempt to use low order descriptions this requires a set of assumptions that need to be validated. One advantage of low order modeling is that it requires far less computational resources than complex calculations relying on large eddy simulations or unsteady Reynolds-Averaged Navier-Stokes (RANS) simulations. This allows parametric studies if the low order model suitably reflects the physics of the problem. The method used in what follows was initially proposed by Lores and Zinn (1973) and extensively explored by Culick and his co-workers (Culick (2006)). The principles of the low

order framework are presented in this chapter. Equations that must be solved are derived in Section 6.2. It is shown that the problem can be separated in two parts. First the Helmholtz equation, which needs to be solved, is addressed in section 6.3. Some simple geometries are considered and the modal structures and eigenfrequencies are reviewed. In more complex geometries, it is necessary to use a numerical solver to obtain the eigenfrequencies and eigenfunctions. The AVSP solver is used for that purpose as explained in section 6.4. Finally, section 6.5 explains how combustion instabilities can be determined in the low order framework.

6.2 Governing equations

Low order modeling relies on a physical principle, which consists of an expansion of state variables in terms of the system eigenmodes. It is assumed that the pressure field can be written as a sum of a mean pressure and a fluctuation $p = \overline{p} + p'$ where $\overline{p}$ is the mean pressure and p' the pressure fluctuation. The pressure fluctuations are then projected on the eigenmodes of the system:

$$p'(\mathbf{x}, t) = \sum_{n=0}^{N} \eta_n(t)\Psi_n(\mathbf{x}) \tag{6.1}$$

where η_n is the amplitude of the n^{th} mode and Ψ_n is the n^{th} modal eigenfunction. These eigenfunctions satisfy a boundary value problem defined by a Helmholtz equation, together with boundary conditions on the frontiers of the domain of interest.

$$\nabla^2\Psi_n + \frac{\omega_n^2}{c^2}\Psi_n = 0 \tag{6.2}$$

where c is the sound velocity. Let us assume that the boundary conditions are of the Neumann or Dirichlet or mixed type, i.e. that $\boldsymbol{n} \cdot \nabla\Psi_n = 0$ or that $\Psi_n = 0$ or that $\boldsymbol{n} \cdot \nabla\Psi_n = ik(\rho_0 c/Z)\Psi_n = 0$. Under these conditions it is easy to show that the eigenmodes are orthogonal so that:

$$\int_V \Psi_n\Psi_m = \Lambda_n\delta_{nm} \tag{6.3}$$

where $\delta_{nm} = 0$ when $m \neq n$ and $\delta_{nm} = 1$ when $n = m$. In the previous expression Λ_n represents the integral over the domain of the square of the n^{th} eigenfunction. This quantity has the dimensions of a volume $[\Lambda_n] = L^3$.
One may now derive a wave equation for the pressure field. This is achieved by making use of the mass, momentum and energy equations. Under reacting flow assumptions the equations of mass, momentum and energy can be written

in the form:

$$\frac{\partial \rho}{\partial t} + \nabla \cdot \rho \boldsymbol{u} = 0 \tag{6.4}$$

$$\rho \frac{\partial \boldsymbol{u}}{\partial t} + \rho \boldsymbol{u} \cdot \nabla \boldsymbol{u} = -\nabla p \tag{6.5}$$

$$\rho T \Big(\frac{\partial s}{\partial t} + \boldsymbol{u} \cdot \nabla s \Big) = \dot{Q} \tag{6.6}$$

$$p = \rho^{\gamma} e^{s/c_v} \tag{6.7}$$

where ρ is the density, $\boldsymbol{u} = (u_1, u_2, u_3)$ the velocity vector, γ is the specific heat ratio, s is the constant entropy of the flow, c_v is the specific heat of the mixture at constant volume and $\dot{Q}$ is the heat release rate per unit volume. Small perturbation of the density, pressure and velocity vector are assumed. These variables can be written as a sum of a mean value and a fluctuation $\rho = \bar{\rho} + \rho'$, $p = \bar{p} + p'$ and $\boldsymbol{u} = \bar{\boldsymbol{u}} + \boldsymbol{u}'$ for the density, pressure and velocity vector respectively. By inserting these expressions in equations 6.4 to 6.7, assuming that the mean flow velocity is small and only retaining the first order perturbation terms, one obtains a wave equation which takes the form:

$$\nabla^2 p' - \frac{1}{c^2} \frac{\partial^2 p'}{\partial t^2} = -\frac{\gamma - 1}{c^2} \frac{\partial \dot{Q}'}{\partial t} \tag{6.8}$$

It is convenient to first represent the right hand side of the last equation in the form

$$h = -\frac{\gamma - 1}{c^2} \frac{\partial \dot{Q}'}{\partial t} \tag{6.9}$$

so that the wave equation becomes

$$\nabla^2 p' - \frac{1}{c^2} \frac{\partial^2 p'}{\partial t^2} = h \tag{6.10}$$

and let us assume that the pressure field satisfies boundary conditions of the form:

$$\boldsymbol{n} \cdot \nabla p' = -f \tag{6.11}$$

where f is a function that is equal to zero on rigid boundaries. When this function differs from zero it defines the value of the normal velocity at the boundary.
One may now multiply the wave equation (6.10) by Ψ_m and the Helmholtz equation (6.2) by p' and subtract the second result from the first to get:

$$\Psi_m \nabla^2 p' - p' \nabla^2 \Psi_n - \frac{1}{c^2} \frac{\partial^2 p'}{\partial t^2} \Psi_m - \frac{\omega_n^2}{c^2} p' \Psi_n = h \Psi_m \tag{6.12}$$

This equation may now be integrated over the volume V:

$$\int_V (\Psi_m \nabla^2 p' - p' \nabla^2 \Psi_n) dV + \frac{1}{c^2} \sum_{n=1}^{N} \int_V \frac{d^2\eta_n}{dt^2} \Psi_n \Psi_m dV \\ -\frac{1}{c^2} \omega_n^2 \sum_{n=1}^{N} \eta_n \int_V \Psi_n \Psi_m dV = \int_V h \Psi_m dV \tag{6.13}$$

where the modal expansion (6.1) has been introduced in the last two terms of the left hand side. One may now use the Green's identity to replace the first term of the left hand side by a surface integral on the control surface of the domain A:

$$\int_V (\Psi_m \nabla^2 p' - p' \nabla^2 \Psi_n) dV = \int_A (\Psi_m \nabla p' - p' \nabla \Psi_n) \cdot \boldsymbol{n} dA \tag{6.14}$$

Making use of the boundary conditions on Ψ_n and on the pressure field one obtains:

$$\int_V (\Psi_m \nabla^2 p' - p' \nabla^2 \Psi_n) dV = -\int_A f \Psi_m dA \tag{6.15}$$

Noting that the eigenmodes are orthogonal one finds that

$$\frac{d^2\eta_n}{dt^2} + \omega_n^2 \eta_n = -\frac{c^2}{\Lambda_n} \Big[\int_V h \Psi_n dV + \int_A f \Psi_n dA \Big] \tag{6.16}$$

The modal amplitudes $\eta_n(t)$ are determined by the previous set of coupled differential equations. Inserting the definition of h in the previous equations one obtains:

$$\frac{d^2\eta_n}{dt^2} + \omega_n^2 \eta_n = \frac{\gamma - 1}{\Lambda_n} \int_V \frac{\partial \dot{Q}'}{\partial t} \Psi_n dV - \frac{c^2}{\Lambda_n} \int_A f \Psi_n dA \tag{6.17}$$

The last term on the right hand side corresponds to driving or damping effects associated with boundary values of the normal pressure gradient. This term will be designated in what follows by

$$F_n = -\frac{c^2}{\Lambda_n} \int_A f \Psi_n dA \tag{6.18}$$

It is not difficult to include a damping term in the previous set of equations. This is represented in a formal way by D_n and corresponds to the damping of the n^{th} mode.
Finally, the evolution of the modal amplitudes is defined by the following equations

$$\ddot{\eta}_n(t) + \omega_n^2 \eta_n = \frac{\gamma - 1}{\Lambda_m} \int_V \frac{\partial \dot{Q}'}{\partial t} \Psi_m(\mathbf{x}) dV + F_n - D_n \tag{6.19}$$

where ω_n is the angular eigenfrequency of the nth mode, $\Lambda_m = \int_V \Psi_m^2 dV$ is the norm of the mth mode, $\dot{Q}'$ is the volumetric heat release rate fluctuation (or unsteady heat release), F_n and D_n respectively represent effects associated with fluctuations of the normal pressure gradient at the boundaries and damping in the system. Equation 6.19 can be written in a more formal manner to explicitly list the driving and damping mechanisms.

$$\ddot{\eta}_n(t) + \omega_n^2 \eta_n = S_{comb} + S_{exc} + S_{nl} - S_d \tag{6.20}$$

In this equation S_{comb} is the combustion source term, S_{exc} represents an external modulation, S_{nl} represents nonlinear effects associated to large acoustic amplitudes and S_d reflects damping in the domain. Each of these terms requires a model that may be based on theoretical reasoning, experimental data or simulation. It is interesting to note that a single module can carry several models in order to represent different mechanisms independent from one another.

6.3 Eigenmodes and eigenfrequencies

The previous framework relies on a modal expansion of the pressure field. It is then natural to examine these normal modes and the corresponding eigenfrequencies. The normal modes are solution of a Helmholtz equation.

$$\nabla^2 \Psi_n + \frac{\omega_n^2}{c^2} \Psi_n = 0 \tag{6.21}$$

In general, the walls of the system are rigid and it is then natural to use boundary conditions that describe this situation and can be written as

$$\boldsymbol{n} \cdot \nabla \Psi_n = 0 \tag{6.22}$$

Solutions of the previous boundary value problem are easily be determined for simple geometries. This is exemplified in what follows for rectangular and cylindrical cavities.

6.3.1 Rectangular geometry

This case is examined here because it is the simplest and also because it corresponds to the geometry of the cavities of the NPCC test rig. For rectangular cavities and rectangular geometries in general, the pressure field p must satisfy the Helmholtz equation and it is convenient to chose null velocity boundaries ($\boldsymbol{n} \cdot \nabla \Psi = 0$ with $\boldsymbol{n}$ the unit normal vector at the boundary). The solution of the boundary value problem defined by the Helmholtz equation and rigid wall boundary conditions may be obtained by writing the Ψ in the form of a product $\Psi(x, y, z) = X(x)Y(y)Z(z)$. The Helmholtz equation becomes

$$\frac{X''}{X} + \frac{Y''}{Y} + \frac{Z''}{Z} + k^2 = 0 \tag{6.23}$$

where $k = \omega/c$. The first three terms in the previous expression depend on a different variable, x for the first, y for the second and z for the third. One may then deduced that each of these terms must be constant. It is convenient to designate the respective constants by κ_x^2, κ_y^2 and κ_z^2. These quantities must be so that $k^2 = \kappa_x^2 + \kappa_y^2 + \kappa_z^2$ and the three functions X, Y and Z satisfy $X'' + \kappa_x^2 X = 0$, $Y'' + \kappa_y^2 Y = 0$ and $Z'' + \kappa_z^2 Z = 0$. These three equations with the zero normal velocity boundary conditions yield the following eigenfunctions

$$X = \cos(\kappa_x x) \quad Y = \cos(\kappa_y y) \quad Z = \cos(\kappa_z z) \tag{6.24}$$

with the following values for the wave numbers

$$\kappa_x = \frac{n_x \pi}{l_x} \quad \kappa_y = \frac{n_y \pi}{l_y} \quad \kappa_z = \frac{n_z \pi}{l_z} \tag{6.25}$$

where (n_x,n_y,n_z) is an integer triplet. The pressure field in the domain is then given by equation 6.26.

$$\Psi_{n_x,n_y,n_z} = \cos\left(\frac{n_x \pi x}{l_x}\right) \cos\left(\frac{n_y \pi y}{l_y}\right) \cos\left(\frac{n_z \pi z}{l_z}\right) \tag{6.26}$$

The corresponding angular frequency ω can be deduced from

$$k^2 = \pi^2 \left[\left(\frac{n_x}{l_x}\right)^2 + \left(\frac{n_y}{l_y}\right)^2 + \left(\frac{n_z}{l_z}\right)^2 \right]$$

and the eignefrequency corresponding to the mode (n_x,n_y,n_z) is given by

$$f = \frac{c_0}{2} \left[\left(\frac{n_x}{l_x}\right)^2 + \left(\frac{n_y}{l_y}\right)^2 + \left(\frac{n_z}{l_z}\right)^2 \right]^{\frac{1}{2}} \tag{6.27}$$

To illustrate equation 6.27, the eigenfrequencies of the chamber of NPCC are determined. The inner dimensions of the chamber are 210mmx140mmx50mm, the domain is filed with air at room temperature. Table 6.1 gathers the first few modes of the chamber with their respective frequencies. One may note that the values obtained analytically are close to those determined experimentally in chapter 3.

6.3.2 Cylindrical chamber geometry

We now consider a cylindrical domain of radius R and length L. The analysis closely follows that used in the case of a rectangular geometry. It is natural to use cylindrical coordinate system (r,θ,x) and write the Helmholtz equation in the form

$$\frac{\partial^2 \Psi}{\partial r^2} + \frac{1}{r}\frac{\partial \Psi}{\partial r} + \frac{1}{r^2}\frac{\partial^2 \Psi}{\partial \theta^2} + \frac{\omega^2}{c^2}\Psi = 0 \tag{6.28}$$

n_x, n_y, n_z	Identification	Frequency [Hz]
1,0,0	First longitudinal or 1L	790
2,0,0	Second longitudinal or 2L	1579
0,1,0	First transverse along y or 1T	1184
0,0,1	First transverse along z or 1Z	3316
1,1,0	First longitudinal and first transverse along y of 1L1T	1423
1,0,1	First longitudinal and first transverse along z of 1L1Z	3409

Table 6.1: *Eigenfrequencies of the NPCC chamber determined analytically by making use of expression 6.27. Sound velocity: $c = 332\ m.s^{-1}$.*

One finds after some calculations that the modes are determined by three integers m,n and q corresponding to the radial, azimuthal and longitudinal structures respectively. The eigenmodes are given by the following expression:

$$\Psi_{m,n,q}(r,\theta,x) = J_n\left(\frac{\pi\beta_{mn}r}{a}\right)\cos\left(\frac{q\pi z}{L}\right)\left(ae^{in\theta} + be^{-in\theta}\right) \tag{6.29}$$

where a and b are two complex amplitudes, J_n is the Bessel function of order n and of the first kind, and β_{mn} are the roots of $J_n'(\pi\beta_{mn}) = 0$. The resonant frequencies are then given by

$$f_{mnq} = \frac{c}{2}\left[\left(\frac{\beta_{mn}}{R}\right)^2 + \left(\frac{q}{L}\right)^2\right]^{\frac{1}{2}} \tag{6.30}$$

It is worth noting that the modes defined by expression (6.29) are degenerate. There is an infinity of modal structures corresponding to each of the eigenfrequencies defined by expression (6.30). The corresponding structures are defined by the possible combinations of the complex amplitudes a and b. For example if $b = 0$ and $a \neq 0$, the mode has an azimuthal structure that behaves like $e^{in\theta - i\omega t}$. This is a wave rotating in the positive θ direction (i.e. the counterclockwise direction). If $a = 0$ and $b \neq 0$ the azimuthal structure behaves like $e^{-in\theta - i\omega t}$. This wave rotates in the negative θ direction (i.e. the clockwise direction). If $a = b$, the two complex exponentials combine to form a cosine structure: $\cos(n\theta)e^{-i\omega t}$. This forms a standing mode with a nodal line at $\theta = \pi/2$. The position of the pressure nodal and anti-nodal lines do not change with time.

6.4 Numerical determination of eigenmodes

The numerical determination of eigenmodes can be carried out by a general purpose Helmholtz solver like AVSP. This software is used to determine the eigenmodes and eigenfrequencies in more complex geometries like those found in laboratory-scale experiments or those corresponding to full-scale rocket engines. An overview of the code is given in Nicoud et al. (2007). This three dimensional

acoustic solver is more flexible than the analytical method described previously and it can be used in the design process to determine the modal structures and resonant frequencies. It is also possible to impose more complex impedance boundary conditions rather than the zero normal velocity at the boundary. AVSP can also be used to deal with a non-uniform temperature field. The temperature distribution may then be deduced from a simulation of the reactive flow. It is also possible to specify a local heat release rate, and take into account the flame pattern in the modal determination. The flame can also be considered as an active element which can modify the system stability.

6.5 Combustion instabilities and the Rayleigh criterion

The Rayleigh criterion is often used in the analysis of combustion instabilities. A modern version of this criterion may be derived by considering the balance of acoustic energy. This equation may be written in the form:

$$\frac{\partial E}{\partial t} + \nabla \cdot \boldsymbol{F} = S - D \tag{6.31}$$

All quantities appearing in this equation are integrated over a period of oscillation T. Here E represents the acoustic energy density, $\boldsymbol{F}$ is the acoustic energy flux S represents the Rayleigh source term integrated over a period and D is the damping rate. The Rayleigh source term has the form (Poinsot and Veynante (2001)):

$$S = \frac{1}{T}\int_T \frac{\gamma - 1}{\gamma \overline{p}} p' \dot{Q}' dt \tag{6.32}$$

If this source term is positive, it tends to increase the acoustic energy density. This quantity will grow locally if the source term is greater than the damping rate and the acoustic energy fluxes leaving the local volume. If one integrates the energy balance over the volume of the system one finds that

$$\int_V \frac{\partial E}{\partial t} dV = \int_V S dV - \int_V D dV - \int_A \boldsymbol{F} \cdot \boldsymbol{n} dA \tag{6.33}$$

The acoustic energy integrated over the volume will increase if

$$\int_V S dV > \int_V D dV - \int_A \boldsymbol{F} \cdot \boldsymbol{n} dA \tag{6.34}$$

This indicates that the Rayleigh source term integrated over the volume has to be positive but this is just a necessary condition. It also has to be larger than the integrated damping rate minus the surface integral of the outgoing normal acoustic energy fluxes. Assuming that the volume is essentially isolated from

the external environment the outgoing energy fluxes vanish and the previous condition indicates that the instability will grow if the driving source term integrated over the volume is greater than the volume integral of the damping rate. If the integrated damping rate is greater than the driving source term then the instability oscillation will decay leading to a stable regime of operation.

6.6 Conclusion

The low order model reviewed in this chapter relies on a modal expansion of the pressure field. The modal eigenfunctions are solutions of a Helmholtz equations and the modes can be determined analytically for simple geometries or numerically using a general purpose finite element Helmholtz solver. It is shown that the amplitudes in the modal expansion are determined by a set of second order differential equations. These equations contain, in particular, the modal projection of the rate of change of the non steady heat release rate. Modeling of the unsteady heat release rate and more generally of all the other terms appearing in this set of equations constitutes a difficult issue which is considered in the next chapter. This framework together with the various models described in the following chapter can be used to analyze and eventually predict combustion instabilities with an engineering tool low order tool. The code STAHF based on this modal expansion is presented in chapter 7.

Chapter 7

Models formulations for the STAHF tool

This chapter contains a detailed description of the main models of the reduced order code STAHF. The code relies on a modal expansion of the pressure field. This gives rise to a set of coupled differential equations for the pressure fluctuation amplitudes in the system. The code requires a meshed geometry to calculate the eigenmodes and eigenfrequencies, a sound speed distribution in the domain of interest, an initial solution to initiate the dynamical evolution of the system, a combustion source term projected on the modes, excitation source terms in situations where modulation is generated by an external actuator and damping coefficients reflecting dissipation of acoustic energy in the system. The sound speed distribution may be obtained, for example, from a mean flow solution that may in turn be obtained by averaging large eddy simulations. This provides the pressure field, density and sound speed distributions. The combustion source term reflects the driving mechanisms of combustion instabilities. The FAME model represents the impact of transverse velocity on the heat release rate fluctuations, while the pressure perturbation model and the mass flow rate perturbation model respectively represent the impact of pressure fluctuations and mass flow rate fluctuations on the heat release rate. The excitation source term includes energy deposition, initial pressure pulse and mass flow rate modulations induced by the VHAM. The driving source terms included in STAHF were determined with large eddy simulations presented in previous chapters.

7.1 Introduction

The analysis of combustion instabilities developed in the present chapter relies on the low order modeling reviewed in chapter 6. This method, based on modal projection on the eigenmodes, is interesting because it provides a physical de-

scription of the system dynamics and allows integration of a broad variety of models. Reduced order modeling is carried out in the time domain, allowing direct comparisons with temporal signals detected by sensors. The code developed for reduced order modeling was initiated in the work of Méry (2010). This software is designated as STAHF for STAbility High Frequency. This chapter presents the corresponding framework and the dynamical equations forming the basis of the STAHF code. The models used in the code are mainly derived from experimental observation or simulations (results from chapters 1, 2, 4 and 5 for example).
The models used in the reduced order dynamical code STAHF are presented in detail. The first section (section 7.2) discusses the general framework underlying this software. The main part of this chapter is concerned with the different driving mechanisms of combustion instabilities. The corresponding source terms are detailed in section 7.3. One then considers the representation of damping (section 7.4). The determination of the field that is used to initiate the dynamical calculation is described in section 7.5. The final section 7.6 concerns the representation of an external modulator and specifically considers the VHAM case.

7.2 Global framework

Reduced order modeling consists in replacing complex coupled processes with simpler descriptions. These simplified models are treated independently and linked together in the final stage. The objective is to derive a state space description of the coupled dynamics of the system under investigation. This description involves a system of differential equations in combination with a set of algebraic relations. Stability calculations are then carried out in the time or frequency domains. The aim of reduced order dynamical modeling of combustion instabilities is to represent, in an idealized fashion, the processes which govern the system dynamics. The low order modeling code, STAHF, was developed at the EM2C, CNRS laboratory in the doctoral dissertation Méry (2010). The code can be used to test dynamical models and validate novel formulations of the processes driving instabilities. STAHF relies on a physical expansion of state variables in terms of the system eigenmodes (equation 6.1). There are many possible expressions for the different terms appearing in equation 6.1. Specific formulations can be chosen at the start of the simulation to represent a particular condition. The various options are defined by the user and the code then integrates the set of equations 6.19 providing the space-time distribution of unsteady pressure in the system. To run a dynamical simulation one has to follow the steps indicated in figure 7.1.

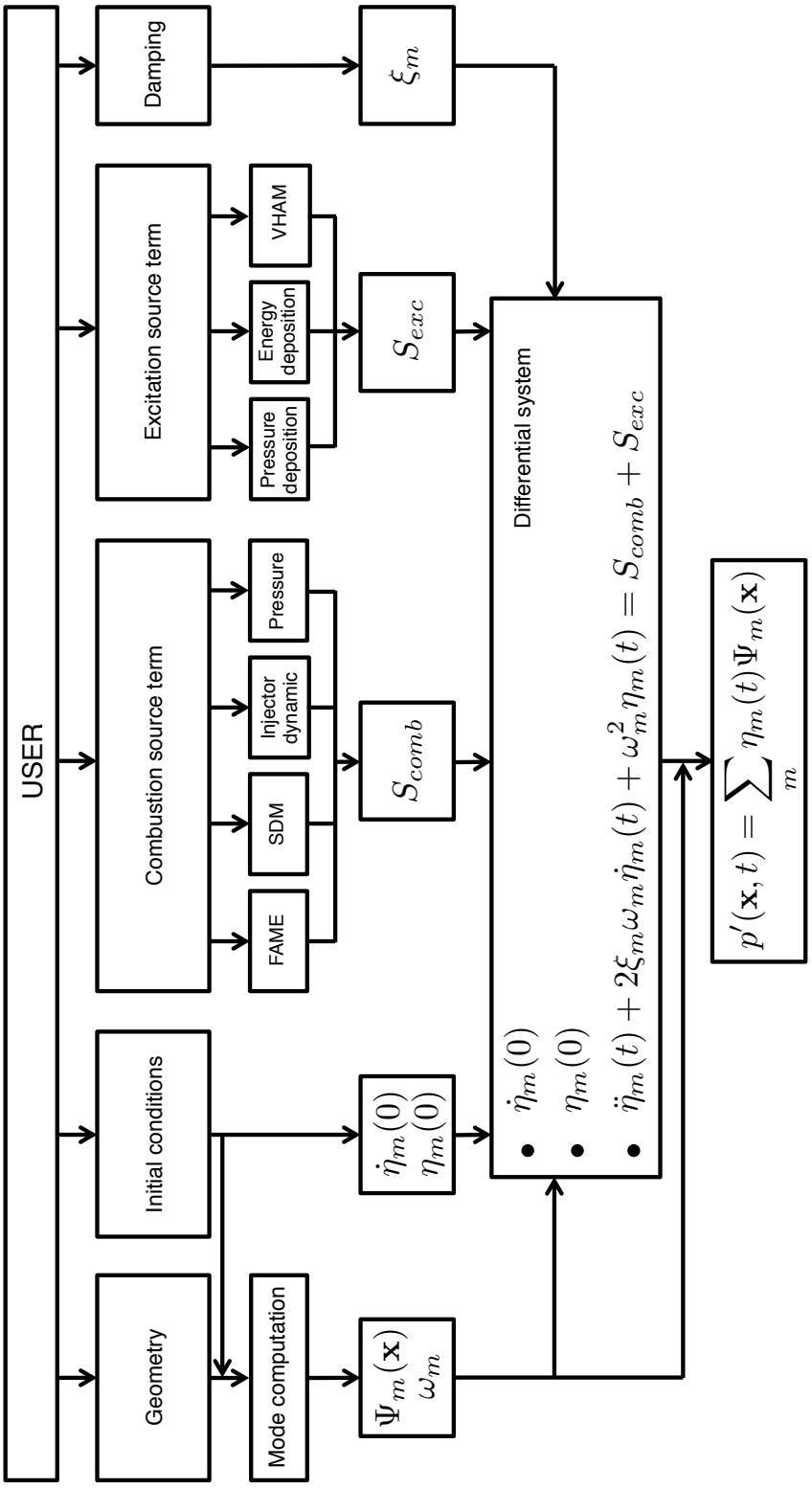

Figure 7.1: *Schematic representation of the STAHF framework.*

For a typical geometry like that of a rocket engine (to fix the ideas one may consider the BKD engine described in the appendix C) one has to prepare a mesh describing the system cavities (injection plenum, thrust chamber, injector channels). This is then used to determine the eigenfrequencies and eigenfunctions using a Helmholtz solver. In its present form, STAHF uses AVSP (Nicoud et al. (2007); Selle et al. (2006)) to determine the modal structures and eigenfrequencies. When this preliminary step is fulfilled, the user has to choose the models to be included in the simulation.

7.3 Source term modeling

Driving processes are considered in what follows. There are many possible mechanisms that may drive instabilities in rocket engines. In what follows, we specifically consider effects of transverse velocity fluctuations, sensitive time lag modeling, heat release rate perturbations induced by mass flow rate modulations and by bulk pressure fluctuations.

7.3.1 Source term induced by transverse velocity fluctuations

Fluctuations of the jet are induced by transverse velocity fluctuations. The dense core jet is transported by the acoustic motion, this assumption is at the heart of the Flame Acoustic Motion Equation (FAME), first developed by Méry (2010). The name of the model implies that the unsteady heat release is caused by the flame motion itself. By assuming that the flame is a thin sheet, the aim of this model is to describe the relation between the pressure p and the unsteady heat release rate $\dot{Q}'$ through the transverse velocity v. From this point on, two different types of geometries can be assumed for the writing of the FAME model; a cartesian geometry that represents box-like combustion chambers like that of the MIC used on the Mascotte facility and a cylindrical geometry that is closer to the combustion chamber of rocket engines.
We first consider the source term induced by transverse velocity fluctuations in rectangular geometries.
The transverse velocity field can be deduced by making use of the framework introduced in equation 6.19. The momentum equation yields the transverse velocity fluctuations written in equation 7.1.

$$v'(\boldsymbol{x},t) = \frac{c^2}{\bar{p}\gamma}\sum_{m=1}^{\infty}\frac{1}{\omega_m^2}\dot{\eta}_m(t)\nabla\Psi_m(x) \tag{7.1}$$

There are no transverse velocity fluctuations for a pressure mode corresponding to $m = 0$ this is why the sum in equation 7.1 begins with $m = 1$. Figure 7.2 illustrates the type of configuration in which the FAME model can be applied. The flame of length L_f is positioned at y_0 and oscillates up and down. This

motion is induced by the acoustic velocities inside the domain and it is reasonable to assume that only 1T modes generate this displacement since higher order transverse modes cannot be excited in these types of configurations. By using the eigenfunction of the 1T mode $\Psi_1 = cos(\frac{\pi}{l}y)$, equation 7.1 becomes equation 7.2.

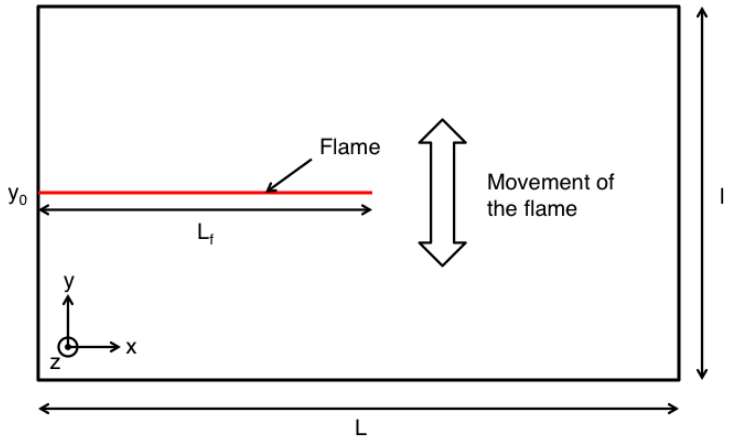

Figure 7.2: *Schematic view of a moving flame in a Cartesian geometry. The length and width of the domain are L and l respectively, the length of the flame is L_f and its initial vertical position is at y_0.*

$$\frac{dy}{dt}(t) = -\frac{c^2}{\bar{p}\gamma\omega_1}\dot{\eta}_1(t)\sin(\frac{\pi}{l}y) \tag{7.2}$$

The instantaneous vertical position of the flame is then given by equation 7.3.

$$y(t) = \frac{2l}{\pi}\arctan\left(\tan\left(\frac{\pi y_0}{2l}\right)e^{-\frac{\eta_1(t)}{\bar{p}\gamma}}\right) \tag{7.3}$$

The steady heat release rate from an injector is Q, assuming an infinitely thin flame the heat release is defined by equation 7.4.

$$\dot{Q}(\boldsymbol{x},t) = \frac{Q}{L_f}\delta(y - y(t))\delta(z - z_0) \tag{7.4}$$

Where z_0 designates the initial position of the flame in the z direction. Equation 7.4 indicates that the steady heat release rate Q of the flame is generated over

its entire length L_f and the flame is found at its coordinates $(y(t),z_0)$. The integration over a time period T of equation 7.4 yields equation 7.5, the average heat release.

$$\overline{\dot{Q}}(\boldsymbol{x},t) = \frac{1}{T}\int_0^T \frac{Q}{L_f}\delta(y-y(t))\delta(z-z_0)dt \tag{7.5}$$

Subtracting equation 7.5 from equation 7.4 yields the heat release fluctuation defined in equation 7.6.

$$\dot{Q}(\boldsymbol{x},t) = \frac{Q}{L_f}\left(\delta(y-y(t))\delta(z-z_0) - \frac{1}{T}\int_0^T \delta(y-y(t))\delta(z-z_0)dt\right) \tag{7.6}$$

In the modal definition, the source term $(\gamma-1)/\Lambda_m \int \partial\dot{Q}'/\partial t\Psi_m dV$ is simplified into equation 7.7 by assuming that only 1T eigenmodes displace the flame.

$$S_F^m(t) = \frac{\gamma-1}{\Lambda_1}\int\int\int \frac{\partial\dot{Q}'}{\partial t}(t)\cos\left(\frac{\pi}{l}y\right)dxdydz \tag{7.7}$$

Where $\Lambda_1 = \int\int\int \cos^2(\frac{\pi}{l}y)dxdydz = Lhl/2$ represents the square of the norm of Ψ_1. By plugging equation 7.6 into 7.7, the source term of the FAME model is provided by equation 7.8.

$$S_F^m(t) = 4\frac{\gamma-1}{\gamma}\frac{Q}{\overline{p}\Lambda_1}\dot{\eta}_1(t)\frac{\tan\left(\frac{\pi y_0}{2l}\right)e^{-\frac{2\eta_1(t)}{\gamma\overline{p}}}}{\left(1+\tan^2\left(\frac{\pi y_0}{2l}\right)e^{-\frac{2\eta_1(t)}{\overline{p}\gamma}}\right)^2} \tag{7.8}$$

One may note that the previous expression is always a positive source of acoustic energy, indicating that the flame displacement augments the amplitude level. The source term expressed in equation 7.8 corresponds to a single injector. In a multiple injector configuration, each flame generates a heat release rate fluctuation through the motion induced by the acoustic field. It is considered that there are no interactions between the different flames composing the group and that their heat release rate fluctuations may be combined linearly. The different flame contributions are simply added together:

$$S_{FE}^m(t) = 4\frac{\gamma-1}{\gamma}\frac{Q}{\overline{p}\Lambda_1}\dot{\eta}_1(t)\sum_{n=1}^{N_f}\frac{\tan\left(\frac{\pi y_0^n}{2l}\right)e^{-\frac{2\eta_1(t)}{\gamma\overline{p}}}}{\left(1+\tan^2\left(\frac{\pi y_0^n}{2l}\right)e^{-\frac{2\eta_1(t)}{\overline{p}\gamma}}\right)^2} \tag{7.9}$$

where N_f is the total number of flames and y_0^n is the initial position of the n^{th} flame. The FAME source term indicates that in configurations with multiple injectors such as rocket engines, the combined heat release fluctuations from the unit flames add up to produce a source term that could drive the instability.

7.3.2 Source term induced by azimuthal velocity fluctuations

One may now derive the source term associated to azimuthal velocity fluctuations in a cylindrical chamber. The development of the source term follows similar tracks but with some adaptations. In cylindrical geometries the transverse displacement is replaced by an angular displacement of the flame. In a cylindrical configuration the fluctuating velocity is given by:

$$\mathbf{v'_m}(\boldsymbol{x},t) = \dot{r}(\boldsymbol{x},t)\mathbf{u_r} + r(\boldsymbol{x},t)\dot{\theta}(\boldsymbol{x},t)\mathbf{u}_\theta \tag{7.10}$$

where r is the radial position of the flame and θ is its angular location. The flame is here considered to only move in the azimuthal direction on a cylinder of radius r. Figure 7.3 illustrates the cylindrical configuration and the type of movement executed by the flame. Under these conditions, $\dot{r}$ is equal to zero, indicating that equation 7.10 can be simplified into equation 7.11 when projected onto $\mathbf{u}_\theta$.

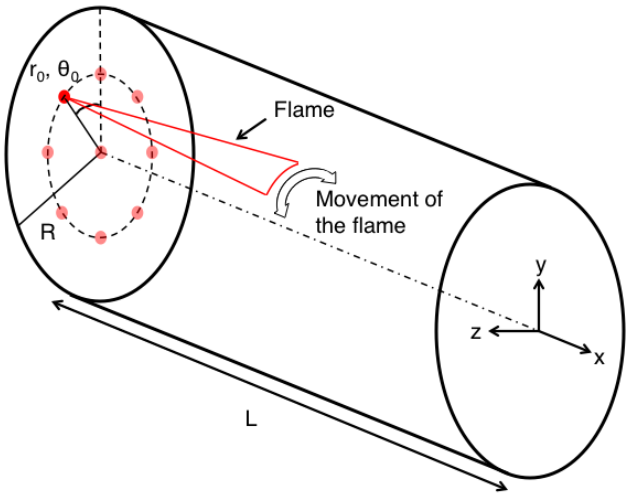

Figure 7.3: *Schematic view of a moving flame in a cylindrical geometry. The length and radius of the domain are L and R respectively, the initial position of the flame is (r_0, θ_0).*

$$v'_m(\boldsymbol{x},t) = r\dot{\theta}(\boldsymbol{x},t) = \frac{c^2}{\bar{p}\gamma}\sum_{m=1}^{\infty}\frac{1}{\omega_m^2}\dot{\eta}_m(t)\frac{1}{r}\frac{\partial\Psi_m}{\partial\theta}(\boldsymbol{x}) \tag{7.11}$$

There are no transverse velocity fluctuations for a pressure component corresponding to $m = 0$ this is why the sum in equation 7.1 begins at 1. Just like

in the cartesian configuration it is assumed that the flame motion is only due to 1T modes. The angular velocity is then given by:

$$\dot{\theta}(\boldsymbol{x},t) = \frac{c^2}{\overline{p}\gamma\omega_1^2}\dot{\eta}_1(t)\frac{1}{r^2}\frac{\partial\Psi_1}{\partial\theta}(r,\theta(t)) \tag{7.12}$$

The steady heat release rate from an injector is Q, assuming an infinitely thin flame the heat release is defined by:

$$\dot{Q}(\boldsymbol{x},t) = \frac{Q}{L_f}\frac{1}{r}\delta(r-r_0)\delta[\theta-\theta(t)] \tag{7.13}$$

where r_0 is the initial radial position of the flame. For every eigenfrequency in a cylindrical geometry there are two different eigenmodes. The first is defined by:

$$\Psi_{mc} = \cos\left(\frac{\pi q}{L}x\right) J_m(\frac{\beta_{m1}\pi r}{R})\cos m\theta \tag{7.14}$$

while the second corresponds to:

$$\Psi_{ms} = \cos\left(\frac{\pi q}{L}x\right) J_m(\frac{\beta_{m1}\pi r}{R})\sin m\theta \tag{7.15}$$

where J_m is the Bessel function of order m and of the first kind. In the previous expressions β_{m1} designates the first zero of $dJ_m(\beta_{m1}\pi R)/dr = 0$ and R is the radius of the cylindrical chamber. In order to simplify the following analysis it is assumed that all flames originate from a flat backplane at $x = 0$ and only azimuthal modes generate the motion of the flame ($m = 1$). The total pressure fluctuation can then be reconstructed by summing the components corresponding to Ψ_{mc} and Ψ_{ms} together

$$p' = \sum_{m=1}^{\infty} \eta_{mc}\Psi_{mc} + \eta_{ms}\Psi_{ms}$$

. The FAME term has two components S_{Fc} and S_{Fs}. The following development corresponds to S_{Fc} but the development of S_{Fs} follows the same lines. Equation under these conditions can be written in the form of equation 7.16.

$$S_{Fc}^m(t) = \frac{\gamma-1}{\Lambda_{mc}}\int_x\int_r\int_\theta \frac{\partial\dot{Q}'}{\partial t}(t)\Psi_{mc}(r_0,\theta_0)rdrd\theta dx \tag{7.16}$$

The unsteady heat release rate of equation 7.13 is introduced in equation 7.16 and a hypothesis of small oscillations is considered. This means that the flame

remains close to its initial position ($\theta(t) = \theta_0$ where θ_0 is the initial angular position of the flame). This leads to equation 7.17 and 7.18.

$$S^m_{Fc}(t) = \frac{\gamma - 1}{\Lambda_{mc}} Q \frac{c^2}{\gamma \overline{p} \omega_m^2} \dot{\eta}_m(t) \frac{1}{r_0^2} \left[\frac{\partial \Psi_{mc}}{\partial \theta}(r_0, \theta_0) \right]^2 \tag{7.17}$$

$$S^m_{Fs}(t) = \frac{\gamma - 1}{\Lambda_{ms}} Q \frac{c^2}{\gamma \overline{p} \omega_m^2} \dot{\eta}_m(t) \frac{1}{r_0^2} \left[\frac{\partial \Psi_{ms}}{\partial \theta}(r_0, \theta_0) \right]^2 \tag{7.18}$$

Where $\Lambda_{mc} = \int_V \Psi^2_{mc} r dr d\theta dx$. It is interesting to note that Λ_{mc} is equal to Λ_{ms} and in the following the norm will be defined as Λ_m. Finally, the FAME model in a cylindrical coordinates can be cast in a compact form. For a multiple injector configuration equations 7.19 and 7.20 provide explicit representations of the FAME source terms.

$$S^m_{Fc}(t) = \frac{\gamma - 1}{\gamma} \frac{1}{b_m} \frac{Q}{\overline{p} V} \frac{1}{(\kappa_m R)^2} \dot{\eta}_m(t) \sum_{n=1}^{N_f} \frac{R^2}{r_n^2} \left[\frac{\partial \Psi_{mc}}{\partial \theta}(r_n, \theta_n) \right]^2 \tag{7.19}$$

$$S^m_{Fs}(t) = \frac{\gamma - 1}{\gamma} \frac{1}{b_m} \frac{Q}{\overline{p} V} \frac{1}{(\kappa_m R)^2} \dot{\eta}_m(t) \sum_{n=1}^{N_f} \frac{R^2}{r_n^2} \left[\frac{\partial \Psi_{1s}}{\partial \theta}(r_n, \theta_n) \right]^2 \tag{7.20}$$

Where $b_m = \Lambda_m / \pi R^2 L$ and $V = \pi R^2 L$ is the volume of the cylindrical domain, $\kappa_m = \omega_m / c$ is the wave number and (r_n, θ_n) are the cylindrical coordinates of the n^{th} flame.

Another combustion source term is also implemented in the code under the name "Spray Dynamics Model" (SDM). This model relies on a description of the dynamics of liquid droplet sprays as formulated in the work of Méry (2010). This model, intended to represent processes that may occur under subcritical conditions, will not be used in what follows.

7.3.3 Sensitive time lag formulation

Time lag concepts were introduced during the early period of rocket development (see for example Crocco and Cheng (1956)). The central idea is that propellants introduced in the thrust chamber at time $t - \tau$ react at a later time t and are converted into products. The delay τ may be constant in some special cases but in general, it is a function of parameters defining the state of the system such as the pressure p and gas temperature T_g. As a consequence, the time lag is sensitive to these parameters. It is possible to show that the unsteady heat release can be linked to the time derivative of the time lag and that this can be expressed in terms of differences between the state variables

taken at times t and $t-\tau$. A link is established between the relative heat release rate fluctuation and the pressure difference through an "interaction index" n. In its simplest form one may write:

$$\frac{\dot{Q}'}{\overline{Q}} = n\frac{p'(\boldsymbol{x},t) - p'(\boldsymbol{x},t-\tau)}{\overline{p}} \tag{7.21}$$

where $\overline{p}$ is the mean value of the pressure and p' is the fluctuating part of the pressure. Models of this type have been widely used to analyse longitudinal instabilities in the low frequency range (Crocco and Cheng (1956)). The time lag τ corresponds to the phenomena that occur before combustion (primary and secondary atomization, heating, vaporization, mixing, chemical reactions etc). The interaction index n describes the intensity of the coupling between combustion and perturbations of the state variables. The model is easy to implement (Culick and Yang (1995); Mitchell (1995)) but there are some drawbacks. There is a lack of physical justification as far as transverse oscillations are concerned. One does not quite know what the interaction index n represents when one wishes to consider transverse oscillations. The delay τ must be determined from experimental data or simulations. These types of models are generally adjusted to fit a particular configuration but they might not be able to reflect changes associated with modifications of the combustion process and it is also known that they cannot represent the diverse processes ocurring in model or real scale experiments (Hulka and Hutt (1995)). It is however useful to have implement this kind of model in a reduced order dynamical model.

7.3.4 Source term induced by mass flow rate fluctuations

An important process that can drive the combustion instability is the mass flow rate fluctuation (as described in chapter 2). In the presence of a pressure difference between the injector inlet and outlet it is shown in chapter 4 that the injector responds in the form of a mass flow rate fluctuation. The combination of these two phenomena, which are the injector dynamic and the mass flow rate response, comprise the model illustrated here. The link between the pressure difference in the injector and the injection velocity is described by a differential equation 4.7. In the low frequency range the injector operates in a quasi-steady fashion and one may directly deduce the velocity perturbation from the difference in pressure perturbation acting on the injector. If this is assumed, the velocity is directly proportional to the pressure difference:

$$v'(t) = \frac{p'_1 - p'_4}{\rho\xi\overline{v}} \tag{7.22}$$

It is then possible to use the time lag formalism and link the velocity fluctuation

and the heat release rate fluctuation through the following expression:

$$\frac{\dot{Q}'}{\overline{\dot{Q}}} = n\frac{v'(t-\tau)}{\overline{v}} \tag{7.23}$$

Injecting equation 7.22 in equation 7.23 gives the heat release rate caused by a pressure difference inside one particular injector.

$$\dot{Q}'(t) = \frac{(p'_1 - p'_4)n\overline{\dot{Q}}}{\xi\rho\overline{v}^2} \tag{7.24}$$

Now let us assume that the heat release fluctuation is produced at the injector exhaust located at $\boldsymbol{x}_{Ej}$. The volumetric rate of heat release fluctuation becomes:

$$\dot{Q}'_j(t) = \frac{[p'(\boldsymbol{x}_{Ij}) - p'(\boldsymbol{x}_{Ej})]n\overline{\dot{Q}}}{\xi\rho\overline{v}^2}\delta(\boldsymbol{x} - \boldsymbol{x}_{Ej}) \tag{7.25}$$

One may now insert expansions of the pressure fluctuations in terms of the normal modes to obtain:

$$\dot{Q}'_j(t) = \sum_{n=1}^{M}[\Psi_n(\boldsymbol{x}_{Ij}) - \Psi_n(\boldsymbol{x}_{Ej})]\eta_n(t-\tau)\frac{n\overline{\dot{Q}}}{\xi\rho\overline{v}^2}\delta(\boldsymbol{x} - \boldsymbol{x}_{Ej}) \tag{7.26}$$

This expression can now be projected on the m^{th} mode to derive the source term S^m_{inj} corresponding to the j^{th} injector:

$$S^m_{inj}(t, \boldsymbol{x}_{Ej}) = \frac{(\gamma-1)n\overline{\dot{Q}}}{\Lambda_m\xi\rho\overline{v}^2}\Psi_m(\boldsymbol{x}_{Ej})\sum_{n=1}^{M}[\Psi_n(\boldsymbol{x}_{Ij}) - \Psi_n(\boldsymbol{x}_{Ej})]\dot{\eta}_n(t-\tau) \tag{7.27}$$

To obtain the complete source term one has to sum the previous expression over all injectors:

$$S^m_{inj}(t) = \sum_{j=1}^{N_f} S^m_{inj}(t, \boldsymbol{x}_{Ej}) \tag{7.28}$$

In principle one should use an interaction index n (not to be confused with the index n) and a time lag τ that are depending on the frequency of the different eigenmodes. This can be included, somewhat empirically by replacing the term $n\eta_m(t-\tau)$ by $n(\omega_m)\eta_m[t-\tau(\omega_m)]$. The values of $n(\omega_m)$ and $\tau(\omega_m)$ may then be determined at every iteration by reading a table. The table is in turn obtained via a simulation of a modulated jet as exemplified in chapter 2 where the interaction index is the gain shown in figure 2.32.

7.3.5 Source term induced by pressure fluctuations

As described in chapter 2 the influence of pressure on the heat release rate is relatively straight forward. In the case of cryogenic combustion there is no time lag since the combustion process can be considered to be infinitely fast. The interaction index is a constant and the model described in equation 2.40 indicates that this constant is approximately equal to 1/2.
Let us now consider the j^{th} injector and let $\dot{Q}_T$ the total heat release rate corresponding to the flame established by this injector. It is convenient to assume that the heat release takes place at a point $\boldsymbol{x}_{Ej}$ of this flame. The mean heat release rate per unit volume may then be described by $\overline{\dot{Q}}_j = \overline{\dot{Q}}_T \delta(\boldsymbol{x} - \boldsymbol{x}_{Ej})$ and the fluctuation of this quantity may then be deduced from:

$$\frac{\dot{Q}'_j}{\overline{\dot{Q}}_j} = \frac{1}{2}\frac{p'}{\overline{p}} \tag{7.29}$$

Hence,

$$\dot{Q}'_j = \frac{1}{2\overline{p}}\overline{\dot{Q}}_T \sum_{n=1}^{M} \eta_n(t)\Psi_n \delta(\boldsymbol{x} - \boldsymbol{x}_{Ej}) \tag{7.30}$$

The rate of change of the previous expression takes the form

$$\frac{\partial \dot{Q}'_j}{\partial t} = \frac{1}{2\overline{p}}\overline{\dot{Q}}_T \sum_{n=1}^{M} \dot{\eta}_n(t)\Psi_n \delta(\boldsymbol{x} - \boldsymbol{x}_{Ej}) \tag{7.31}$$

and this may be projected on the eignefunction Ψ_m to get the source term for a single injector:

$$\frac{\gamma - 1}{\Lambda_m}\int_V \frac{\partial \dot{Q}'_j}{\partial t}\Psi_m dV = \frac{1}{2\overline{p}}\frac{\gamma - 1}{\Lambda_m}\overline{\dot{Q}}_T \sum_{n=1}^{M} \dot{\eta}_n(t)\int_V \Psi_n \Psi_m \delta(\boldsymbol{x} - \boldsymbol{x}_{Ej}) dV \tag{7.32}$$

For a single injector one obtains:

$$[S_p^m]_j(t) = \frac{1}{2\overline{p}}\frac{\gamma - 1}{\Lambda_m}\overline{\dot{Q}}_T \sum_{n=1}^{M} \dot{\eta}_n(t)\Psi_n(\boldsymbol{x}_{Ej})\Psi_m(\boldsymbol{x}_{Ej}) \tag{7.33}$$

It is convenient to use the definition $b_m = \Lambda_m / V$ and write the last expression in the form:

$$[S_p^m]_j(t) = \frac{1}{2}\frac{\gamma-1}{b_m}\frac{\overline{\dot{Q}}_T}{\overline{p}V}\sum_{n=1}^{M}\dot{\eta}_n(t)\Psi_n(\boldsymbol{x}_{Ej})\Psi_m(\boldsymbol{x}_{Ej}) \tag{7.34}$$

One may now sum the previous expression over all the injectors to get

$$S_p^m(t) = \frac{1}{2}\frac{\gamma-1}{b_m}\frac{\overline{\dot{Q}}_T}{\overline{p}V}\sum_{n=1}^{M}\dot{\eta}_n(t)\sum_{j=1}^{N_f}\Psi_n(\boldsymbol{x}_{Ej})\Psi_m(\boldsymbol{x}_{Ej}) \tag{7.35}$$

This expression may be simplified by remembering that the eigenmodes are orthogonal so that

$$\sum_{j=1}^{N_f}\Psi_n(\boldsymbol{x}_{Ej})\Psi_m(\boldsymbol{x}_{Ej}) \simeq \delta_{nm}\sum_{j=1}^{N_f}\Psi_n^2(\boldsymbol{x}_{Ej}) \tag{7.36}$$

and the source term becomes

$$S_p^m(t) = \frac{1}{2}\frac{\gamma-1}{b_m}\frac{\overline{\dot{Q}}_T}{\overline{p}V}\dot{\eta}_m(t)\sum_{j=1}^{N_f}\Psi_m^2(\boldsymbol{x}_{Ej}) \tag{7.37}$$

7.4 Damping modeling

Dissipation of acoustic energy is represented by damping terms representing energy losses through the nozzle and in the injector channels. Damping can be increased by connecting resonators or quarter wave cavities to the thrust chamber or by inserting baffles to subdivide the injection backplane. Under reactive conditions, further damping can be induced by temperature fluctuations (Richecoeur et al. (2009)), mass momentum, flow reconfiguration and heat transfer relaxation associated with the spray of droplets. Acoustic non-linearities may have a great impact on damping as well. It has been shown (Culick and Yang (1995)) that non-linear terms define the limit cycle observed during high-frequency instabilities. In its present form the damping terms are constant parameters, which are typically included in the differential set of equations as first order time derivatives. If the source term becomes more important than damping, the system becomes unstable and the oscillation amplitude grows exponentially. In actual situations, the non-linear combustion response leads to a finite amplitude limit cycle. A realistic estimation of the chamber acoustic damping is difficult to achieve in the general case. One may for example try to estimate the linear damping at the chamber walls following an analytical method described in Searby et al. (2008).

7.5 Initial field

To start the simulation it is necessary to provide initial distributions of the state variables. This may be done by defining an initial energy release rate distribution corresponding to a deposition of energy over a finite region. One may also start in a more direct way by imposing a pressure distribution. These two possibilities are considered in what follows.

7.5.1 Initial energy deposition

In order to trigger an instability one has to perturb initial fields. If the initial field is at rest, needs to be locally taken out of equilibrium. In this section, a perturbation, which could also be attributed to a "bomb" or to other types of perturbations that naturally occur in a rocket engine ("spike" or "pops"), are modeled. The model is based on the work of Lacaze et al. (2009), in which ignition of rocket engines by a laser is modeled in a LES framework by defining an energy deposition scheme. The power added to the energy equation solved by the LES code follows a Gaussian distribution in space and time (equation 7.38).

$$\dot{Q}(\boldsymbol{x},t) = \frac{\epsilon_i}{4\pi^2\sigma_r^3\sigma_t}\exp\left(-\frac{1}{2}\left(\frac{r}{\sigma_r}\right)^2\right)\exp\left(-\frac{1}{2}\left(\frac{t-t_0}{\sigma_t}\right)^2\right) \tag{7.38}$$

Where r is the distance to the energy deposition center, t_0 is the time when the heat release $\dot{Q}$ is maximum, ϵ_i is the total amount of deposited energy, and σ_r and σ_t are the spatial and temporal widths of the deposition. To simplify the integration of this equation to the code, it is considered that the entire energy is unsteady, so that $\dot{Q} = \dot{Q}'$. The source term provided by this initial distribution of energy is:

$$S_{ext}^m(t) = \frac{\gamma-1}{\Lambda_m}\int_V \frac{\partial \dot{Q}'}{\partial t}(\boldsymbol{x},t)\Psi_n(\boldsymbol{x})dV \tag{7.39}$$

Contrary to other source terms, the energy deposition is time dependent and can be set at any given time during the simulation. For the Gaussian distribution the perturbation vanishes after a few σ_t.

7.5.2 Initial pressure distribution

To obtain the initial values, $\eta_n(0)$ and their time derivative $\dot{\eta}_n(0)$, one may consider that the initial pressure field is uniform except perhaps in a region of the chamber where some kind of perturbation is produced. This is modeled in

the present implementation by a Gaussian distribution of pressure. The initial pressure field is projected onto the eigenmodes providing the initial amplitudes:

$$p'(\boldsymbol{x},0) = \sum_{n=1}^{\infty} \eta_n(0)\Psi_n(\boldsymbol{x}) \tag{7.40}$$

This infinite sum must be truncated to a finite number of eigenmodes N. One may then obtain the corresponding initial amplitudes (equation 7.41).

$$\eta_n(0) = \frac{1}{\Lambda_n}\int_V p'(\boldsymbol{x},0)\Psi_n(\boldsymbol{x})dV \tag{7.41}$$

Where $\Lambda_n = \int_V \Psi_n^2 dV$. The integration is carried out on the mesh used to solve the Helmholtz equation. This yields N initial amplitudes $\eta_n(0)$. To obtain the initial derivatives of the modal amplitudes $\dot{\eta}_n(0)$ one applies a similar procedure to the initial distribution of the pressure time derivative, $\dot{p}'(\boldsymbol{x},0)$.

$$\dot{\eta}_n(0) = \frac{1}{\Lambda_n}\int_V \dot{p}'(\boldsymbol{x},0)\Psi_n(\boldsymbol{x})dV \tag{7.42}$$

It is interesting to note that the initial pressure field can only be reconstructed with an infinite number of eigenmodes since the theoretical projection basis is infinite. A large number of eigenmodes for projection will provide an initial projected pressure field that will be close to the solution.
The pressure deposition method is designed to represent the sudden pressure rise caused by the detonation of a small bomb. Bomb tests are commonly used in the certification of rocket engines for high frequency instabilities. It is difficult to precisely quantify the energy deposition in a combustion chamber since the amount of energy transmitted from the spark plug to the domain is not precisely known. The pressure deposition method bypasses the first few moments of the energy deposition to directly account for the sudden pressure rise due to local combustion. The value of the pressure deposition is well known and can even be theoretically quantified. The initial pressure distribution is conveniently based on a double Gaussian distribution of pressure in space and time.

$$p'(\boldsymbol{x},t) = p_0 \exp\left(-\frac{1}{2}\left(\frac{r}{\sigma_r}\right)^2\right)\exp\left(-\frac{1}{2}\left(\frac{t-t_0}{\sigma_t}\right)^2\right) \tag{7.43}$$

Where p_0 is the value of the pressure peak. The pressure gradient imposed by equation 7.43 is projected onto all eigenmodes of the system (equation 7.44).

This method can be used to test the stability of an operating point and verify if the system goes back to a equilibrium state after being pushed out of stability.

$$S_{ext}^{m}(t) = p_0 \omega_m^2 \exp\left(-\frac{1}{2}\left(\frac{r}{\sigma_r}\right)^2\right) \exp\left(-\frac{1}{2}\left(\frac{t-t_0}{\sigma_t}\right)^2\right) \tag{7.44}$$

7.6 External modulation by an actuator

It is useful to implement an external actuator to allow calculations of modulated configurations. In what follows we specifically wish to represent an actuator corresponding to the VHAM because this device has been used in hot fire experiments on the multiple injector combustor (MIC) and has also been employed in the NPCC experiments. The modulated cases investigated previously can serve as verification cases for the STAHF code. The VHAM described in chapter 3 may be represented by a combination of two isolated acoustic sources operating in phase opposition. These sources appear as fluctuating mass flow rates in the mass balance equation (equation 7.45).

$$\frac{\partial \rho}{\partial t} + \nabla \cdot \rho \mathbf{v} = \dot{m}_1 \delta(\boldsymbol{x} - \boldsymbol{x}_1) + \dot{m}_2 \delta(\boldsymbol{x} - \boldsymbol{x}_2) \tag{7.45}$$

Where $\boldsymbol{x}_1$ and $\boldsymbol{x}_2$ represent the nozzle positions where modulation occurs. The resulting wave equation takes the form:

$$\frac{1}{c^2}\frac{\partial^2 p'}{\partial t^2} - \nabla^2 p' = \frac{\partial \dot{m}_1}{\partial t}\delta(\boldsymbol{x} - \boldsymbol{x}_1) + \frac{\partial \dot{m}_2}{\partial t}\delta(\boldsymbol{x} - \boldsymbol{x}_2) \tag{7.46}$$

By using the modal expansion appearing in equation 6.19, equation 7.46 yields a differential equation system for the modal amplitudes exhibiting the source term due to the action of the VHAM. Once identified this term can be cast in the form :

$$S_{VHAM}^{m}(t) = \frac{1}{\Lambda_m}\left(\frac{d\dot{m}_1}{dt}\Psi_m(\mathbf{x_1})c^2 + \frac{d\dot{m}_2}{dt}\Psi_m(\mathbf{x_2})c^2\right) \tag{7.47}$$

The total mass flow rate is modulated by the VHAM and $\dot{m}_1 + \dot{m}_2 = \dot{m}_{tot}$. Considering the experimental results of part II, it is reasonable to consider a sinusoidal mass flow rate modulation. The modulated mass flow rates are then given by:

$$\dot{m}_1 = \frac{\dot{m}_{tot}}{2}(1 + \cos(\omega_e t)) \tag{7.48}$$

$$\dot{m}_2 = \frac{\dot{m}_{tot}}{2}(1 - \cos(\omega_e t)) \tag{7.49}$$

where ω_e is the modulation angular frequency. Finally the VHAM source term is expressed as:

$$S^m_{VHAM}(t) = \frac{\dot{m}_{tot}}{2\Lambda_m}\omega_e c^2(\Psi_m(\boldsymbol{x}_1) - \Psi_m(\boldsymbol{x}_2))\sin(\omega_e t) \tag{7.50}$$

The VHAM posses a semi-perforated wheel, this wheel can be modeled by considering its position at any given time during a run. If the nozzles are in the perforated part of the wheel then the source term is given in equation 7.50, otherwise $S^m_{VHAM} = 0$.

7.7 Conclusions

This chapter discusses the different models developed for the STAHF code. The modal expansion of the pressure field is used to specify the various possible source terms that can drive instabilities. These source terms are suggested by previous hot fire experiments (FAME model) or deduced from large eddy simulations carried out in the second chapter of this document. There is no intention here to cover all the possible processes leading to instabilities but merely to focus on those which appear to be the most important.

Chapter 8

Analysis of instabilities in a liquid rocket engine using the STAHF code

The final chapter in this document reports calculations carried out with the STAHF tool. These calculations are aimed at predicting combustion instabilities in a full-scale rocket engine designated as the BKD and operated by DLR. This engine features natural high frequency instabilities. Simulations are carried out for two load points, one of which is stable while the other is unstable. The STAHF framework is first tested in the NPCC configuration to show that pressure fluctuations obtained with STAHF are in good agreement with experimental data recorded on the lateral boundaries of the main chamber, provided that suitable damping coefficients are included in the dynamical solver. Calculations of the eigenmodes of the BKD test rig are carried out and reveal that there is a strong coupling between the injector plenum or dome and the combustion chamber for the unstable load point. The damping coefficients were tuned in order to make the unstable load point just unstable and then kept constant to study the stable load point case. FAME as well as the pressure model were used as driving mechanisms for the instability. Simulations were also carried out by making use of the pressure deposition scheme to initiate the calculations. Results of the simulations demonstrate that these load points feature stable and unstable dynamics as expected, the pressure fluctuations are reduced in the stable load point case while they diverge for the unstable load point. The introduction of a pressure bomb in the domain triggers pressure fluctuations, which makes the pressure fluctuations diverge for the unstable load point but does not trigger an instability for the stable load point.

8.1 Introduction

The possible occurrence of high frequency combustion instabilities in engines needs to be carefully investigated and usually requires systematic testing. The high frequency certification of rocket engines (see Klem and Fry (1997)) relies on a large number of tests that assure that there are no accessible regions in the domain of operation where combustion instabilities might occur. The engine is usually tested on a bench in a range of conditions. This is shown schematically in figure 8.1 where an engine operating point is represented. This point is defined by two or more parameters. Around this point are areas (blue and red rings in figure 8.1), that represent limit conditions under which the engine has to perform correctly. A lot of operating conditions belonging to the areas around the operating points have to be tested in a systematic fashion. Engine tests

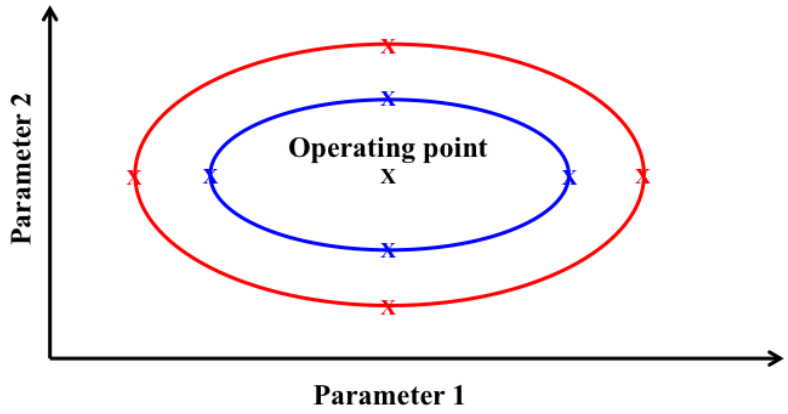

Figure 8.1: *Operating point of an engine defined by two parameters. The red and blue areas around the operating point represent operating conditions where the engine has to correctly perform with regard to combustion instabilities.*

are quite expensive and some of them are believed to be superfluous. Ideally only a handful of operating conditions should be experimentally validated while the rest might be analyzed by simulation. These simulations need to provide a trend that indicates which parameters could trigger and drive combustion instabilities. It is believed that these simulations could be performed by using reduced order dynamical modeling. Ultimately, the reduced order dynamical code STAHF might be able to provide the required information. As the model essentially relies on integration in the time domain of a set of coupled differential equations one can imagine to scan many operating conditions on any kind of geometry, provided the correct models are used for the simulation (see chapter 7 for a description of the models implemented in STAHF).
The STAHF tool is used in what follows to provide a short assessment of its predictive capacities. A partial validation is first carried out in section 8.2

where the STAHF tool is tested on the NPCC configuration. This illustrates the performance of the tool in a well controlled cold flow experiment. A full-scale rocket engine is then analyzed in section 8.3 and is used to study combustion instabilities. Results obtained in this special case are discussed in section 8.4.

8.2 STAHF validation

Before using the STAHF tool on a full-scale rocket configuration, it is necessary to check the method presented in chapter 6 and some of the models provided in chapter 7. To do so the STAHF tool is used to examine the model scale cold flow geometry, the NPCC test rig. The experimental database is used for direct comparison with calculations. The NPCC test rig, presented in chapter 3, is a good candidate to test the STAHF tool. The NPCC test rig is a cold flow experiment, which requires a small number of models to operate.

8.2.1 Simulation preparation

The first step in the application of STAHF consists in choosing the appropriate framework as described in figure 7.1. The geometry is that of the NPCC test rig equipped with the VHAM (see chapter 3). The acoustic field is projected onto four eigenmodes: 1T, 1T1L, 1T2L and 1T3L. The initial pressure field inside the NPCC test rig corresponds to no pressure fluctuation $p'(\mathbf{x}, 0) = 0$. There are no combustion source terms in this cold flow case. The VHAM, described in chapter 7 as an excitation source, requires a mass flow rate as well as a modulation frequency. The mass flow rate chosen is that specified in chapter 4 and the modulation frequencies correspond to the 1T, 1T1L, 1T2L and 1T3L determined with AVSP. The choice of the damping coefficient for each eigenmode is based on the values found in chapter 5 (table 5.1).
With this particular framework, the data from chapters 3, 4 and 5 provide a basis for comparisons with results obtained from the simulation.

8.2.2 Results

The pressure sensors positions of the NPCC test rig (mentioned in figure 3.6) can be used to compare the temporal evolution of pressure fluctuations in the domain during the simulation. A pressure sensor at the HFc1 position is used to compare simulation results to the experimental data of the NPCC test rig. Results are presented for four eigenmodes in figure 8.2. The efficiency of the VHAM is an unknown of the simulation. As presented in figure 3.9, some of the mass flow rate exhausted by the nozzles does not traverse the perforated wheel. It is difficult to evaluate the lateral leakage directly on the test rig but an efficiency coefficient needs to be used to reduce the mass flow rate modulated in the simulation. To determine this coefficient, the pressure signal of the 1T eigenmode shown in figure 8.2 provides a reference. The pressure

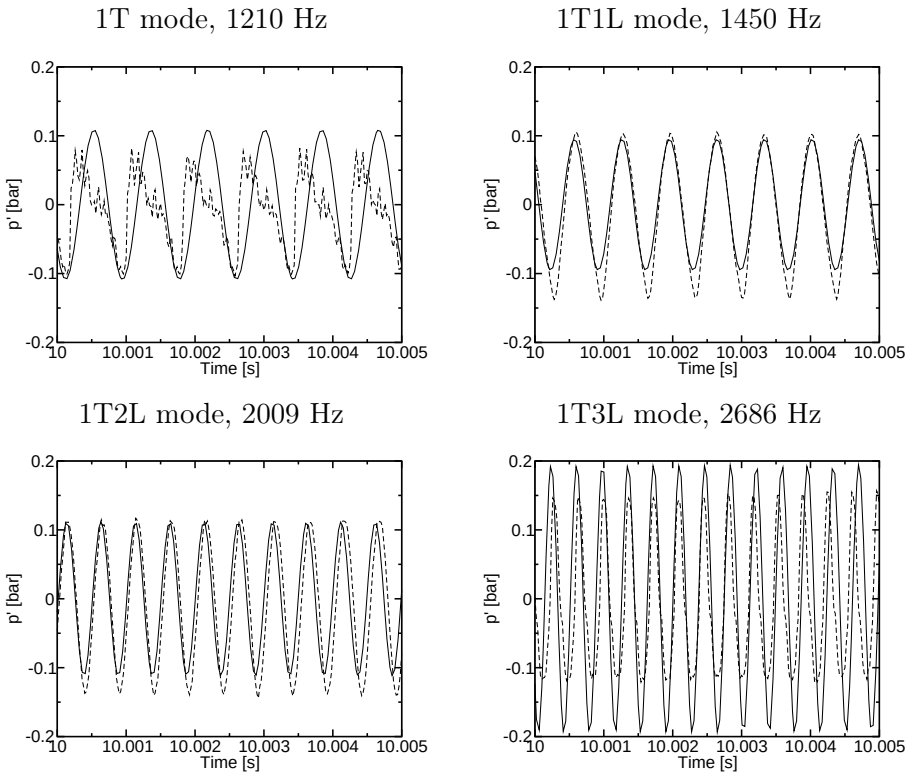

Figure 8.2: *Comparison between pressure signals from −− (dashed line) the experimental data and −(solid line) the simulation for four eigenmodes.*

signal of 1T is used since its quality is low. The efficiency coefficient is tuned until the experimental curve and the simulation curve of the 1T eigenmode are superimposed. The efficiency coefficient is then kept constant for all other simulated cases. One can see that for all these cases the experimental curves and the simulation curves are in good agreement. The small phase shift between the experimental and simulated data is due to the difference in the frequencies found for the eigenmodes (table 3.2) and the experimental eignefrequencies.
The STAHF software works well in this case and yields a temporal evolution of pressure fluctuations that is in agreement with experimental data. This means that the STAHF tool may give useful results if the models defined in the previous chapter are physically relevant.

8.3 Modeling of a full scale rocket engine

The full-scale rocket engine proposed for this study is the BKD presented in more detail in appendix C (DLR (2013)). This engine is interesting because it is a naturally unstable engine. Two different load points, or LP, are considered in what follows: LP3, that is naturally stable and LP4, that is naturally unstable. Details of LP3 and LP4 are given in table C.1 of appendix C.

8.3.1 Sound velocity

LP3 and LP4 have the same mixture ratio, which give rise to an adiabatic flame temperature of 3500 K approximately. Under such a high temperature and even for a high pressure (of about 8 MPa) the perfect gas equation of state can be assumed for the burnt gases. The sound velocity c can be deduced from equation 8.1:

$$c = \sqrt{\gamma r T} \tag{8.1}$$

where γ is the specific heat ratio which is typically equal to 1.3 for burnt gases, r is the gas constant for the burnt gases and T the temperature. The analytical value of the sound velocity for the LP3 and LP4 are around 1400 $\mathrm{m.s^{-1}}$. While it is in good agreement with the experimental data from DLR for LP4, average sound speed for LP3 is experimentally determined to be around 1200 $\mathrm{m.s^{-1}}$. In order to properly match the eigenfrequencies of the test bench, the sound velocities estimated by DLR are used in the following calculations. The disagreement between the previous simple analytical calculations and the experimental measurements could be due to the strong inhomogenities of sound speed in the chamber, especially for LP3 where flames are expected to be much longer than for the unstable LP4 (Urbano et al. (2016)).

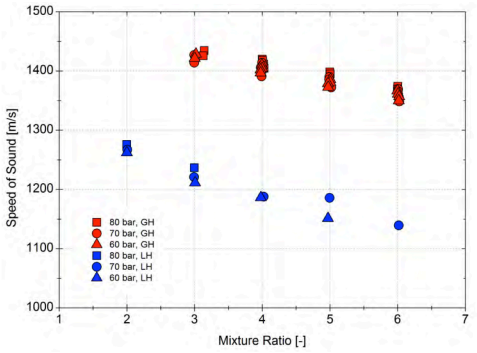

Figure 8.3: *Experimental sound speed in the BKD chamber. Image courtesy of DLR.*

8.3.2 Initial conditions

The initial field for the simulation corresponds to cold propellants in the dome and injectors and hot burnt gases in the thrust chamber. The combustion region is represented by a thin zone located at the injection plane. This generates a local gradient of sound velocity in the injector area. The initial solution provides the field of sound velocity inside the geometry to solve the Helmholtz equation (equation 6.21). It is interesting to note that the initial field could be replaced by a mean field deduced by averaging an LES solution. The mean pressure and sound velocity deduced from LES solution would then be projected onto the mesh (figure 8.4) used to solve the Helmholtz equation.

8.3.3 Modal identification

The eigenmodes and eigenfrequencies are obtained with the AVSP code, a Helmholtz solver developed at CERFACS (Nicoud et al. (2007); Selle et al. (2006)). Before running this code it is necessary to impose the mean temperature distribution onto the mesh of the BKD test rig, figure 8.4. This mesh comprises 228 000 nodes and 1 105 000 tetrahedra. Hydrogen dome and feeding lines are neglected, as they are expected to be weakly coupled with the chamber. The initial solution provides the initial conditions defining the mean density and temperature in the system.
The thermodynamic conditions in the dome are those of a real gas. The data was taken from the NIST database (Lemmon et al. (2012)). In the injectors downstream side, the temperature and pressure are set to reflect the hot environment of the combustion chamber. Sound velocities in the chamber are those determined experimentally by DLR. The various walls are treated as rigid boundaries (zero normal velocity) except for the nozzle of the domain, which is represented by an admittance condition (Marble and Candel (1977)). A set of eigenfrequencies for LP3 (the stable load point corresponding to injection of low temperature hydrogen) are displayed in figure 8.5 while the eigenfrequencies for LP4 (the unstable load point corresponding to higher temperature

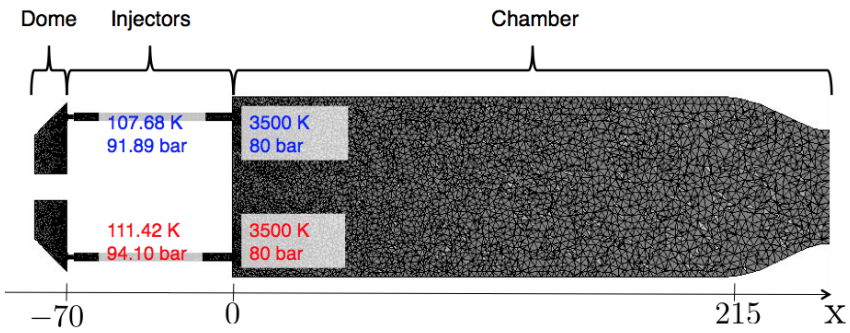

Figure 8.4: *Longitudinal slice of the mesh used in the modal identification carried out with AVSP and injection conditions corresponding to LP3 and LP4 operating points.*

hydrogen injection) are displayed in figure 8.6.
The AVSP code yields a large number of eigenmodes and eigenfrequencies. Some of these frequencies correspond to purely longitudinal modes such as the 3L mode at 6565 HZ and others pertain to mixed modes like the spinning-longitudinal modes. It is interesting to note that the 1A, 1A1L and 1A2L are respectively found at frequencies of 8167 Hz, 8606 Hz and 9482 Hz (the A in the mode stands for azimuthal, the mode may be spinning or standing), the modal structure in the chamber is coupled with the modal structure inside the dome. In this cavity, for the three modes presented in figure 8.5, the azimuthal mode is weakly coupled to the chamber indicating that the maximum pressure in the dome faces a maximum of pressure in the chamber. This type of coupling will only create small pressure differences between the inlet and outlet of the various injectors and, following the injector dynamics model presented in chapter 7, it is expected to induce weak mass flow rate fluctuations in the injection channels. This may probably be less favorable for instability.
In the LP4 case, a set of eigenfrequencies found by the AVSP solver are displayed in figure 8.6.
In comparison with the modes for LP3, the modes for LP4 correspond to significantly higher values. The 3L mode is at 9991 Hz and the mixed modes 1A, 1A1L and 1A2L are at 10280 Hz, 10749 Hz and 11811 Hz, respectively. These frequencies are close to the frequencies of self-sustained instabilities found in the experiment. Contrary to LP3, the maximum pressure in the dome faces a minimum of pressure in the chamber. This type of coupling will promote a process of mass flow rate fluctuation which could sustain the instability by a kind of "push-pull" response of the injection units. Eigenfrequencies for cases LP3 and LP4 are indicated in table 8.1.
The most dangerous modes are the azimuthal ones and will be used as basis of projection. Longitudinal modes, that occur only at lower frequencies, are not taken into consideration here since only high frequency oscillations are being investigated. Higher order azimuthal modes (like 2A and above) occur frequen-

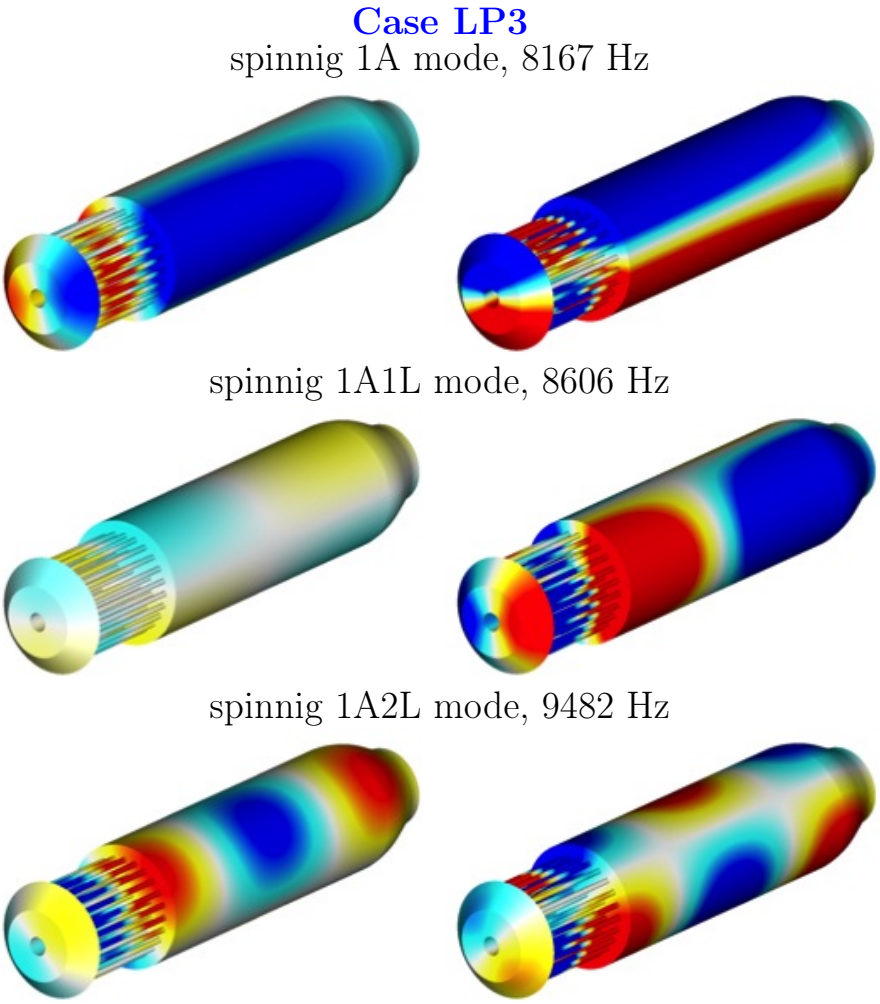

Figure 8.5: *Eigenmodes for case LP3.*

Mode	3L	1A	1A1L	1A2L
Frequencies for case LP3 [Hz]	6565	8167	8606	9482
Frequencies for case LP4 [Hz]	9991	10280	10749	11811

Table 8.1: *Eigenfrequencies for cases LP3 and LP4 corresponding to the modes displayed in figure 8.5 and 8.6.*

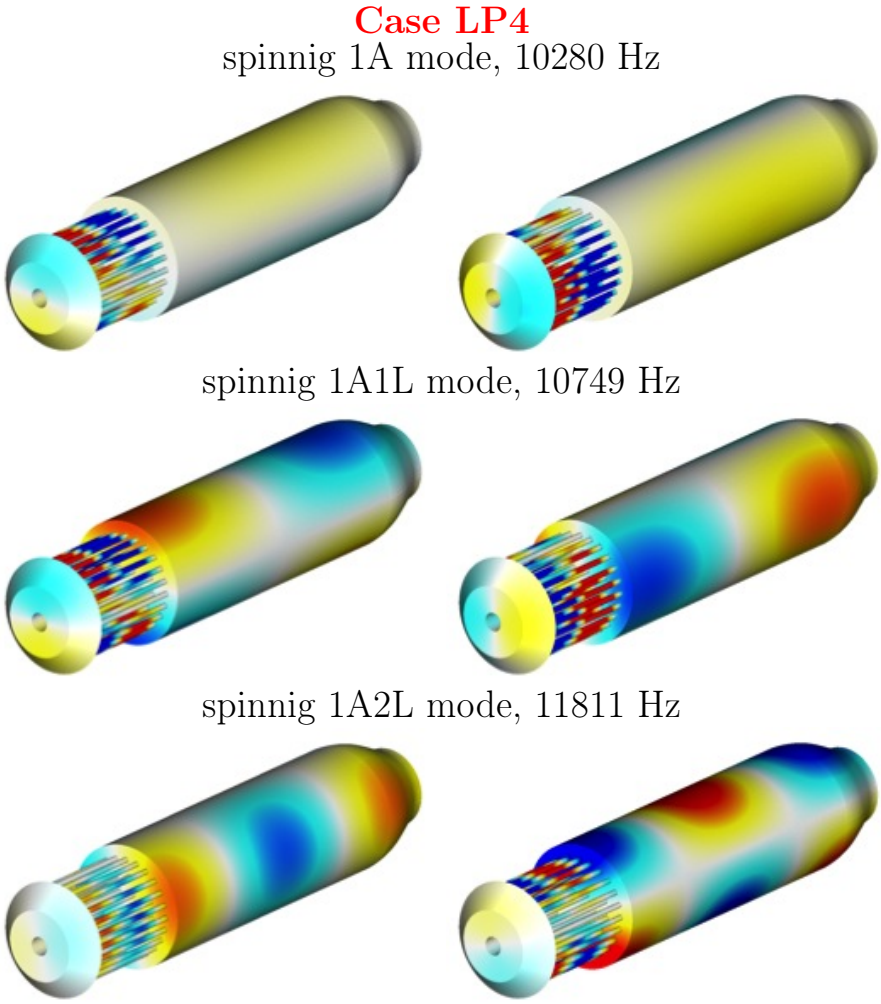

Figure 8.6: *Eigenmodes for case LP4.*

cies that can be left out, at least in a first analysis. The basis of projection is then 1A, 1A1L and 1A2L for LP3 and LP4.

8.3.4 Combustion source term

Chapter 7 provides expressions for the source terms that potentially drive combustion instabilities. These source terms directly compete with damping.
Transverse velocity nodes and anti-nodes are expected in the combustion chamber, therefore the FAME model in its cylindrical formulation is used. For the studied load points, LP3 and LP4, the average pressure in the chamber is 8 MPa. The total engine power of the BKD engine can be estimated around 87.27 MW for LP3 and 86.97 MW for LP4. The BKD has 42 injectors which means that the average heat release rate of a single injector is 2.08 MW and 2.07 MW for LP3 and LP4 respectively.
Chapter 2 has revealed that pressure fluctuations may be an important driving mechanism of combustion instabilities. It is also worth noting that combustion of oxygen and hydrogen is quite fast so that combustion in the BKD engine may be treated in the infinitely fast chemistry limit. For the pressure source term described in chapter 2, this means that there is no delay between the pressure fluctuations and the heat release rate fluctuations and that the interaction index is equal to the theoretical value of 0.5.
The influence of mass flow rate fluctuations on the heat release, described in chapter 2, showed that for very high frequencies the gain of the FTF was quite low, indicating that the heat release rate is probably not affected by mass flow rate fluctuations. In figure 8.7, the FTF between mass flow rate fluctuation and heat release rate fluctuation, for the studied load points of the BKD, is plotted by making use of the model that utilizes an average heat release rate from LES (defined in chapter 2). It can be seen that for frequencies greater than 6000 Hz the gain is relatively low. For the BKD the modal projection involves eigenmodes at frequencies exceeding 8000 Hz and one may consider that the injector dynamics source term is negligible in the range of interest and does not need to be considered.

8.3.5 Excitation source term

Rocket engines are tested by making use of small bombs that may eventually trigger an instability. The bomb excites the resonant modes and drives the system away from its equilibrium state and this is used to see if the system goes back to its stable state or if oscillations occur and grow into a limit cycle. In order to see if LP3 and LP4 are stable or unstable, an initial pressure distribution is placed in the middle of the combustion chamber with a pressure peak equal to 20% of the average pressure in the combustion chamber. The spatial and temporal characteristics of the bomb are displayed in figure 8.8.

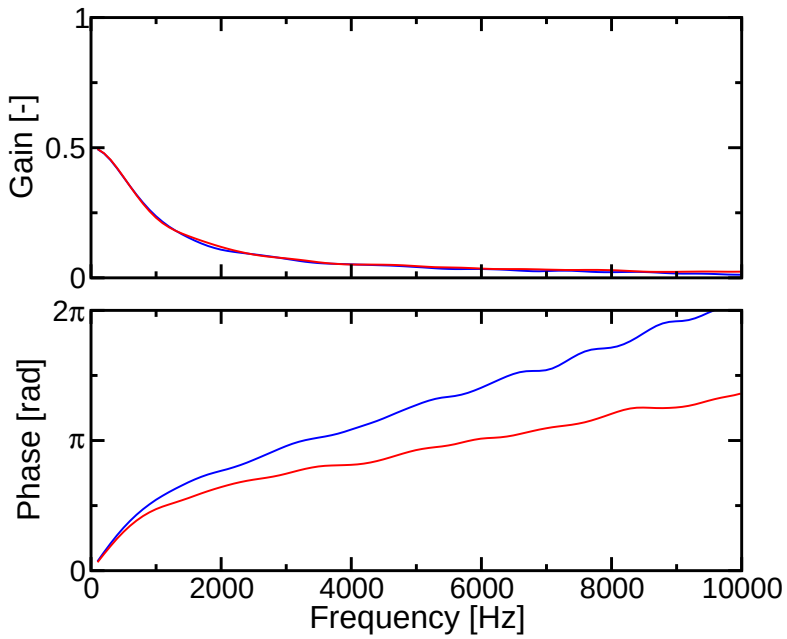

Figure 8.7: *Flame transfer function between the injection velocity fluctuations and the heat release rate fluctuations for LP3 and LP4 operating points.*

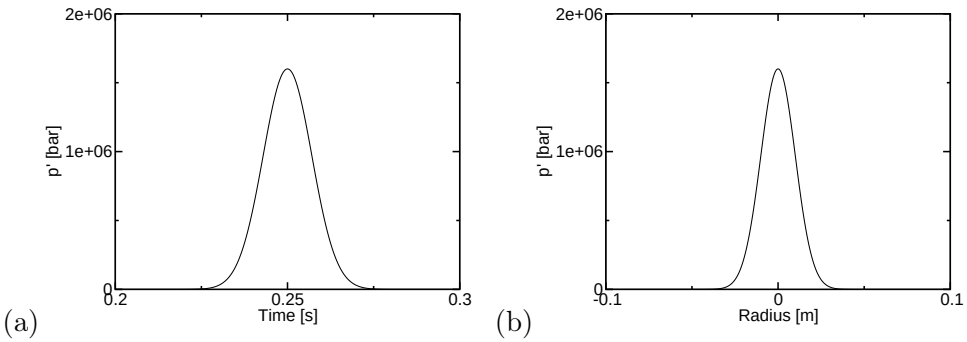

Figure 8.8: *(a) Temporal and (b) spatial characteristics of the bomb. It is characterized by a 20% average combustion pressure peak and is set off in the middle of the combustion chamber.*

8.3.6 Damping

It was indicated previously that the level of damping was not easy to determine because the sources of damping are not well identified and there is no analytical method to estimate the damping coefficient of a given geometry. There are currently no information on the damping coefficient on the BKD test rig. The determination of the damping coefficient is necessary for the STAHF tool. It is worth noting that the damping coefficients in STAHF ξ_m need to be multiplied by the angular frequency to obtain the damping rates α_m. The relation between ξ_m and α_m is $\xi_m = \alpha_m/(2\pi f_m)$, where f_m is the frequency of the m^{th} eigenmode. The damping rate of each eignemode of LP4 is set to a specific value where LP4 is just unstable. The damping coefficients are then kept constant in all other calculations and in particular in those corresponding to LP3. Table 8.2 provides the damping rate values used for LP3 and LP4.

Mode	1A	1A1L	1A2L
Damping rate [s^{-1}]	2258	2482	2592

Table 8.2: *Values, for each eigenmodes, of the damping rates used for the reduced order modeling of the BKD.*

8.4 Results and discussion

During the STAHF simulation, the pressure signal is recorded at two positions corresponding to two of the pressure sensors of the BKD test rig (figure C.2). This signal is used to follow the evolution of the pressure field in the near field of the thrust chamber backplane.

8.4.1 Spatially uniform initial perturbation

The initial solution is, in this test, uniform over the whole domain (this corresponds to a spatially constant perturbation). This initial solution is projected on a basis comprising the first three azimuthal modes (1A, 1A1L and 1A2L). Other modes are also triggered but their influence will not be calculated. This is acceptable if the modes are weakly coupled (i.e. each mode is essentially independent of the other modes). Figure 8.9 displays the pressure signal for LP3. The oscillations generated by the uniform perturbation are damped so that the pressure oscillation amplitude diminishes with time. The instability driving mechanisms are weaker than the damping mechanisms. This behavior is characteristic of a stable system. A closer look at the pressure signal (figure 8.10) reveals the presence of more than one frequency however one in particular stands out, the frequency corresponding to 1A2L. The power spectral density of the signal reveals that the frequency content is essentially defined by the modal eigenfrequencies.

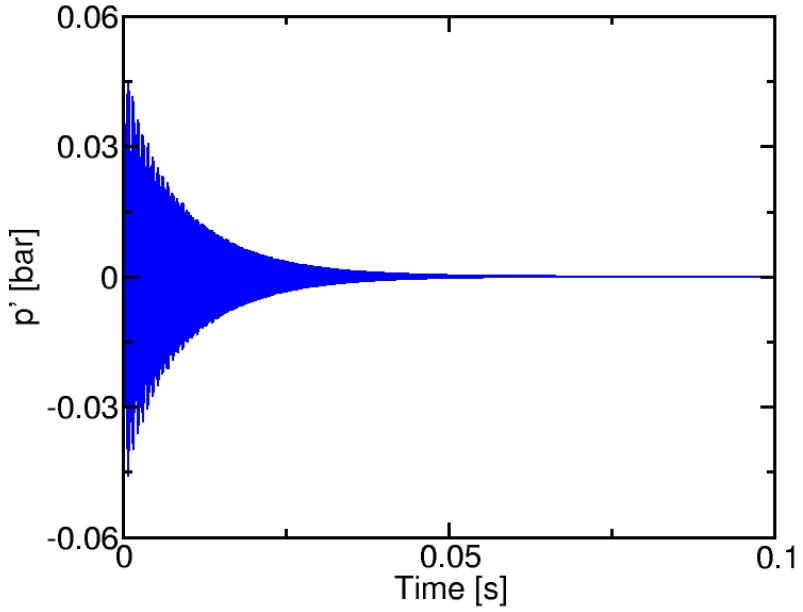

Figure 8.9: *Temporal evolution of the pressure fluctuation inside the BKD test rig for LP3.*

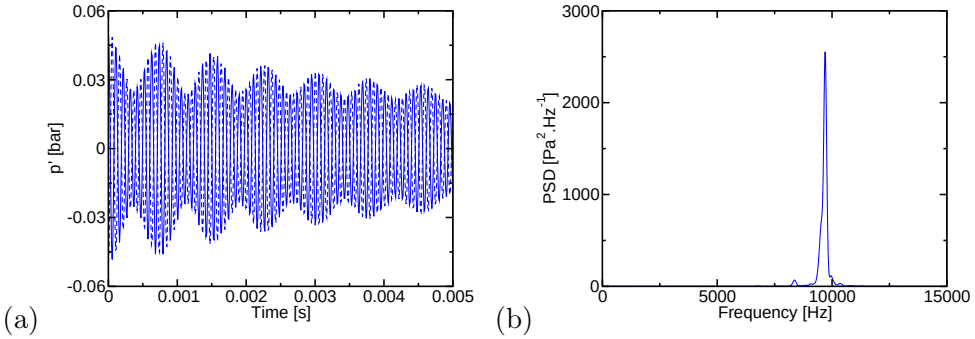

Figure 8.10: *(a) Temporal evolution and (b) Power spectral density of the pressure fluctuation inside the BKD test rig for LP3 using Welch's method, with 5 blocks, 50 % overlapping, zero-padding and a frequency resolution of $\Delta f = 20$ Hz.*

The pressure signal corresponding to the simulation of LP4 is displayed in figure 8.11. In this case the pressure fluctuations increase with time. The growth rate exceeds the damping rate and the system is unstable. A closer look at

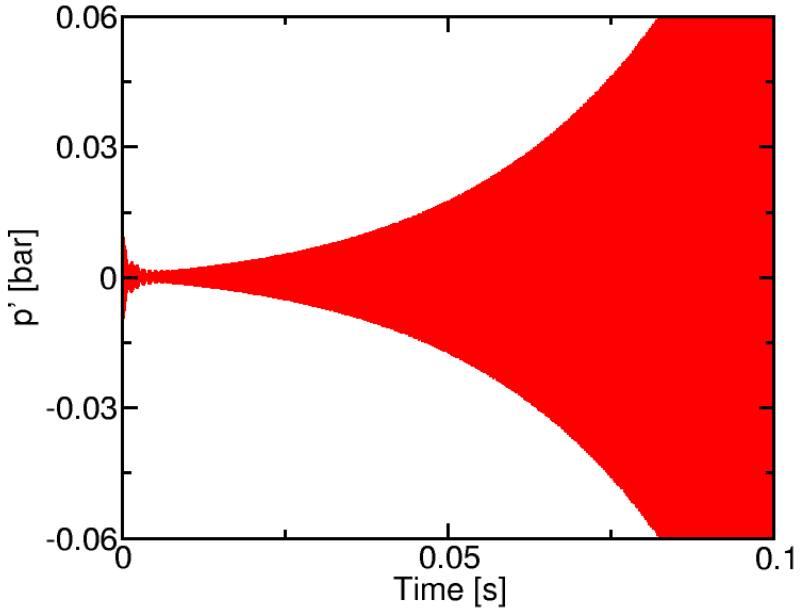

Figure 8.11: *Temporal evolution of the pressure fluctuation inside the BKD test rig for LP4.*

the temporal evolution of pressure fluctuations for LP4 (figure 8.12) indicates that the pressure divergence is fairly quick. In general a limit cycle will be reached in this case and requires a model that handles non-linear effects, which is not present in the current version of STAHF. The PSD, indicates that the pressure oscillations for LP4 are defined by the eigenfrequencies of the azimuthal eigenmodes with one frequency standing especially out, the frequency of 1A2L. Because of the increase of pressure fluctuations amplitude, the amplitude of the PSD of LP4 is a higher than that observed in the PSD for LP3.
The previous simulations indicate that the STAHF code is able to distinguish between stable and unstable conditions after adjusting the damping coefficients of the different modes.

8.4.2 Triggering with an initial pressure distribution

It is interesting to attempt instability triggering by making use of an initial pressure distribution. Results obtained with such a method (corresponding to a bomb test) are displayed in figure 8.13 for LP3 and LP4. The initial perturbation is seen to die-off while small oscillation appear for LP3 and LP4. After some time the pressure signal from LP3 is lower in amplitude and it

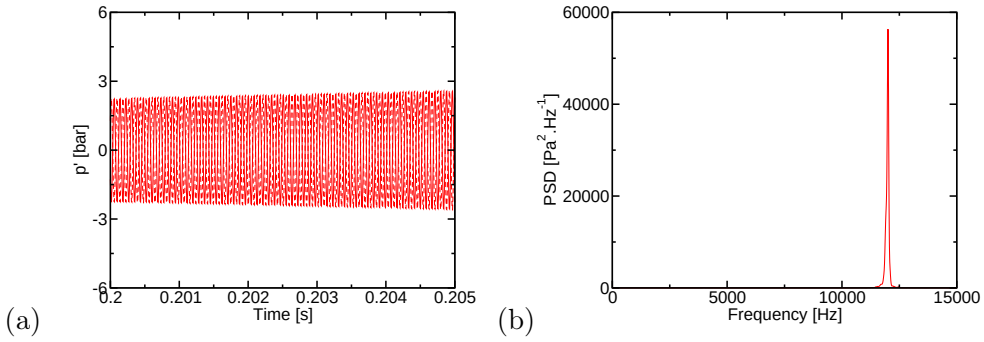

Figure 8.12: *(a) Temporal evolution and (b) Power spectral density of the pressure fluctuation inside the BKD test rig for LP4 using Welch's method, with 5 blocks, 50 % overlapping, zero-padding and a frequency resolution of $\Delta f = 20$ Hz.*

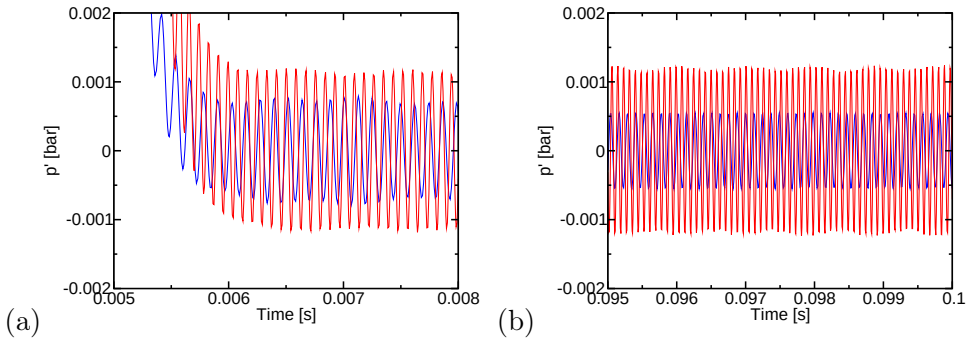

Figure 8.13: *Temporal evolution of pressure (a) right after a bomb test and (b) a small time after for LP3 and LP4 operating points.*

decays. The pressure oscillations of LP4 are larger and they grow very slightly in time indicating that the system is unstable. It is unclear why the growth rates of the oscillations after a bomb test (figure 8.13) are different from those displayed in figures 8.9 and 8.11. The only difference between these two cases is initial solution.
The PSD of the signals presented in figure 8.13 are displayed in figure 8.14. The power spectral density of LP3 and LP4 after a bomb test shows that, just like in figures 8.10(b) and 8.12(b), the frequency content is mostly defined by the frequency values of the respective eigenmodes of LP3 and LP4. These tests

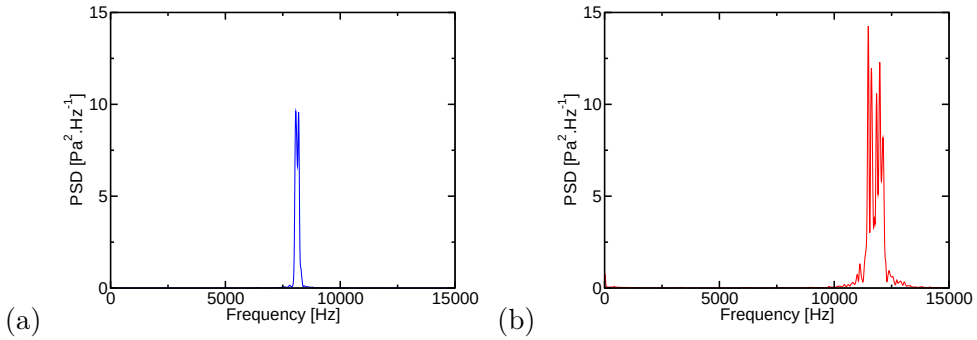

Figure 8.14: *Power spectral density of the pressure signals after a bomb test for (a) LP3 and (b) LP4 using Welch's method, with 5 blocks, 50 % overlapping, zero-padding and a frequency resolution of* $\Delta f = 10$ *Hz.*

indicate that the instability may be triggered by a "bomb" like test. The outcome of this test is naturally dependent on the driving models chosen for the simulation. It would also be important to model the combustion nonlinearity to obtain limit cycles instead of exponentially diverging signals. Concerning damping one possible route might be to use computational methods such as that developed by Lorentz (Fiala (2010)) and Lieuwen (Lieuwen et al. (2001); Lieuwen (2005)). Alternatively damping coefficients might be determined experimentally from bomb tests in combination with low order simulations. This may be assimilated to a calibration which would be carried out once and the code could then be used with no further adjustment.

8.5 Conclusion

In this chapter the reduced order modeling tool STAHF is first used to retrieve experimental data gathered in the NPCC test rig. By using one of the results of the test rig to calibrate the model, the code was able to closely reproduce experimental data. This partially validates the global framework underlying the STAHF tool and indicates that the code can be used to analyze more complex configurations such as full-scale rocket engines.

The BKD test rig, a naturally unstable rocket engine operated at DLR Lampoldshausen, is used to test STHAF in a real life application. The eigenmodes found with the Helmholtz solver AVSP reveal that there is a notable difference in the modes corresponding to the stable and unstable load points. In the last case the dome and chamber feature a strong coupling which is expected to promote instability. The central issue in this analysis is to provide a suitable model for the unsteady heat release rate. This is done by making use of the FAME model which is based on the idea that the fluctuations in heat release rate are a direct consequence of the flame displacement by the transverse velocity components induced by the acoustic pressure field in the chamber as well as by a pressure model based on the idea that the pressure fluctuations have a direct impact on the heat release rate fluctuations. Various methods are used to initiate the calculation. One central issue is that of the proper estimation of the damping coefficients. The damping coefficients need to be defined for the various resonant modes. The absence of data on the damping of the BKD test rig requires an adjustment of the damping coefficients for one case in order to make the LP4 marginally unstable. It is then found that LP3 is stable. One may then consider that the code is able to retrieve the observed behavior after adjusting the damping rates. The reduced order dynamic modeling implemented in STAHF tool constitutes an attempt to represent complicated couplings between acoustic modes and combustion. One advantage is its simplicity and effectiveness. On the other hand, the value of predictions heavily rely on the quality of the modeling. It would be important to represent the nonlinearity inherent to combustion processes to predict limit cycles and eventually account for possible triggering and mode switching processes. It would be interesting to include higher order azimuthal radial modes in the pressure modal expansion. Damping rates might also be improved to account for nonlinear effects and to better describe the processes dissipating acoustic energy. In this respect, much can be obtained from Large eddy simulations as exemplified in the first part of this document. Furthermore experiments can provide benchmark data to be compared with specific STAHF simulations.

Conclusion

Combustion dynamics issues are often encountered during the development of high performance devices like rocket engines. The subject has been around for a long time and has been extensively investigated. Efforts carried out in the REST (Rocket Engine STability) framework have led to a range of novel results pertaining to the fundamental mechanisms driving instabilities and much work has focused on experimentation and development of new simulation tools. The present investigation carried out at EM2C laboratory was aimed at acquiring knowledge and deriving tools for reduced order modeling of combustion instabilities. The general idea has been to use simulation and experimentation in parallel to derive simplified descriptions that could be included in a dynamical description of instabilities. Investigations were focused on liquid rocket engines fed with cryogenic propellants which have been in the core of the Ariane launcher developments in Europe.

The first part of the present investigation is focused on the numerical study of jets under different modulation conditions. Large eddy simulations are used to examine the dynamics of a round transcritical nitrogen jet interacting with a transverse acoustic mode. The jet stream is injected under transcritical conditions into a hot quiescent medium. It was found that the jet motion is notably influenced by the modulation frequency and amplitude. This was examined by considering a wide range of Strouhal numbers and modulation amplitudes. The study indicates that, in the presence of acoustic modulation, the jet is shortened in the axial direction and is flattened in the span wise direction. The data indicates that low pressure regions formed on both sides of the jet could explain the observed span wise flattening. Another set of calculations where the jet is placed in a traveling acoustic wave field indicates that the jet dynamics is quite similar to what is observed in a standing wave field. These calculations were then used to propose a model describing the kinematics of the jet centerline which combines hydrodynamic and acoustic components. This can be used in a reduced order model to represent the jet dynamics in the thrust chamber.
Large eddy simulations were also used to examine a coaxial flame of LO_x/GCH_4 submitted to mass flow rate and pressure modulations. The analysis focuses on the heat release response of the jet when the mass flow rate is perturbed. A simple model indicates that the global heat release response is controlled by

a Helmholtz number based on the modulation frequency, the flame extent and the injection velocity. It was found that the gain and phase are directly influenced by these parameters. Large eddy simulations confirm that this is indeed the case. Some simple arguments indicate that the pressure effect results from changes in the rate of conversion in the flame elements submitted to strain rates induced by the turbulent flow field. Simulations are used to examine this interaction and in particular to deduce the gain and phase of this process. A model was then developed to link the heat release rate fluctuations to pressure fluctuations.

The second part of this study is concerned with issues related to the injector impedance, coupling between the plenum and thrust chamber and damping rates. A test rig was developed to study these acoustic features of combustion instabilities by making use of a laboratory scale experiment. The test rig was designed to allow measurements of injection velocities at the injector outlets and pressure fluctuations at the lateral boundaries of the two cavities composing the test rig. Acoustic modulation was achieved by making use of a set of perforated wheels. The test rig allows the study of injector response and possible coupling mechanisms between the plenum and the thrust chamber. These questions are investigated by making use of a model scale simulator, which links the injection velocity fluctuations to the pressure drop between the cavities. The model outputs are in good agreement with experimental results. There is no reliable theoretical method for the determination of damping rates. In this study a method has been developed to measure the damping rates of different eigenmodes in the test rig. This experimental method has proven to be robust and shows good repeatability.

The third group of investigations reported in this document pertains to the dynamical modeling of combustion instabilities. The framework relies on modal expansion of the state variables. This modal approach provides a physical description of the interactions inside the system. It is used to represent the driving and damping processes and the many other processes which can be at work. The reduced order model is embedded in the STAHF code. Models deduced from simulations and experimentation during the course of the present investigation are implemented in the STAHF code. The code was first checked by making use of cold flow experiments on the test rig. Results of the simulation are in good agreement with experimental measurements. STAHF was then used to examine the stability behavior of a rocket engine designated as the BKD and operated by DLR. Experiments on the BKD indicate that under certain conditions this system becomes unstable. After adjustment of some control parameters, STAHF was able to reproduce this behavior.

The various investigations reported in this document have all been focused on advanced understanding and developing predictive methods for combustion in-

stability in liquid rocket engines. This study has allowed a better identification of the driving sources of instabilities and the derivation of some simplified descriptions of the sources driving the instabilities. The flexibility of the test rig developed in this study allows also investigations of the influence of parameters such as chamber length, injector number and average chamber pressure and temperature on the dynamic of combustion instabilities. In addition to the findings of this research further studies could be carried out in the future. For example: the study of nonlinearity of the combustion response, the use of radial mode in the modal expansion and a extended determination of damping mechanisms in rocket engines.

Appendix A

Real gas thermodynamics

Perfect gas laws cannot be used in the high pressure environments found in rocket engines. Third order state equations have to be used in the solvers (Oefelein (2005)). The Soave-Redlich-Kwong (SRK) and the Peng-Robinson (PR) Equations Of State (EOS) are well adapted for large eddy simulation of high pressure cryogenic systems. Figure A.1 displays the evolution of nitrogen density with temperature at a supercritical pressure of 10 MPa. The Soave-

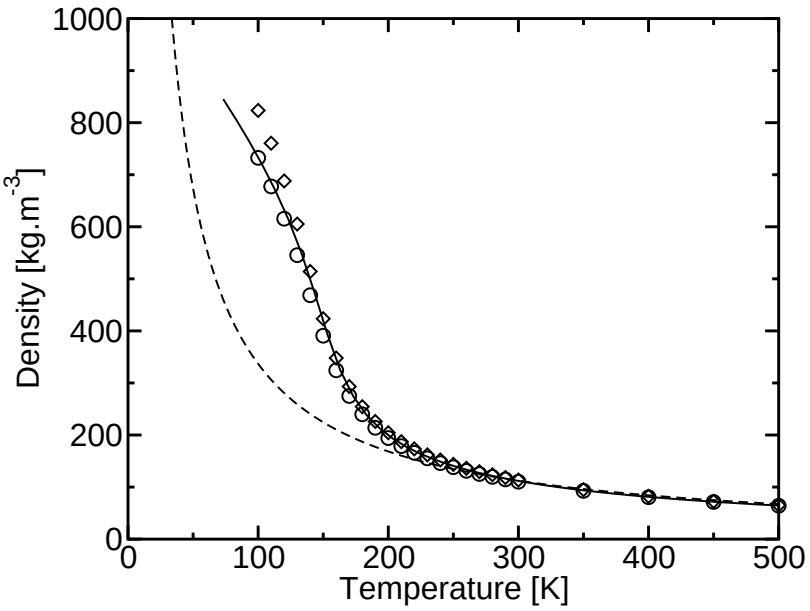

Figure A.1: *Evolution of nitrogen density with temperature at a supercritical pressure of 10 MPa ($p_c = 3.3956 MPa$, $T_c = 126.192 K$, $\omega = 0.0372$) for different EOS.– NIST database, −− perfect gas EOS, ∘ SRK EOS and ◊ PR EOS.*

Redlich-Kwong EOS yields suitable results when compared to the reference curve obtained from NIST (National Institute of Standards and Technology,

Lemmon et al. (2012)).
The SRK (equation A.1, Soave (1977)) and PR EOS (equation A.2, Peng and Robinson (1976)) are written as follows:

$$p = \frac{\rho r T}{1 - \rho b_m} - \frac{\rho^2 a_m(T)}{1 + \rho b_m} \tag{A.1}$$

$$p = \frac{\rho r T}{1 - \rho b_m} - \frac{\rho^2 a_m(T)}{1 + 2\rho b_m - \rho^2 {b_m}^2} \tag{A.2}$$

Where ρ is the density, T the temperature and $r = R/W$ where R designates the universal gas constant and W is the mixture molar mass. The specific coefficients $a_m(T)$ and b_m, associated to the mixing, account for the correction for attractive potential of molecules and the correction for volume, respectively. They are deduced from pure gas coefficients according to:

$$a_m(T) = \sum_{i=1}^{N} \sum_{j=1}^{N} a_{ij}(T) Y_i Y_j \tag{A.3}$$

$$b_m = \sum_{i=1}^{N} b_i Y_i \tag{A.4}$$

$$a_{ij}(T) = \sqrt{a_i(T) a_j(T)}(1 - k_{ij}) \tag{A.5}$$

Where N is the total number of species in the mixture, Y_i is the mass fraction of the i^{th} species, k_{ij} is the binary interaction parameter. The coefficients $a_i(T)$ and b_i are given by the following.

$$a_i(T) = \Phi_{c_i} \Psi(T)^2 \tag{A.6}$$

$$b_i = 0.08664 \frac{r_i T_{c_i}}{p_{c_i}} \tag{A.7}$$

Where

$$r_i = \frac{R}{W_i} \tag{A.8}$$

$$\Phi_{c_i} = 0.42747 \frac{(r_i T_{c_i})^2}{p_{c_i}} \tag{A.9}$$

$$\Psi(T) = 1 + c_i \left(1 - \sqrt{\frac{T}{T_{c_i}}}\right) \tag{A.10}$$

$$c_i = 0.48598 + 1.5517\omega_i - 0.15613\omega_i^2 \tag{A.11}$$

T_{c_i}, p_{c_i} and $omega_i$ are the critical temperature, critical pressure and the acentric factor of gas i.
The real gas EOS (equations A.1 and A.2) are used for a consistent derivation of the thermodynamic properties (internal energy, enthalpy, specific heats,

compressibility and so on) that are dependent on pressure, as described in Yang (2000). These quantities are expressed as the sum of the ideal gas value and a departure function (Hirschfelder et al. (1954) and Reid et al. (1987)). Departure functions for internal energy ($\Delta e = e(\rho, T) - e^0(T)$) and specific heat at constant volume ($\Delta c_v = c_v(\rho, T) c_v^0(T)$) are written as:

$$\Delta e = \int_{\rho^0}^{\rho} \left\{ \frac{T}{\rho^2} \left(\frac{\partial p}{\partial T} \right)_{\rho, Y_i} - \frac{p}{\rho^2} \right\}_T d\rho \tag{A.12}$$

$$\Delta c_v = T \int_{\rho^0}^{\rho} \left\{ \left(\frac{1}{\rho^2} \frac{\partial^2 p}{\partial T^2} \right)_{\rho, Y_i} \right\}_T d\rho \tag{A.13}$$

Enthalpy and specific heat at constant pressure are deduced from these departure functions.

Viscosity and heat conductivity coefficients are calculated using the method described in Chung et al. (1988). For perfect gases, mass diffusion coefficients are derived from viscosity coefficient by assuming constant Schmidt numbers $D_k = \mu / (\rho S_{c_k})$.

Appendix B

AVBP-RG solver

In this appendix are presented the main points of the Advance Virtual Burner Program (AVBP) initially developed by Moureau et al. (2005) and Gourdain et al. (2009)(I), Gourdain et al. (2009)(II).

B.1 Filtered equations for LES

The unstructured AVBP solver, currently developed by CERFACS and IFPEN, integrates the three-dimensional compressible Navier-Stokes equations for multicomponent mixtures of reactive flows. In the context of large eddy simulations, the balance equations are spatially filtered and solved using subgrid scale models to represent effects of unresolved turbulent eddies. In practice, the mesh size determines the resolution limit (implicit filtering):

$$\overline{\rho}\widetilde{f}(\mathbf{x},t) = \int_{-\infty}^{+\infty} \rho f(\mathbf{x'},t) F(\mathbf{x}-\mathbf{x'}) dx' \tag{B.1}$$

where f is a general variable and $F = 1/\Delta^3 \chi_\Delta$, with χ_Δ the characteristic function of the mesh cell of size Δ. Poinsot and Veynante (2011) gives in detail the filtered equations:

$$\frac{\partial \overline{\rho}}{\partial t} + \frac{\partial \overline{\rho}\widetilde{u}_j}{\partial x_j} = 0 \tag{B.2}$$

$$\frac{\partial \overline{\rho}\widetilde{Y}_k}{\partial t} + \frac{\partial \overline{\rho}\widetilde{u}_j\widetilde{Y}_k}{\partial x_j} = -\frac{\partial \overline{J_{k,j}}}{\partial x_j} - \frac{\partial \overline{J_{k,j}}^t}{\partial x_j} + \overline{\dot{\omega}}_k \tag{B.3}$$

$$\frac{\partial \overline{\rho}\widetilde{u}_i}{\partial t} + \frac{\partial \overline{\rho}\widetilde{u}_j\widetilde{u}_i}{\partial x_j} = -\frac{\partial \overline{p}}{\partial x_i} + \frac{\partial \overline{\tau_{ij}}}{\partial x_j} - \frac{\partial \overline{\tau_{ij}}^t}{\partial x_j} \tag{B.4}$$

$$\frac{\partial \overline{\rho}\widetilde{E}}{\partial t} + \frac{\partial \overline{\rho}\widetilde{u}_j\widetilde{E}}{\partial x_j} + \frac{\partial \overline{p}\widetilde{u}_j}{\partial x_j} = -\frac{\partial \overline{q_j}}{\partial x_j} + \frac{\partial \widetilde{u}_i\overline{\tau_{ij}}}{\partial x_j} - \frac{\partial q_j^t}{\partial x_j} + \overline{\dot{\omega}}_T \tag{B.5}$$

Equations B.2 to B.5 represent the conservation of mass, species, momentum and energy respectively. In these equations ρ is the density, $\boldsymbol{u} = (u_1, u_2, u_3)$

the velocity vector, E the total energy (*i.e.* the sum of internal and the kinetic energies), p the pressure, $\boldsymbol{x}$ the spatial coordinate vector, t the time and Y_k is the mass fraction of the species k. $\boldsymbol{\tau}$ is the viscous stress tensor and $\boldsymbol{q}$ the heat flux vector and $\boldsymbol{J}_k$ is the species diffusive flux. The turbulent stresses is $\overline{\tau_{ij}}^t$ and turbulent species fluxes is $\overline{J_{j,k}}^t$, $\overline{\dot{\omega}}_T$ and $\overline{\dot{\omega}}_k$ are the heat and species source term respectively. The diffusion of heat and chemical species are modeled using a gradient assumption:

$$\overline{q_j} = -\overline{\lambda}\frac{\partial \widetilde{T}}{\partial x_j} \text{ and } \overline{J_{j,k}} = \overline{\rho V_{k,j} Y_k} = -\overline{\rho} \overline{D_k} \frac{\partial \widetilde{Y_k}}{\partial x_j} \tag{B.6}$$

where $V_{k,i}$ is the i^{th} component of the diffusion velocity of species k, T is the temperature ,λ is the heat conductivity and D_k is the species diffusion coefficient.

All large eddy simulations presented in this thesis were carried out using the TTGC scheme, which is a low-dissipation centered scheme of order three in space and time (Colin and Rudgyard (2000), Lamarque (2007)). Boundary conditions are handled according to the NSCBC method as described in Poinsot and Lele (1992) and Baum et al. (1994).

The AVBP solver, which is an efficient massively parallel CFD solver, has been validated for several applications (Selle et al. (2004); Vermorel et al. (2007); Lacaze et al. (2009).

Within the framework of the collaboration between CERFACS and EM2C Laboratory a real-gas version of the AVBP solver (AVBP-RG) under transcritical conditions and turbulent combustion of non-premixed flames has been developed (Pons (2009); Schmitt (2009); Ruiz (2012)). Both the SRK and PR EOS are implemented in AVBP-RG.

B.2 Numerical aspects

The convective Jacobian matrices, used in the numerical scheme, and NSCBC method have been modified to take into account the properties of non-ideal gas (Okong'o and Bellan (2002), Schmitt et al. (2010)). The non-linear character of thermodynamics under transcritical conditions generates high gradients of density and internal energy at the injector exhaust where temperature changes from 80 K in the oxygen core up to more than 3000 K in the flame front through a very short distance. These gradients are usually spatially unresolved and may cause large errors on the pressure field. Real gas simulations therefore require a specific numerical stabilization procedure. The artificial viscosity models, already available in the perfect gas version of AVBP, is here applied as follows (CERFACS (2011)):

- Zones of under-resolved gradients are detected using Jameson or Colin sensors (Jameson et al. (1981); Colin (2000)).

- After that, operators are applied to the zones of interest using a combination of two artificial viscosity terms: a "shock capturing"or 2^{nd} order artificial viscosity, and a "background dissipation", or 4^{th} order artificial viscosity.

A new sensor better adapted to the high gradients encountered in real gas simulations was presented in Schmitt et al. (2010):

$$\xi_{\Omega_j} = \frac{1}{2}\left(\tanh\left(\frac{\psi-\psi_0}{\delta}\right) - \tanh\left(\frac{-\psi_0}{\delta}\right)\right) \tag{B.7}$$

with

$$\psi = \underset{k\in\Omega_j}{max}(0, \zeta_{k,j}) \tag{B.8}$$

$$\zeta_{k,j} = \frac{|\rho_{\Omega_j} - \rho_k - (\nabla\rho)_k \cdot (x_{\Omega_j} - x_k)|}{|\rho_{\Omega_j} - \rho_k| + |(\nabla\rho)_k \cdot (x_{\Omega_j} - x_k)| + |\rho_k^0|} \tag{B.9}$$

The model constants are $\psi_0 = 0.2$ and $\delta = 0.05$. $\zeta_{k,j}$ detects the under-resolved gradients at the node k in the cell Ω_j and ρ_k^0 is the value of density at the node k for a perfect gas. The operator is applied to all variables (ρ, $\rho\mathbf{u}$, ρE). This is done by first applying the operator on ρ and $\rho\mathbf{u}$ and then correct ρE so that $dP = 0$ according to:

$$dP = \frac{\alpha}{\rho\beta c_v} d(\rho E) + \sum_{k=1}^{N}\left(\frac{c_p v_k}{c_v\beta} - \frac{\alpha h_{s,k}}{\rho\beta c_v} + \frac{\alpha e_c}{\rho\beta c_v}\right) d(\rho Y_k) - \frac{\alpha u_i}{\rho\beta c_v} d(\rho u_i) \tag{B.10}$$

where α is the thermal expansion coefficient and β is the isothermal compressibility coefficient, c_p and c_v are the specific heat capacities, $h_{s,k}$ is the enthalpy per unit of mass of species k and e_c is the kinetic energy per unit of mass. v_k is the partial specific volume of species k. This strategy is effective (Schmitt et al. (2010), Schmitt et al. (2011), Schmitt et al. (2012)) but it does not fully conserve energy.

B.3 Subgrid scale models

The following computations are based on the WALE subgrid scale model (Nicoud and Ducros (1999)). WALE properly handles the viscosity behavior near-wall $\nu^t = O(y^3)$, where the y-axis is perpendicular to the wall and ν^t is the subgrid scale viscosity. This subgrid scale model takes also into account the strain rate and rotational rate for energy dissipation according to Hunt et al. (1988). making use of the velocity gradient tensor $\widetilde{g}_{ij} = \partial\widetilde{u}_i/\partial\widetilde{x}_j$, the subgrid scale viscosity is derived as follows:

$$\nu^t = (C_w\Delta)^2 D_w(\widetilde{\mathbf{u}}) \tag{B.11}$$

where $C_w = 0.5$ and:

$$D_w(\widetilde{\mathbf{u}}) = \frac{(S_{ij}^d S_{ij}^d)^{3/2}}{(\widetilde{S}_{ij}\widetilde{S}_{ij})^{5/2} + (S_{ij}^d S_{ij}^d)^{5/4}} \tag{B.12}$$

In the expression of $D_w(\widetilde{\mathbf{u}})$, S_{ij}^d and $\widetilde{S}_{ij}$ are the traceless symmetric part of $\widetilde{g}^2$ and the symmetric part of $\widetilde{g}$ respectively.
According to Bricteux et al. (2009) and Duponcheel (2009) WALE overdamps vortices in cases with pure rotation. A more recent model(Nicoud et al. (2011)), called σ-model, avoids this difficulty by using the singular values of the resolved velocity gradient tensor. Good results at low computational cost are gathered in simple configurations compared to the Dynamic Smagorinsky Model (Smagorinsky (1963), Germano et al. (1991)).
Heat and species fluxes are handled using the standard gradient transport equations:

$$\overline{q_j}^t = -\lambda^t \frac{\partial \widetilde{T}}{\partial x_j} \tag{B.13}$$

$$\overline{J_{j,k}}^t = -\overline{\rho} D_k^t \frac{\partial \widetilde{Y}_k}{\partial x_j} \tag{B.14}$$

Where $\lambda^t = \rho c_p \nu^t / Pr^t$ is the subgrid scale conductivity and Pr^t is the turbulent Prandtl number, which is supposed to be constant ($Pr^t = 0.7$). $D_k^t = \nu^t / Sc_k$ is the subgrid scale species diffusion coefficient and $Sc_k = 0.7$ is the turbulent Schmidt number for species k.
All viscosity subgrid scale models available in AVBP-RG are written for incompressible flows. For compressible flows, the trace part of the Reynolds stress tensor has to be modeled. Some models were extended to compressible flows for low to moderate Mach numbers (Speziale et al. (1988),Moin et al. (1991),Garnier et al. (2009)). To simulate real gases, it is necessary to take into account the non-linearity of the EOS and the large variations in the transport properties (Bellan (2006), Selle et al. (2007) and Taskinoglu and Bellan (2010)).
Simulations of transcritical configurations using these subgrid scale models (Schmitt et al. (2010), Selle and Schmitt (2010), Schmitt et al. (2012)) were in good agreement with experimental data.

B.4 Combustion model

In reactive LES applications a model that provides the spatially filtered reaction rates is a problem which has received considerable attention in recent years. In high pressure cryogenic rocket engines and in laboratory experiments, reactants are injected separately in a high pressure combustion chamber. As shown in some experiments with the MASCOTTE facility (Herding et al. (1998); Juniper et al. (2000); Juniper and Candel (2003c); Singla et al. (2005); Singla

et al. (2006); Candel et al. (2006); Singla et al. (2007)), as well as in other experimental setups (Mayer and Tamura (1996); Mayer et al. (2000); Mayer et al. (2001)), the flame, which is attached to the injection device, is affected by a transverse acoustic field.

A model called IFCM, for Infinitely Fast Chemistry Model, has been developed (Méry (2010); Schmitt et al. (2011)) provides a filtered reaction rate. The model used in this thesis is a modified version of IFCM that takes into account the equilibrium composition of burnt products.

In liquid rocket engine combustion processes, chemical reactions are much faster than mixing (Ivancic and Mayer (2002); Pons et al. (2008)). The mixing rates then dominate the whole process, which means that "if it is mixed it is burnt" (Veynante and Vervisch (2002)). The idea is to estimate the mass fraction of chemical species after one time step that takes into account convection and diffusion in the presence of an infinitely fast chemical reaction. The filtered mass fractions are expressed using a presumed probability density function. The reaction rate is then calculated from the difference between these mass fraction estimates and the tabulated ones. The tables are generated from equilibrium calculations using EQUIL program from CHEMKIN package (Kee et al. (1993)).

To calculate the species source term, it is a good idea to define Y_k^+ as the unreactive part of the conservation species equation, which takes into account convection and diffusion:

$$\frac{\partial \overline{\rho}\widetilde{Y}_k^+}{\partial t} + \frac{\partial \overline{\rho}\widetilde{u}_j\widetilde{Y}_k}{\partial x_j} = -\frac{\partial \overline{J_{k,j}}}{\partial x_j} - \frac{\partial \overline{J_{k,j}}^t}{\partial x_j} \tag{B.15}$$

By subtracting equation B.15 from B.3, one obtains the filtered reaction rates.

$$\overline{\dot{\omega}}_k = \frac{\partial \overline{\rho}(\widetilde{Y}_k - \widetilde{Y}_k^+)}{\partial t} \tag{B.16}$$

For one time step of simulation, equation B.16 becomes:

$$\overline{\dot{\omega}}_k = \frac{\delta[\overline{\rho}(\widetilde{Y}_k - \widetilde{Y}_k^+)]}{\delta t} \tag{B.17}$$

with

$$\delta[\overline{\rho}(\widetilde{Y}_k - \widetilde{Y}_k^+)] = \overline{\rho}(t+\delta t)[\widetilde{Y}_k(t+\delta t) - \widetilde{Y}_k^+(t+\delta t)] - \overline{\rho}(t)[\widetilde{Y}_k(t) - \widetilde{Y}_k^+(t)] \tag{B.18}$$

At the beginning of an iteration, one can assume that the mass fraction field is the same as the one of the previous iteration, that is $\widetilde{Y}_k(t) = \widetilde{Y}_k^+(t)$. The predicted mass fractions that take into account combustion, $\widetilde{Y}_k(t+\delta t) = \widetilde{Y}_k(\widetilde{Z}, \widetilde{Z''^2})_{t+\delta t}$, depend on the filtered mixture fraction $\widetilde{Z}$ and the subgrid scale

variance of Z ($\widetilde{Z''^2}$). The predicted mass fractions are tabulated with respect to $\widetilde{Z}$ and $\widetilde{Z''^2}$ using a presumed β-PDF (Cook and Riley (1994); Peters (2001)):

$$\widetilde{Y_k}(\widetilde{Z}, \widetilde{Z''^2}) = \int_0^1 Y_k(Z^*)\widetilde{p}(Z^*; \mathbf{x}, t)dZ^* \tag{B.19}$$

The mixture fraction variance $\widetilde{Z''^2}$ is calculated with an algebraic model (Pierce and Moin (1998)):

$$\widetilde{Z''^2} = C\Delta|\nabla\widetilde{Z}|^2 \tag{B.20}$$

C is a parameter, in the reactive calculations of this thesis it is set to $C = 0.13$ as suggested by Forkel and Janicka (2000).
The filtered heat release is calculated using the filtered reactions rates:

$$\overline{\dot{\omega}_T} = -\sum_{k=1}^{N} \overline{\dot{\omega}_k}\Delta h^0_{f,k} \tag{B.21}$$

Where $\Delta h^0_{f,k}$ is the mass enthalpy of formation of species k at temperature $T_0 = 0$ K.

Appendix C

Presentation of the BKD test rig

This appendix focuses on the geometry of an injector of the BKD test rig at the DLR laboratory. The BKD test rig is a cylindrical combustion chamber featuring 42 coaxial injectors injecting liquid oxygen and hydrogen and operating in the transcritical regime. Depending on the injection conditions, it has the peculiarity to develop self-sustained combustion instabilities. Figure C.1 shows an illustration of the chamber and the 42-injectors back plane. More detailed information may be found in DLR (2013).

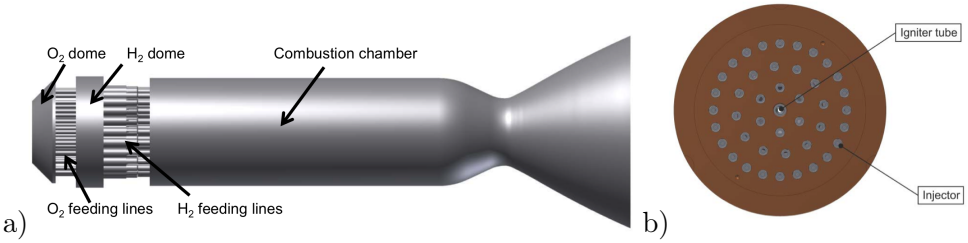

Figure C.1: *(a) The BKD chamber, (b) Injection plate featuring 42 injectors.*

The chamber is instrumented with a ring of 8 high frequency pressure sensors around the injector plate (figure C.2) and in the dome. This information are completed with optical probes and thermo-couples at the walls. This arrangement allows a proper detection (frequency, amplitude) of high frequency spinning modes in the azimuthal direction inside the chamber.
Four Load Points (LP) have been studied at the DLR, table C.1 sums up these load points. The present simulations concentrate on LP3 and LP4, as LP3 is found to be stable, while LP4 presents large amplitude (around 2.0 MPa peak-to-peak) high frequency acoustic fluctuations. In addition, these two cases features similar injection conditions (mass flow rate, oxygen temperature), except for the hydrogen temperature, lower for LP3 than for LP4. Under LP3 or LP4 injection conditions, the chamber in the pressure is around 8.0 MPa.
In this chapter single injector transcritical flames with mass flow rate modulation have been studied. Among all the phenomena that can generate unsteady

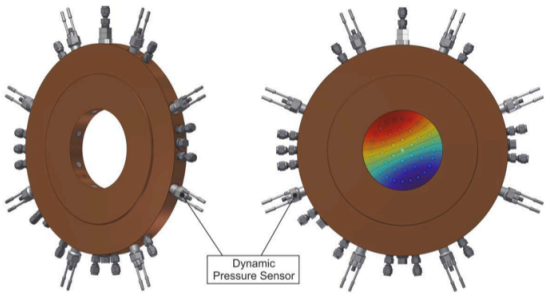

Figure C.2: *HF measurement ring with 8 dynamic pressure sensors.*

Load Point	LP1	LP2	LP3	LP4
$\dot{m}_{LOx}$ [kg.s^{-1}]	4.44	5.04	5.77	5.75
$\dot{m}_{H_2}$ [kg.s^{-1}]	1.11	0.84	0.96	0.96
$T_{O_2}^{dome}$[K]	126.46	126.21	123.06	126.16
$T_{H_2}^{dome}$[K]	111.80	112.77	79.74	113.38
$p_{O_2}^{dome}$[MPa]	7.841	8.111	9.189	9.410
$p_{H_2}^{dome}$[MPa]	10.003	8.966	9.012	10.292
MR	4	6	6.01	5.99
J	5.21	11.07	27.65	16.11

Table C.1: *The four operating points studied at DLR. Operating point chosen for the simulation are put in color. p^{dome} is the dome mean pressure, T^{dome} is the dome mean pressure, $\dot{m}_{LOx}$ and $\dot{m}_{H_2}$ are the mass flow rates of oxygen and hydrogen, respectively. MR is the mixture ratio and J the momentum flux ratio.*

heat release, focus has been set on the influence of injection mass flow rate modulation to begin. Locally there is a strong response of the heat release to the modulation however the global heat release does not seem to be affected by the mass flow rate modulation. This can be explained by the fact that the positive and negative local heat releases cancel each other out when taking the whole flame into account. Other phenomena that influence unsteady heat release will be explored.

References

Angelberger, C., F. Egolfopoulos, and D. Veynante (2000). Large eddy simulations of chemical and acoustic effects on combustion instabilities. *Flow, Turbulence and Combustion 65*(2), 205–22. *(p. 48)*

Baillot, F., J. B. Blaisot, G. Boisdron, and C. Dumouchel (2009, 12). Behaviour of an air-assisted jet submitted to a transverse high-frequency acoustic field. *Journal of Fluid Mechanics 640*, 302–342. *(p. 37, 48)*

Banuti, D. T. (2015). Crossing the Widom-line - Supercritical pseudo-boiling. *Journal of supercritical fluids 98*, 12–16. *(p. 19)*

Baum, M., T. J. Poinsot, and D. Thévenin (1994). Accurate boundary conditions for multicomponent reactive flows. *Journal of Computational Physics 116*, 247–261. *(p. 210)*

Bellan, J. (2000). Supercritical (and subcritical) fluid behavior and modeling: drops, streams, shear and mixing layers, jets and sprays. *Progress in Energy and Combustion Science 26*, 329–366. *(p. 20)*

Bellan, J. (2006). Theory, modelling and analysis of turbulent supercritical mixing. *Combustion Science and Technology 178*, 253–281. *(p. 212)*

Birbaud, A. L., D. Durox, and S. Candel (2007). Dynamics of free jets submitted to upstream acoustic modulations. *Physics of Fluids 19*. *(p. 72)*

Borgnis, F. E. (1953, July). Acoustic radiation pressure of plane compressional waves. *Rev. Mod. Phys. 25*(3), 653 – 664. *(p. 37)*

Bricteux, L., M. Duponcheel, and G. Winckelmans (2009). A multiscale subgrid model for both free vortex flows and wall-bounded flows. *Physics of Fluids 21*. *(p. 212)*

Buffum, F. G., L. G. Dehority, R. O. Slates, and E. W. Price (1966). Acoustic losses of a subscale, cold-flow rocket motor for various 'J' values. Technical report, Bureau of Naval Weapons. *(p. 140)*

Candel, S. (2002). Combustion dynamics and control: progress and challenges. *Proc. Comb. Inst. 29*, 1–28. *(p. 7, 64)*

Candel, S., D. Durox, T. Schuller, N. Darabiha, L. Hakim, and T. Schmitt (2013). Advances in combustion and propulsion applications. *European Journal of Mechanics - B/Fluids 40*, 87 – 106. *(p. 16, 17)*

Candel, S., G. Herding, R. Synder, P. Scouflaire, C. Rolon, L. Vingert, M. Habiballah, F. Grisch, M. Péalat, P. Bouchardy, D. Stepowski, A. Cessou, and P. Colin (1998). Experimental investigation of shear coaxial cryo-

genic jet flames. *Journal of Propulsion and Power 14*(5), 826–834. *(p. 4)*

Candel, S., M. Juniper, G. Singla, P. Scouflaire, and C. Rolon (2006). Structure and dynamics of cryogenic flames at supercritical pressure. *Combust. Sci. Technol. 178*, 161–192. *(p. 5, 6, 7, 213)*

Candel, S., T. Schmitt, and N. Darabiha (2011). Progress in transcritical combustion : experimentation, modeling and simulation. In *23rd International Conference on Dynamics of Explosions and Reactive Systems*. *(p. 47)*

Carpentier, J.-B., F. Baillot, J.-B. Blaisot, and C. Dumouchel (2009). Behavior of cylindrical liquid jets evolving in a transverse acoustic field. *Physics of Fluids 21*(2), 023601. *(p. 37, 48)*

CERFACS (2011). AVBP Handbook. `http://www.cerfacs.fr/~avbp/AVBP_V6.X/HANDBOOK/handbook.php`. *(p. 210)*

Chehroudi, B., D. Talley, and E. Coy (2002, february). Visual characteristics and initial growth rate of round cryogenic jets at subcritical and supercritical pressures. *Physics of Fluids 14*(2), 850–861. *(p. 5)*

Chen, C. J. and W. Rodi (1980). *Vertical turbulent buoyant jets: A review of experimental data*. Pergamon Press. *(p. 25)*

Cheuret, F. and G. Searby (2003). Numerical and experimental studies of the Common Research Chamber. In CNES (Ed.), *Fourth High Frequency combustion instability scientific workshop*, Paris, France, pp. 83–96. *(p. 48)*

Cheuret, F. and G. Searby (2004). Experimental studies of the Common Research Chamber. In *5th French-German Workshop on high frequency combustion instabilities*, Paris, France. CNES. *(p. 48)*

Chung, T. H., M. Ajlan, L. L. Lee, and K. E. Starling (1988). Generalized multiparameter correlation for nonpolar and polar fluid transport properties. *Industrial & engineering chemistry research 27*(4), 671–679. *(p. 18, 49, 207)*

Colin, O. (2000). *Simulations aux grandes échelles de la combustion turbulente prémélangée dans les statoréacteurs*. Phd thesis, INP Toulouse. *(p. 210)*

Colin, O. and M. Rudgyard (2000). Development of high-order Taylor-Galerkin schemes for LES. *Journal of Computational Physics 162*(2), 338 – 371. *(p. 18, 50, 210)*

Cook, A. W. and J. J. Riley (1994). A subgrid scale model for equilibrium chemistry in turbulent flows. *Physics of Fluids 6*(8), 2868–2870. *(p. 214)*

Crocco, L. (1951). Aspects of combustion instability in liquid propellant rocket motors. part i: Fundamentals. low frequency instability with monopropellants. *J. Am. Rocket Soc. 21*, 163–178. *(p. 7, 16)*

Crocco, L. (1952). *Supercritical Gaseous Discharge with High Frequency Oscillations*. Defense Technical Information Center. *(p. 140)*

Crocco, L. and S. I. Cheng (1956). *Theory of combustion instability in liquid propellant rocket motors*, Volume Agardograph No 8. Butterworths

Science. *(p. 7, 49, 173, 174)*

Crocco, L., R. Monti, and J. Grey (1961). Verification of nozzle admittance theory by direct measurement of the admittance parameter. *ARS Journal 31*(6), 771–775. *(p. 140)*

Crow, S. C. and F. H. Champagne (1971). Orderly structure in jet turbulence. *Journal of fluid mechanics 48*(3), 547–591. *(p. 26, 58)*

Culick, F. E. C. (2006, December). *Unsteady Motions in Combustion Chambers for Propulsion Systems*, Volume RTO-AG-AVT-039 of *RTO AGARDograph*. The Research and Technology Organisation (RTO) of NATO. *(p. 6, 7, 155)*

Culick, F. E. C. and G. L. Dehority (1969). Analysis of acoustic waves in a cold-flow rocket. *Journal of Spacecraft and Rockets 6*(5), 591–595. *(p. 140)*

Culick, F. E. C. and V. Yang (1995). Overview of Combustion Instabilities in Liquid-Propellant Rocket Engines. In V. Yang and W. E. Anderson (Eds.), *Liquid Rocket Engine Combustion Instability*, Volume 169, pp. 3–37. Washington, DC: AIAA, Inc. *(p. 174, 177)*

Davis, D. W. and B. Chehroudi (2006). Shear-coaxial jets from a rocket-like injector in a transverse acoustic field at high pressures. In *44th AIAA Aerospace Sciences Meeting & Exhibit*. AIAA, Reno, Nevada. *(p. 48)*

DLR (2013). TEST CASE HF-7 - LOx/H2 Combustion with self-sustained acoustic excitation. Technical report, REST. *(p. 3, 187, 215)*

Duchamp de Lageneste, L. and H. Pitsch (2001). Progress in large-eddy simulation of premixed and partially-premixed turbulent combustion. In *Annual Research Briefs* , pp. 97–107. Center for Turbulence Research, NASA Ames/Stanford Univ. *(p. 47)*

Ducros, F., F. Nicoud, and T. Poinsot (1998). Wall-adapting local eddy-viscosity models for simulations in complex geometries. In *ICFD*, pp. 293–300. Baines M. J. *(p. 18, 50)*

Duponcheel, M. (2009). *Direct and Large-Eddy Simulation of turbulent wall-bounded flows: further development of parallel solver, improvment of multiscale subgrid modelsand investigation of vortex pairs in ground effect*. Ph. D. thesis, Université catholique de Louvain, Ecole polytechnique de Louvain. *(p. 212)*

Durox, D., T. Schuller, N. Noiray, A. L. Birbaud, and S. Candel (2009). Rayleigh criterion and acoustic energy balance in unconfined self-sustained oscillating flames. *Combustion and Flame 156*, 106 – 119. *(p. 72)*

Fiala, T. (2010). *Bestimmung der Dämpfung akustischer Wellen in einer Raketenbrennkammer*. Ph. D. thesis, Technische Universität München. *(p. 198)*

Forkel, H. and J. Janicka (2000). Large-eddy simulation of a turbulent hydrogen diffusion flame. *Flow, Turbulence and Combustion 65*(2), 163–175. *(p. 214)*

Garnier, E., N. Adams, and P. Sagaut (2009). Large eddy simulation for compressible flows. *Springer*. *(p. 212)*

Germano, M., U. Piomelli, P. Moin, and W. Cabot (1991). A dynamic subgrid-scale eddy viscosity model. *Physics of Fluids 3*(7), 1760–1765. *(p. 212)*

Gourdain, N., L. Gicquel, M. Montagnac, O. Vermorel, M. Gazaix, G. Staffelbach, M. Garcia, J. Boussuge, and T. Poinsot (2009). High performance parallel computing of flows in complex geometries: I. Methods. *Computational Science & Discovery 2*, 015003. *(p. 48, 209)*

Gourdain, N., L. Gicquel, G. Staffelbach, O. Vermorel, F. Duchaine, J. Boussuge, and T. Poinsot (2009). High performance parallel computing of flows in complex geometries: II. Applications. *Computational Science & Discovery 2*, 015004. *(p. 48, 209)*

Habiballah, M., M. Orain, F. Grisch, L. Vingert, and P. Gicquel (2006). Experimental studies of high-pressure cryogenic flames on the mascotte facility. *Combustion Science and Technology 178*, 101–128. *(p. 5, 107)*

Hakim, L. (2013, Febuary). *Dynamics of transcritical coaxial flames in high-frequency transverse acoustic fields: application to liquid rocket engine instabilities*. Ph. D. thesis, Ecole Centrale Paris, France. *(p. 2, 8, 40, 49, 50, 51, 107, 109)*

Hakim, L., A. Ruiz, T. Schmitt, M. Boileau, G. Staffelbach, S. Ducruix, B. Cuenot, and S. Candel (2015). Large eddy simulations of multiple transcritical coaxial flames submitted to a high-frequency transverse acoustic modulation. *Proceedings of the Combustion Institute 35*(2), 1461 – 1468. *(p. 8, 16, 17, 27, 37, 48)*

Hakim, L., T. Schmitt, S. Ducruix, and S. Candel (2015). Dynamics of a transcritical coaxial flame under high-frequency transverse acoustic forcing: the effect of a modulation frequency. *Combustion and Flame 162*, 3482–3502. *(p. 8, 16, 17, 27, 48, 49, 51, 55)*

Hardi, J., M. Oschwald, and B. Dally (2011). Flame response to acoustic excitation in a rectangular rocket combustor with LOx/H_2 propellants. *CEAS Space Journal*, 1–9. *(p. 8, 48)*

Hardi, J. S., H. C. Gomez Martinez, and M. Oschwald (2014, March-April). LOx jet atomization under transverse acoustic oscillations. *Journal of propulsion and power 13*, 337–349. *(p. 18, 48)*

Harrje, D. J. and F. H. Reardon (1972). Liquid propellant rocket instability. Technical Report Report SP-194, NASA. *(p. 7)*

Hasegawa, T., Y. Hino, A. Annou, H. Noda, M. Kato, and N. Inoue (1993). Acoustic radiation pressure acting on spherical and cylindrical shells. *The Journal of the Acoustical Society of America 93*(1), 154–161. *(p. 37)*

Herding, G. (1997). *Analyse expérimentale de la combustion d'ergols cryotechniques*. Ph. D. thesis, Ecole Centrale de Paris. *(p. 4)*

Herding, G., R. Snyder, C. Rolon, and S. Candel (1998). Investigation of cryogenic propellant flames using computerized tomography of OH emis-

sion images. *Journal of Propulsion and Power 13*, 146–151. *(p. 4, 213)*

Herding, G., R. Snyder, P. Scouflaire, C. Rolon, and S. Candel (1996). Flame stabilization in cryogenic propellant combustion. *Symposium (International) on Combustion 26*(2), 2041 – 2047. *(p. 4)*

Hirschfelder, J., C. Curtiss, R. Bird, et al. (1954). *Molecular theory of gases and liquids*, Volume 26. Wiley New York. *(p. 207)*

Hulka, J. and J. J. Hutt (1995). *Instability Phenomena in Liquid Oxygen/Hydrogen Propellant Rocket Engines*, Chapter 2. AIAA. *(p. 174)*

Hunt, J. C. R., A. A. Wray, and P. Moin (1988). Eddies, streams, and convergence zones in turbulent flows. In *Proceedings of the Summer Program*, Center for Turbulence Research, Stanford University, pp. 193–208. *(p. 211)*

Ivancic, B. and W. Mayer (2002). Time and length scales of mixing and combustion processes in high-pressure LOx/GH_2 rocket combustors. *Journal of Propulsion and Power 18*(2), 247–253. *(p. 213)*

Jameson, A., W. Schmidt, and E. Turkel (1981). Numerical solutions of the Euler equations by finite volume methods using Runge-Kutta time-stepping schemes. In *14th Fluid and Plasma Dynamic Conference*. *(p. 210)*

Juniper, M. (2001). *Structure et stabilisation des flammes cryotechniques*. Ph. D. thesis, Ecole Centrale de Paris. *(p. 4, 16)*

Juniper, M. and S. Candel (2003a). Edge diffusion flame stabilization behind a step over a liquid reactant. *Journal of propulsion and power 19*(3), 332–341. *(p. 4, 5)*

Juniper, M. and S. Candel (2003b). The effect of damköhler number on the stand-off distance of cross-flow flames. *Combustion Theory and Modelling 7*(3), 563–577. *(p. 4)*

Juniper, M. and S. Candel (2003c). The stability of ducted compound flows and consequences for the geometry of coaxial injectors. *Journal of Fluid Mechanics 482*, 257–269. *(p. 4, 213)*

Juniper, M., N. Darabiha, and S. Candel (2003). The extinction limits of a hydrogen counterflow diffusion flame above liquid oxygen. *Combust. Flame 135*(1-2), 87–96. *(p. 4)*

Juniper, M., A. Tripathi, P. Scouflaire, J. Rolon, and S. Candel (2000). Structure of cryogenic flames at elevated pressures. *Proceedings of the Combustion Institute 28*(1), 1103–1110. *(p. 4, 5, 213)*

Kee, R. J., F. M. Rupley, and J. A. Miller (1993). Chemkin-II: A fortran chemical kinetics package for the analysis of gas phase chemical kinetics. *SANDIA Report, Unlimited release*. *(p. 213)*

Kendrick, D., G. Herding, P. Scouflaire, C. Rolon, and S. Candel (1999). Effects of a recess on cryogenic flame stabilization. *Combustion and Flame 118*(3), 327 – 339. *(p. 4)*

Kirchhoff, G. (1868). Über den einfluss der wärmeleitung in einem Gase auf dis Schallbewegung. *Annalen der Physik und Chemie 210*, 177–193.

(p. 140)

Klem, M. D. and R. S. Fry (January 1997). Guidelines for combustion stability specifications and verification procedures for liquid propellant rocket engines. Technical report, CPIA Publication 655. *(p. 184)*

L. Vingert, M. H. and J. Traineau (1999). Mascotte, a research test facility for high pressure combustion of cryogenic propellants. In *12th European Aerospace Conference, 3rd European Conference of cryogenic propellants, Paris, France*. *(p. 107)*

Lacaze, G., B. Cuenot, T. Poinsot, and M. Oschwald (2009). Large eddy simulation of laser ignition and compressible reacting flow in a rocket-like configuration. *Combustion and Flame 156*(6), 1166 – 1180. *(p. 178, 210)*

Lamarque, N. (2007). *Schémas numériques et conditions limites pour la simulation aux grandes échelles de la combustion diphasique dans les foyers d'hélicoptère*. Ph. D. thesis, Institut National Polytechnique de Toulouse. *(p. 210)*

Lambert, R. F. (1953). A study of the factors influencing the damping of an acoustical cavity resonator. *The Journal of the Acoustical Society of America 25*, 1068 – 1083. *(p. 140)*

Lee, C. P. and T. G. Wang (1993). Acoustic radiation pressure. *Journal of the Acoustical Society of America 94*(2), 1099–1109. *(p. 37)*

Lemmon, E., M. McLinden, and D. Friend (2012). *Thermophysical Properties of Fluid Systems*. In the WebBook of Chemistry NIST, Standard Data Base NIST Number 69, Eds. P.J. Linstrom and W.G. Mallard, National Institute of Standards and Technology, Gaithersburg MD, 20899, http://webbook.nist.gov. *(p. 188, 206)*

Lespinasse, F., F. Baillot, and T. Boushaki (2013). Responses of v-flames placed in an {HF} transverse acoustic field from a velocity to pressure antinode. *Comptes Rendus Mécanique 341*(1–2), 110 – 120. *(p. 48)*

Leyva, I., J. Rodriguez, B. Chehroudi, and D. Talley (2008). *Preliminary Results on Coaxial Jet Sprean Angles and the Effects of Variable Phase Transverse Acoustic Fields*. American Institute of Aeronautics and Astronautics. *(p. 17, 48)*

Lieuwen, T. (2005, 06). Online combustor stability margin assessment using dynamic pressure data. *Journal of Engineering for Gas Turbines and Power 127*(3), 478–482. *(p. 198)*

Lieuwen, T., H. Torres, C. Johnson, and B. Zinn (2001). A mechanism of combustion instability in lean premixed gas turbine combustors. *Journal of Engineering for Gas Turbines and Power 123*(1), 182–189. *(p. 198)*

Lores, M. E. and B. T. Zinn (1973). Nonlinear longitudinal combustion instability in rocket motors. *Combustion Science and Technology 7*(6), 245–256. *(p. 155)*

Mahesh, K., G. Constantinescu, S. Apte, G. Iaccarino, F. Ham, and P. Moin (2002). Progress toward large-eddy simulation of turbulent reacting and non-reacting flows in complex geometries. In *Annual Research Briefs*

, pp. 115–142. Center for Turbulence Research, NASA Ames/Stanford Univ. *(p. 47)*

Marble, F. E. (1953). Servo-stabilization of low-frequency oscillations in a liquid bipropellant rocket motor. *Journal of the American Rocket Society 23*(2), 63–74. *(p. 7, 49)*

Marble, F. E. and S. Candel (1977). Acoustic disturbances from gas nonuniformities convected through a nozzle. *Journal of Sound and Vibration 55*, 225–243. *(p. 134, 188)*

Martin, C., L. Benoit, Y. Sommerer, F. Nicoud, and T. Poinsot (2006). Les and acoustic analysis of combustion instability in a staged turbulent swirled combustor. *AIAA Journal 44*(4), 741–750. *(p. 48)*

Masquelet, M., S. Menon, Y. Jin, and R. Friedrich (2009). Simulation of unsteady combustion in a LOx-GH2 fueled rocket engine. *Aerospace Science and Technology 13*(8), 466 – 474. *(p. 16)*

Mayer, W., B. Ivancic, A. Schik, and U. Hornung (2001). Propellant atomization and ignition phenomena in liquid oxygen/gaseous hydrogen rocket combustors. *Journal of Propulsion and Power 17*, 794–799. *(p. 213)*

Mayer, W., A. Schik, M. Schäffler, and H. Tamura (2000, September-October). Injection and mixing processes in high-pressure liquid oxygen/gaseous hydrogen rocket combustor. *Journal of Propulsion and Power 16*(5), 823–828. *(p. 213)*

Mayer, W., A. Schik, B. Vielle, C. Chauveau, I. Gökalp, D. Talley, and R. Woodward (1998). Atomization and breakup of cryogenic propellants under high-pressure subcritical and supercritical conditions. *Journal of Propulsion and Power 14*(5), 835–842. *(p. 5)*

Mayer, W. and H. Tamura (1996). Propellant injection in a liquid oxygen/gaseous hydrogen rocket engine. *Journal of Propulsion and Power 12*(6), 1137–1147. *(p. 213)*

Mayer, W., J. Tellar, R. Branam, G. Schneider, and J. Hussong (2003). Raman measurement of cryogenic injection at supercritical pressure. *Heat and Mass Transfer 39*, 709–719. *(p. 5)*

McManus, K., T. Poinsot, and S. Candel (1993). A review of active control of combustion instabilities. *Progress in Energy and Combustion Science 19*, 1–29. *(p. 7)*

Méry, Y. (2010). *Mécanismes d'instabilités de combustion haute-fréquence et application aux moteurs-fusées*. Ph. D. thesis, Ecole Centrale Paris. *(p. xxviii, 2, 8, 106, 108, 109, 166, 168, 173, 213)*

Méry, Y., S. Ducruix, P. Scouflaire, and S. Candel (2009). Injection coupling with high amplitude transverse modes: Experimentation and simulation. *Compt. Rend. Mécan. 337*(6-7), 426–437. *(p. 8, 48, 107, 109)*

Méry, Y., L. Hakim, P. Scouflaire, L. Vingert, S. Ducruix, and S. Candel (2013). Experimental investigation of cryogenic flame dynamics under transverse acoustic modulations. *Comptes Rendus Mécanique 341*(1-2), 100–109. *(p. 18, 48)*

Mitchell, C. E. (1995). *Analytical Models for Combustion Instability*, Chapter 15. AIAA. *(p. 174)*

Moin, P., K. D. Squires, W. Cabot, and S. Lee (1991). A dynamic subgrid-scale model for compressible turbulence and scalar transport. *Physics of Fluids A 3*(11), 2746–2757. *(p. 212)*

Moureau, V., G. Lartigue, Y. Sommerer, C. Angelberger, O. Colin, and T. Poinsot (2004). Numerical methods for unsteady compressible multi-component reacting flows on fixed and moving grids. *Journal of Computational Physics 202*(2), 710–736. *(p. 18, 49)*

Moureau, V., G. Lartigue, Y. Sommerer, C. Angelberger, O. Colin, and T. Poinsot (2005). High-order methods for DNS and LES of compressible multi-component reacting flows on fixed and moving grids. *J. of Comput. Phys. 202*(2), 710–736. *(p. 48, 209)*

Müller, H., C. A. Niedermeier, J. Matheis, M. Pfitzner, and S. Hickel (2016). Large-eddy simulation of nitrogen injection at trans-and supercritical conditions. *Physics of fluids 28*. *(p. 24)*

Nicoud, F., H. Baya Toda, O. Cabrit, S. Bose, and J. Lee (2011). Using singular values to build a subgrid scale model for large-eddy simulation. *Physics of Fluids 23*. *(p. 212)*

Nicoud, F., L. Benoit, and C. Sensiau (2007). Acoustic modes in combustors with complex impedances and multidimensional active flames. *AIAA Journal 45*, 426–441. *(p. 119, 161, 168, 188)*

Nicoud, F. and F. Ducros (1999). Subgrid-scale stress modelling based on the square of the velocity gradient. *Flow, Turbulence and Combustion 62*(3), 183–200. JX. *(p. 211)*

Nielsen, A. K. (1949). *Acoustic Resonators of Circular Cross-Section and with Axial Symmetry*. Danish Academy of Technical Sciences. *(p. 140)*

Noiray, N., D. Durox, T. Schuller, and S. Candel (2008). A unified framework for nonlinear combustion instability analysis based on the flame describing function. *Journal of Fluid Mechanics 615*, 139–167. *(p. 72, 78)*

Noiray, N., D. Durox, T. Schuller, and S. Candel (2009). Mode conversion in acoustically modulated confined jets. *AIAA Journal 47*(9), 2053–2062. *(p. 80, 83)*

Oefelein, J. C. (2005). Thermophysical characteristics of shear-coaxial LOx-H2 flames at supercritical pressure. *Proceedings of the Combustion Institute 30*(2), 2929 – 2937. *(p. 16, 205)*

Oefelein, J. C. and V. Yang (1993, September-October). Comprehensive Review of Liquid-Propellant Combustion Instabilities in F-1 Engines. *Journal of Propulsion and Power 9*(5), 657–677. *(p. 2, 6, 16, 35)*

Oefelein, J. C. and V. Yang (1998). Modeling high-pressure mixing and combustion processes in liquid rocket engines. *J. Propul. Power 14*(5), 843–857. *(p. 6, 8)*

Okong'o, N. and J. Bellan (2002). Consistent boundary conditions for multi-

compoment real gas mixtures based on characteristic waves. *Journal of Computational Physics 176*, 330–344. *(p. 210)*

Oschwald, M., Z. Farago, G. Searby, and F. Cheuret (2008). Resonance frequencies and damping of a combustor acoustically coupled to an absorber. *Journal of Propulsion and Power 24*(3), 524–533. *(p. 140)*

Oschwald, M. and A. Schik (1999). Supercritical nitrogen free jet investigated by spontaneous raman scattering. *Experiments in Fluids 27*, 497–506. *(p. 5)*

Peng, D. and D. B. Robinson (1976). A new two-constant equation of state. *Ind. Eng. Chem. Fundam. 15*, 59–64. *(p. 18, 49, 206)*

Peters, N. (2001). *Turbulent Combustion*. Cambridge University Press. *(p. 214)*

Petit, X., G. Ribert, and P. Domingo (2015). Framework for real-gas compressible reacting flows with tabulated thermochemistry. *The Journal of Supercritical Fluids 101*, 1 – 16. *(p. 24)*

Petit, X., G. Ribert, G. Lartigue, and P. Domingo (2013). Large-eddy simulation of supercritical fluid injection. *The Journal of Supercritical Fluids 84*, 61 – 73. *(p. 24)*

Pierce, C. D. and P. Moin (1998). A dynamic model for subgrid scale variance and dissipation rate of a conserved scalar. *Physics of Fluids 10*(12), 3041–3044. *(p. 214)*

Pierce, C. D. and P. Moin (2004). Progress-variable approach for large eddy simulation of non-premixed turbulent combustion. *Journal of Fluid Mechanics 504*, 73–97. *(p. 47)*

Poinsot, T., T. Baritaud, S. Henriot, A. Torres, and A. Trouvé (1994). Direct numerical simulation of turbulent combustion and implications for piston engine computations. In *ECCOMAS Conference*, pp. 113–122. J. Wiley, Stuttgart. *(p. 20)*

Poinsot, T. and S. Lele (1992). Boundary conditions for direct simulations of compressible viscous flows. *Journal of Computational Physics 101*(1), 104–129. *(p. 210)*

Poinsot, T. and D. Veynante (2001). *Theoretical and numerical combustion*. R.T. Edwards. *(p. 72, 78, 98, 162)*

Poinsot, T. and D. Veynante (2011). Theoretical and numerical combustion - Third Edition. pp. 588. *(p. 209)*

Poling, B. E., J. M. Prausnitz, and J. P. O'Connel (2001). *The properties of gases and liquids* (Fifth ed.). McGraw-Hill. *(p. 5)*

Pons, L. (2009). *Modélisation et simulation de la combustion transcritique*. Ph. D. thesis, Ecole Centrale Paris. *(p. 48, 210)*

Pons, L., N. Darabiha, and S. Candel (2008). Pressure effects on nonpremixed strained flames. *Combustion and Flame 152*(1–2), 218 – 229. *(p. 5, 98, 213)*

Pons, L., N. Darabiha, S. Candel, G. Ribert, and V. Yang (2009). Mass transfer and combustion in transcritical non-premixed counterflows. *Combus-*

tion Theory and Modelling 13(1), 57–81. *(p. 6, 98)*

Pons, L., N. Darabiha, S. Candel, T. Schmitt, and B. Cuenot (2009). The structure of multidimensional strained flames under transcritical conditions. *Comptes Rendus Mécanique 337*(6-7), 517–527. *(p. 6)*

Reid, R., J. Prausnitz, and B. Poling (1987). *The properties of gases and liquids*. McGraw Hill Book Co., New York, NY. *(p. 207)*

Rey, C. (2004). *Interaction collectives dans les instabilités de combustion hautes fréquences. Application aux moteurs fusée à ergols liquides*. Ph. D. thesis, Ecole Centrale Paris. *(p. 2)*

Rey, C., S. Ducruix, and S. Candel (2005). A method for the transverse modulation of reactive flows with application to combustion instability. *Combustion Theory and Modelling 9*, 5–22. *(p. 20, 54)*

Ribert, G., N. Zong, V. Yang, L. Pons, N. Darabiha, and S. Candel (2008). Counterflow diffusion flames of general fluids: Oxygen/hydrogen mixtures. *Combust. Flame 154*(3), 319–330. *(p. 5, 6, 74, 76)*

Richecoeur, F. (2006). *Expérimentations et simulations numériques des intéractions entre modes acoustiques transverses et flammes cryotechniques*. Ph. D. thesis, Ecole Centrale de Paris. *(p. xxviii, 2, 106, 107, 108, 112)*

Richecoeur, F., S. Ducruix, P. Scouflaire, and S. Candel (2009). Effect of temperature fluctuations on high frequency acoustic coupling. *Proceedings of the Combustion Institute 32*(2), 1663 – 1670. *(p. 107, 177)*

Richecoeur, F., P. Scouflaire, S. Ducruix, and S. Candel (2006). High-Frequency Transverse Acoustic Coupling in a Multiple-Injector Cryogenic Combustor. *Journal of Propulsion and Power 22*(4), 790–799. *(p. 8, 48, 107)*

Rodriguez, J., I. Leyva, B. Chehroudi, and D. Talley (2008). *Results of Subcritical One-Phase Coaxial Jet Spread Angles and Subcritical to Supercritical Acousticall-Forced Coaxial Jet Dark Core Lengths*. American Institute of Aeronautics and Astronautics. *(p. 17)*

Roux, S., M. Cazalens, and T. Poinsot (2007). Influence of outlet boundary condition for large eddy simulation of combustion instabilities in gas turbine. *submitted to AIAA Journal* . *(p. 48)*

Ruiz, A. (2012). *Simulations numériques instationnaires de la combustion turbulente et transcritique dans les moteurs cryotechniques*. Ph. D. thesis, Institut National Polytechnique de Toulouse - INPT. *(p. 210)*

Schmitt, T. (2009). *Simulation des grandes échelles de la combustion turbulente à pression supercritique*. Ph. D. thesis, Institut National Polytechnique de Toulouse. *(p. 48, 210)*

Schmitt, T., L. Hakim, M. Boileau, G. Staffelbach, A. Ruiz, S. Ducruix, B. Cuenot, and S. Candel (2014). Large-eddy simulation of a multiple injector cryogenic combustor under transcritical conditions and large amplitude high frequency modulations. *Proceedings of Space Propulsion*. *(p. 8)*

Schmitt, T., Y. Méry, M. Boileau, and S. Candel (2011). Large-eddy simulation of oxygen/methane flames under transcritical conditions. *Proc.*

Combust. Inst. 33, 1383–1390. *(p. 6, 8, 16, 17, 49, 50, 211, 213)*

Schmitt, T., J. Rodriguez, I. A. Leyva, and S. Candel (2012). Experiments and numerical simulation of mixing under supercritical conditions. *Physics of Fluids 24*, 055104. *(p. 8, 17, 211, 212)*

Schmitt, T., A. Ruiz, L. Selle, and B. Cuenot (2011). Numerical investigation of destabilization of supercritical round turbulent jets using large eddy simulation. *Progress in Propulsion Physics 2*, 225–238. *(p. 24)*

Schmitt, T., L. Selle, B. Cuenot, and T. Poinsot (2009). Large-eddy simulation of transcritical flows. *Compte Rendus-Mécanique 337*(6-7), 528–538. *(p. 6, 24)*

Schmitt, T., L. Selle, A. Ruiz, and B. Cuenot (2010, September). Large-eddy simulation of supercritical-pressure round jets. *AIAA journal 48*(9), 2133–2144. *(p. 8, 18, 19, 24, 25, 49, 50, 210, 211, 212)*

Schönfeld, T. and T. Poinsot (1999). Influence of boundary conditions in LES of premixed combustion instabilities. In *Annual Research Briefs* , pp. 73–84. Center for Turbulence Research, NASA Ames/Stanford Univ. *(p. 48)*

Schönfeld, T. and M. Rudgyard (1999). Steady and unsteady flows simulations using the hybrid flow solver AVBP. *AIAA Journal 37*(11), 1378–1385. *(p. 18, 49)*

Schuller, T., D. Durox, and S. Candel (2003). Self-induced combustion oscillations of laminar premixed flames stabilized on annular burners. *Combustion and Flame 135*(4), 525 – 537. *(p. 140)*

Searby, G., M. Habiballah, A. Nicole, and E. Laroche (2008). Prediction of the efficiency of acoustic damping cavities. *Journal of Propulsion and Power 24*(3), 516–523. *(p. 140, 177)*

Segal, C. and S. Polikhov (2008). Subcritical to supercritical mixing. *Physics of Fluids 20*, 052101. *(p. 5)*

Selle, L., L. Benoit, T. Poinsot, F. Nicoud, and W. Krebs (2006). Joint use of compressible large-eddy simulation and helmoltz solvers for the analysis of rotating modes in an industrial swirled burner. *comb. flame 145*(1-2), 194–205. *(p. 168, 188)*

Selle, L., G. Lartigue, T. Poinsot, R. Koch, K.-U. Schildmacher, W. Krebs, B. Prade, P. Kaufmann, and D. Veynante (2004). Compressible large-eddy simulation of turbulent combustion in complex geometry on unstructured meshes. *Combustion and Flame 137*(4), 489–505. *(p. 48, 210)*

Selle, L. and T. Schmitt (2010). Large-eddy simulation of single-species flows under supercritical thermodynamic conditions. *Combustion Science and Technology 182*(4), 392–404. *(p. 212)*

Selle, L. C., N. A. Okong'o, J. Bellan, and K. G. Harstad (2007). Modelling of subgrid-scale phenomena in supercritical transitional mixing layers: an *a priori* study. *Journal of Fluid Mechanics 593*, 57–91. *(p. 212)*

Siebert, W. M. (1985). *Circuits, Signals, and Systems*. The MIT Press. *(p. 142)*

Simeoni, G. G., T. Bryk, F. A. Gorelli, M. Krisch, G. Ruocco, M. Santoro, and T. Scopigno (2010). The Widom-line as the crossover between liquid-like and gas-like behaviour in supercritical fluids. *Nature Physics 6*(7), 503–507. *(p. 19)*

Singla, G. (2005). *Etude des Flammes Cryotechniques Oxygène Liquide/Méthane à Haute Pression*. Ph. D. thesis, Ecole Centrale de Paris. *(p. 4)*

Singla, G., P. Scouflaire, C. Rolon, and S. Candel (2005). Transcritical oxygen/transcritical or supercritical methane combustion. *Proceedings of the Combustion Institute 30*(2), 2921–2928. *(p. 4, 6, 213)*

Singla, G., P. Scouflaire, C. Rolon, and S. Candel (2006). Planar laser-induced fluorescence of OH in high-pressure cryogenic LOx/GH2 jet flames. *Combust. Flame 144*(1-2), 151–169. *(p. 4, 213)*

Singla, G., P. Scouflaire, C. Rolon, S. Candel, and L. Vingert (2007). OH-PLIF and emission imaging in high pressure cryogenic LOx/methane flames. *Journal Propulsion and Power 3*(23), 593–602. *(p. 4, 5, 213)*

Singla, G., P. Scouflaire, J. Rolon, and S. Candel (2007). Flame stabilization in high pressure LOx-GH2 and GCH4 combustion. *Proceedings of the Combustion Institute 31*(2), 2215 – 2222. *(p. 4, 19)*

Smagorinsky, J. (1963). General circulation experiments with the primitive equations: 1. the basic experiment. *Monthly Weather Review 91*, 99–164. *(p. 212)*

Smirnov, A., S. Shi, and I. Celik (2001). Random flow generation technique for large eddy simulations and particle-dynamics modeling. *Trans. ASME. Journal of Fluids Engineering 123*, 359–371. *(p. 19)*

Snyder, R., G. Herding, J. C. Rolon, and S. Candel (1997). Analysis of flame patterns in cryogenic propellant combustion. *Combustion Science and Technology 124*(1-6), 331–370. *(p. 4)*

Soave, G. (1977). Equilibrium constants from a modified redlich-kwong equation of state. *Chemical Engineering Science 27*, 1197–1203. *(p. 206)*

Speziale, C., G. Erlebacher, T. Zang, and M. Y. Hussaini (1988). The subgrid-scale modelling of compressible turbulence. *Physics of Fluids 31*, 940–942. *(p. 212)*

Stokes, G. G. (1868). On the communication of vibration from a vibrating body to a surrounding gas. *Philosophical Transactions of the Royal Society of London 158*, 447–463. *(p. 140)*

Tang, P., D. Harrje, and W. Sirignano (1973). Experimental verification of the energy dissipation mechanism in acoustic dampers. *Journal of Sound and Vibration 26*(2), 263 – 276. *(p. 140)*

Taskinoglu, E. and J. Bellan (2010). A posteriori study using a DNS database describing fluid disintegration and binary-species mixing under supercritical pressure: heptane and nitrogen. *Journal of Fluid Mechanics 645*, 211–254. *(p. 212)*

Terashima, H. and M. Koshi (2013, November-December). Unique charac-

teristics of cryogenic nitrogen jets under supercritical pressures. *Journal of propulsion and power 29*(6), 1328–1336. *(p. 24)*

Tong, A. Y. and W. A. Sirignano (1986). Multicomponent transient droplet vaporization with internal circulation: Integral equation formulation and approximate solution. *Numerical Heat Transfer 10*(3), 253–278. *(p. 140)*

Tripathi, A. (2001). *Structure de flammes cryotechniques à haute pression.* Ph. D. thesis, Ecole Centrale de Paris. *(p. 4)*

Tsien, H. S. (1952a). Servo-stabilization of combustion in rocket motors. *J. Am. Rocket Soc. 22*(5), 256–262. *(p. 7, 49)*

Tsien, H. S. (1952b). The transfer functions of rocket nozzles. *Journal of the American Rocket Society* (May-June), 139–143. *(p. 140)*

Urbano, A., Q. Douasbin, L. Selle, G. Staffelbach, B. Cuenot, T. Schmitt, S. Ducruix, and S. Candel (2016). Study of flame response to transverse acoustic modes from the {LES} of a 42-injector rocket engine. *Proceedings of the Combustion Institute*, –. *(p. 48, 80)*

Urbano, A., L. Selle, G. Staffelbach, B. Cuenot, T. Schmitt, S. Ducruix, and S. Candel (2016). Exploration of combustion instability triggering using large eddy simulation of a multiple injector liquid rocket engine. *Combustion and Flame 169*, 129 – 140. *(p. 48, 187)*

Vermorel, O., S. Richard, O. Colin, C. Angelberger, A. Benkenida, and D. Veynante (2007). Multi-cycle LES simulations of flow and combustion in a PFI SI 4-valve production engine. *SAE* (2007-01-0151). *(p. 210)*

Veynante, D. and L. Vervisch (2002). Turbulent combustion modeling. *Progress in Energy and Combustion Science 28*, 193 – 266. *(p. 213)*

Vingert, L., M. Habiballah, P. Hervat, F. Dugue, and P. Vuillermoz (1997). Evolution of the mascotte test bench ti high pressure operation and related combustor technology issues. In *Third French-German Colloquium on Rocket Engine Propulsion, Marseille, France.* *(p. 107)*

Vingert, L., M. Habiballah, P. Vuillermoz, and S. Zurbach (2000). Mascotte, a test facility for cryogenic combustion research at high pressure. In *51st International Astronautical Congress, Rio de Janeiro, Brazil.* *(p. 107)*

Wawrzak, K., A. Boguslawski, and A. Tyliszczak (2015). LES predictions of self-sustained oscillations in homogeneous density round free jet. *Flow, Turbulence and Combustion 95.* *(p. 17)*

Wei, W., D. B. Thiessen, and P. L. Marston (2004). Acoustic radiation force on a compressible cylinder in a standing wave. *The Journal of the Acoustical Society of America 116*(1), 201–208. *(p. 37)*

Wolf, P., R. Balakrishnan, G. Staffelbach, L. Y. Gicquel, and T. Poinsot (2012). Using les to study reacting flows and instabilities in annular combustion chambers. *Flow, turbulence and combustion 88*(1-2), 191–206. *(p. 48)*

Wolf, P., G. Staffelbach, A. Roux, L. Gicquel, T. Poinsot, and V. Moureau (2009). Massively parallel les of azimuthal thermo-acoustic instabilities in annular gas turbines. *Comptes rendus de l'Académie des sciences Mé-*

canique 337(6-7), 385–394. *(p. 48)*

Wu, J., G. Du, S. S. Work, and D. M. Warshaw (1990). Acoustic radiation pressure on a rigid cylinder: An analytical theory and experiments. *The Journal of the Acoustical Society of America 87*(2), 581–586. *(p. 37)*

Yang, V. (2000). Modeling of supercritical vaporization, mixing, and combustion processes in liquid-fueled propulsion systems. *Proceedings of the Combustion Institute 28*, 925–942. *(p. 6, 207)*

Yang, V. and W. Anderson (1995). *Liquid rocket engine combustion instability*. AIAA. *(p. 7)*

Zong, N. and V.Yang (2006). Cryogenic fluid jets and mixing layers in transcritical and supercritical environments. *Combustion Science and Technology 178*, 193–227. *(p. 17, 24, 25)*

Zong, N. and V. Yang (2007). Near-field flow and flame dynamics of LOX/methane shear-coaxial injector under supercritical conditions. *Proceedings of the Combustion Institute 31*(2), 2309–2317. *(p. 6)*

ÉCOLE DOCTORALE
Sciences mécaniques et énergétiques, matériaux et géosciences (SMEMAG)

Titre : Contributions en simulation, expérimentation et modélisation destinées à l'analyse des instabilités de combustion hautes fréquences des moteurs fusées à ergols liquides

Mots-clefs : Instabilités de combustion, moteur-fusée, cryotechnique, SGE, flamme transcritique, jet rond, acoustique, banc expérimental, amortissement, ordre réduit

Résumé : Cette recherche se focalise sur les problèmes d'instabilités de combustion hautes fréquences dans les moteurs fusées. Ces instabilités sont connues pour avoir des effets néfastes et peuvent, dans certains cas, causer la destruction du système propulsif. Pour éviter l'apparition de ces instabilités, il est important de connaître les mécanismes qui entretiennent ces phénomènes dynamiques et de comprendre le couplage complexe entre l'injection, la combustion et la résonnance acoustique du système. Ce travail comprend trois parties.
La première partie traite de la simulation numérique de jets non-réactifs et réactifs soumis à différentes conditions de modulation afin de comprendre les interactions entre les jets, les flammes et leur environnement. Les calculs numériques de jets ronds non-réactifs ainsi que des flammes plus complexes formées par des injecteurs coaxiaux dans des conditions transcritiques ont été effectuées avec des simulations aux grandes échelles (SGE), adaptées aux conditions gaz réels à l'aide du solveur AVBP-RG. Les jets ronds ont été soumis à des fluctuations de vitesse transverse. Il a été trouvé que pour toutes les amplitudes et fréquences de modulation, le jet est déformé et oscille dans la direction transverse. Ce comportement peut être représenté par un modèle. Les flammes coaxiales ont été soumises à une modulation de débit et de pression. La modulation induit des variations du dégagement de chaleur global. Un modèle mathématique reliant les paramètres modulés au dégagement de chaleur est proposé.
La seconde partie contient les travaux expérimentaux. Dans ce cadre, un nouveau banc expérimental a été développé pour l'étude de cavités couplées pressurisées (NPCC). Le couplage entre le plénum (ou dôme) et la chambre a été étudié. Un modèle reliant les fluctuations de pression et de vitesse en sortie des injecteurs a été développé et comparés aux données d'essais. Le banc NPCC a aussi été utilisé pour acquérir plus de connaissances sur le niveau d'amortissement. Les coefficients d'amortissement ont été déterminés.
La dernière partie de ce document traite du développement d'un modèle ordre réduit qui représente des mécanismes qui entretiennent et amortissent les instabilités de combustion hautes fréquences. Cette description dynamique a été incorporée dans un code de stabilité haute fréquence (STAHF). Ce code a été utilisé pour étudier un moteur à ergols liquides d'une puissance de 87 MW (le banc BKD du DLR en Allemagne) qui présente des instabilités hautes fréquences. Après le recalage de certains paramètres de contrôle, STAHF a été capable de retrouver des résultats obtenus d'essais au DLR.

Title: Simulation, experimentation and modeling contributions to the analysis of high frequency combustion instabilities in liquid propellant rocket-engines

Keywords: Combustion instabilities, rocket-engine cryogenic, LES, transcritical flame, round jet, acoustic, experimental test rig, damping, reduced order

Abstract: This research concerns some of the issues raised by high frequency combustion instabilities in rocket engines. These instabilities are known to have detrimental effects leading, in some cases, to the destruction of the propulsion system. To avoid the appearance of such instabilities it is important to gain an understanding of the processes driving such dynamical phenomena. One has to consider the complex coupling between injection, combustion and the acoustic resonances of the system. The present work contributes to this objective by developing three items.
The first deals with numerical simulations of non-reactive and reactive jets submitted to different modulation conditions to understand the interaction between jets, flames and their environment. Numerical simulations of non-reactive round jets as well as more complex flames formed by coaxial injectors operating under transcritical conditions were carried out using large eddy simulation (LES) adapted to real gas situations by making use of the AVBP-RG flow solver. Round jets were submitted to transverse velocity fluctuations. It has been found that for all amplitudes and frequencies of modulation, the modulated jet is deformed and oscillates. This behavior can be represented by a model. The coaxial flames were submitted to mass flow rate and pressure modulation. For these cases it has been found that the modulation induces variations of the global heat release rate. A mathematical relationship between the modulated parameters and the heat release rate has been proposed.
The second item includes experimental investigations. For this purpose a New Pressurized Coupled Cavities (NPCC) laboratory test rig has been developed. The possible coupling between the plenum and the thrust chamber was studied. A model, linking pressure and velocity fluctuations between the plenum and the thrust chamber, has been developed. The laboratory test rig was also used to gather some knowledge on the levels of damping and the damping coefficients could be determined.
The last item of this document deals with the development of a reduced order dynamical model which includes some of the driving and damping mechanisms of high frequency combustion instabilities. This dynamical description was implemented in a high frequency stability code (STAHF). This code was used to examine a 87 MW liquid rocket engine (BKD operated at DLR, Germany) exhibiting high frequency oscillations. After the adjustment of some control parameters, STAHF was able to retrieve some the features observed in experiments carried out at DLR.

Université Paris-Saclay
Espace Technologique / Immeuble Discovery
Route de l'Orme aux Merisiers RD 128 / 91190 Saint-Aubin, France